12 June 2009 | $10

Science

AAAS

Affymetrix

Revolutionize life

With a limited view, you're simply left guessing.

With GeneChip® Exon and Gene 1.0 ST Arrays, you don't have to guess. Whole-transcript expression arrays allow you to measure the entire transcript, enabling you to detect gene-level expression, exon-level expression, and alternative splicing in a single experiment. Why settle for incomplete results when you can look beyond the 3′ end of a gene? Extrapolation can only take you so far—Affymetrix will take you the rest of the way.

See the real biology at www.affymetrix.com/genechip/wtexpression

cell sciences®

www.CytokineCenter.com

www.cellsciences.com

Cytokine Center

Browse our web site with over 1300 proteins, including recombinant cytokines, growth factors, chemokines and neurotrophins. Daily shipping and competitive pricing are offered. Bulk quantities of many proteins available.

PROTEINS

4-1BBL
4-1BB Receptor
6 Ckine
ACAD8
ACAT2
gAcrp30/Adipolean
Activin A
Activin B
ACY1
ADAT1
Adiponectin
ADRP
AITRL
Akt1
Alpha-Feto Protein (AFP)
Alpha-Galactosidase A
Angiopoietin-1 (Ang-1)
Angiopoietin-2 (Ang-2)
Angiostatin K1-3
Annexin-V
apo-SAA
Apoliprotein A-1
Apoliprotein E2
Apoliprotein E3
Apoliprotein E4
APRIL
Artemin
ATF2
Aurora A
Aurora B
BAFF
BAFF Receptor
BCA-1 / BLC / CXCL13
BCMA
BD-1
BD-2
BD-3
BDNF
Betacellulin
Bivalirudin
BMP-2
BMP-4
BMP-6
BMP-7
BMP-13
sBMPR-1A
Brain Natriuretic Protein
BRAK
Breast Tumor Antigen
C5a
C5L2 Peptide
C-10
C-Reactive Protein
C-Src
Calbindin D-9K
Calbindin D-28K
Calbindin D-29K
Calmodulin
Calcitonin Acetate
Carbonic Anhydrase III
Carcino-embryonic Antigen
Cardiotrophin-1
Caspase-3
Caspase-6
CD4
CD14
CD22
CD40 Ligand / TRAP
CD95 / sFas Ligand
CD105 / Endoglin
CHIPS
CNTF
Collagen
CREB
CTACK / CCL27
CTGF
CTGFL / WISP-2
CTLA-4 / Fc
CXCL16
CYR61
Cytokeratin 8
DEP-1
Desmopressin
Disulfide Oxidoreductase
E-selectin
ECGF
EGF
Elafin / SKALP
EMAP-II
ENA-78 / CXCL5
Endostatin
Enteropeptidase
Eotaxin / CCL11
Eotaxin-2
Eotaxin-3 (TSC)
EPHB2
EPHB4
Epigen
Epiregulin
Eptifbatide
Erk-2
Erythropoietin (EPO)
Exodus-2
Fas Ligand
Fas Receptor
FGF-1 (acidic)
FGF-2 (basic)
FGF-4
FGF-5
FGF-6
FGF-7 / KGF
FGF-8
FGF-9
FGF-10
FGF-16
FGF-17
FGF-18
FGF-19
FGF-20
sFGFR-1 (IIIc) / Fc Chimera
sFGFR-2 (IIIc) / Fc Chimera
sFGFR-3 / Fc Chimera
sFGFR-4 / Fc Chimera
sFlt-1 (native)
sFlt-1 (D3)
sFlt-1 (D4)
sFlt-1 (D5)
sFlt-1 (D7)
Flt3-Ligand
sFlt-4
sFlt-4 / Fc Chimera
Follistatin
FSH
Fractalkine / CX3C
G-CSF
α-Galactosidase A
Galectin-1
Galectin-3
Gastrointestinal CA
GCP-2
GDF-3
GDF-9
GDF-11
GDNF
GLP-1
Glucagon
GM-CSF
Goserelin
GPBB
Granzyme B
GROα
GROβ
GROγ
GRO/MGSA
Growth Hormone
Growth Hormone BP
GST-p21/WAF-1
HB-EGF
HCC-1
HGF
Histdyl-tRNA synthetase
Histrelin
HRG1-β1
I-309
I-TAC
IFN-α
IFN-α A
IFN-α 2a
IFN-α 2b
IFN-β
IFN-γ
IFN-Omega
IGF-I
IGF-II
proIGF-II
IGFBP-1
IGFBP-2
IGFBP-3
IGFBP-4
IGFBP-5
IGFBP-6
IGFBP-7
IL-1α
IL-1β
IL-2
IL-3
IL-4
sIL-4 Receptor
IL-5
IL-6
sIL-6 Receptor
IL-7
IL-8 (72 a.a.)
IL-8 (77 a.a.)
IL-9
IL-10
IL-11
IL-12
IL-13
IL-13 analog
IL-15
IL-16 (121 a.a.)
IL-16 (130 a.a.)
IL-17
IL-17B
IL-17D
IL-17E
IL-17F
IL-19
IL-20
IL-21
IL-22
IL-31
Insulin
IP-10
JE
JNK2a1
JNK2a2
KC / CXCL1
KGF
L-asparaginase
LAG-1
LALF Peptide
LAR-PTP
LBP
LC-1
LD-78β
LDH
LEC / NCC-4
Leptin
LIGHT
LIX
LKM
LL-37
Lungkine / CXCL15
Lymphotactin
sLYVE-1
M-CSF
MCP-1 (MCAF)
MCP-2
MCP-3
MCP-4
MCP-5
MDC (67 a.a.)
MDC (69 a.a.)
MDH
MEC
Mek-1
MIA
Midkine
MIG / CXCL9
MIP-1α / CCL3
MIP-1β / CCL4
MIP-3 / CCL23
MIP-3α / CCL20
MIP-3β / CCL19
MIP-4 (PARC) / CCL18
MIP-5 / CCL15
MMP-3
MMP-7
MMP-13
Myostatin
Nanog
NAP-2
Neurturin
NFAT-1
β-NGF
NOGGIN
NOV
NP-1
NT-1/BCSF-3
NT-3
NT-4
Ocreotide
Oncostatin M
Osteoprotegerin (OPG)
OTOR
Oxytocin
p38-α
PAI-1
Parathyroid Hormone
PDGF-AA
PDGF-AB
PDGF-BB
PDGF-CC
Persephin
PF-4
PIGF-1
PIGF-2
PKA α-subunit
PKC-α
PKC-γ
Pleiotrophin
PLGF-1
Polymyxin B (PMB)
PRAS40
PRL-1
PRL-2
PRL-3
Prokineticin-2
Prolactin
Protirelin
PTHrP
PTP1B
PTP-IA2
PTP-MEG2
PTP-PEST
sRANK
sRANKL
RANTES
RELM-α
RELM-β
Resistin
RPTPβ
RPTPγ
RPTPμ
SCF
SCGF-α
SCGF-β
SDF-1α
SDF-1β
Secretin
SF20
SHP-2
STAT1
c-Src
TACI
TARC
TC-PTP
TECK
TFF2
TGF-α
TGF-β1
TGF-β2
TGF-β3
Thymosin α1
sTIE-1/Fc Chimera
sTIE-2/Fc Chimera
TL-1A
TNF-α
TNF-β
sTNF-receptor Type I
sTNF-receptor Type II
TPO
sTRAIL R-1 (DR4)
sTRAIL R-2 (DR5)
TRAIL/Apo2L
TSG
TSH
TSLP
TWEAK
TWEAK Receptor
Urokinase
EG-VEGF
VEGF121
VEGF145
VEGF165
VEGF-C
VEGF-C I125
VEGF-E
HB-VEGF-E
sVEGFR-1
sVEGFR-2
sVEGFR-3
Visfatin
WISP-1
WISP-2
WISP-3
WNT-1

480 Neponset Street, Building 12A, Canton, MA 02021 • TEL (781) 828-0610 • EMAIL info@cellsciences.com

CALL TOLL FREE (888) 769-1246 • FAX (781) 828-0542 • VISIT www.cellsciences.com

GE Healthcare

Coordinate your application focus. Achieve greater operational efficiency.

GE Healthcare is focused on helping you develop efficient biopharmaceutical process flows and eliminating wasteful practices, taking your value stream to new frontiers. Through our wide range of technology platforms and services, upstream and downstream from process development to final manufacturing scale, GE Healthcare can connect you to the power of operational excellence.

Learn more about operational excellence at: www.gelifesciences.com/opex

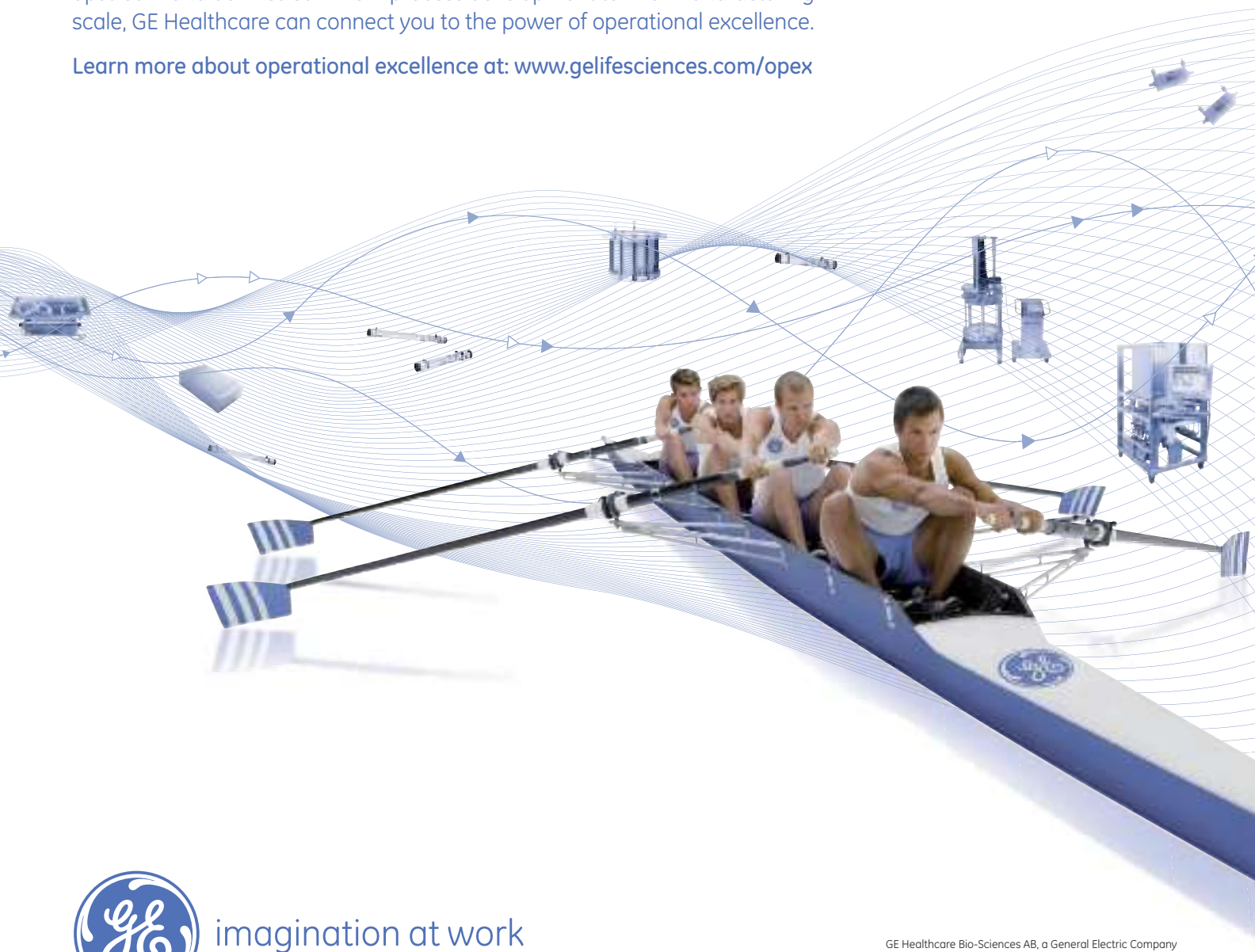

imagination at work

GE Healthcare Bio-Sciences AB, a General Electric Company
Björkgatan 30, 751 84 Uppsala, Sweden

GE04-09. First printetd 09/2008.

EDITORIAL

1365 Reset Cooperation with Russia
Glenn Schweitzer

NEWS OF THE WEEK

1372 Congress Takes First Step Toward One-Stop Shopping for Climate

1373 Macau Launches Late Bid to Cure Its Pearl River Delta Blues

1374 U.S. Supreme Court Delves Into What Is and Isn't Patentable

1375 Science Windfall Stimulates High Hopes—and Political Maneuvering

1375 From *Science*'s Online Daily News Site

1376 Scientists Seek Easier Access to Seed Banks

1377 U.S. Promises to Reduce Delays in Granting Visas for Scientists

1377 From the *Science* Policy Blog

NEWS FOCUS

1378 A Medical Mystery in Middle China
>> Science *Podcast*

1382 Russia's Polar Hero
Diving Into the Sacred Sea

1385 Authors Scramble to Make Textbooks Conform to Texas Science Standards

1386 Minority Retention Rates in Science Are Sore Spot for Most Universities
Following the Leaders

LETTERS

1389 Redesigning the Wildlife Trade System
A. P. Pernetta
Wood Energy: Predicting Costs
F. D. Doty
Wood Energy: Protect Local Ecosystems
B. D. Titus et al.
Wood Energy: The Dangers of Combustion
F. J. Ries et al.
Response
D. deB. Richter Jr. et al.

1391 CORRECTIONS AND CLARIFICATIONS

1391 TECHNICAL COMMENT ABSTRACTS

BOOKS *ET AL.*

1392 SuperSense
B. M. Hood, reviewed by M. Shermer

1393 Dread
P. Alcabes, reviewed by K. R. Foster

POLICY FORUM

1394 Repurposing with a Difference
M. S. Boguski et al.

PERSPECTIVES

1396 Extreme Spinning Tops
M. Kramer
>> Report p. 1411

1397 Novel Probes for Molecular Electronics
E. Meyer and T. Glatzel
>> Report p. 1428

1398 Silicon Carbide as a Platform for Power Electronics
C. R. Eddy Jr. and D. K. Gaskill

1400 Breaching the Cancer Fortress
P. Olson and D. Hanahan
>> Report p. 1457

1401 Yield Stress Fluids Slowly Yield to Analysis
D. Bonn and M. M. Denn

REVIEW

1403 Comprehensive Control of Atomic Motion
M. G. Raizen

BREVIA

1407 Herapathite
B. Kahr et al.
Discovered in 1852 and used for polarizing light, the crystal structure of iodoquinine sulfate has been solved.

CONTENTS continued **>>**

page 1378

page 1393

COVER

The flight path of a maple seed visualized in a composite multiflash photograph. Autorotating seeds slow their descent by exploiting the low pressure generated by a vortex that forms at the leading edge of their spinning wing. A similar leading-edge vortex also elevates the lift of insect, bat, and hummingbird wings. See page 1438.

Photo: David Lentink

DEPARTMENTS

1362 This Week in *Science*
1366 Editors' Choice
1368 *Science* Staff
1371 Random Samples
1462 New Products
1463 *Science* Careers

Epigenetics sample and assay technologies by QIAGEN

Trust in methylation analysis

Rely on QIAGEN epigenetics sample and assay technologies for:

- **DNA purification**
- **Bisulfite conversion**
- **Whole bisulfitome amplification**
- **Methylation-specific PCR**
- **Methylation detection and quantification with Pyrosequencing**

Making improvements in life possible — www.qiagen.com

QIAGEN®

Sample & Assay Technologies

ADNAEpigenetics0309S1WW

REPORTS

1408 Magnetic Fields in the Formation of Massive Stars
J. M. Girart et al.
Observations of polarized dust emission show that the magnetic field controls the dynamical evolution of a massive star-forming region.

1411 A Radio Pulsar/X-ray Binary Link
A. M. Archibald et al.
Radio observations reveal a system undergoing the transition from a low-mass x-ray binary star to a millisecond radio pulsar.
>> *Perspective p. 1396*

1414 Determining the Dynamics of Entanglement
O. Jiménez Farías et al.
The evolution of quantum mechanically entangled photon pairs can now be measured as they interact with their environment.

1417 Colloidal Nanocrystals with Molecular Metal Chalcogenide Surface Ligands
M. V. Kovalenko et al.
Chalcogenide-based ligands are used to link colloidal nanocrystals together and can be converted into semiconducting complexes.

1421 Polarization Control of Electron Tunneling into Ferroelectric Surfaces
P. Maksymovych et al.
High electric fields delivered with an atomic force microscope tip pattern polarization domains in ferroelectric thin films.

1425 Isotopic Homojunction Band Engineering from Diamond
H. Watanabe et al.
Nanoscale multilayers of diamond that alternate in isotopic composition create quantum wells that confine electrons.

1428 Measuring the Charge State of an Adatom with Noncontact Atomic Force Microscopy
L. Gross et al.
Charging of gold and silver atoms on salt films changes the force detected by the tip of a scanning probe microscope.
>> *Perspective p. 1397;* Science *Podcast*

1431 Oxygen-18 of O_2 Records the Impact of Abrupt Climate Change on the Terrestrial Biosphere
J. P. Severinghaus et al.
Ice core studies show that changes in low-latitude rainfall accompanied abrupt climate change over the past 100,000 years.

1435 Boom-and-Bust Development Patterns Across the Amazon Deforestation Frontier
A. S. L. Rodrigues et al.
Rainforest loss in the Amazon is associated with ephemeral increase in people's relative prosperity.
>> Science *Podcast*

1438 Leading-Edge Vortices Elevate Lift of Autorotating Plant Seeds
D. Lentink et al.
Winged plant seeds use leading-edge vortices to create lift, in the same way that flying animals do.

1441 Fluorescent False Neurotransmitters Visualize Dopamine Release from Individual Presynaptic Terminals
N. G. Gubernator et al.
Optical tracking of neurotransmitter release in the brain reveals multiple synaptic populations that depend on brain activity.

1444 Structure of Rotavirus Outer-Layer Protein VP7 Bound with a Neutralizing Fab
S. T. Aoki et al.
Binding of neutralizing antibodies to rotavirus stabilizes coat-protein trimers and blocks cell entry.

1447 Extensive Demethylation of Repetitive Elements During Seed Development Underlies Gene Imprinting
M. Gehring et al.
Gene function in *Arabidopsis* endosperm depends on whether a gene is maternally or paternally inherited.

1451 Genome-Wide Demethylation of *Arabidopsis* Endosperm
T.-F. Hsieh et al.
The endosperm genome of *Arabidopsis* shows extensive gene imprinting.

1454 Hyper-Recombination, Diversity, and Antibiotic Resistance in Pneumococcus
W. P. Hanage et al.
Promiscuity not only leads to diversity in streptococcal bacteria, but also to an increased likelihood of acquiring drug resistance.

1457 Inhibition of Hedgehog Signaling Enhances Delivery of Chemotherapy in a Mouse Model of Pancreatic Cancer
K. P. Olive et al.
Pancreatic tumors are unresponsive to chemotherapy because their limited vasculature precludes efficient drug delivery.
>> *Perspective p. 1400*

CONTENTS continued **>>**

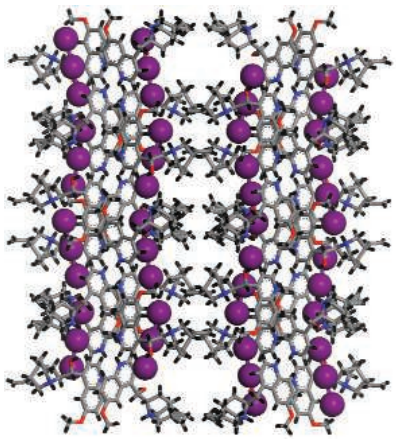

page 1407

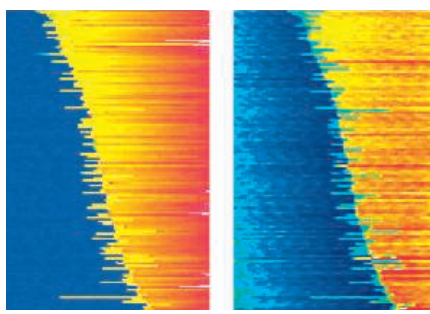

page 1421

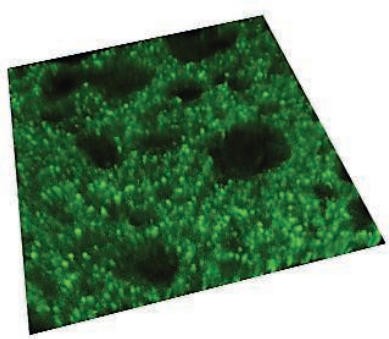

page 1441

Published by AAAS

enzymagic.

PCR enzymes with extraordinary capabilities.

For 10 years, Bio-Rad has been innovating real-time PCR by listening to the experts: you.

Introducing SsoFast™ EvaGreen® supermix — a unique Sso7d fusion polymerase combined with EvaGreen dye and optimized buffer that delivers unrivaled speed and performance for a variety of qPCR applications. Using our patented* Sso7d fusion protein technology, SsoFast EvaGreen supermix offers:

- Minimal inhibition of PCR — ensures maximum efficiency, sensitivity, and reproducibility while providing higher fluorescence
- Instant polymerase activation and rapid polymerization kinetics for fast qPCR results in less than 30 min
- Guaranteed high resolution melt capability for genotyping studies

Together, we've rethought PCR. Please visit **www.bio-rad.com/ad/ssofast/** for more information.

Research. Together.

* U.S. patent 6,627,424.

EvaGreen is a trademark of Biotium, Inc. Bio-Rad Laboratories, Inc. is licensed by Biotium, Inc. to sell reagents containing EvaGreen dye for use in real-time PCR, for research purposes only.

Purchase of this product includes an immunity from suit under patents specified in the product insert to use only the amount purchased for the purchaser's own internal research. No other patent rights are conveyed expressly, by implication, or by estoppel. Further information on purchasing licenses may be obtained by contacting the Director of Licensing, Applied Biosystems, 850 Lincoln Centre Drive, Foster City, California 94404, USA.

SCIENCEONLINE

SCIENCEXPRESS
www.sciencexpress.org

Genome-Wide RNAi Screen Identifies Genes Involved in Intestinal Pathogenic Bacterial Infection
S. J. F. Cronin et al.

In vivo RNA interference screen reveals regulators of innate immunity in *Drosophila*.
10.1126/science.1173164

Meningococcal Type IV Pili Recruit the Polarity Complex to Cross the Brain Endothelium
M. Coureuil et al.

Adhesion of bacteria to cells lining blood vessels in the brain induces them to part and allows pathogen invasion.
10.1126/science.1173196

LXR Regulates Cholesterol Uptake Through Idol-Dependent Ubiquitination of the LDL Receptor
N. Zelcer et al.

Cholesterol metabolism is regulated by a signaling pathway that targets the LDL receptor for degradation.
10.1126/science.1168974

Self-Assembling Sequence-Adaptive Peptide Nucleic Acids
Y. Ura et al.

A synthetic DNA analog can dynamically adapt its sequence in response to changing templates.
10.1126/science.1174577

Experimental Realization of a Three-Dimensional Topological Insulator, Bi_2Te_3
Y. L. Chen et al.

Bi_2Te_3 is identified as a three-dimensional topological insulator with a single metallic surface state.
10.1126/science.1173034

TECHNICALCOMMENTS

Comment on "Tail Reconnection Triggering Substorm Onset"
A. T. Y. Lui

full text at www.sciencemag.org/cgi/content/full/324/5933/1391-b

Response to Comment on "Tail Reconnection Triggering Substorm Onset"
V. Angelopoulos et al.

full text at www.sciencemag.org/cgi/content/full/324/5933/1391-c

SCIENCENOW
www.sciencenow.org
Highlights From Our Daily News Coverage

Snakes on a Pane
Researchers figure out how snakes move over flat surfaces.

Physicists Put the Quantum Into Mechanics
Experiment demonstrates weird quantum connection between tiny "machines."

Case Closed: Scientists Nab Birds That Brought Down Airplane
Forensic analysis of feathers fingers culprit in Hudson River crash.

SCIENCESIGNALING
www.sciencesignaling.org
The Signal Transduction Knowledge Environment

RESEARCH ARTICLE: PI3Kγ Adaptor Subunits Define Coupling to Degranulation and Cell Motility by Distinct PtdIns(3,4,5)P_3 Pools in Mast Cells
T. Bohnacker et al.

PERSPECTIVE: Finding Partners for PI3Kγ—When 84 Is Better Than 101
T. Balla

PODCAST
M. P. Wymann and A. M. VanHook

Adaptor subunits of phosphoinositide 3-kinase γ specify different cellular responses.

PERSPECTIVE: Insulin Signaling in Sporadic Alzheimer's Disease
F.-F. Liao and H. Xu

Amyloid-β and its oligomers disrupt insulin signaling by targeting the insulin receptor or downstream kinases.

SCIENCECAREERS
www.sciencecareers.org/career_magazine
Free Career Resources for Scientists

Speed Networking for Scientists
L. Holmes and K. Travis

Speed networking can be an effective way to promote new research collaborations.

Reaching for the Stars
C. Thomas

Maggie Aderin-Pocock's passion for science drives her career and public outreach.

Science Careers on Facebook
Science *Careers Staff*

Become a Facebook fan at http://www.facebook.com/pages/Science-Careers/11799201290.

SCIENCEPODCAST
www.sciencemag.org/multimedia/podcast
Free Weekly Show

Download the 12 June *Science* Podcast to hear about deforestation and development in the Amazon, stamping out Kashin-Beck disease in China, measuring the charge state of gold and silver atoms, and more.

ORIGINSBLOG
blogs.sciencemag.org/origins
A History of Beginnings

SCIENCEINSIDER
blogs.sciencemag.org/scienceinsider
Science Policy News and Analysis

SCIENCE**NOW**
How dost thou slither?

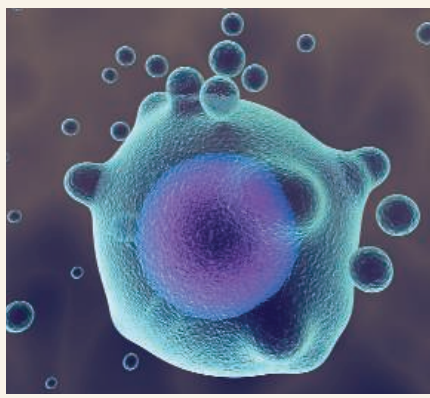

SCIENCE**SIGNALING**
Mast cell degranulation.

SCIENCE**CAREERS**
Find a lot of collaborators all at once.

CREDITS: (*SCIENCE NOW*) GRACE PRYOR AND DAVID HU; (*SCIENCE SIGNALING*) CHRIS BICKEL; (*SCIENCE CAREERS*) LOUISE HOLMES

SCIENCE (ISSN 0036-8075) is published weekly on Friday, except the last week in December, by the American Association for the Advancement of Science, 1200 New York Avenue, NW, Washington, DC 20005. Periodicals Mail postage (publication No. 484460) paid at Washington, DC, and additional mailing offices. The title SCIENCE is a registered trademark of the AAAS. Domestic individual membership and subscription (51 issues): $146 ($74 allocated to subscription). Domestic institutional subscription (51 issues): $835; Foreign postage extra: Mexico, Caribbean (surface mail) $55; other countries (air assist delivery) $85. First class, airmail, student, and emeritus rates on request. Canadian rates with GST available upon request, GST #1254 88122. Publications Mail Agreement Number 1069624. **Printed in the U.S.A.**

Change of address: Allow 4 weeks, giving old and new addresses and 8-digit account number. **Postmaster:** Send change of address to AAAS, P.O. Box 96178, Washington, DC 20090–6178. **Single-copy sales:** $10.00 current issue, $15.00 back issue prepaid includes surface postage; bulk rates on request.

AAAS
ADVANCING SCIENCE, SERVING SOCIETY

EDITED BY STELLA HURTLEY

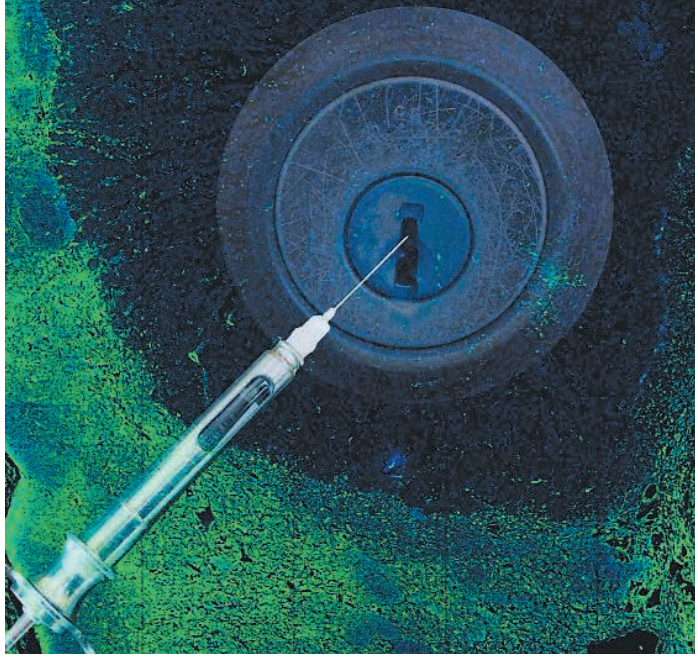

It's All in the Delivery >>

Pancreatic cancer is almost universally associated with a poor prognosis, in part because the tumors are resistant to chemotherapeutic drugs. Working with a mouse tumor model that displays many features of the human disease, **Olive *et al.*** (p. 1457, published online 21 May; see the Perspective by **Olson and Hanahan**) found that the tumors were poorly vascularized, a factor likely to impede drug delivery. Treatment of the mice with the chemotherapeutic drug gemcitabine in combination with a drug that depletes tumor-associated stromal tissue led to an increase in tumor vasculature, enhanced delivery of gemcitabine, and a delay in disease progression. Thus, drugs targeting the tumor stroma may merit investigation as a way to enhance the efficacy of conventional chemotherapy for pancreatic cancer.

Stellar Hourglass Figure

Star-forming clouds are thought to be supported against gravity by ordered interstellar magnetic fields, which are strong enough to slow gravitation collapse but too weak to prevent it. **Girart *et al.*** (p. 1408) measured polarized radio waves from dust particles around a forming massive star, which reveal an hourglass shape. The data imply that a magnetic field strength dominates over turbulence—the telltale signs of magnetically controlled star formation. These conditions mimic those found in low-mass star-forming regions, suggesting that the magnetic field plays an important role in star formation, irrespective of differences in mass.

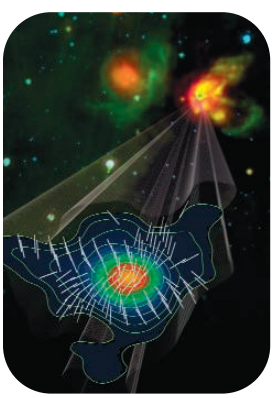

From X-ray Binary to Pulsar

Pulsars with millisecond rotational periods are thought to originate from neutron stars in low-mass x-ray binaries that had their spin frequencies increased by long-lasting mass transfer from their companion stars. Using data from a radio pulsar survey, **Archibald *et al.*** (p. 1411, published online 21 May; see the Perspective by **Kramer**) found a neutron star in a low-mass X-ray binary that is in the process of turning into a radio millisecond pulsar. The system, which consists of a solar-like star and a 1.69-millisecond radio pulsar, has gone through a recent accretion phase, characteristic of low-mass X-ray binaries, but it shows no accretion disk anymore, confirming the evolutionary connection between millisecond radio pulsars and low-mass X-ray binaries.

Confining Carriers in Diamond

Charge carriers can be confined in thin layers created by quantum wells. These multilayer structures alternate nanoscale layers of materials with slightly different band-gap energies, such as AlGaAs and GaAs, and create a confining potential. **Watanabe *et al.*** (p. 1425) demonstrate quantum confinement of electrons by diamond multilayers that vary only in isotopic composition; the carbon-12 and carbon-13 layers differ in band-gap energy by ~17 millielectron volts. Cathodoluminescence experiments performed at 80 kelvin showed that in alternating layers (as thin as 30 nanometers or as thick as 350 nanometers), emission comes from charge carriers recombining in the carbon-12 layer, which has a lower band gap. Carriers from the carbon-13 layer appear to transfer with little loss into carbon-12 layers.

Cooling All Atoms

Laser cooling can be used to chill atoms to ultralow temperatures. However, the characteristics of the atoms and of the lasers limit the technique to a select few elements of the periodic table. Techniques are thus being explored that can be applied more generally. **Raizen** (p. 1403) reviews recent work on the magnetic coilgun cooling technique—where a series of magnetic pulses are applied to a cloud of atoms or molecules and can cool them to millikelvin temperatures. The only requirement of the atoms is paramagnetism—a property of most of the elements in the periodic table.

Spotting Charges

Many nanoscale physical systems are sensitive to the position of isolated charges, such as single-electron transistors and molecular assemblies that separate charges with energy from photons. In order to probe the location of a charged atom, the most general methods would work on insulating surfaces. **Gross *et al.*** (p. 1428; see the Perspective by **Meyer and Glatzel**) show that a tuning-fork atomic force microscope (AFM) operating in a noncontact mode at cryogenic temperatures can resolve the charge state of gold and silver atoms absorbed on a sodium chloride film. Charged atoms set up image charges in the AFM tip, which creates an electrostatic force not present with a neutral atom.

Planted Evidence

To understand the spatial patterns and consequences of past climate change requires the identification of reliable proxies that reflect specific aspects of those changes, such as temperature or rainfall in a given location. Also of interest are proxies for broader categories of change, such as methane production or the sources of carbon dioxide. **Severinghaus *et al.*** (p. 1431) present a 100,000-year-long record of the oxygen isotopic composition of atmospheric O_2 ($\delta^{18}O_{atm}$) extracted from air from polar ice cores. $\delta^{18}O_{atm}$ is a general measure of the strength of low-latitude terrestrial photosynthesis and thus of local rainfall because plant metabolism is controlled in large part by water availability. $\delta^{18}O_{atm}$ changes were related to Heinrich and Dansgaard-Oeschger events, two modes of abrupt climate change common over that interval, and $\delta^{18}O_{atm}$ was controlled mostly by the strength of the Asian and North African monsoons. The rapid changes observed should also help to synchronize ice core records.

CREDITS (TOP TO BOTTOM): ARDEN STERN; MANEL CARRILLO, JOSEP MIQUEL GIRART (CSIC-IEEC), NIMESH PATEL (SMA), AND SPITZER

Published by AAAS

Helicopter Seed Lift

The "helicopter" seeds of maple trees and other similar autorotating seeds detach from their parent tree under windy conditions and gyrate as they are dispersed by the wind. The reproductive success of the tree depends on the flight performance of its seeds. Autorotating seeds are known to generate high lift as they slowly descend through the air, but the means by which they do so is unclear. **Lentink *et al.*** (p. 1438, see the cover) have elucidated the aerodynamic mechanism for high lift in autorotating seeds using a robot model seed and a three-dimensional flow measurement technique. Maple seeds and a hornbeam seed create a prominent leading-edge vortex that is similar to the flow structures that are responsible for the high lift generated by the wings of hovering insects and bats. Thus, both animals and plants have converged on an identical aerodynamic solution for generating lift.

Boom and Bust

The Brazilian Amazon is renowned for its biodiversity and for its influence on climate regulation and geochemical cycles. It is also one of the country's poorest regions. For decades, much economic development has been pursued through conversion of forest for agriculture and cattle-ranching. **Rodrigues *et al.*** (p. 1435) investigated whether this pattern of land use brings lasting prosperity by analyzing data on the economic development of nearly 300 municipalities across the deforestation frontier. Relative development, in terms of life expectancy, literacy, and standard of living, increases as deforestation begins but then declines again as the frontier passes through. As a result, pre- and postfrontier levels of development are similarly low, indicating a pattern of boom and bust.

Neurotransmission in Living Color

Neurotransmission involves the release of small molecular neurotransmitters from one neuron to another across a synapse. **Gubernator *et al.*** (p. 1441, published online 7 May) introduce a means to observe neurotransmitter release optically, by the design of fluorescent false neurotransmitters, which act as substrates for the synaptic vesicle monoamine transporter. These endogenous monoamine optical tracers enabled visualization of neurotransmitter uptake and release from individual synaptic terminals and were used to evaluate dopamine neurotransmission in the striatum. The fraction of synaptic vesicles that release neurotransmitter per stimulus was frequency dependent, and a frequency-dependent selection of presynaptic terminals was observed.

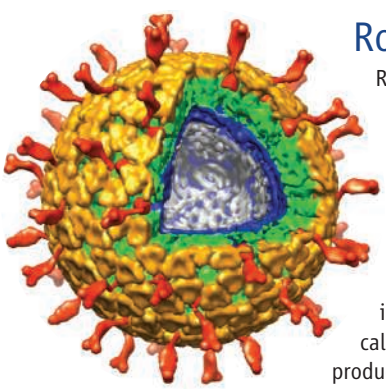

CREDIT: AOKI *ET AL.*

Rotavirus Rumbled

Rotavirus infection is the primary cause of severe diarrhea in infants. For the virus to enter cells, a Ca^{2+}-stabilized trimer of the outer layer protein VP7 must be dissociated. **Aoki *et al.*** (p. 1444) report the structure of the VP7 trimer in complex with the Fab fragment of a neutralizing monoclonal antibody. Based on the structure and an analysis of positions of neutralization escape mutations, the authors propose that many neutralizing antibodies inhibit cell entry by stabilizing the VP7 trimer even at low calcium concentrations. A disulfide-linked trimer was then produced that is a potential subunit immunogen.

Dynamic Imprinting

Gene imprinting—the silencing of either a maternally derived or paternally derived gene allele—is controlled in large part by DNA methylation. In plants, imprinting occurs in the endosperm, which nourishes the embryonic plant. **Gehring *et al.*** (p. 1447) and **Hsieh *et al.*** (p. 1451) analyzed the dynamics of DNA methylation in the endosperm and embryo of *Arabidopsis* and found extensive demethylation in the endosperm, suggesting that many imprinted genes are likely to exist. Gehring *et al.* characterized five imprinted genes in detail. Four of the 10 known imprinted genes are related homeodomain transcription factors. Furthermore, 5′ sequences demethylated in several of the genes were found to be derived from transposable elements, which supports the idea that imprinting arose as a by-product of silencing invading DNA.

Submission deadline August 1

Rewarding brilliance since 1995.

The GE & Science Prize for Young Life Scientists. Because brilliant ideas build better realities.

Imagine standing on the podium at the Grand Hotel in Stockholm, making your acceptance speech. Imagine joining the ranks of those published in Science magazine and having your essay on your work in molecular biology read by your peers around the world. Imagine taking part in a seminar with the other Prize winners and Nobel Prize laureates and discussing your work with leaders in the field. Imagine what you could do with the $25,000 prize money. Imagine what a brilliant start to your career, and where it could lead. Now stop imagining. If you were awarded your Ph.D in 2008, submit your 1000-word essay by August 1 and make it reality.

Want to build a better reality? Go to www.gelifesciences.com/science

GE & Science Prize for Young Life Scientists

imagination at work

Science AAAS

* For the purpose of this prize, molecular biology is defined as "that part of biology which attempts to interpret biological events in terms of the physico-chemical properties of molecules in a cell".

(McGraw-Hill Dictionary of Scientific and Technical Terms, 4th Edition).

Glenn Schweitzer is the director of Eurasian Programs at the U.S. National Academies in Washington, DC. E-mail: gschweitzer@nas.edu

Reset Cooperation with Russia

ON 17 AND 18 JUNE 2009, IN MOSCOW, THE U.S. NATIONAL ACADEMIES AND THE RUSSIAN Academy of Sciences will celebrate the 50th anniversary of the signing of the first interacademy agreement on scientific cooperation between the National Academy of Sciences and the Soviet Academy of Sciences. An important goal of this jubilee is to help revitalize bilateral cooperation in science and technology (S&T), which has declined in recent years. The anniversary comes just before President Obama and President Medvedev meet next month in Moscow to continue efforts to reset U.S.-Russian relations on a broad basis.

The U.S. National Academy of Engineering and the Institute of Medicine are now also parties to the agreements, and the Academy of Medical Sciences and the Academy of Agricultural Sciences play supporting roles on the Russian side. Collectively, these academies support only a small portion of U.S.-Russian scientific cooperation, which also involves many other public- and private-sector organizations. But as they did in 1959, the academies can help to energize cooperation on a broad basis by highlighting the payoffs for researchers, institutions, and government agencies of carefully designed joint efforts.

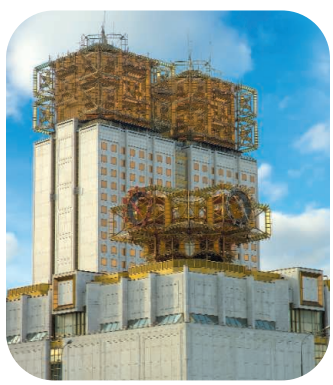

More than 2500 U.S. scientists and a comparable number of Russian scientists from hundreds of institutions have participated in interacademy projects. History has shown that unlocking laboratory doors can be an important step in building confidence between both individuals and governments. In Moscow, the academies undoubtedly will cheer past successes, which should bode well for the future. During the 1960s, many scientists were pioneers in uniting important communities of the two countries; and in the 1970s, the academies paved the way for bilateral government efforts to explore space, investigate the atom, and share data banks of ocean, Earth, and atmospheric research findings. In the following decade, they helped set the stage for reaching arms control agreements, finding common ground on human rights, and expanding explorations of the polar ice caps. And in the 1990s, they provided important stability in U.S.-Russian relations at a time of political and economic turmoil in Russia. Most recently, the academies have provided an important impetus for expanding international nuclear nonproliferation efforts, reducing the likelihood of the malevolent use of dual-use biotechnologies, and countering the dangers of urban terrorism.

The next half-century will continue to challenge the best scientific talent that the United States, Russia, and other countries have to offer. Responding to threats to global security must be paramount: Confronting climate change with clean energy technologies, containing infectious diseases while benefiting from new discoveries in the biomedical sciences, and keeping nuclear weapons materials safe and secure are all essential. Both basic and applied research and improved technology transfer from laboratory to practice will be key.

The interactions of the academies with their respective governments are critically important. Providing advice on scientific developments has become a standard practice for the academies in both Washington and Moscow. But helping their governments to jointly address bilateral cooperation is also an urgent task. From catalyzing more vigorous implementation of the U.S.-Russian bilateral S&T agreement to optimizing intergovernmental approaches for reducing nuclear threats, the academies can help ensure that their two governments are in tune with the changing global landscape. When such advice reflects the views of specialists from both countries, its influence can carry well beyond the United States and Russia. Thus, enhancing the ability to speak in unison on science-related policy issues will be an important agenda item for the academies' anniversary celebration in Moscow.

When Peter the Great established the Russian Academy of Sciences in 1724, he wisely predicted that "science and education will determine Russia's future." When Abraham Lincoln signed the Act of Incorporation for the National Academy of Sciences, he proclaimed, "I know of nothing so pleasant to the mind, as the discovery of anything which is at once new and valuable." With common roots, shared purposes, and joint efforts, the academies of the two countries can continue to be a strong force for global peace and prosperity. **– Glenn Schweitzer**

10.1126/science.1175097

Published by AAAS

EVOLUTION

Mapping Life's History

The tropical region of the New World hosts the richest plant diversity in the world, a richness that owes much to the complex tectonic history of this part of the Earth. Focusing on two tribes of the family Rubiaceae (which includes the coffee plant among many others), Antonelli *et al.* have traced how the uplift of the Andes has influenced the spatial and temporal evolution of neotropical plant diversity—not only in the mountains but also in the lowlands. Molecular phylogeographic analysis shows how the initial uplift of the western and central Andes beginning in the Eocene inhibited dispersal and led to diversification in the lowlands, while creating new montane habitats and taxa. Further barriers to dispersal between Amazonia and the mountains were imposed by marine incursions and the formation during the Miocene of the huge, but now-vanished, wetland (referred to as Lake Pebas or the Pebas Sea) to the east of the Andes. The disappearance of Lake Pebas and the establishment of the modern Amazon drainage are reflected in the distribution and speciation of younger lowland taxa in western Amazonia. The Miocene uplift of the eastern Cordillera of the Andes (shown above) meanwhile promoted dispersal of montane taxa. — AMS

Proc. Natl. Acad. Sci. U.S.A. **106**, 10.1073/pnas.0811421106 (2009).

BIOCHEMISTRY

Fit to Function

In bacteria, low–copy number plasmids provide a model system for studying the segregation of DNA into daughter cells—partitioning requires only a centromere-like DNA site, a partition NTPase, and a centromere-binding protein. The type II systems use the actinlike partition protein ParM to drive plasmid separation. The *Escherichia coli* plasmid P1 uses the type I system of the partition ATPase ParA, the centromere binding protein ParB, and the DNA site *parS*. ParA with ATP bound interacts with centromere-bound ParB to mediate segregation; however, ADP-bound ParA acts as a transcription factor that represses *parAB* transcription.

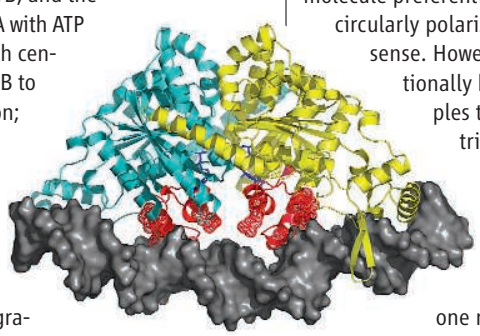

Using crystallography and biochemistry, Dunham *et al.* found that ParA forms a conformationally flexible dimer that relies on an interaction involving the N-terminal α helix. ADP binding locked the monomers (blue, yellow) into agreeable conformations for DNA binding and induced the folding of two positively charged regions (red) that docked onto the DNA (gray). In contrast, electron microscopy showed that ATP-bound ParA forms filaments that likely facilitate segregation. — VV

EMBO J. **28**, 10.1038/emboj.2009.120 (2009).

CHEMISTRY

Perils in Circular Dichroism

Circular dichroism (CD) spectra nominally measure the extent to which a particular chiral molecule preferentially absorbs one sense of circularly polarized light over the other sense. However, the spectra have traditionally been acquired using samples that comprise millions of trillions of molecules, and they have largely been treated as empirical data. In this context, a study that probed the interaction of circularly polarized light with one molecule at a time (Hassey *et al.*, Reports, p. 1437, 1 December 2006) potentially offered deep mechanistic insight. The authors found that on an individual basis, single stereoisomers of a helicene molecule differed across a huge range in their CD response—some, in fact, appeared to favor light polarized opposite to the sense preferentially absorbed overall in an ensemble of like enantiomers. The method relied on fluorescence microscopy to achieve single-molecule resolution, and Tang *et al.* have now suggested that the data might be more easily explained by an artifact associated with the apparatus than by an inherent molecular property. Specifically, the second group of authors attempted to reproduce the findings, but observed that the circular polarization of incoming light was distorted into an ellipse upon reflection at a dichroic mirror, thus becoming more sensitive to molecular orientation. After correcting for this effect, they failed to detect distinct signals from the different single stereoisomers. They therefore propose that the previously observed wide-ranging CD response was actually a manifestation of linear dichroism (a function of orientation rather than chirality), and they argue for careful analysis of mirror-induced distortions in future related studies. — JSY

J. Phys. Chem. A **113**, 6213 (2009).

CLIMATE SCIENCE

Life in the Long Run

The idea that we are already committed to a certain amount of surface air temperature increase and sea-level rise over the coming

CREDITS (TOP TO BOTTOM): ULF MOLAU, UNIVERSITY OF GOTHEMBURG, SWEDEN; DUNHAM *ET AL.*, *EMBO J.* **28**, 10.1038/EMBOJ.2009.120 (2009)

century, even if we could immediately halt all CO_2 emissions, has become well known in scientific and science policy circles. The longer-term outlook is less well understood. Eby *et al.* use a complex, coupled climate-carbon cycle model to investigate how long anthropogenic climate change will persist as a function of how high the concentration of atmospheric CO_2 rises. They calculate how long it will take for half of the total emissions to be removed from the atmosphere, what the maximum global average sea surface temperature increase will be, and how long it will take for 80% of that sea surface thermal anomaly to decay. The results suggest that atmospheric CO_2 can persist at high concentrations for several thousand years, and that sea surface temperature increases can last many times longer than that. It looks, then, like we are in this for the long haul. — HJS

J. Climate **22**, 2501 (2009).

GEOLOGY

Holes in Rocks

Most minerals in Earth's crust are built on a $Si–O^{(2-)}–Si$ framework. Commonly, these minerals contain minor $O^{(-)}–O^{(-)}$ dimers as impurities distributed throughout the bulk of the crystal. When minerals within rocks experience mechanical stress, the weak bonds holding the dimers together are broken, creating a charge imbalance that gives rise to mobile positive holes. These holes travel through stressed mineral grains to other nearby minerals—like current passing through a p-doped semiconductor—until they eventually arrive at the rock's surface. Through a series of electrochemical experiments, Balk *et al*. demonstrate that such holes at the surface of rocks in simulated seawater rapidly oxidize water to form H_2O_2. Because crustal rocks are predominately in contact with water and are almost always experiencing some type of stress from processes such as plate tectonics, glacial movement, and lithostatic pressuring, the oxidation of water by stressed minerals might have helped to contribute oxygen to Earth's early atmosphere. Conceivably, H_2O_2 generated at rock-water interfaces could also have provided evolutionary pressure for local organisms to develop survival mechanisms in highly oxidizing microenvironments. — NW

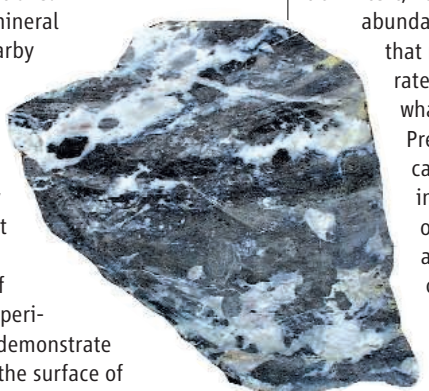

CREDIT: UNIVERSITY OF WASHINGTON

Earth Planet. Sci. Lett. **283**, 87 (2009).

HUMAN GENETICS

Imperfect Assortment

Cancer cells use multiple mechanisms to evade the normally stringent control on cell behaviors such as growth and differentiation. These mechanisms can involve chromosomal instability, a common occurrence in solid tumors whereby cells lose or gain whole chromosomes or parts thereof.

Using microarray-based methods to analyze with high resolution the chromosomal changes in individual cells, Vanneste *et al.* have observed that chromosomal instability occurs at a remarkably high frequency in human cleavage-stage embryos. In 2 of 23 3- to 4-day-old embryos from young healthy couples, all of the cells isolated contained normal chromosomes. The remainder contained various numbers of cells with extra whole chromosomes or chromosomal fragments. Although this study analyzed embryos generated by in vitro fertilization, there may be in vivo implications, given that half of spontaneous abortions display chromosomal imbalances. — HP

Nature Med. **15**, 577 (2009).

NEUROSCIENCE

I Hear What You're Saying

The widespread adoption of multiple technologies for distinct channels of data communication—text, voice, and video—has made it abundantly clear to even the casual user that more bandwidth allows for higher rates of information transfer. But what happens on the receiving end? Presumably, recipients of phone calls are processing a lot more information, such as emotional overtones, than just the words that are spoken. Does this emotional content register in their brains? Ethofer *et al.* apply the method of multivariate pattern analysis and show that pseudowords spoken with five distinct emotional melodies (anger, sadness, relief, joy, or neutrality) do evoke recognizable neural responses within the auditory cortex. Each of these emotions could be discriminated against the others, and decoding algorithms trained on any nine of the speakers' voices were accurate in classifying the emotional identity of the tenth speaker's speech. Furthermore, the five distributed maps of neuronal activity segregated more closely to levels of arousal than valence, suggesting a possible affective organization within the auditory cortex. — GJC

Curr. Biol. **19**, 10.1016/j.cub.2009.04.054 (2009).

www.sciencemag.org

Science

1200 New York Avenue, NW
Washington, DC 20005
Editorial: 202-326-6550, FAX 202-289-7562
News: 202-326-6581, FAX 202-371-9227
Bateman House, 82-88 Hills Road
Cambridge, UK CB2 1LQ
+44 (0) 1223 326500, FAX +44 (0) 1223 326501

Subscription Services For change of address, missing issues, new orders and renewals, and payment questions: 866-434-AAAS (2227) or 202-326-6417, FAX 202-842-1065. Mailing addresses: AAAS, P.O. Box 96178, Washington, DC 20090-6178 or AAAS Member Services, 1200 New York Avenue, NW, Washington, DC 20005

Institutional Site Licenses please call 202-326-6755 for any questions or information

Reprints: Author Inquiries 800-635-7181
Commercial Inquiries 803-359-4578

Permissions 202-326-7074, FAX 202-682-0816

Member Benefits AAAS/Barnes&Noble.com bookstore www.aaas.org/bn; AAAS Online Store www.apisource.com/aaas/ code MKB6; AAAS Travels: Betchart Expeditions 800-252-4910; Apple Store www.apple/eppstore/aaas; Bank of America MasterCard 1-800-833-6262 priority code FAA3YU; Cold Spring Harbor Laboratory Press Publications www.cshlpress.com/affiliates/aaas.htm; GEICO Auto Insurance www.geico.com/landingpage/go51.htm?logo=17624; Hertz 800-654-2200 CDP#343457; Office Depot https://bsd.officedepot.com/portalLogin.do; Seabury & Smith Life Insurance 800-424-9883; Subaru VIP Program 202-326-6417; VIP Moving Services www.vipmayflower.com/domestic/index.html; Other Benefits: AAAS Member Services 202-326-6417 or www.aaasmember.org.

science_editors@aaas.org	(for general editorial queries)
science_letters@aaas.org	(for queries about letters)
science_reviews@aaas.org	(for returning manuscript reviews)
science_bookrevs@aaas.org	(for book review queries)

Published by the American Association for the Advancement of Science (AAAS), *Science* serves its readers as a forum for the presentation and discussion of important issues related to the advancement of science, including the presentation of minority or conflicting points of view, rather than by publishing only material on which a consensus has been reached. Accordingly, all articles published in *Science*—including editorials, news and comment, and book reviews—are signed and reflect the individual views of the authors and not official points of view adopted by AAAS or the institutions with which the authors are affiliated.

AAAS was founded in 1848 and incorporated in 1874. Its mission is to advance science, engineering, and innovation throughout the world for the benefit of all people. The goals of the association are to: enhance communication among scientists, engineers, and the public; promote and defend the integrity of science and its use; strengthen support for the science and technology enterprise; provide a voice for science on societal issues; promote the responsible use of science in public policy; strengthen and diversify the science and technology workforce; foster education in science and technology for everyone; increase public engagement with science and technology; and advance international cooperation in science.

Information for Authors
See pages 807 and 808 of the 6 February 2009 issue or access www.sciencemag.org/about/authors

EDITOR-IN-CHIEF **Bruce Alberts**
EXECUTIVE EDITOR **Monica M. Bradford**
NEWS EDITOR **Colin Norman**
MANAGING EDITOR, RESEARCH JOURNALS **Katrina L. Kelner**
DEPUTY EDITORS **R. Brooks Hanson, Barbara R. Jasny, Andrew M. Sugden**

Editorial senior editor/perspectives Lisa D. Chong; **senior editors** Gilbert J. Chin, Pamela J. Hines, Paula A. Kiberstis (Boston), Marc S. Lavine (Toronto), Beverly A. Purnell, L. Bryan Ray, Guy Riddihough, H. Jesse Smith, Phillip D. Szuromi (Tennessee), Valda Vinson; **associate editors** Kristen L. Mueller, Nicholas S. Wigginton, Jake S. Yeston, Laura M. Zahn; **online editor** Stewart Wills; **associate online editors** Robert Frederick, Tara S. Marathe; **web content developer** Martyn Green; **book review editor** Sherman J. Suter; **associate letters editor** Jennifer Sills; **editorial manager** Cara Tate; **senior copy editors** Jeffrey E. Cook, Cynthia Howe, Harry Jach, Barbara P. Ordway, Trista Wagoner; **copy editors** Chris Filiatreau, Lauren Kmec; **editorial coordinators** Carolyn Kyle, Beverly Shields; **publications assistants** Ramatoulaye Diop, Carlos L. Durham, Joi S. Granger, Jeffrey Hearn, Lisa Johnson, Scott Miller, Jerry Richardson, Jennifer A. Seibert, Brian White, Anita Wynn; **editorial assistants** Emily Guise, Michael Hicks, Patricia M. Moore; **executive assistant** Sylvia S. Kihara; **administrative support** Maryrose Madrid

News deputy news editors Robert Coontz, Eliot Marshall, Jeffrey Mervis, Leslie Roberts; **contributing editors** Elizabeth Culotta, Polly Shulman; **news writers** Yudhijit Bhattacharjee, Adrian Cho, Jennifer Couzin, David Grimm, Constance Holden, Jocelyn Kaiser, Richard A. Kerr, Eli Kintisch, Andrew Lawler (New England), Greg Miller, Elizabeth Pennisi, Robert F. Service (Pacific NW), Erik Stokstad; **intern** Jackie D. Grom; **contributing correspondents** Dan Charles, Jon Cohen (San Diego, CA), Daniel Ferber, Ann Gibbons, Robert Koenig, Mitch Leslie, Charles C. Mann, Virginia Morell, Evelyn Strauss, Gary Taubes; **copy editors** Linda B. Felaco, Melvin Gatling, Melissa Raimondi; **administrative support** Scherraine Mack, Fannie Groom; **bureaus** New England: 207-549-7755, San Diego, CA: 760-942-3252, FAX 760-942-4979, Pacific Northwest: 503-963-1940

Production director James Landry; **senior manager** Wendy K. Shank; **assistant manager** Rebecca Doshi; **senior specialists** Steve Forrester, Chris Redwood; **specialist** Anthony Rosen; **Preflight director** David M. Tompkins; **manager** Marcus Spiegler; **specialist** Jason Hillman

Art director Yael Kats; **associate art director** Laura Creveling; **illustrators** Chris Bickel, Katharine Sutliff; **senior art associates** Holly Bishop, Preston Huey, Nayomi Kevitiyagala; **art associates** Jessica Newfield, Matthew Twombly; **photo editor** Leslie Blizard

***Science* International**

Europe (science@science-int.co.uk) **editorial: international managing editor** Andrew M. Sugden; **senior editor/perspectives** Julia Fahrenkamp-Uppenbrink; **senior editors** Caroline Ash, Stella M. Hurtley, Ian S. Osborne, Peter Stern; **associate editor** Maria Cruz; **locum editor** Helen Pickersgill; **editorial support** Deborah Dennison, Rachel Roberts, Alice Whaley; **administrative support** John Cannell, Janet Clements, Louise Moore; **news: europe news editor** John Travis; **deputy news editor** Daniel Clery; **contributing correspondents** Michael Balter (Paris), John Bohannon (Vienna), Martin Enserink (Amsterdam and Paris), Gretchen Vogel (Berlin); **intern** Claire Thomas

Asia Japan Office: Asca Corporation, Eiko Ishioka, Fusako Tamura, 1-8-13, Hirano-cho, Chuo-ku, Osaka-shi, Osaka, 541-0046 Japan; +81 (0) 6 6202 6272, FAX +81 (0) 6 6202 6271; asca@os.gulf.or.jp; **asia news editor** Richard Stone (Beijing: rstone@aaas.org); **contributing correspondents** Dennis Normile (Japan: +81 (0) 3 3391 0630, FAX +81 (0) 3 5936 3531; dnormile@gol.com); Hao Xin (China: +86 (0) 10 6307 4439 or 6307 3676, FAX +86 (0) 10 6307 4358; cindyhao@gmail.com); Pallava Bagla (South Asia: +91 (0) 11 2271 2896; pbagla@vsnl.com)

EXECUTIVE PUBLISHER **Alan I. Leshner**
PUBLISHER **Beth Rosner**

Fulfillment Systems and Operations (membership@aaas.org); **director** Waylon Butler; **senior systems analyst** Nomuna Nyamaa; **customer service supervisor** Pat Butler; **specialists** Latoya Casteel, LaVonda Crawford, Vicki Linton, April Marshall; **data entry supervisor** Cynthia Johnson; **specialists** Shirlene Hall, Tarrika Hill, William Jones

Business Operations and Administration director Deborah Rivera-Wienhold; **assistant director, business operations** Randy Yi; **manager, business analysis** Michael LoBue; **manager, business operations** Jessica Tierney; **financial analysts** Priti Pamnani, Celeste Troxler; **rights and permissions: administrator** Emilie David; **associate** Elizabeth Sandler; **marketing director** Ian King; **marketing manager** Allison Pritchard; **marketing associates** Aimee Aponte, Alison Chandler, Mary Ellen Crowley, Julianne Wielga, Wendy Wise; **marketing executive** Jennifer Reeves; **director, site licensing** Tom Ryan; **director, corporate relations** Eileen Bernadette Moran; **publisher relations, eresources specialist** Kiki Forsythe; **senior publisher relations specialist** Catherine Holland; **publisher relations, east coast** Phillip Smith; **publisher relations, west coast** Philip Tsolakidis; **fulfillment supervisor** Iquo Edim; **fulfillment coordinator** Laura Clemens; **marketing associate** Mary Lagnaoui; **electronic media: manager** Lizabeth Harman; **project manager** Trista Snyder; **assistant manager** Lisa Stanford; **senior production specialists** Christopher Coleman, Walter Jones; **production specialists** Nichele Johnston, Kimberly Oster

Advertising director, worldwide ad sales Bill Moran

Product (science_advertising@aaas.org); **midwest/west coast/w. canada** Rick Bongiovanni: 330-405-7080, FAX 330-405-7081; **east coast/e. canada** Laurie Faraday: 508-747-9395, FAX 617-507-8189; **uk/europe/asia** Roger Goncalves: TEL/FAX +41 43 243 1358; **japan** Mashy Yoshikawa: +81 (0) 3 3235 5961, FAX +81 (0) 3 3235 5852; **senior traffic associate** Deiandra Simms

Commercial Editor Sean Sanders: 202-326-6430

Project Director, Outreach Brianna Blaser

Classified (advertise@sciencecareers.org); **u.s.: sales manager** Daryl Anderson: 202-326-6543; **inside sales representative** Tina Burks: 202-326-6577; **key account manager/midwest** Joribah Able; **east coast** Alexis Fleming: 202-326-6578; **west/south central** Nicholas Hintibidze: 202-326-6533; **sales coordinators** Rohan Edmonson, Shirley Young; **international: sales manager** Tracy Holmes: +44 (0) 1223 326525, FAX +44 (0) 1223 326532; **sales** Susanne Kharraz, Dan Pennington, Alex Palmer; **sales assistant** Lisa Patterson; **japan** Mashy Yoshikawa: +81 (0) 3 3235 5961, FAX +81 (0) 3 3235 5852; **advertising support manager** Karen Foote: 202-326-6740; **advertising production operations manager** Deborah Tompkins; **senior production specialist/graphic designer** Amy Hardcastle; **senior production specialist** Robert Buck; **senior traffic associate** Christine Hall

AAAS Board of Directors retiring president, chair James J. McCarthy; **president** Peter C. Agre; **president-elect** Alice Huang; **treasurer** David E. Shaw; **chief executive officer** Alan I. Leshner; **board** Alice Gast, Linda P. B. Katehi, Nancy Knowlton, Cherry A. Murray, Julia M. Phillips, Thomas D. Pollard, David S. Sabatini, Thomas A. Woolsey

AAAS
ADVANCING SCIENCE, SERVING SOCIETY

It becomes you.

Introducing the 3500 Series Genetic Analyzer.

Get ready to make an amazing discovery: the new 8-capillary and 24-capillary 3500 Series Genetic Analyzers take DNA analysis to an entirely new level of performance. A level where your daily workflow seems like a natural extension of your own intuition. Where precise, quality-assured data inspires greater confidence. And where a new consumables design and intuitive software interface keep you current and in control.

Take a closer look, and you'll find the new 3500 and 3500xL Genetic Analyzers are like second nature. Which is our first priority when it's your research.

Discover the 3500 System at **www.appliedbiosystems.com/3500Series**

Easy-to-Use Consumables

Control at Your Fingertips

Quality-Assured Data

Applied Biosystems

For those who require IVD-marked devices, the 3500 Dx and the 3500xL Dx Genetic Analyzers and system accessories meet the requirements of the In Vitro Diagnostics Medical Devices Directive (98/79/EC). The 3500 Dx and 3500xL Dx systems are for distribution and use in specific European countries only. For more information about the 3500 Dx Series Systems, contact your Applied Biosystems representative.

Coming Fourth Quarter 2009

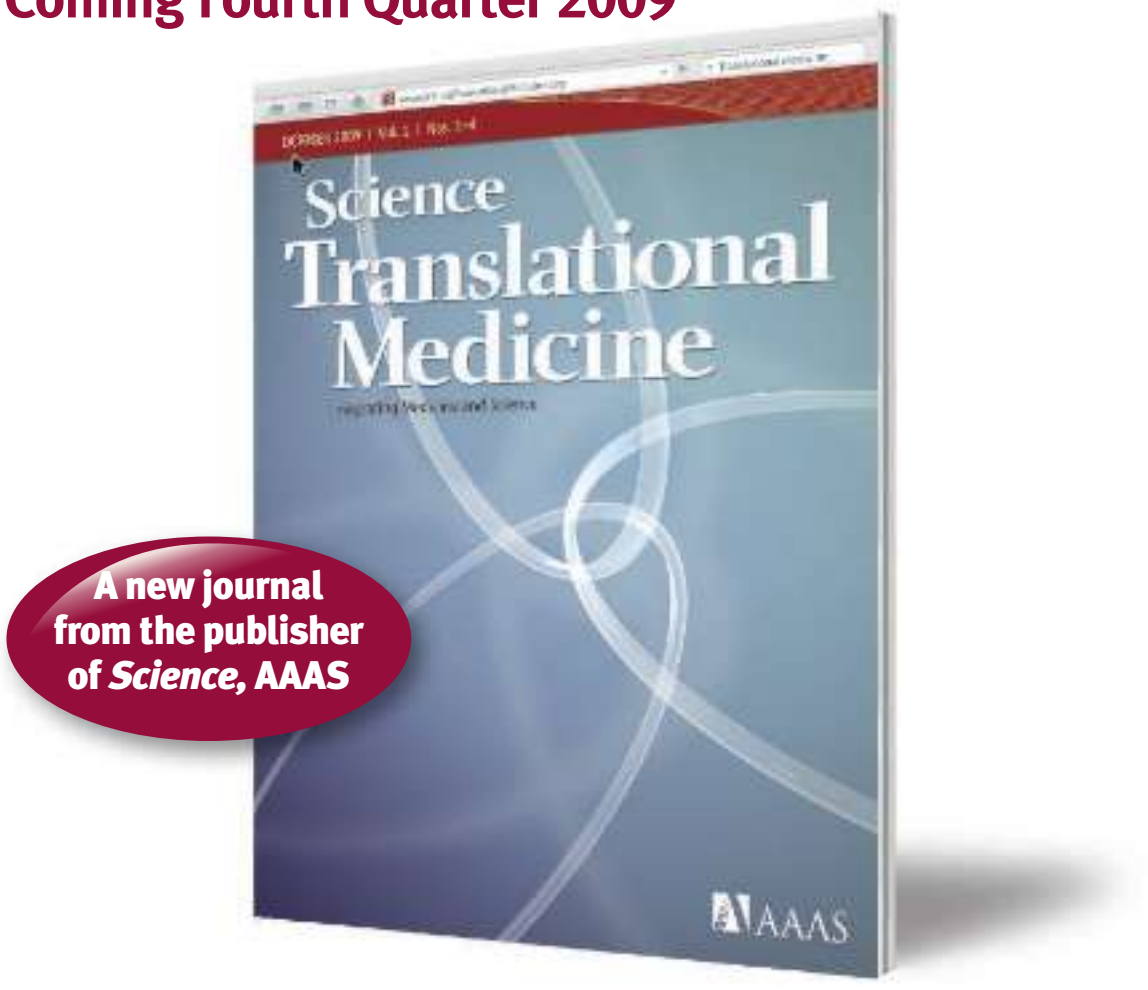

A new journal from the publisher of *Science*, AAAS

Introducing *Science Translational Medicine*, the new journal from AAAS and *Science*.

This fall, AAAS and *Science* will launch *Science Translational Medicine*, a new journal focused on how basic research knowledge can be applied to positively impact human health.

The goal of *Science Translational Medicine* is simple: to help the scientific community harness decades of progress in basic research and translate these complex biological discoveries into medical advances.

Headed by Editor Katrina Kelner, Ph.D., and Chief Scientific Adviser, Elias Zerhouni, M.D., former Director of the NIH, the journal will feature original research articles, in-depth reviews, and commentary. Both in print and online, *Science Translational Medicine* promises a unique forum where biologists, engineers, chemists, and physicians can come together to exchange ideas and information.

Science Translational Medicine is now accepting manuscripts. To submit your work for consideration please visit: **www.sciencemag.org/marketing/stm/papers.dtl.**

For information on institutional or individual subscriptions, please contact **sciencemedicine@aaas.org**.

Science Translational Medicine
AAAS

www.ScienceTranslationalMedicine.org

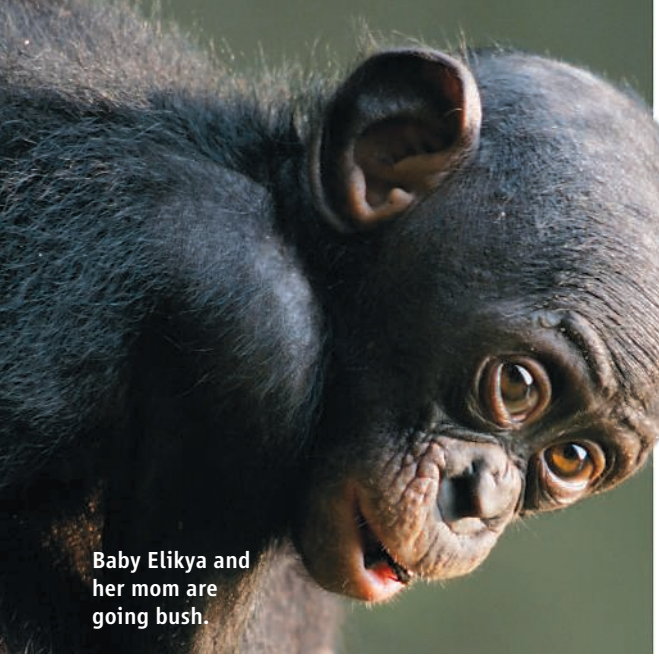
Baby Elikya and her mom are going bush.

Back to the Woods

This month, conservationists will make the first attempt to reintroduce bonobos, the most endangered of Africa's great apes, into the wild. Seventeen animals will be moved from their sanctuary in the Democratic Republic of the Congo (D.R.C.) to a 20,000-hectare forested preserve in the northwestern part of the country near the Congo River. Known for settling group conflicts with sex rather than violence, bonobos are found today only in the D.R.C., where a mere 10,000 may remain in the wild. Belgian conservationist Claudine André started the 30-hectare Lola ya Bonobo sanctuary in the D.R.C. 15 years ago. "This is a strategically designed release," says the reintroduction project's scientific adviser, primatologist Brian Hare of Duke University in Durham, North Carolina. The apes will be closely monitored and supplied with food if necessary. André has hired local villagers to guard the animals from bushmeat hunters. If all goes well, more of the sanctuary's 62 bonobos, some of whom were abused as pets or mutilated for witchcraft ceremonies, will one day move back to the woods.

Cold Spring Harbor Chilly to Tweets

Cold Spring Harbor Laboratory (CSHL) in New York state is revamping its meeting rules to bind scientists by the same restrictions that apply to reporters.

Journalists at CSHL meetings must agree not to write anything without the permission of the speaker. But during a meeting last month, several scientists—including Daniel MacArthur of the Wellcome Trust Sanger Institute in Hinxton, U.K., and Francis Collins, former director of the National Human Genome Research Institute in Bethesda, Maryland—reportedly posted comments about talks in Twitter "tweets" and on Web pages.

A Web-based news service, GenomeWeb, complained. Now the lab is cracking down. Meetings organizer David Stewart says he is revising the meeting registration form so that all participants, reporters or otherwise, will agree to get prior permission for any Internet postings.

Relief in Zero G

As if cramped quarters and freeze-dried ice cream weren't enough, astronauts face the unpleasant necessity of urinating in near-zero gravity. Apollo crews solved this problem with condomlike devices. Current models consist of a vacuum-cleaner-like hose with attachable funnels for males and females—now more sophisticated, but still sometimes uncomfortable and messy.

Floating test for pee machine.

So 10 engineering students from the University of California, San Diego, have teamed up with thermal and fluids engineer Eugene Ungar of the Johnson Space Center in Houston, Texas, to develop something better. In January, they were accepted into NASA's Microgravity University, a program that gives undergraduates the chance to conduct experiments on board a plane that performs parabolic maneuvers to simulate ultralow gravity. By April, the students were in the air testing their "pee machine," a contraption that pushes a column of water through a simulated urethra into an acrylic box where they can track the flow dynamics with high-speed cameras.

"We're really going to hit hard with designing and testing different methods for collecting urine in the coming years," says Timothy Havard, student leader of the project. One promising design, he says, is a receptacle filled with a honeycomb network that harnesses surface tension and the velocity of the fluid to capture the urine with minimal splash-back.

BLOW IT LIKE BACH

Scottish physicists have helped a Swiss conservatory recreate the mysterious lituus, a horn used in the time of Johann Sebastian Bach.

Bach wrote a part for the lituus in his cantata "O Jesu Christ, meins Lebens Licht." Musicians at Schola Cantorum Basiliensis in Basel, Switzerland, wanted to perform the cantata with a real lituus. But they had no idea what the instrument looked like—only the range of notes it played and its likely sound characteristics. So they turned to fluid dynamicists Murray Campbell and Alistair Braden of the University of Edinburgh in the United Kingdom. Braden has designed a computer program that models the acoustic properties of wind instruments. The hardest problem, he says, was generating "realistic instrument shapes."

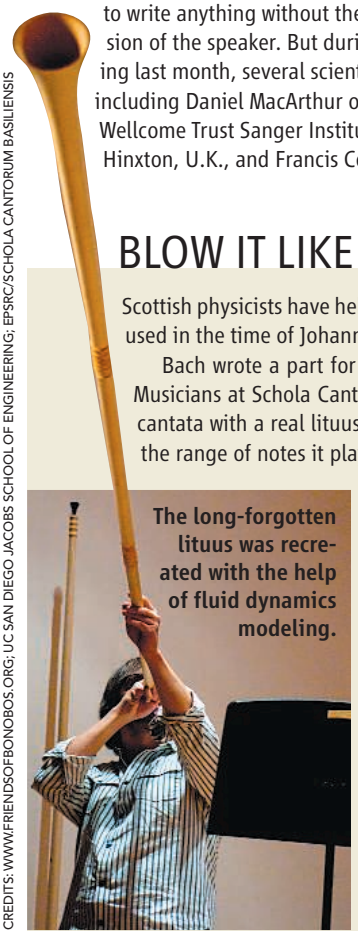
The long-forgotten lituus was recreated with the help of fluid dynamics modeling.

The resulting design is a horn made of light wood some 2.5 meters long. Played with no holes or valves, it has a roughly three-octave range and makes a "haunting" sound, says Braden who explains that the length is necessary for the quality of the higher notes. The conservatory has been giving "experimental performances" with two copies of the horn based on Braden's design and is now investigating how a curved version would sound. "Scientists are seldom able to contribute so directly to art," says Braden. "It's like making a new paintbrush and seeing it in the hands of a master painter."

CREDITS: WWW.FRIENDSOFBONOBOS.ORG; UC SAN DIEGO JACOBS SCHOOL OF ENGINEERING; EPSRC/SCHOLA CANTORUM BASILIENSIS

A supreme test of patentability
1374

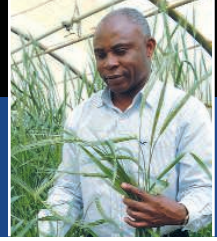

Opening up the seed banks
1376

Uncertain fate. Regional climate change forecasts would help relocation planning for villages threatened by global warming, such as Shishmaref, Alaska.

U.S. CLIMATE POLICY

Congress Takes First Step Toward One-Stop Shopping for Climate

Congress is moving quickly to lay a framework for a new federal body that would generate scientifically credible predictions about the impact of global warming, for use by everyone from city planners to state wildlife managers. The entity, dubbed the National Climate Service, would be managed by the National Oceanic and Atmospheric Administration (NOAA) and draw on research from many federal agencies. But building such a service, which proponents say would do for climate what the National Weather Service (NWS) does for weather predictions, won't be cheap or easy.

The idea of providing government and industry with one place to go for climate information has been around for more than 20 years. It would offer short-term products such as drought forecasts, as well as guidance on decades-long phenomena such as whether a particular region will continue to have optimal conditions for wind or solar power. The task requires integrating existing data from many federal agencies and expanding research efforts in areas such as high-resolution regional climate modeling. "There's intense interest in the climate science world" in a National Climate Service, says Terrence Schaff, who directs government relations for the Woods Hole Oceanographic Institution in Massachusetts.

Last week, the House Committee on Science and Technology moved the concept closer to reality by approving a bill (H.R. 2407) that directs the White House to evaluate how to coordinate all the federal agencies that study and monitor climate change. The legislation, introduced in May by the panel's chair, Representative Bart Gordon (D–TN), was adopted largely along party lines, with the ranking Republican saying he was not convinced that a climate service is necessary. Gordon hopes the language will be added to major climate change legislation drafted by representatives Henry Waxman (D–CA) and Edward Markey (D–MA) that is working its way to the House floor. Another bill (H.R. 2685), introduced last week and referred to the science committee, would speed the process by spelling out how the service should be organized.

Also last week, the House panel that controls NOAA's budget added $100 million in 2010 for a variety of climate research programs already under way to help grease the wheels. "We've moved from talking about this on the cocktail circuit to serious business about how we're going to do it," says Robert Corell of the Heinz Center in Washington, D.C., about the climate service.

The former head of NOAA, retired Vice Adm. Conrad Lautenbacher Jr., began talking up the idea last year, and his successor, marine ecologist Jane Lubchenco, has carried it forward. Both say it makes sense for NOAA to take the lead, as the agency already gathers much climate data from buoys, satellites, and other monitoring platforms. It could also tap a network of regional collaborations on climate impacts as well as the local offices of NWS.

The science committee's bill directs NOAA to create an office that would manage the day-to-day operations of a climate service. A key issue is how to integrate all relevant federal agencies. Even if NOAA manages operations, it can't tell another agency to change its research strategy, for example. "We probably need White House authority to ensure that all the pieces come together," says Eric Barron, director of the National Center for Atmospheric Research in Boulder, Colorado, who chaired a NOAA advisory committee that studied organizational issues.

Gordon's bill asks the White House's Office of Science and Technology Policy (OSTP) to investigate possible solutions over the next 2 years. "I'm hopeful we can move much more rapidly than that," Lubchenco says.

The second bill, introduced by Representative Madeline Bordallo (D–Guam), would mandate an Interdepartmental Oversight Board, chaired by the OSTP director, that would set priorities and develop a cross-agency budget. Science lobbyists prefer this bill because it gives the extramural community a greater role in setting the research agenda. The bill has been referred to the science committee, and a staffer says members are open to a discussion of Bordallo's concerns.

House Speaker Nancy Pelosi (D–CA) has told the chairs of various House committees with jurisdiction over aspects of climate change to finish reviewing the Waxman-Markey bill by 19 June, although no vote has been scheduled. (The Senate is waiting to see what the House produces.) NOAA and other agencies don't need legislation to create a climate service, but Lubchenco says that congressional approval validates the need for a climate service. "This is an idea whose time has come," she says.

–ERIK STOKSTAD

Published by AAAS

China launches attack on mystery disease
1378

A deep-diving Russian
1382

ENVIRONMENTAL SCIENCE

Macau Launches Late Bid to Cure Its Pearl River Delta Blues

MACAU—Hard up against the luxury casinos of Cotai Strip, a tiny remnant of native Macau is fenced off with barbed wire—for its own protection. "This is what it looked like before they filled in the wetlands and built casinos," says Wang Zhishi, a professor of environmental engineering at the University of Macau.

Taipa-Coloane Wetland Reserve may appear more memorial than functional, but Wang and others hope that the 15 hectares of marsh will offer a sanctuary for an embattled symbol of Macau: the black-faced spoonbill, a critically endangered species with some 2000 individuals left in the wild. A few dozen of the migratory birds with the distinctive lute-shaped bill stay here in winter; their ranks have dwindled as the city's human denizens have multiplied. Macau's government restored Taipa-Coloane wetland and 40 more hectares of mangrove coast in a last-ditch effort, Wang says, to "call the bird back."

Fits the bill? Macau hopes tiny Taipa-Coloane reserve will attract rare black-faced spoonbills.

For Macau, a gambling haven known more for unbridled development than for ecological awareness, the reserve's creation this year is a milestone on an uncertain road to sustainability. Another milestone will be passed on 29 June, when Macau establishes an Environmental Protection Bureau. "We started a little too late. But now the public is demanding a better living environment, and we have to catch up with international standards," says Vong Man Hung, acting president of the Macau Environment Council's executive committee. The 10-year-old council has no authority to enforce laws; the bureau that will supplant it, on the other hand, will have full rein to go after polluters. "Without doubt, it will be a more powerful voice for the environment," says Vong.

The new bureau faces daunting problems, including severe air pollution and toxicants flowing into the Pearl River Delta, a region that includes Macau, Hong Kong, and mainland China's Guangdong Province. In a report last month, Guangdong's oceans and fisheries bureau noted that at least 8 million tons of pollutants and sewage discharged into the delta last year entered the South China Sea. Macau is the recipient of much of this toxic largess. "The waters off Macau's coast are a giant sink for pollutants," says Wang.

For researchers, at least, Macau's afflictions offer a rare opportunity to probe pollution in a setting that, thanks to the city's small size, scientists can fully characterize. "Macau is a unique urban environmental laboratory," says Mok Kai Meng, dean of the University of Macau's science and technology faculty.

Distress signals

The waters of the Pearl River Delta are growing fouler and fouler. Red tides in the estuary once lasted a few days and were limited to coastal fish farms. In recent years, the harmful algal blooms have persisted longer and covered a larger area, says red tide expert Ho Kin-chung, dean of science and technology at The Open University of Hong Kong. "It's changing into a regional phenomenon," he says.

Prevailing currents sweep industrial effluents and pesticide runoff down the delta and deposit toxicants in coastal sediments. "A huge amount of pollutants are transferred to Macau," says Ming Wong, director of the Croucher Institute for Environmental Sciences at Hong Kong Baptist University. A recent survey by the University of Macau and the Research Institute of Geochemistry in Guangzhou found that concentrations of organochlorine pesticides and polycyclic aromatic hydrocarbons were higher in Macau's inner harbor than at any other site sampled in the delta. Readings of DDT, which China and some other countries still use for mosquito control, were off the chart: 1628.8 parts per billion in Macau harbor compared with 2.6 ppb in Shenzhen Bay, for instance.

The witches' brew, which includes heavy metals, gets into local fish. "These days, we warn people in Hong Kong about eating too much fish," says Wong. A rising incidence of skin disorders in children in the region, he says, has been linked to elevated levels of four elements in hair, blood, and urine: mercury, arsenic, cadmium, and lead. An increasing prevalence of neurological disorders in Hong Kong may also be linked to blood mercury levels in infants, he says, and mercury has been associated with impaired male fertility in Hong Kong.

Macau cannot stem the toxic tide. But the environment bureau, to be headed by the current chief of Macau's cartography office, Cheong Sio Kei, is expected to forge tighter connections with counterparts in Hong Kong and Guangdong. "There will be more collaboration in the region to define a common strategy," says Mok.

A more visible menace in the Pearl River Delta is filthy air. Regional air quality is so appalling that each year an estimated 10,000 people in the delta die from respiratory ▶

CREDITS: R. STONE/*SCIENCE*; (INSET) COURTESY OF LEUNG VA

distress, Hong Kong researchers reported last year. The primary culprits are coal-fired power plants and rising automobile exhaust emissions. In recent years, concentrations of fine particulates (PM10) in Macau have been at least double—and in bad years, quadruple—the U.S. Environmental Protection Agency's annual PM10 standard of 50 micrograms per cubic meter. Conditions worsen in winter, when a northeasterly monsoon brings dry, particle-laden air.

Improving air quality is one area in which the new bureau can quickly assert itself, says Vong. Already, she notes, Macau has moved to lessen its reliance on coal and produce more electricity from natural gas. And last year, the government passed legislation that tightened vehicle emissions standards. The bureau should put some teeth into these standards, Vong says, as well as work harder to promote public transportation.

Also on the bureau's agenda is noise pollution. Macau is one of the most densely populated regions in the world: Some half a million people are crowded onto Macau peninsula and two islands, equating to more than 18,000 inhabitants per km^2—and that doesn't even count the roughly 27 million visitors each year.

Dialing down the decibels may calm frayed nerves—and soothe spoonbills. One of six spoonbill species, the black-faced spoonbills breed in late spring and early summer in Korea and China's Liaoning Province, and they winter on a stretch of coast from Japan to Vietnam. "The bird is quite sensitive to environmental change," says zoologist Leung Va, a spoonbill expert at Macau's Seac Pai Van Park. Leung rattles off a number of interventions necessary to ensure that the 50-odd spoonbills that flock to Macau keep doing so: reduce light pollution from the casinos, limit vehicular and pedestrian traffic along the coastal reserve, and curtail fishing in spoonbill habitat. "The government has to do a lot; otherwise for the birds there is no hope," Leung says.

For Macau's new environmental watchdog, that's one of many challenges it must meet to satisfy a citizenry with rising expectations.

–RICHARD STONE

PATENTS

U.S. Supreme Court Delves Into What Is and Isn't Patentable

For more than a decade, two entrepreneurs have been battling without success to win a U.S. patent on their method of doing commodity deals. Last week, the U.S. Supreme Court agreed to hear their plea, signaling that it may pounce on the case to clarify rules about what is, or is not, patentable. Patent attorneys say a decision could affect not just business methods but some biotech claims and process inventions.

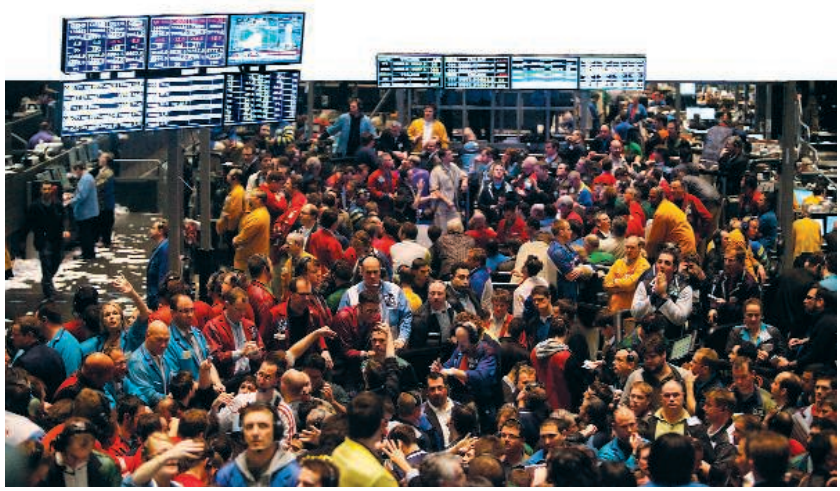

Patent futures. A rejected patent on a commodity-trading strategy could have broad implications.

CREDIT: UPI PHOTO/BRIAN KERSEY/NEWSCOM

The business duo, Bernard Bilski and Rand Warsaw, have been jousting with the U.S. Patent and Trademark Office (PTO) since the late 1990s because it refuses to award them a patent on their idea for buying and selling bulk materials, such as coal, while hedging their bets with contracts at different prices. PTO rejected this "invention" as too abstract—it doesn't even include an algorithm—and the top U.S. patent court, the Court of Appeals for the Federal Circuit (CAFC), upheld the rejection.

The news that the Supreme Court has agreed to hear this case jolted legal experts last week. Hans Sauer, associate counsel for the Biotechnology Industry Association (BIO) in Washington, D.C., says it's a "big deal" and has snapped "most patent attorneys in the country" to attention. For BIO members, Sauer sees a risk that the Supreme Court—which hasn't ventured into the territory of what is patentable in a couple of decades—could come up with a new definition that excludes certain diagnostic procedures or techniques to analyze genes, chemicals, or other natural phenomena. Physicians' groups, on the other hand, view such restrictions more favorably because they fear patents may limit access to diagnostics.

The biotech industry's concern is justified, says Christopher Holman, a law professor at the University of Missouri, Kansas City, and former pharma biochemist. He notes that the Bilski patent was rejected by CAFC because the judges said it did not involve a machine or a process that transforms a material from one thing to another. Since then, this logic has been used by a lower court to reject a biotech patent on vaccination scheduling; the court said simply that it violated the Bilski rule. Now CAFC is poised to decide about another biotech patent, this one held by Prometheus Laboratories of San Diego, California, on setting doses for the immune suppressant drug azathioprine. It's been challenged on grounds that it violates Bilski and is based on natural phenomena.

Holman has joined four academics in an amicus brief to CAFC saying that judges need to be cautious in knocking down such patents: They should not call a person's response to azathioprine a natural phenomenon, for example, because the drug itself isn't natural. BIO also weighed in with a brief to CAFC, arguing that "significant and important sectors of the biotechnology industry" could be harmed if the Bilski logic is applied too broadly. Meanwhile, the American Medical Association and six other medical groups have filed a brief on the opposite side, arguing that the Prometheus patent should be rejected because it is abstract and based on natural phenomena.

The Supreme Court's review of the Bilski case could set the ground rules for deciding this case and others involving biotech and analytical process inventions. The court hasn't set a date for accepting briefs but could do so as soon as this fall.

–ELIOT MARSHALL

Published by AAAS

JAPAN

Science Windfall Stimulates High Hopes—and Political Maneuvering

TOKYO—A handful of stellar researchers could be in line for grants of as much as $90 million over 5 years, thanks to a new program included in a stimulus package approved by Japan's legislature on 29 May. But some scientists worry that a political selection process could steer money toward industry-favored projects. "I'm pessimistic about [the prospects for] basic science," says Masao Ito, a neuroscientist at RIKEN, near Tokyo.

In Japan, most grant programs are conceived by the ministries of education or economy, trade, and industry in consultation with the scientific community. But the new program, which aims to strengthen support for "world-leading research," is the brainchild of Seiko Noda, who as minister for Science and Technology Policy heads a small bureau in the Cabinet office that coordinates positions on research issues across ministries.

A career politician, Noda had no prior research-related responsibilities. But after taking the science policy post in August 2008, she heard long-running complaints about how scientists spend more time applying for grants than conducting research and how they are required to spend all grant money in the year it's awarded, says Eisuke Futamura, an official in the science policy bureau. In what Futamura calls a "rare case" of a science policy minister initiating a new program, Noda proposed a $2.7 billion fund to support about 30 world-beating research teams. The group leader would be able to spend the money as needed over 5 years and hire administrators to handle paperwork.

Noda personally presented the plan to the Council for Science and Technology Policy, the nation's highest science advisory body, in late April. With the council's endorsement, the proposal was added to the $141 billion supplemental budget bill, which is intended to help Japan spend its way out of recession. The bill includes $13.7 billion for science-related funding, mostly to upgrade facilities and equipment, in addition to Noda's pet project.

Jockeying over control of the program has already begun. Sadayuki Sakakibara, president of Toray Industries and a member of the science policy council, called for half of the members of any selection panel to come from industry, and Prime Minister Taro Aso has declared that he will make the final call on grantees. Not surprisingly, many researchers worry that the program will be slanted toward applied research and that the selection process will be politicized. "We need to try to cook this to get [proper] priorities," says Kiyoshi Kurokawa, former dean of Tokai University School of Medicine and a former science adviser to Japan's prime minister.

Whatever areas win funding, the program would set an important precedent in allowing more flexible use of research funds, argues Tasuku Honjo, a member of the science policy council and a molecular geneticist at Kyoto University. "Once established, this principle could be used again for other grant programs," he says. Futamura says proposals would be accepted from all fields and the selection process would likely rely on expert recommendations endorsed by the prime minister. Details will be clarified when the program is formally announced, Futamura says.

Before Noda's program can disburse funds, a law must be amended so that money appropriated in one fiscal year can be spent over several years. Legislation is in the works, Honjo says, but passage depends on support of the prime minister and his Cabinet. Futamura says he has no idea when the amendment might be voted on.

–DENNIS NORMILE

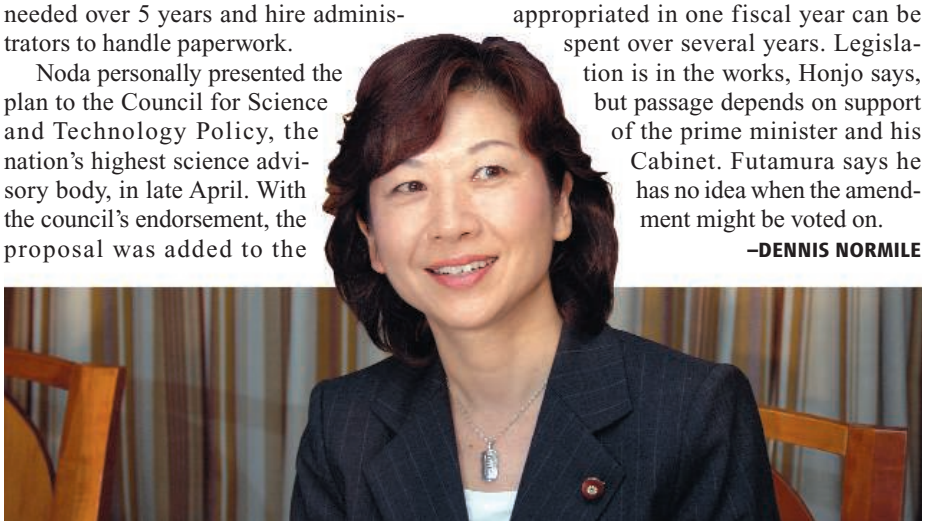

Top-down. Seiko Noda, Japan's science policy minister, wants to rewrite the rules on research funding.

CREDITS (TOP TO BOTTOM): MIRIAM WESSELS/UNIVERSITY OF VETERINARY MEDICINE; FCCJ

ScienceNOW.org

From *Science*'s Online Daily News Site

Unfriendly Skies. Call it CSI: Bird Strike. For the first time, researchers have used a sophisticated chemical analysis to finger the fowl that brought down an airplane. The case? Figuring out just which type of bird caused a US Airways jet to crash into New York's Hudson River in January. http://tinyurl.com/ngz5zc

A 10-Million-Year-Old Laugh. It's something all humans do, regardless of race, culture, language, or creed: laugh. And, it turns out, some 10 million to 16 million years ago, the last common ancestor of humans and apes was laughing, too, most likely when tickled. That's the conclusion of an analysis of the recorded laughs of young orangutans, chimpanzees, and human children. http://tinyurl.com/ldffvt

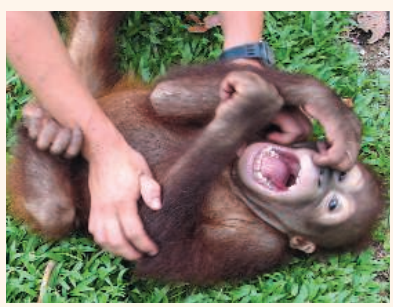

Snakes on a Pane. Snakes just wouldn't be snakes without their characteristic slither. Known scientifically as "lateral undulation," the creatures wiggle their bodies like a sideways wave and leave a perfect S-shaped track as they go. But just how does slithering get snakes from point A to point B? A new mathematical model may reveal the answer. http://tinyurl.com/lz3qny

Laser Light Bulbs. Tired of dealing with those newfangled fluorescent and halogen bulbs that tend to blow out and can't quite handle dimmer switches? You might just find solace from an old and trusted source: incandescent lights. A team of physicists has discovered a way to double the efficiency of these ordinary light bulbs. All it takes is a superfast laser blast to their filaments. http://tinyurl.com/kmoc95

Read the full postings, comments, and more on **sciencenow.sciencemag.org**.

Published by AAAS

PLANT BREEDING

Scientists Seek Easier Access to Seed Banks

Frances Ogbonnaya believes Ethiopia's traditional wheat varieties could hold the key to staving off a global food crisis. Wheat around the world is under siege from Ug99, an especially virulent strain of the fungus that causes stem rust, a plant disease. Few commercial wheats can resist the devastating strain (*Science*, 8 May, p. 710). That's why Ogbonnaya, a geneticist at the International Center for Agricultural Research in the Dry Areas in Aleppo, Syria, is using gene mapping to verify that Ethiopian durum wheats in ICARDA's collection harbor novel "slow-rusting" genes that can steel crops against the pathogen.

Still more genetic weapons against Ug99 might be found in Ethiopia's own seed bank, one of Africa's best and home to a vaunted collection of traditional durum wheat varieties. But unlike ICARDA, the Ethiopian seed bank isn't always open to withdrawals. In recent years, Ethiopia has been reluctant to share seeds with other countries—for reasons that threatened to drive a wedge between rich and poor countries at a contentious treaty meeting last week.

Free and timely access to seeds is enshrined in the International Treaty on Plant Genetic Resources for Food and Agriculture, which came into force in 2004. But "free and timely" is not how plant breeders describe their experience with five of the treaty's 120 signatories: China, Ethiopia, India, Iran, and Turkey. "Basically, they're closed gene banks," says Kenneth Street, a legume curator at ICARDA. That's alarming because many seed collections are vulnerable. In the past decade, Afghanistan's collection was lost when the Taliban dumped seeds to scavenge their airtight containers; Iraq's was destroyed in the most recent war; and the Philippine seed bank sustained heavy damage from a typhoon in 2006.

Last week, the treaty's governing body met in Tunis to review implementation and coax reluctant nations to open their seed banks and contribute to a "doomsday vault" on Norway's Svalbard island (*Science*, 23 June 2006, p. 1730). At the forum, Ethiopia and other developing countries asserted that they should be compensated for custodianship and ongoing cultivation of landraces: traditional varieties adapted to local conditions. Despite tensions over such issues, a deadlock was averted when participants found common ground on the need for a major new fund to support the work of traditional farmers. "One thing everyone here agrees on," Francisco López of the U.N. Food and Agriculture Organization (FAO) reported from Tunis, is that "there won't be any agriculture in 50 years unless we have exchanges of germ plasm."

According to many observers, the recalcitrance of Ethiopia and like-minded countries is a throwback to the days of the Convention on Biological Diversity in 1993. A key aim of the convention was to thwart "biopiracy," by which foreigners reaped a windfall from a country's genetic resources without providing compensation. Melaku Worede, founder of the Ethiopian Gene Bank, notes that traditional knowledge of the nation's farmers gave the world prized cultivars of coffee, barley, and wheat—without any benefit for Ethiopia. In the 1980s, he says, an Ethiopian barley landrace saved North America's crop from an epidemic of barley yellow dwarf virus, even as his country was suffering famine. The biodiversity convention was meant to redress that imbalance. Instead, countries drafted an array of bilateral seed-trade agreements so complex that they constricted the international exchange of seeds and technical know-how—the lifeblood of plant breeding.

Once bitten, twice shy. Frances Ogbonnaya says Ethiopian durum wheats could help thwart a fungus now sweeping the globe—but Ethiopia is reluctant to share seeds.

That tourniquet was supposed to be undone by the genetic resources treaty, which superseded the biodiversity convention when dealing with 64 crop varieties deemed vital to global food security. In place of bilateral deals, treaty signatories in 2004 adopted a standard material transfer agreement providing access to the 64 varieties held in signatories' seed banks. Any owner of an exclusively patented variety developed from such seeds would pay a 1.1% royalty to a common FAO-administered pool to support crop biodiversity and conservation.

A bone of contention for some countries is that they will not receive direct payments for sharing seeds. "Countries think, 'We give access in the here and now, but what do we get back?' " acknowledges Shakeel Bhatti, secretary of the treaty's governing body. "The benefits are nonmonetary. It's access to the biggest [seed] bank in the world—the global gene pool." Sorting out which countries should be remunerated for a valuable variety would be daunting. Pedigrees are complex, and "determining the value of any particular contribution is nearly impossible," says Cary Fowler, who as executive director of the Global Crop Diversity Trust (GCDT) is charged with preserving the world's seed diversity.

In a bid for faster, more tangible relief for traditional farmers, Worede made a pitch in Tunis for a biodiversity fund for developing nations on a par with GCDT. (The trust, which relies on voluntary contributions, has so far received about $120 million of a pledged $150 million.) Seed banks like Svalbard are invaluable for preserving landraces, Worede says, but so are the skills and experience that traditional farmers bring to bear in selecting seeds to breed landraces season after season. After all, he says, Svalbard's dormant accessions won't have a chance to adapt to climate change.

In a remarkable and unexpected climax as the meeting drew to a close, the treaty governing body agreed to raise $116 million for a biodiversity fund that would support traditional farmers. That helped avert a crisis of confidence in the treaty, says Bhatti, who calls the meeting "a real turning point." Worede, more circumspect, describes the biodiversity fund as a "little progress." However, he says, "Anything voluntary is like the dew on a leaf: It can fall down at any time. The contributions should be binding." **–ELIZABETH FINKEL**

Elizabeth Finkel is a writer in Melbourne, Australia.

CREDIT: COURTESY OF FRANCES OGBONNAYA/ICARDA

IMMIGRATION POLICY

U.S. Promises to Reduce Delays In Granting Visas for Scientists

The U.S. government has streamlined procedures for processing visa applications from foreign students and researchers trying to enter the United States. Officials say these changes, announced last week, should make a lasting improvement in a review process that at times has resulted in long delays, pinched the flow of scientific talent into the country, and stymied scientific collaborations. But, citing security concerns, they have declined to spell out how the new approach differs from current practices, which have yo-yoed since the September 2001 terrorist attacks.

"We don't expect the long wait times to crop up again," says Stephen Heifetz, deputy assistant secretary for policy development at the Department of Homeland Security. "We think this is more of a real fix than the last one."

Marilyn Speedie, dean of the college of pharmacy at the University of Minnesota, Twin Cities, hopes that Heifetz is right. In April, the college was forced to postpone indefinitely a workshop on treatments for orphan diseases after three senior Indian researchers learned that their visas, for which they had applied several weeks earlier, would not be issued in time. In solidarity, several of their Indian colleagues canceled their travel plans, torpedoing the conference. "We were extremely disappointed," says Speedie.

The visa process became agonizingly slow in the aftermath of 9/11, when the government clamped down on anyone wishing to enter the country who had scientific and technical expertise deemed potentially useful to terrorists. However, even government officials acknowledged that the system to screen such applicants, known as a Visa Mantis, had begun to stifle the free flow of scientific information. By 2005, additional staff and better training for consular officials appeared to have resolved the problem. But a few years later, the review process began to bog down again for reasons that are not clear. "By the end of 2008, the average delay for applicants from China had climbed to 4 months," says an official with the U.S. National Academies, which has tried to help scientists caught in the system.

David Donahue, a State Department official, says the recent delays were due to inadequate staffing and procedural problems implementing the Mantis review. Both issues have been fixed as of last month, he says. Donahue says all agencies involved in Mantis checks have agreed to complete the process within 2 weeks. The checks can currently take 2 months or longer.

Top-down changes don't always translate into improvements on the ground, however. Although the State Department decided in 2005 that Mantis clearances for students would remain valid for 4 years rather than 1 year, the academies official notes that many consular officials were still requiring a new Mantis review for any student seeking to return to the United States after traveling home for a vacation or a family visit. That additional review left many students in limbo for several months.

CREDIT: UNIVERSITY OF MINNESOTA

Waiting game. A conference on orphan diseases organized by Minnesota's Marilyn Speedie fell victim to visa delays.

Speedie plans to reschedule the workshop once the Indian participants obtain their visas, and she hopes that the latest changes clear up the problem once and for all. The recent snafu delayed potential collaborations aimed at "fighting diseases and improv[ing] global health," she says. In other words, they are precisely the sort of partnerships that could eventually ease global tensions and lower the threat of terrorism.

–YUDHIJIT BHATTACHARJEE

ScienceInsider

From the *Science* Policy Blog

Despite the tough economic climate, Germany plans to spend **€18 billion more on research** over the next 10 years. Chancellor Angela Merkel announced last week that she and the heads of the 16 German states had signed off on the increase in funding, which was negotiated in April. The chancellor, who has a Ph.D. in physical chemistry and is married to a chemistry professor, said the agreement will send a **"signal of predictability"** to researchers and help them draw up long-term plans for the money.

In a win for the **open-access** movement, **University College London** (UCL) announced last week that it would soon begin posting copies of faculty members' published journal articles in a **free online repository**. UCL follows the lead of other prominent institutions, including Harvard and Stanford universities and the Massachusetts Institute of Technology. UCL plans to follow the copyright policies of the relevant journals, including waiting to post until after the journal itself has made the full text freely available.

The British government has **scrapped** its Department for **Innovation, Universities and Skills**, which oversees most academic research programs. Created 2 years ago, the department will now be merged with the Department for Business, Enterprise and Regulatory Reform to form a **new Department for Business, Innovation and Skills**. It's not yet clear if the restructuring will increase the pressure on scientists to make their research more economically relevant.

U.S. President **Barack Obama** signaled his intent to use **science diplomacy** to win over the **Islamic world** in his 4 June speech in Cairo, Egypt. The president promised new **science envoys, centers of excellence, and a technological development** fund for the Middle East, North Africa, and Southeast Asia. Officials in the State Department and the White House Office of Science and Technology Policy are now scrambling to add substance to those words.

For science policy news daily, visit **blogs.sciencemag.org/scienceinsider**.

Published by AAAS

A Medical Mystery in Middle China

China has launched a massive effort to stamp out Kashin-Beck disease, including moving populations from affected areas, but the cause of this crippling ailment remains elusive

XI'AN, CHINA—Since he was a boy, the short middle-aged man with gnarled fingers and misshapen legs has suffered from deformed joints. But in the past couple of years, even taking a step has been agony for Ma Ming-An, a 50-year-old farmer. "I stay home and cook. Now my wife works in the fields," says Ma, sitting on a gurney at Shaanxi Provincial Institute of Endemic Disease Control (SEDC) in Xi'an. Last month, Ma traveled from his home in southwest Shaanxi to the province's capital to receive treatment for Kashin-Beck disease (KBD)—a little-known ailment that has crippled and stunted the growth of hundreds of thousands of people in China's heartland.

A surgeon at SEDC, Yu Yue-Xiang, leans over Ma and presses a lump above his right knee. It is deteriorated cartilage that has dislodged from its moorings at the end of the femur—a symptom of advanced KBD. A week earlier, Yu removed four bullet-sized chunks from Ma's left knee. He's about to wash out the right one. The arthroscopic surgery is no cure, but within a week Ma should be back on his feet.

Yu and his colleagues are on the front lines of a battle against a baffling ailment. Although fungal toxins, tainted water, and trace-element deficiencies have all been implicated in the debilitating disease, KBD's precise cause is an enduring mystery. "We have no idea what triggers it," says SEDC vice director Bai Guanglu, who leads Shaanxi's KBD response.

China has mounted an aggressive attack against KBD, including providing millions of people with supplements and clean water—and condemning whole villages as part of the biggest relocation effort in history to combat a disease. Over the past 2 years in Shaanxi, some 85,000 people were relocated from land considered irredeemably tainted. Since 1995, several hundred thousand people in five provinces have been uprooted and resettled. "I don't know of any similar response to an issue like this," says Ellen Silbergeld, an environmental scientist at Johns Hopkins University in Baltimore, Maryland. The measures are gaining traction: KBD incidence is falling, as is the rate of dwarfism, the disease's most-severe manifestation.

Earlier this year, China launched a 5-year, $240 million initiative that aims to stamp out the disease altogether. The State Council–led program will first fine-tune intervention and treatment strategies in a pilot area—an ethnic Tibetan enclave in Sichuan Province—before expanding them to other regions. Some researchers say victory is near: Liu Yunqi, a professor at Harbin Medical University's Kashin-Beck Disease Institute in China, predicts that by 2020, there will be no new KBD cases. "The disease will be totally under control," he says.

At the front line. Pediatrician Philippe Goyens of the Kashin-Beck Disease Foundation examines a girl in Tibet.

CREDIT: FRANÇOISE MATHIEU

Kashin-Beck disease may be fading, but the riddle of its origin is as potent as ever. Researchers have made strides in unraveling how KBD warps skeletal growth, and the hunt is on for genes that confer susceptibility or resistance. Figuring out the ailment's cause could offer insights into cartilage metabolism and common degenerative maladies of the Western world, such as osteoarthritis. "Understanding this disease will have global significance," says Virginia Kraus, a rheumatologist at Duke University in Durham, North Carolina.

But KBD is no easy target. "Researchers have been grappling with this disease for a long, long time," says Bruce Caterson, a connective-tissue biologist at Cardiff University, U.K. "The harder we look, the more frustrating it gets."

Molecular carnage

The first inklings of an endemic blight came in a report in 1849 by a Russian surveyor who noted that people in villages along the Urov River, east of Siberia's Lake Baikal, suffered bone deformities. A few years later, Nikolai Kashin, a doctor with a Cossack military detachment in Russia's Far East, described Urov disease and sketched crippled patients. A second Cossack doctor, Evgeny Beck, documented cases in a 1906 monograph *Osteoarthritis Deformans Endemica*. The disease later came to light in what is now northern North Korea—where it had long been known as *tojiru*—and in China, where it's called *da gu ji bing*, or "big joint disease."

KBD afflicts at least 1 million people in 14 provinces, according to the Chinese Center for Disease Control and Prevention's surveillance of sentinel sites. Other estimates put the affected population in China and neighboring parts of Russia and North Korea as high as 2.5 million. Prevalence peaked in the late 1950s, when in many severely hit villages 60% to 90% of children showed signs of KBD, says Liu. Now, he says, the incidence is about 5%. In comparison, some 60% of adults over age 65 have symptoms of osteoarthritis.

The clinical picture is in sharp focus. "The disease severely erodes health," says Xiong Yongmin, vice director of the Institute of Endemic Diseases at Xi'an Jiaotong University (XJTU). Initial signs include cracking or popping sounds in the finger joints indicating loss of cartilage, and ankle and knee stiffness and pain. As KBD progresses, joints deform, muscles wither, and mobility decreases. (Inexplicably, cartilage padding the spine is not affected.) Many patients are unusually short, have stubby fingers and a waddling gait, and suffer chronic fatigue and weakness. The younger a victim is at onset, the worse the symptoms tend to become.

Scientists are beginning to unravel the damage that KBD unleashes at a molecular level. It begins at the epiphyseal growth plate: the nexus of growing bone and cartilage. Cartilage is a simple tissue—it has a single cell type,

Hallmark symptoms. Like many KBD patients, Ma Ming-an has severely deformed joints.

chondrocytes—but it takes a biochemical balancing act to maintain it. Chondrocytes produce proteoglycans, which pull water into a collagen mesh. That gives cartilage its elasticity and resilience to the pounding meted out to our joints. Aggrecan, the major proteoglycan in cartilage, binds to a link protein and hyaluronic acid, which in turn is anchored to chondrocytes by the protein CD44. A healthy body is constantly swapping in new aggrecan for old but is much less adept at replacing collagen.

In KBD patients—as well as in the tens of millions of people with osteoarthritis and rheumatoid arthritis—replacement of aggrecan and collagen lost to disease is inadequate, and joints degrade. The cartilage matrix collapses, and pressure piles up on the chondrocytes. Cartilage begins to buckle under daily wear and tear. "In osteoarthritis, this triggers repair responses that go awry and tends to chew up the joints. We suspect the same occurs in KBD," says Caterson.

Although osteoarthritis is a disease of aging, in KBD the mechanical breakdown of cartilage often starts early, in children as young as 2 or 3. As victims grow, "their joints just go in all directions," says Caterson. Other KBD abnormalities include disturbed CD44 metabolism and elevated interleukin-1β and tumor necrosis factor-α, associated with inflammation. It's unclear whether these anomalies contribute to or are a consequence of cartilage erosion.

Unmasking the chondrocyte killer is critical to solving the KBD puzzle. As with Viliuisk encephalomyelitis, another disease that emerged in Siberia and continues to confound experts (*Science*, 26 April 2002, p. 642), the culprit appears to be lurking in the environment. "There are many theories," says Feng Qinghua, SEDC's provincial disease director.

Gallery of rogues

In 1992, Françoise Mathieu, a physical therapy specialist, was working for Médecins Sans Frontières (MSF) in the Philippines when colleagues at the nonprofit's newly opened office in Lhasa, Tibet's capital, encountered dozens of people in two counties in Lhasa Prefecture with a severe form of osteoarthritis. "They were wondering what kind of disease it is. They had never seen anything like it before," Mathieu says. That spring, after MSF physicians understood they were dealing with KBD, they invited Mathieu to Lhasa for a 6-week stint to explore whether physical therapy would ease symptoms. She has since devoted her career to KBD.

Early on, Mathieu and her colleagues were struck by how KBD was rife in certain valleys in Tibet, especially east of Lhasa, and rare or absent elsewhere. Peasants are vulnerable, they found, but urban populations and nomads are spared.

In the hunt for environmental clues, one startling peculiarity stood out early on. If you overlay a map of KBD incidence on a map of soil poor in selenium (a trace element) in China, the correspondence is striking. Nowhere in the world are selenium levels as low as in a swath of land that arcs from Tibet in the southwest to Heilongjiang Province in the northeast (see map, p. 1380). In this region's population, the mean serum selenium concentration is roughly 20 nanograms per milliliter—one-tenth the U.S. level. KBD occurs almost exclu-

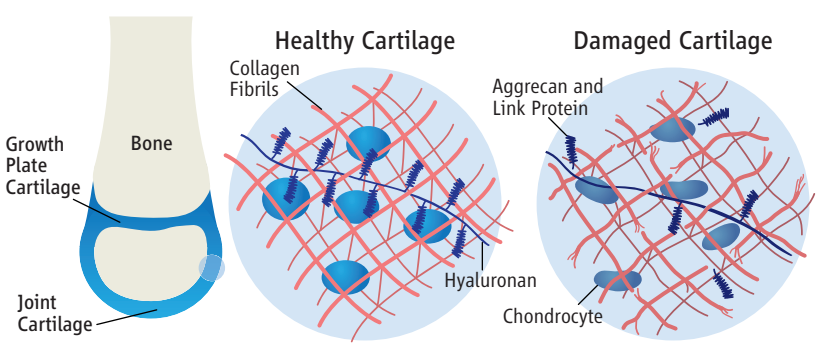

Misery in the joints. In Kashin-Beck victims, damage begins at the epiphyseal growth plate and progresses to joint surface articular cartilage. As the disease progresses, the body fails to adequately swap in new aggrecan for old, the collagen mesh frays and fibrils break, and collagen degrades. Chondrocytes die and lose their nuclei, persisting as ghost cells before the dead tissue is replaced by scar tissue. Surviving chondrocytes cannot meet demand for molecules to repair cartilage battered by daily wear and tear.

CREDIT: R. STONE/*SCIENCE*; SOURCE: BRUCE CATERSON

Published by AAAS

sively in this selenium-poor belt. A 1991 study by researchers at the Shanghai Institute of Metallurgy found that people in KBD-endemic areas in Shaanxi ingested 4.6 micrograms of selenium per day on average. Since then, selenium intakes have increased, XJTU researchers say, but are still far below the U.S. recommended daily intake of 70 mg.

Selenium is a compelling suspect. The element is a component of a couple of dozen human proteins, including a key enzyme—glutathione peroxidase—that defends the body against oxygen-free radicals, molecular wrecking crews that corrode anything in their path. Adequate dietary selenium may help ward off cancers and diseases of aging presumed to arise from accumulated free-radical damage. That appears to be true for osteoarthritis: In 2007, a team led by rheumatologist Joanne Jordan of the University of North Carolina (UNC), Chapel Hill, reported that low selenium levels increased the odds of severe knee and hip osteoarthritis in U.S. women. And animal disease suggests a link to KBD, Caterson says: Epiphyseal-plate malformations occur in sheep in selenium-poor parts of New Zealand.

But selenium deficiency alone does not explain KBD, researchers say. Although many villages in selenium-poor areas have high KBD rates, nearby villages are often disease-free. In surveys in Tibet in the mid-1990s, Mathieu's team found that children with or without KBD have equally low selenium levels. They also observed many children with goiter: KBD villages have high rates of hypothyroidism. Many of China's selenium-deficient areas, it turns out, are also iodine-poor.

In Tibet, says Mathieu, KBD is more strongly correlated with iodine deficiency than selenium deficiency. Acute iodine deprivation harms thyroid function. Because severe hypothyroidism in children impairs the epiphyseal plate and stunts growth, it can masquerade as KBD. Yet in most other KBD-endemic areas in China, iodized salt is widely available and hypothyroidism is rare.

Another bane of Kashin-Beck country is fungi. In some Shaanxi villages, for example, people have lived for centuries in moldy underground dwellings, says Caterson, who collaborates with XJTU's Cao Junling and has visited KBD hot spots four times since 2002. "It's an unhealthy environment," he says. Geography may be a factor: The KBD belt is a climatic crucible in which cold, dry continental air mixes with humid air from the Pacific Ocean.

In the 1960s, Russian scientists linked KBD to consumption of cereals tainted with *Fusarium*, a common fungal genus. Throughout KBD-endemic areas of China, researchers have detected extensive fungal contamination of grains and bread by genera such as *Fusarium*, *Trichothecium*, and *Alternaria*. These may affect two Tibetan staples: *tsampa*—roasted barley dough balls—and *chang*—fermented barley beer. "In preliminary studies, we saw a very strong correlation between fungi in the barley and KBD," says Mathieu.

Mycotoxins produced by *Fusarium* and its brethren are especially nasty. Scientists have zeroed in on three trichothecenes: nivalenol, butenolide, and T-2 toxin. Caterson's lab has found that nivalenol inhibits proteoglycan synthesis in cultured chondrocytes. Similarly, butenolide damages chondrocytes and engineered cartilage, Cao and colleagues reported in the February issue of *Toxicology in Vitro*.

T-2, the most abundant mycotoxin in KBD-endemic areas, may be the worst of the lot. In cell culture, T-2 triggers apoptosis of chondrocytes, revs up synthesis of an enzyme that degrades aggrecan, and inhibits CD44 production. Guinea pigs fed T-2 develop cartilage damage similar to that seen in KBD patients. There may even be a connection between mycotoxins and selenium. In cell culture, selenium blocks T-2-induced chondrocyte apoptosis, a team led by XJTU's Wang Zhilun reported in 2006 in *Food and Chemical Toxicology*.

But like selenium or iodine deficiency, fungal toxins fall tantalizing short of solving the riddle: Many villages that consume mycotoxin-tainted grain do not have elevated KBD risk. "That's the thing with this disease," says Caterson. "The jigsaw puzzle seems to fall into place, then something mixes up the pieces."

Another suspect lurks in the drinking water. In many KBD-endemic villages, springs, streams, and wells are chock-full of organic matter. As the material decomposes, it releases humic acid and fulvic acid. Mathieu and colleagues have found that families with at least one KBD-afflicted member are more likely to store drinking water in small containers, which may not allow organic matter to easily settle. Fulvic acid, in cell culture, inhibits collagen formation, blocks selenium uptake, and triggers chondrocytes to make the corrosive compound hydrogen peroxide. Rats fed a selenium-poor diet laced with fulvic acid have impaired bone and collagen formation.

In a stab at a grand unified KBD theory, Chinese researchers, as well as Mathieu and her colleagues in a 2008 monograph *Big Bone Disease*, suggest that free radicals generated by mycotoxins and fulvic acid damage chondrocytes in people with an impaired antioxidant defense due to trace-element deficiencies or malnourishment. But to many experts, things still don't add up. If unquenched free radicals were the sole culprit, smokers should be at higher KBD risk—but they aren't as far anyone knows, and the disease often strikes children, says Duke's Kraus. "There could be an unknown environmental factor," adds Feng.

One dark horse is a virus. In 2004, Li Guang-Sheng and colleagues at Jilin University in Changchun, China, isolated Coxsackie B3 virus from the hearts of victims of Keshan disease, a rare heart malady that occurs in the same region as KBD. Coxsackie B3 is known to destroy heart tissue. And XJTU's Wang Zhilun and Bi Huayin have detected human parvovirus B19 in patients in Shaanxi. A common scourge, B19 triggers periodic outbreaks of so-called fifth disease in schools and nurseries. In adults, the virus can cause arthritis-

Cause or coincidence? Most KBD cases (dots represent incidence in representative villages) occur in a swath of China with extremely low selenium levels, depicted on map in lighter blue. KBD incidence in endemic regions, according to cases confirmed by x-ray diagnosis, has declined steadily since 2000.

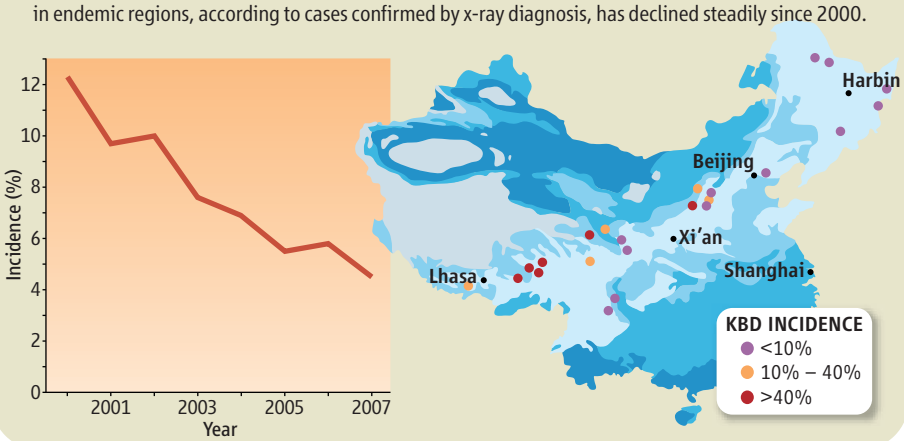

SOURCES (LEFT TO RIGHT): CHINESE CENTER FOR DISEASE CONTROL AND PREVENTION; COURTESY OF XJTU

Online

sciencemag.org

Podcast interview with author Richard Stone.

like symptoms in the hands, wrists, and knees. It's unclear how widespread B19 infections are among KBD patients in Shaanxi, let alone other endemic areas, says XJTU's Xiong.

Undercutting a connection, B19's mild symptoms usually clear up quickly. But selenium deficiency might be a cofactor: Influenza and Coxsackie virus are more virulent in animals fed a selenium-depleted diet, Melinda Beck and her colleagues at UNC Chapel Hill have found. "The same virus might result in a quite different clinical picture according to the nutritional environment," says Jean Vanderpas, a doctor at the Scientific Institute of Public Health in Brussels who has studied KBD.

In addition to searching for suspects in the environment, researchers are pursuing new genetic leads that might explain why some populations are particularly vulnerable. Cases cluster in families, which could be due to environmental or genetic factors. An obvious place to hunt for variants is among the two dozen known human proteins bearing selenium, including glutathione peroxidase and selenoprotein P, which governs selenium metabolism. To test whether there are gene variants that confer susceptibility or resistance to KBD, Caterson and colleagues in 2007 collected spit samples and toenail clippings from KBD patients in Shaanxi. It took a year to satisfy Chinese officials that exporting the samples would not compromise personal information of Chinese citizens. The samples are now in North Carolina, where Jordan's team is analyzing toenail clippings for selenium and other trace elements and Kraus's group is scanning DNA from spit for variants in selenium-related genes.

One promising candidate is *DIO2*, a gene encoding a selenoprotein that converts thyroxine to its active form. Last year, Ingrid Meulenbelt and colleagues at Leiden University Medical Center in the Netherlands identified a *DIO2* variant that increases osteoarthritis risk. KBD, says Kraus, "may very well result from an interaction between genes and the environment."

Pinpointing KBD-related genes would enable vulnerable populations to be screened. "Then we'd know if the disease is all due to a lack of selenium or iodine or if other agents are involved," says Kraus.

A final push

With so many targets to shoot at, KBD interventions, not surprisingly, have been hit or miss. A decade ago, Mathieu's team gave iodized oil to one group of children with the disease, iodine followed by sodium selenate tablets to a second group, and placebos to a third. Correcting iodine deficiency markedly improved symptoms. "Young patients respond well," Mathieu says. But the selenium offered no apparent additional health benefit, the researchers reported in *The New England Journal of Medicine* in 2003. "We urgently need to clarify selenium's role. High doses are extremely toxic," says Kraus.

Recent studies reveal an even more complex nutritional picture, says Mathieu, who cofounded the Kashin-Beck Disease Foundation to carry on work in Tibet after MSF pulled out in late 2002. Her team has documented not only iodine and selenium deficits but also low levels of calcium and vitamins A, D, and E. The biggest clinical improvement, they have found, happens when children with KBD consume a more diverse diet including nettles, a traditional food full of vitamins that is largely eschewed by younger Tibetans. To test whether several deficiencies conspire to give rise to KBD, Mathieu's group just finished a 3-year trial in which 1064 children ages 3 to 10 were given iodine and selenium and either a cocktail of micronutrients—copper, manganese, zinc, and vitamins A, C, and E—or a placebo. Results are expected later this year.

Searching for answers. Françoise Mathieu analyzes grains in Gansu (*top*); a Tibetan boy with severe KBD.

CREDITS (TOP TO BOTTOM): CAMILE CHASSEUR; FRANÇOISE MATHIEU

Experience shows that a strategy that reduces KBD in one village can flop in the next. "There is no single method of primary prevention," says Xiong. In Shaanxi last year, 5.47 million people—nearly 15% of the population—received selenium supplements. Another 672,000 were given uncontaminated wheat. Some interventions may not be feasible, notes Vanderpas. "It seems almost impossible, operationally, to change fulvic acid in drinking water or decrease mycotoxins in cereals at the population level," he says.

When all else fails, authorities in five KBD hot spots—Gansu, Qinghai, Shaanxi, Sichuan, and Tibet—have ordered relocations. Former settlements are converted to farmland or rangeland for livestock. Some Chinese scientists are ambivalent about this approach. "We don't support relocation because it costs a lot of money, but we don't object to it either," says Liu. Relocation is a hardship for many, adds SEDC's Bai. "The elderly especially are reluctant to move," he says. "Moving people is the last resort." Or as Silbergeld suggests, "Perhaps the government needs to consider acting aggressively on food safety and improving diets rather than moving people around."

Although experts differ on the best approach to combating KBD, they concur that it is a disease of deprivation. Heading northeast from Shaanxi, China's population is more affluent, on average, and KBD rates fall off sharply. Xi'an, a city of 3 million people, is in the heart of KBD territory, but the only cases doctors here see are people from the countryside, SEDC's Yu says. KBD, Liu says, "only occurs in China's rural areas."

With that in mind, China's latest KBD initiative, overseen by the State Council's Leading Group of Poverty Alleviation and Development, has an overarching aim of improving people's lives. Measures will include providing untainted grains and selenium supplements, improving drinking-water quality, and relocating people from hundreds of villages. A pilot scheme is being rolled out this year in Sichuan's Aba Prefecture.

China's strategy may be controversial, but it is working. "There are fewer and fewer victims," says Bai. Most patients are now in their 40s or older, he says. That may be a blessing for China but a curse for KBD sleuths: As the disease retreats, so does the likelihood of unlocking its secrets.

–RICHARD STONE

Flag-waving. After his 2007 dive to the Arctic Ocean floor, Artur Chilingarov shows off a picture of the Russian flag his team planted there.

PROFILE: ARTUR CHILINGAROV

Russia's Polar Hero

Artur Chilingarov has led researchers exploring the polar regions, the Arctic ocean floor, and the world's deepest lake. But is he promoting science or his homeland?

MOSCOW—Artur N. Chilingarov says he has a "dream," and coming from a 69-year-old midranking Russian politician, it sounds at first like an improbable one. Chilingarov wants to dive to the bottom of the Mariana Trench, the deepest part of the world's oceans at 10,911 meters, near the Pacific island of Guam. The site has been visited by people only once before, back in 1960 by divers from the U.S. Navy in the bathyscaphe *Trieste*, and Chilingarov feels it's time to go back—and that Russians should lead the way.

"I'm discussing the possibilities with our shipbuilders," he says. "It will be a manned craft. The Americans [at Woods Hole Oceanographic Institution] have constructed a robotic vehicle to dive there—but we want to descend ourselves." Chilingarov raises an eyebrow and smirks. "We may even get out and have a walk around on the bottom."

Don't bet against him. Although Chilingarov has made a steady political ascent to become deputy chair of the Duma, Russia's lower house of parliament, and a leading member of the pro-presidential United Russia party, the diminutive man with the unruly seaman's beard is at heart an explorer and scientist—one with the political and business connections within Russia to raise money for costly expeditions. He has traveled on atomic icebreakers and helicopters to the polar regions, led research teams adrift on ice, and already reached another ocean floor, the Arctic's, 2 years ago. In doing the latter, Chilingarov confirmed his status as a Russian hero, literally, and set off an international furor that still echoes today.

Little known outside his homeland at the time, Chilingarov shot to fame in August 2007 when he led a team that descended in two minisubmarines to the ocean floor under the North Pole, planting a titanium Russian flag on the seabed. Overnight, the oceanographer—Chilingarov has a Ph.D. in geographical sciences—was transformed into Russian's public mouthpiece on the Arctic. Vladimir Putin, then president, awarded him the Hero of Russia medal—to add to the Hero of the Soviet Union gong he earned for organizing the rescue of a ship stuck in polar ice in the

DIVING INTO THE SACRED SEA

At 25 million years old, 640 kilometers long, and with at least 1600 endemic species of flora and fauna, Lake Baikal is the largest, deepest, most ancient, and most biologically diverse freshwater lake on Earth. Set in the heart of Siberia, the crescent-shaped lake, which curls toward Russia's border with Mongolia, is often called "the Sacred Sea."

Yet although the Kremlin has long professed interest in preserving Baikal, a pulp and paper mill was allowed to spew harmful dioxins into the lake for decades, until it closed last year. Environmental campaigners chalked it up as a victory; they had forced the factory to go to a closed water-production cycle, which cut contamination and ended the making of profitable chlorine-bleached pulp. Long-term effects of the jettisoned waste, however, remain unknown. Another threat—detailed by a group of American and Russian scientists last month in the journal *BioScience*—is the effect of climate change on Baikal. The lake's warming water—temperatures increased by 1.21°C between 1946 and 2008—have caused a longer ice-free season, which hinders the growth of algae that bloom under the ice in spring, the principal source of food for crustaceans, themselves eaten by fish. Added to these questions is the unknown influence of tons of crude oil that naturally seep into the lake every year from fissures in the bedrock.

Prompted by such potential menaces to the lake, scientists from the Russian Academy of Sciences (RAS) last year began a program of research using two deep-water *Mir* minisubmarines to make physicochemical analyses, obtain geological and biological specimens, and monitor tectonic processes on the lakebed. They also want to examine gas and oil seeps and the mud volcanoes discovered on the lake floor in 1999, which produce gas hydrates, a methane-containing form of ice created at great depths and normally found in oceans, not lakes.

Marc De Batist of the Renard Centre of Marine Geology at Ghent University in Belgium, who has traveled to Baikal for 15 years and was one of two foreigners to dive in the *Mirs* last year, says the expedition was first conceived as a "prestige project" focused on setting depth records but developed into a serious scientific research trip when limnologists, geographers, and biologists from heavyweight institutions signed up. Russian scientists say it is the most extensive study of the lake since they dove in Canadian Pisces submersibles in 1990 and 1991.

The *Mirs* team carried out 52 deep-water dives in 2008 and, starting next week, plan another 100 submersions this summer.

Last year, diving in the lake's Barguzinsky Bay, researchers were able to take samples from outcrops of bitumen on the bottom, where oil leaks into the water at a depth of

CREDIT: FOMICHEV MIKHAIL/ITAR-TASS/LANDOV

Published by AAAS

1980s—and Chilingarov made strident speeches about Moscow's rights to the region. "The Arctic is ours and we should demonstrate our presence," he declared.

Abroad, Chilingarov's flag-waving was widely interpreted as a blunt attempt by the Kremlin to assert ownership over the vast hydrocarbon reserves in what Russians call "the high latitudes." Today, wearing a sharp dark suit rather than the submersible jumpsuit or fur-collared parka he's often pictured wearing, Chilingarov rejects that accusation and argues that his North Pole dive stimulated other countries to study the polar region. "I'm very pleased that we've jogged them onto new research—they ought to be grateful to me for that!" he says. Chilingarov, Russia's representative for the International Polar Year (IPY) research effort that ran from 2007–08, also points out that his Arctic dive contributed to growing calls in the United States to ratify the U.N. Convention on the Law of the Sea.

Criticism of Chilingarov inside Russia is muffled but tends to focus on suggestions that his more recent achievements are stunts, with few concrete scientific results. "They are impressive sporting expeditions more than anything else," says German Burkov, head of the polar countries' department of the Russian Geographical Society.

Similar disparagements were heard last year when Chilingarov headed a scientific expedition conducting dozens of submersible dives in Siberia's Lake Baikal (see sidebar). The effort, which resumes next week with new dives, has garnered more publicity for the subs' attempts to set dive-depth records than for any new data—even though no records have been set so far.

> ***"[Chilingarov] has dedicated his whole life to polar research, so when he defends Russia's interests in the Arctic, he is doing nothing less than defending his own home."***
>
> **—VLADIMIR GRUZDEV, DUMA MEMBER**

Yet that blemish has done little to shake Russia's love for its favorite explorer—and his bullish, sometimes near-jingoistic tone. "Artur Nikolayevich gets accused in the West of being a nationalist, but he is a patriot, which is something very different," says Vladimir Gruzdev, the Duma member and joint owner of a supermarket chain who part-funded the North Pole dive. "He has dedicated his whole life to polar research, so when he defends Russia's interests in the Arctic, he is doing nothing less than defending his own home."

On, and below, the ice

Born in 1939 in Leningrad, Chilingarov graduated from a naval academy in 1969 with a major in oceanography and was immediately dispatched to a research station in the Arctic port of Tiksi. He then worked his way through the ranks, heading two ice-floe-drifting stations in the Arctic. These staffed outposts, which shelter a small band of researchers dropped on free ice to conduct studies for months at a time, have been a staple of Soviet, and now Russian, Arctic science since 1937.

Afterward, Chilingarov took on increasingly responsible state posts connected to hydrometeorology and the polar regions. Since 1985, when he led a successful mission to save the ice-surrounded research ship *Mikhail Somov* in the Antarctic, Chilingarov's career has been marked by high-profile polar trips in aircraft and ships, with the flag-planting submersible dive being his crowning glory. Last year, he was named Russia's presidential envoy for international cooperation in the Arctic and Antarctic. So does Chilingarov the diplomat now regret the tone of his pronouncements after the North Pole dive?

"Look," he says, his sonorous voice filling an office dotted with reminders of his explorations: a waist-high wooden carving of a penguin, large photographs of polar bears, a huge pair of insulated boots, "It was not only my dream but that of polar researchers of many countries—for many years they dreamed of reaching the Poles. Before, it was all on ice. And all of them, of course, went there with the flags of their country. Amundsen, Scott, Peary, the Bolsheviks, the Russian explorers of later years—all these expeditions carried the flag of their motherland. We took our flag to the bottom of the

Going down. This *Mir* sub and another one are diving into Lake Baikal for records and data.

CREDIT: DMITRY KOSTYUKOV/AFP/GETTY IMAGES

850 meters. "These sources have been known about since the 18th century, but before us no one had seen how the oil is released drop by drop into the water," says expedition member Tamara Zemskaya, a microbiologist from the Limnological Institute in Irkutsk, near Baikal. "Only thanks to the *Mirs* were we able to study the process at first-hand and take targeted samples."

The probes have already yielded intriguing new data. "We were amazed by the abundance of fauna on and in these bitumen formations—it was much higher than the background level in the lake," Zemskaya explains. "We were also surprised that in sediment soaked with oil, there were benthic organisms that were actively moving about, and it appeared that the oil had not inhibited their development."

De Batist agrees that the chance to descend in one of the *Mirs* was "exciting" and "unique." "My dive was directed towards one of the mud volcanoes we discovered in 1999," he says. "We managed to find it on the lake floor and to sample the mud, observe cracks and faults, and make some temperature measurements."

As for the future, Robert Nigmatulin, director of RAS's P. P. Shirshov Institute of Oceanology and one of the scientists who dove into Baikal last year, believes there are encouraging signs that the lake has protected itself from the mill and other threats using its own living decontamination system. "Baikal is not just H_2O; it's a kind of bouillon where there are many living organisms at all layers of depth," he says. "Thanks to these plankton, the composition of the water has remained stable because they constantly filter and purify it."

Artur Chilingarov, the oceanographer and explorer who leads the expedition, stresses that the emphasis of research must be on preserving the lake for future generations. "We must increase our knowledge of Baikal in order to save its unique ecosystem," he says. **–T.P.**

Published by AAAS

Arctic Ocean under the Pole." He picks up a 15-cm model of the Russian tricolor and plants it in the middle of his desk. "What's the difference?"

The difference may be that it is precisely the ocean bed that is now the Arctic's greatest prize. According to the latest estimates from the U.S. Geological Survey, about 13% of the world's undiscovered oil and 30% of the world's undiscovered gas may be found north of the Arctic Circle, with the latter being largely concentrated in offshore zones near Russia (*Science*, 29 May, p. 1175). The speed of the polar ice melt and the advance of drilling technology have raised the possibility that these vast natural resources will become increasingly exploitable just as onshore hydrocarbon reserves begin to dwindle. In a scramble to cash in on the Arctic's riches, Russia, the United States, Canada, Norway, and Denmark (via Greenland) are now lobbying U.N. bodies to decide who has jurisdiction over the region, each providing geographic evidence. According to international law, the five countries with an Arctic coastline have exploitation rights over a 320-km zone extending north of their borders, but the Kremlin is claiming a much bigger territory on the controversial theory that the underwater Lomonosov Ridge running toward the North Pole is connected to Russia's continental shelf, making it by law a "natural prolongation" of Russian land (*Science*, 16 March 2007, p. 1525).

During Chilingarov's North Pole dive in 2007, the minisubmarines *Mir 1* and *Mir 2* collected samples from the seabed, which the explorer suggested could strengthen Russia's claim. Putin fanned the flames by telling Chilingarov shortly after the dive that "we need the results of your expedition to act as the basis of Russia's position" on shelf limits.

That suggestion brought scorn from some quarters in Russia, with one polar expert saying "you can't determine anything with a single bucket of mud from the Pole." Only a complex program of seismic and geological tests could come anywhere close to proving the Lomonosov theory, the critics pointed out. Russia has been preparing a new claim for review by the United Nations; Valery Kaminsky, director of VNII Okeangeologiya, the oceanography institute in St. Petersburg, which is coordinating the work, stressed last year that the task had been going on for years. Scientists on the research ship that transported Chilingarov's minisubs to the Pole in 2007 contributed to it, he said. But Kaminsky indicated that Chilingarov's efforts had been of little importance, remarking with indifference that "the fate of the samples raised from the bottom of the Arctic Ocean [by the *Mir* submersibles] is unknown to us."

Perhaps stung by such criticism, Chilingarov now claims there was no intention to use seabed samples from his expedition to shore up Russia's claim to the Arctic. "The two things were not related," he says. "Whoever says they were is mixing up their fantasy with reality." He adds: "It was just politicians who talked that up. In principle, it [the dive] was a geographical first, an outstanding one; … we were the first people on Earth to see the floor of the Arctic Ocean, at a depth of 4300 meters, and to move along it. That's how it should be presented."

Polar presence. Chilingarov has made many visits to the polar regions, such as this one to an Antarctic research station.

Political scientist

Chilingarov has close ties with members of the powerful military-security clique of senior officials, such as Putin, now prime minister, and the head of the Security Council, Nikolai Patrushev, yet his political influence may go only so far. "Chilingarov is an imposing character with a striking background," says Alexei Makarkin, an analyst with the Moscow think tank Center for Political Technologies. "But in terms of geopolitics and Russia's strategy on the Arctic, I don't think he takes major decisions. He is seen more in the Kremlin as a reliable status figure with good patriotic credentials whose expeditions help confirm Russia's status as a great power."

As for scientific credibility, Jan-Gunnar Winther, director of the Norwegian Polar Institute in Tromsø, Norway, agrees with Burkov that many of Chilingarov's trips to polar regions are "spectacular expedition events" or simply "visits." "For the last decade of his life, or maybe the last 2 decades, he has been a polar expert on the strategic and political level and not as a hands-on scientist, that's quite clear," says Winther.

Some see the ongoing Lake Baikal effort as another example, so far, of style over scientific substance. Chilingarov proudly participated in the early media-covered dives last summer, although that publicity backfired somewhat when members of the team had to backtrack from their initial claims that the submersibles had reached a record depth in the world's deepest lake; the subs actually reached only 1580 meters, short of the 1637 meters achieved by a previous Russian sub in 1990.

Nonetheless, Winther argues that Chilingarov has played a key role in securing funding for the scientific community, particularly for those working in the often-neglected polar regions: "He has been a very important player who has ensured good financial support for Russian scientists who are doing the data-collecting that is needed for the continental shelf commission—and other science" such as for the IPY. Colleagues say he also attracted vital funding for the Baikal dives.

On the Arctic, Chilingarov seems to have softened his rhetoric as he points out the Lomonosov Ridge on a large globe. "Everything must be done in accordance with international law," he says, admitting it could be up to 4 years before Russian experts collect enough data to prove a connection between the ridge and the country's continental shelf. (He had earlier predicted a new submission to the U.N. would be made by this year.)

Still, Chilingarov's pride in Russia's Arctic presence remains strong. "Today, the North Pole-36 drifting station is Russian!" He enunciates the syllables in Russian for emphasis, "Ro-ssi-ska-ya!" He continues, "Our team spends the winter on the ice right next to the Pole. No one else is there."

And there's no denying that those outside Russia hear that booming voice. Mead Treadwell, chair of the U.S. Arctic Research Commission, confirms that Chilingarov's Arctic expedition in 2007 did prompt thoughts that "we needed to be doing a much stronger mapping effort ourselves" so as not to miss out on the Arctic "Cold Rush."

"As someone who advocates for American science, I was quite grateful that the world had this reaction because then people [in the United States] said, 'Well we have a geostrategic interest in following through ourselves.' And when I met Dr. Chilingarov at an Explorers' Club dinner last year, I did say thank you for giving us that stimulus."

–TOM PARFITT

Tom Parfitt is a freelance writer based in Moscow.

Published by AAAS

EVOLUTION

Authors Scramble to Make Textbooks Conform to Texas Science Standards

The Texas market is so large that publishers must pay heed to new guidelines on what students should learn

Kenneth Miller, a Brown University biologist and author of a popular high school textbook, has spent years battling advocates of intelligent design (ID) and their argument that students need to be taught the "strengths and weaknesses" of evolution. So it was more than a little embarrassing when defense lawyers for the Dover, Pennsylvania, school board, on trial in 2005 for its policy to accommodate ID in biology classes, asked Miller, a prosecution witness, why he had used the same phrase in the 2004 edition of his textbook.

He had done so, Miller explained, so that his textbook could be used in classrooms throughout Texas, the second largest market in the United States. (Texas standards also shape what's sold nationally, as publishers often use the same version in other states.) The "weaknesses" were nothing more than unresolved questions about evolution, Miller insists. "We wanted to show, without compromising scientific integrity, that we had met the literal standard requiring strengths and weaknesses," he says.

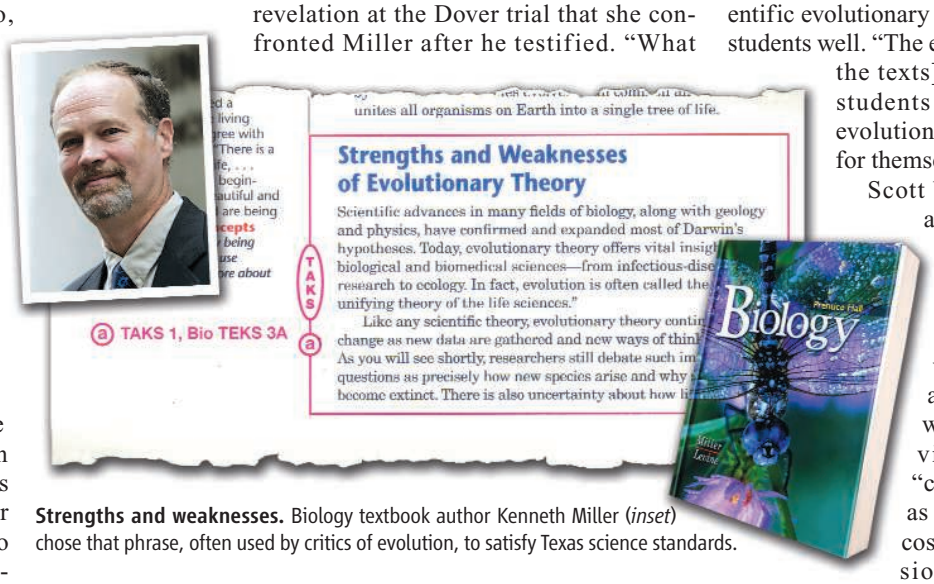

Strengths and weaknesses. Biology textbook author Kenneth Miller (*inset*) chose that phrase, often used by critics of evolution, to satisfy Texas science standards.

In March, the Texas school board approved new science standards that omit the "strengths and weaknesses" line (*Science*, 3 April, p. 25). But many scientists view the new version as more insidious than the previous one. Among other things, it requires that students have the chance to "analyze and evaluate scientific explanations concerning the complexity of the cell." The language is seen as an opening for ID proponents to argue that such "irreducible complexity" points to an external organizing force.

Those standards pose a new challenge for Miller and other textbook authors as the board prepares for a new round of textbook adoption in 2011. Eugenie Scott of the National Center for Science Education in Oakland, California sees Miller's earlier revision as a failed "attempt to be clever." And she's worried that history might repeat itself.

"When you put 'weaknesses' and 'evolution' in the same line, you reinforce doubts that creationists are trying to sow," says Scott, whose organization monitors the issue as it plays out in state and local districts. In fact, Scott was so incensed by the revelation at the Dover trial that she confronted Miller after he testified. "What were you thinking?" she asked him.

Miller's answer, then and now, is not to get too excited. The new Texas standards leave plenty of room for authors to explain the robustness of evolutionary theory, he says, and that's precisely what he and his publisher, Prentice Hall, plan to do. "The advocates of these standards underestimate the strength of the scientific evidence for structures and phenomena that they mistakenly believe evolution cannot account for," Miller says. "The new wording is an opportunity to make biology texts even stronger."

For example, Miller intends to "introduce more material on the evolution of organelles" within the cell to show that the cell's complexity is in fact explained by evolution. Likewise, he sees the standard requiring explanations of "sudden appearance, stasis, and sequential nature of groups in the fossil record"—although written with the intent to undermine evolution—as "an invitation to introduce students to punctuated equilibrium."

Steve Nowicki, a biologist at Duke University in Durham, North Carolina, plans to take the same approach when he asks Texas to adopt his biology book, published by Holt McDougal. "I understand that there may be a political agenda behind the standards, but I am taking them at face value," he says. "If a state thinks students need more information to understand evolution, I am happy to provide that."

Don McLeroy had wanted the standards to require textbooks and other materials to offer an even more skeptical view of evolution. But McLeroy, whom the state legislature declined to reappoint as chair last month although he remains on the board, says he's satisfied that requiring "more scientific evolutionary discussions" will serve students well. "The explanations offered [in the texts] will be so weak that students who are skeptical of evolution will see the weakness for themselves," he says.

Scott believes that Miller's approach is a "wonderful way to beef up content" while sticking to the letter of the standards. But she's worried that McLeroy and others on the board who embrace ID may view phrases such as "complexity of the cell" as a victory, even if only cosmetic. "Sowing confusion is their goal," she says. How far they will push on the actual content will depend on the composition of the publicly elected board in 2011, she says. "I'm just hoping publishers don't get weak-kneed and give in."

Alton Biggs, a co-author of a popular biology textbook published by Glencoe, concedes that that may have happened in 2003, when 12 lines about "divine creation" were included in a section of his book that describes various "beliefs and hypotheses" for the origin of life. But those words were dropped in the next edition. He says his team expects that the version to be submitted for adoption will "meet the Texas standards as well as benchmarks and other standards set by scientific societies."

–YUDHIJIT BHATTACHARJEE

Published by AAAS

U.S. HIGHER EDUCATION

Minority Retention Rates in Science Are Sore Spot for Most Universities

A few universities have demonstrated what it takes to help more minority students earn science degrees. But their efforts are only beginning to be widely replicated

CATONSVILLE, MARYLAND—Yohance Allette didn't panic when he hit a "rough stretch" of science courses last year as a sophomore at the University of Maryland, Baltimore County (UMBC) here. He knew that, as a Meyerhoff Scholar, he could lean on what he calls his "friends and family"—older students, faculty members, and university staff—to help him make it through organic chemistry, physics, and genetics.

Having such a support group is a big reason why Allette, a biology major, and other Meyerhoff scholarship students are twice as likely to earn a bachelor's degree in a science field, and five times as likely to enroll in graduate study, as their peers who were accepted but chose not to enter the program. "It's like being able to talk with your older brother or sister," says Allette, whose parents are from the Caribbean.

Begun in 1989, the Meyerhoff program has tried to address a glaring failure of U.S. higher education: the high attrition rates among minority students (predominantly African-Americans and Hispanics) who declare an interest in science, technology, engineering, and mathematics (*Science*, 31 March 2006, p. 1870). Although minority students entering U.S. colleges are just as interested as their white peers in these STEM fields, they are only two-thirds as likely as whites to earn bachelor's degrees in those fields within 6 years. (Asian Americans, who are not considered a minority in STEM fields, are more likely than whites to earn such degrees.)

"Most institutions have the *intent* to improve retention rates; they simply don't know how to do it," says mathematician Freeman Hrabowski, UMBC's president. He's also a standard-bearer for the program, backed by Baltimore philanthropists Robert and Jane Meyerhoff. Their family foundation supplies two-thirds of the program's $3.5 million budget for 2008–09.

A team approach. John Matsui and students in the Biology Scholars Program at UC Berkeley.

On the West Coast, the 16-year-old Biology Scholars Program (BSP) at the University of California (UC), Berkeley, has also succeeded in helping underrepresented minorities make it through college. Since 2000, 69% of its 650 students have graduated within 4 years, topping the 61% rate for the rest of the student body. Among African-American students—some of whom take more than 4 years to complete their studies—scholars have a 93% graduation rate versus 73% for their nonprogram peers. Only 0.15% of biology scholars are dismissed for poor academic performance, notes evolutionary biologist John Matsui, who directs the program, compared with 3.5% for all UC Berkeley undergraduates. The program's annual budget of $1.5 million comes from the Howard Hughes Medical Institute (HHMI) and, since 2004, the Gordon and Betty Moore Foundation.

Although the two programs differ in many respects, their ability to lend minority students a helping hand at the right time seems to be critically important. For his first 2 years at UC Berkeley, Eric Octavio Campos, a graduating senior, says, "I was very much alone on this huge campus, and there were so few Latinos or African Americans in my science

Following the Leaders

Several institutions have begun to imitate aspects of the Meyerhoff program at the University of Maryland, Baltimore County, and the Biology Scholars Program at the University of California (UC), Berkeley (see main text). However, none has published comprehensive data on what has been accomplished.

Five years ago, Louisiana State University, Baton Rouge, began a program to serve disadvantaged science students. LA-STEM tries to replicate Meyerhoff's tiered mentoring and summer programs but without the same level of financial aid. With this month's graduation, 46 students have completed the program, with a retention rate of 90%. Even so, its driving force, vice chancellor and analytical chemist Isaiah Warner, admits that "we are far behind Meyerhoff in terms of getting and measuring results."

This past summer, about 50 incoming engineering students at the University of Michigan (UM) joined a new academy that includes a summer program, mentoring, research internships, and modest student grants. "Our challenge was, How could we put a Meyerhoff-like model to work in a large research institution?" says Derek Scott, who directs UM's multicultural engineering program.

The UC Berkeley program has been an inspiration for two other UC campuses, and in 2007, Cornell University embraced its name and concepts to tackle its attrition rate among minorities in biology, says virologist Laurel Southard, who directs the department's undergraduate research and outreach. The Cornell program takes in 20 to 25 first-year students each year, offering them mentoring, special events, and research opportunities. Southard is seeking outside support to supplement a small budget provided by the department and the vice provost's office.

The biology department at Harvard University offers a Howard Hughes Medical Institute–sponsored program that each year enrolls about 40 freshmen students from disadvantaged backgrounds. "We stick with them for all 4 years," says biologist Robert Lue. "They are assigned to a faculty lab and mentored by faculty and others." In 2006, Harvard started a wider effort—the Program for Research in Science and Engineering—that offers summer research opportunities to undergraduates from all of the sciences. Lue says that the number of women and underrepresented minorities majoring in the life sciences has risen by 16% over the past 4 years. He's now analyzing the program's impact on attrition rates. **–R.K.**

CREDIT: COURTESY OF UNIVERSITY OF CALIFORNIA, BERKELEY

Published by AAAS

classes." But joining the Scholars program "gave me a sense of community and helped advise me on how to get where I wanted to go in science." This fall, Campos will enter a Ph.D. program in biology at the University of Washington, Seattle.

Good intentions, scant data

UMBC and UC Berkeley often figure prominently in discussions of how to bolster the numbers of minorities entering STEM fields. It's a perennial topic among those who worry about whether the United States is producing enough scientists and engineers. Michael Summers, a biochemist at UMBC who has been active in the Meyerhoff program, wondered why more universities haven't been able to match its success.

Summers took his concerns to HHMI, which supports Summers' lab as an HHMI investigator. With help from the institute and contributions from the National Institutes of Health, Summers and colleagues invited diversity specialists from 75 research universities and leading 4-year colleges to discuss undergraduate STEM diversity and retention.

Summers recalls that many administrators who attended the group's first meeting in 2004 at Harvard University "were shocked at how low STEM retention was among disadvantaged students" and by how few institutions actually tracked dropout rates from STEM fields. They vowed to do better. Educators met again in 2007 and 2008 to report on their progress, including the status of new programs.

Success in situ. Yohance Allette says the Meyerhoff program has helped him stay in biology.

But Summers says few have developed good empirical data. "Most institutions don't track their students and thus don't know their own performance when it comes to retaining and educating underrepresented minorities," he says. And it will take years to collect and analyze the data at institutions that have begun to do so.

One problem, says John Slaughter, president of the National Action Council for Minorities in Engineering in White Plains, New York, is that most universities that care about diversity have concentrated on entry points rather than completion rates. "We need to focus more of our attention on outcomes like retention and graduation rather than simply enrolling more minority students," he argues.

Another issue is the paucity of good studies of what Matsui calls "the sociology of science diversity." Conventional wisdom values summer bridge programs for incoming freshmen and the chance to do undergraduate research, for example, but Matsui says "we need more rigorous study to understand what works, for which students, and under what conditions." Such comparisons are hard to make when most programs preselect students, notes social psychologist Martin Chemers of UC Santa Cruz, who adds that the lack of control groups hinders empirical studies.

A third problem is the absence of data on what happens after students graduate. "We have no idea whether most of these programs are working or not," says Willie Pearson Jr., a sociologist at the Georgia Institute of Technology in Atlanta who studies science education. "There's a great need for follow-up data." The National Science Foundation hopes to address that need, says Kellina Craig-Henderson, a manager within NSF's cognitive sciences program, with an initiative, labeled "The Science of Broadening Participation," that would fund research on effective programs and how they can be scaled up.

Different approaches

The UMBC and UC Berkeley programs take different paths to help their target populations. UMBC recruits high-achieving high-school seniors, two-thirds of them underrepresented minorities, gives them generous financial aid, uses a summer bridge program to create group cohesion, plunges them quickly into research, and surrounds them with mentors. Rather than focus mainly on what he calls "high flyers," Matsui looks for "those on the margins, who will succeed if given the right environment and opportunities." The UC Berkeley program offers mentoring and group cohesion but does not include a summer program, offer a separate stipend, or require freshmen to do research.

Meyerhoff's results are impressive. Seven of eight graduates (more than 650) have earned degrees in STEM fields, and they have gone on to receive 53 Ph.D. degrees, 74 medical degrees, and 21 combined degrees. Hrabowski says that makes UMBC, with an enrollment that is 14% African-American and 3% Hispanic, "one of the few predominantly white universities producing significant numbers of African-Americans who go on to get Ph.D.s."

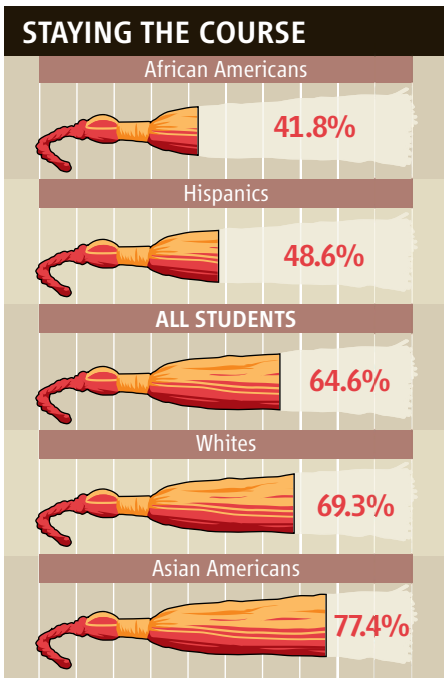

Elusive degree. A minority of African-American and Hispanic students who begin as science majors actually graduate with a STEM degree.

UC Berkeley's program, which has helped 2000 students, can't match those retention numbers: So far, about 70% of BSP students have graduated with biology degrees. Matsui is proud of having created what he calls a sense of community among students, advisers, and "culturally sensitive" faculty members. "The network of close-knit students and mentors gives you a basis to succeed," says UC Berkeley senior Dannielle McBride, an African American who joined Matsui's group after four part-time years at a community college.

Although they disagree on some of the necessary ingredients, Hrabowski and Matsui are both passionate about collecting and analyzing data to evaluate and improve their programs. They are also eager to share their knowledge with other universities. "We place a great deal of emphasis on evaluation, and other institutions should also," says Hrabowski, who chairs a National Research Council panel for the National Academies that is assessing minority STEM education.

Allette, a rising senior who hopes to earn a combined M.D.-Ph.D. degree, says programs like Meyerhoff provide students with the support they need to persevere. "The challenge for science majors is not so much, 'Do I *want* to do it?' as '*Can* I do it?' Once you are confident of success, you can go far."

–ROBERT KOENIG

CREDITS (FROM TOP TO BOTTOM): SOURCE: U.S. DEPARTMENT OF EDUCATION BEGINNING POSTSECONDARY STUDENT LONGITUDINAL STUDY:1996/01; ADAPTED BY M. TWOMBLY/*SCIENCE*; ROBERT KOENIG/*SCIENCE*

Published by AAAS

The David Starr Jordan Prize
For Innovative Contributions to the Study of Evolution, Ecology, Population and Organismal Biology

In 1986, Cornell, Indiana and Stanford Universities established a joint endowment to fund a prize in honor of David Starr Jordan, a scientist, educator and institution builder of enormous influence on higher education in the United States who had important ties to each of these universities. The prize is international in scope and presented approximately every three years to a young scientist (40 years of age or less) who is making novel innovative contributions in one or more areas of Jordan's interest: evolution, ecology, population and organismal biology.

The intent of this prize is to recognize young scientists who are making research contributions likely to redirect the principal foci of their fields. In addition to a cash award, the recipient will receive a commemorative medal, will attend an awards ceremony, visit each of the sponsoring institutions and give scholarly presentations of his/her work. The selection of the prize winner will be made by a committee composed of representatives from each of the three institutions.

The sixth David Starr Jordan Prize will carry a prize of $20,000.00 and will be announced in Fall of 2009. This year the award ceremony will be held at Cornell University.

Nomination forms are posted on the David Starr Jordan Prize Website (www.davidstarrjordan.org). Nomination forms with supporting materials should be submitted by email. Questions should be directed to:

Dr. William L. Crepet, Chair
Plant Biology Department
412 Mann Library Building
Cornell University
Ithaca, New York 14853
(607-255-2131 - FAX 607-255-5407) - email WLC1@cornell.edu

All nomination materials must be received prior to August 15, 2009.
For more information including a list of previous prize winners and their accomplishments, visit: **www.davidstarrjordan.org**.

On essences and the supernatural 1392

How pulsars evolve 1396

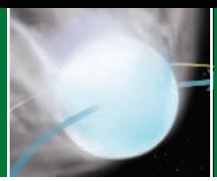

Charging individual atoms 1397

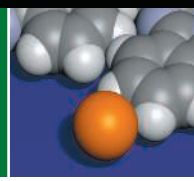

LETTERS

edited by Jennifer Sills

Endangered. The Roti Island snake-necked turtle is one example of a species threatened by wildlife trading.

Redesigning the Wildlife Trade System

K. F. SMITH *ET AL.*'S POLICY FORUM ("REDUCING the risks of the wildlife trade," 1 May, p. 594) aptly proposes the need for a priori restrictions to be placed on newly traded wildlife species to predetermine their environmental, health, and economic impacts. The need for such restrictions is clear for the conservation of these traded species as well. For example, some reptile species collected for the exotic pet trade have been driven to near extinction, or extirpated from their type localities, immediately after their description in the scientific literature (*1*) and before receiving any protection through registration in the Convention on International Trade in Endangered Species (CITES) of wild fauna and flora.

The novelty and potential rarity of newly traded species could result in the occurrence of anthropogenic allele effects (*2*), which may ultimately lead to heavy population declines, even during the time required to process CITES registrations (*3*). Automatically restricting the trade in these species could allow conservation assessments to be undertaken in addition to risk analyses of their potential impact. Given all the knowledge we have accrued about the negative impacts of the wildlife trade, perhaps it would make more sense to adopt a system whereby permissions are sought to include a species in the international trade, rather than requiring hasty applications for limits when it may already be too late.

ANGELO P. PERNETTA

NERC Centre for Ecology and Hydrology, CEH Wallingford, Benson Lane, Crowmarsh Gifford, Wallingford, Oxfordshire OX10 8BB, UK. E-mail: a.p.pernetta@googlemail.com

References

1. B. L. Stuart, A. G. J. Rhodin, L. L. Grismer, T. Hansel, *Science* **312**, 1137 (2006).
2. F. E. Courchamp *et al.*, *PLoS Biol.* **4**, e415 (2006).
3. P. Rivalan *et al.*, *Nature* **447**, 529 (2007).

Wood Energy: Predicting Costs

THE POLICY FORUM "WOOD ENERGY IN America" (D. deB. Richter Jr. *et al.*, 13 March, p. 1432) was a much-needed and long-overdue contribution to energy discussions. However, fossil fuels are not four times more expensive than wood per unit energy. Rather, most fossil fuels are still less expensive than wood in most places, though the price of wood shows more local variation and is more volatile even than that of fossil fuels. Global mean wholesale price for sawlogs in the first quarter of 2008 was about $170 per metric ton (MT), or about $10/GJ (*1*). The mean wholesale price for pellets then was about $200/MT, or about $11/GJ (*2*). Since then (because of the housing crash), the price of sawlogs has dropped dramatically in the United States (*3*), but the global wholesale price of wood pellets has remained stable (*2*).

At $60/barrel, oil is $10/GJ; natural gas currently is about $4/GJ (*4*). The latest Energy Information Administration projections place the mean cost of coal to U.S. utilities in 2009 at $2/GJ, though high-grade coals can be three times as expensive ($180/MT) (*4*).

The cost of wood seems likely to soar again within a few years. A severe pine-beetle blight began in North America in 1999, and today vast expanses (several gigatons, over 500,000 km^2) of the forests in North America are dead (*5*). These forests (containing over four times as much dead wood as current global wood annual usage) will be largely destroyed by wildfires over the next 6 years. Even in the United States, wood pellets have recently sold for over $320/MT in some areas (*6*), and some projections indicate global wood-pellet usage will continue to grow at over 20% annually for the next decade (*7*). It's hard to image wood pellets being under $400/MT ($22/GJ) by 2013.

F. DAVID DOTY

Doty Energy, 700 Clemson Road, Columbia, SC 29229, USA. E-mail: david@dotynmr.com

References

1. UNECE Forest Products Annual Market Review, 2007–2008; http://timber.unece.org/fileadmin/DAM/FPAMR2008.pdf.
2. C. Rakos, *Int. Sustainable Energy Rev.* **1**, 142 (2009).
3. Texas Forest Services, *Texas Timber Price Trends*, (January/February, 2009).
4. Energy Information Administration, "Short-term energy outlook" (2009); www.eia.doe.gov/emeu/steo/pub/mar09.pdf.
5. S. W. Running, *Science* **321**, 652 (2008).
6. E. Russell, "Market for pellets tightens," *Bangor Daily News*, 25 September 2008; www.bangordailynews.com/detail/51497.html.
7. Wood Resources International, LLC; www.woodprices.com.

Wood Energy: Protect Local Ecosystems

IN THEIR POLICY FORUM PAPER "WOOD ENergy in America" (13 March, p. 1432), D. deB. Richter Jr. *et al.* argue cogently for deployment of advanced wood combustion (AWC) systems to meet a range of objectives, and they demonstrate the potential economic and energy values of community-based AWC in the United States. The accuracy of their estimates of U.S. energy potential from AWC is dependent, in part, on estimates of wood supply. This includes logging residue (tops, branches, and foliage) from sustainably

Published by AAAS

managed forests. However, they do not address what proportion of this residue should be left on-site to sustain local ecosystems over multiple rotations.

Neither of the authors' examples of mid-sized state inventories estimate this proportion (*1*, *2*), yet the U.S. national biomass inventory assumes that 35% of total logging residue produced should be left to allay site impact concerns (*3*); other large-scale logging residue inventories have used reductions of 0% (*4*, *5*), 30% (*6*), 50% (*7*), and 100% (*8*). When proportional reductions are used, these are based on expert opinion and one proportion is applied to all sites within large regions (country, state, province, or land ownership system). Which reduction is most appropriate?

In a recent EU report (*9*), expert opinion was used in a biomass inventory study to define different levels of logging residue retention for each of four site sensitivity classes, based on slope, elevation, and soil properties. The resultant site sensitivity map was then combined with a forest inventory map of the same grid size (1 km by 1 km) to create a spatial layer defining the environmentally compatible potential for logging residue removals that could then be scaled up to large-scale resolution across Europe.

Results show a reduction (for 2000 to 2005) in total logging residue inventory of 39% for the EU-13 and 41% for the EU-21 countries. The similarity in the 13- and 21-country results suggests that, for the soil criteria used and for conditions similar to those in the European Union, a 40% reduction for large-scale inventories would be reasonable. The EU study, however, focuses on soil issues; until similar approaches are applied for other aspects of the ecosystem (such as biodiversity and water quality), using a 50% retention proportion therefore may be appropriate, as in some national studies (*7*).

BRIAN D. TITUS,[1]* DOUGLAS G. MAYNARD,[1] CAREN C. DYMOND,[2] GRAHAM STINSON,[1] WERNER A. KURZ[1]

[1]Natural Resources Canada, Pacific Forestry Centre, Victoria, BC V8Z 1M5, Canada. [2]British Columbia Ministry of Forests and Range, Victoria, BC V8W 9C2, Canada.

*To whom correspondence should be addressed. E-mail: Brian.Titus@NRCan-RNCan.gc.ca

References

1. C. D. Ray, "Pennsylvania low-use wood potential" (Pennsylvania State University, State College, PA, 2007); www.outreach.psu.edu/programs/goddard/files/Ray.ppt#256.
2. C. Hopkins, "Potential of biomass to support a renewable portfolio standard in North Carolina" (North Carolina State University, Raleigh, NC, 2006); www.ces.ncsu.edu/nreos/forest/feop/Agenda2006/energy/presentations/hopkins.pdf.
3. R. D. Perlack *et al.*, "Biomass as feedstock for a bioenergy and bioproducts industry: The technical feasibility of a billion-ton annual supply" (DOE/GO-102995-2135 and ORNL/TM-2005/66); available at http://feedstockreview.ornl.gov/pdf/billion_ton_vision.pdf.
4. S. Wetzel, L. Duchesne, M. LaPorte, *Bioproducts from Canadian Forests: New Partnerships in the Bioeconomy* (Springer, Dordrecht, Netherlands, 2006).
5. W. Mabee, E. D. G. Fraser, P. N. McFarlane, J. N. Saddler, *Appl. Biochem. Biotechnol.* **129**, 22 (2006).
6. P. Ralevic, D. B. Layzell, "An inventory of the bioenergy potential of British Columbia" (BIOCAP Canada Foundation, Kingston, Ontario, Canada, 2006); www.biocap.ca/images/pdfs/BC_Inventory_Final-06Nov15.pdf.
7. S. W. Wood, D. B. Layzell, "A Canadian biomass inventory: Feedstocks for a bio-based economy" (BIOCAP Canada Foundation, Kingston, Ontario, Canada, 2003); www.biocap.ca/images/pdfs/BIOCAP_Biomass_Inventory.pdf.
8. J. Etcheverry *et al.*, *Smart Generation: Powering Ontario with Renewable Energy* (David Suzuki Foundation, Vancouver, British Columbia, Canada, 2004); www.davidsuzuki.org/files/Climate/Ontario/Smart_Generation_full_report.pdf.
9. European Environment Agency, "How much bioenergy can Europe produce without harming the environment?" (EEA Report No. 7/2006, 2006); www.eea.europa.eu/publications/eea_report_2006_7/at_download/file.

Wood Energy: The Dangers of Combustion

WE AGREE WITH THE RECENT POLICY FORUM ("Wood energy in America," D. deB. Richter Jr. *et al.*, 13 March, p. 1432) that renewable, clean, and affordable energy sources are desirable; however, there may be detrimental health outcomes associated with widespread adoption of advanced wood combustion (AWC).

Air pollution from wood combustion is associated with a variety of adverse health impacts (*1*), and typical emissions (even from AWC) are significantly higher than those from modern natural gas and fuel oil combustion (*2*). Although pollution control technologies are available, they are not yet consistently applied, even in newer wood boiler installations such as those in the Fuels for Schools program (*3*).

More important, even if emissions from AWC are reduced relative to other sources, the distributed nature of a proposed wood energy system would lead to thousands of small combustion sources in close proximity to population centers, increasing the proportion of harmful emissions that result in human exposure (*4*, *5*). Distributed sources such as AWC would require dramatically lower emissions per unit energy than centralized combustion facilities in order to yield a net reduction in population exposure to air pollution (*6*).

Identifying rational climate-mitigation strategies, whether biomass-related or otherwise, requires integrated assessments that carefully weigh climate and energy security benefits with potential health and other environmental impacts (*7*, *8*).

FRANCIS J. RIES,[1]* JULIAN D. MARSHALL,[2] MICHAEL BRAUER[3]

[1]Institute for Resources, Environment, and Sustainability, University of British Columbia, Vancouver, BC V6T 1Z4, Canada. [2]Department of Civil Engineering, University of Minnesota, Minneapolis, MN 55455, USA. [3]School of Environmental Health, University of British Columbia, Vancouver, BC V6T 1Z3, Canada.

*To whom correspondence should be addressed. E-mail: francisr@interchange.ubc.ca

References

1. L. Naeher *et al.*, *Inhal. Toxicol.* **19**, 67 (2007).
2. U.S. Environmental Protection Agency, *Compilation of Air Pollutant Emission Factors, Vol. 1: Stationary Point and Area Sources* (EPA Publication AP-42, ed. 5, 1995); www.epa.gov/ttn/chief/ap42.
3. Fuels for Schools and Beyond (www.fuelsforschools.info).
4. D. Bennett *et al.*, *Environ. Sci. Technol.* **36**, 206A (2002).
5. F. J. Ries *et al.*, *Environ. Sci. Technol.*; available at http://pubs.acs.org/doi/abs/10.1021/es803127d.
6. G. Heath *et al.*, *Atmos. Environ.* **40**, 7164 (2006).
7. E. Mazzi, H. Dowlatabadi, *Environ. Sci. Technol.* **41**, 387 (2007).
8. J. Hill *et al.*, *Proc. Natl. Acad. Sci. U.S.A.* **106**, 2077 (2009).

Response

FORESTERS AND LOGGERS FROM AROUND THE United States report that energy wood delivered to market runs from less than $20 to $50 per green Mg (ton) with 50% moisture (*1*), prices that convert to about $2 to $5 per GJ. Doty questions these prices based on a common misunderstanding of how wood is harvested in the forest. Energy wood is merchandized as a low-priced product (not to be confused with much higher priced sawtimber), and thus energy wood thinnings can support forest improvement projects for restoration, conservation, and fire-risk reduction. Our estimates of $2 to $5 per GJ for energy wood include a historic range of low-priced wood products and can be compared with the Energy Information Administration reports that indicate industrial users of natural gas paid nearly $7 per GJ in January 2009 and that the spot price of distillate fuel was almost $10 per GJ in March 2009 (*2*, *3*), far above that of energy wood. Doty's letter illustrates the need for wood-energy

CREDIT: JUPITERIMAGES

education, the need for standardized definitions of biomass energy (*4*), and the need to better quantify environmental and social benefits that amplify financial advantages made possible by wood.

Titus and colleagues address wood supply by reviewing estimates for how much energy wood can be recovered from newly logged forests, which is important because sustainability requires that energy-wood harvests not degrade forest ecosystems. Research on harvest impacts on soils is extensive (*5*, *6*), and despite site-to-site variation, Titus and colleagues point to European and North American assessments that 40 to 65% of woody debris left on-site after conventional logging might be marketed as wood energy. These estimates illustrate that the energy-wood supply is enormous, and it is indeed larger still given waste wood from ongoing management of urban forests and the millions of hectares of forests that can be thinned to lower wildfire risks and meet restoration and conservation-forestry objectives. More than abundance alone, our Policy Forum emphasized that wood is too valuable to waste with inefficient combustion and that community-based advanced wood combustion (AWC) systems used for heat, cooling, and power operate at two to three times the efficiency of electricity-generating facilities being planned in response to the Congressionally proposed Renewable Electricity Standard (RES). Burning wood solely for electricity is not AWC as defined in our Policy Forum, given that these facilities will waste 60 to 75% of the energy stored in wood. Such RES-promoted wood electricity helps explain Casten's recent remark that "separate generation of electricity and heat is utter madness" (*7*).

Finally, we heartily agree with Ries and colleagues that integrated assessments can guide society's transition from fossil to efficient and renewable energy systems. Ries and colleagues are concerned, as are we, by health effects of air pollutants from open burning, wildfires, and unregulated stoves and fireplaces. However, none of these combustions qualifies as AWC, which by definition combines high-quality combustion and high-efficiency thermal conversion that together enable systems to strictly control atmospheric emissions. Given the importance of integrated assessments of energy transitions to renewables, Ries and colleagues might be impressed, as are we, with the variety of environmental, economic, and social benefits offered by AWC, including well-demonstrated and ongoing improvements in lowering atmospheric emissions across thousands of systems throughout Europe (*8*, *9*).

DANIEL deB. RICHTER JR.,[1]* DYLAN H. JENKINS,[2] JOHN T. KARAKASH,[3] JOSIAH KNIGHT,[4] LEW R. MCCREERY,[5] KASIMIR P. NEMESTOTHY[6]

[1]University Program in Ecology, Southern Center for Sustainable Forests, Nicholas School of the Environment, Duke University, Durham, NC 27708, USA. [2]The Nature Conservancy, Pennsylvania Forest Conservation Program, Williamsport, PA 17701, USA. [3]Resource Professionals Group, Durham, NC 27707, USA. [4]Pratt School of Engineering, Duke University, Durham, NC 27708, USA. [5]State and Private Forestry, USDA Forest Service, Morgantown, WV 26505, USA. [6]Austrian Chamber of Agriculture, Department of Forestry and Energy, A-1014 Vienna, Austria.

*To whom correspondence should be addressed. E-mail: drichter@duke.edu

References and Notes

1. Resource Information Systems Inc., *Int. Woodfiber Rep.* **15,** 1 (2009).
2. Energy Information Administration (EIA), *Heating Oil and Propane Update* [U.S. Department of Energy (DOE), Washington, DC, 2009].
3. EIA, *Natural Gas Prices* (DOE, Washington, DC, 2009).
4. D. Hagauer, B. Lang, K. P. Nemestothy, *Instruction Manual for the Calculation of Wood Fuel Parameters* (Austrian Energy Agency, Vienna, 2009); www.klimaaktiv.at/filemanager/download/30205.
5. E. L. Stone, in *Impact of Intensive Harvesting on Forest Nutrient Cycling* (State University of New York, Syracuse, NY, 1979), pp. 366–386.
6. D. D. Richter, D. Markewitz, *Understanding Soil Change* (Cambridge Univ. Press, Cambridge, 2001).
7. D. Lindley, *Nature* **458**, 138 (2009).
8. In Austria, not only are AWC systems officially certified for efficiency and emissions before operations, but official test reports of efficiency and emissions are published on the Internet (http://blt.josephinum.at/index.php?id=653).
9. T. Nussbaumer *et al.*, *Particulate Emissions from Biomass Combustion in IEA Countries* (International Energy Agency, Bioenergy Task 32, Zürich, 2008).

Letters to the Editor

Letters (~300 words) discuss material published in *Science* in the previous 3 months or issues of general interest. They can be submitted through the Web (www.submit2science.org) or by regular mail (1200 New York Ave., NW, Washington, DC 20005, USA). Letters are not acknowledged upon receipt, nor are authors generally consulted before publication. Whether published in full or in part, letters are subject to editing for clarity and space.

CORRECTIONS AND CLARIFICATIONS

News Focus: "A long, winding road to ignition" (17 April, p. 327). The item reported that the National Ignition Facility's laser beam travels 305 meters in 25 nanoseconds. In fact, it travels 457 meters in less than 2 microseconds.

Letters: "Creating a common climate language" by T. E. Bowman *et al*. (3 April, p. 36). The atmospheric concentration of CO_2 was 379 ppm in 2005, not 397 ppm.

Editors' Choice: "All washed up" (20 March, p. 1539). The photograph should have shown a red tide in California, but instead showed Gay Head, located on Martha's Vineyard in Massachusetts.

News Focus: "Senate majority leader hands NSF a gift to serve the exceptionally gifted" by J. Mervis (20 March, p. 1548). The longitudinal study of mathematically precocious youth, begun in 1971 by Julian Stanley at Johns Hopkins University, is now being carried out by Camilla Benbow and David Lubinski at Vanderbilt University. Linda Brody directs the Study of Exceptional Youth at Johns Hopkins.

News Focus: "A memorable device" by L. Laursen (13 March, p. 1422). On page 1423, neuropsychologist Georgina Browne's name was spelled incorrectly. The misspelling has been corrected online.

TECHNICAL COMMENT ABSTRACTS

Comment on "Tail Reconnection Triggering Substorm Onset"

A. T. Y. Lui

Angelopoulos *et al*. (Research Articles, 15 August 2008, p. 931) reported that magnetic reconnection in Earth's magnetotail triggered the onset of a magnetospheric substorm. We provide evidence that (i) near-Earth current disruption, occurring before the conventional tail reconnection signatures, triggered the onset; (ii) the observed auroral intensification and tail reconnection are not causally linked; and (iii) the onset they identified is a continuation of earlier substorm activities.

Full text at www.sciencemag.org/cgi/content/full/324/5933/1391-b

Response to Comment on "Tail Reconnection Triggering Substorm Onset"

Vassilis Angelopoulos, James P. McFadden, Davin Larson, Charles W. Carlson, Stephen B. Mende, Harald Frey, Tai Phan, David G. Sibeck, Karl-Heinz Glassmeier, Uli Auster, Eric Donovan, Ian R. Mann, I. Jonathan Rae, Christopher T. Russell, Andrei Runov, Xu-Zhi Zhou, Larry Kepko

Lui challenges our conclusion that magnetic reconnection triggered the onset of a magnetospheric substorm. However, Lui incorrectly uses the auroral electrojet index instead of ground auroral and magnetic field pulsation signatures to determine substorm onset; single velocity and magnetic field components instead of full vectors and particle distributions to identify reconnection onset; and preliminary auroral electrojet–low index (AL) instead of ground magnometer, auroral, and magnetotail data to claim pre-existing activity.

Full text at www.sciencemag.org/cgi/content/full/324/5933/1391-c

Comment on "Tail Reconnection Triggering Substorm Onset"

A. T. Y. Lui

Angelopoulos *et al.* (Research Articles, 15 August 2008, p. 931) reported that magnetic reconnection in Earth's magnetotail triggered the onset of a magnetospheric substorm. We provide evidence that (i) near-Earth current disruption, occurring before the conventional tail reconnection signatures, triggered the onset; (ii) the observed auroral intensification and tail reconnection are not causally linked; and (iii) the onset they identified is a continuation of earlier substorm activities.

Angelopoulos *et al.* (*1*) reported that a magnetospheric substorm was initiated by reconnection in Earth's magnetotail based on observations from NASA's Time History of Events and Macroscale Interactions during Substorms (THEMIS) mission. Here, we reevaluate the evidence focusing on the event analyzed in the main text of (*1*). Figure 1A shows the relative positions of THEMIS satellites for that event. Let us first examine the conventional signatures of reconnection during this interval. By conventional signatures, we mean Earthward plasma flow with positive B_z (the north-south component of the magnetic field) in locations Earthward of the reconnection site and tailward plasma flow with negative B_z in locations tailward. Because only convective plasma flows, that is, flows perpendicular to the magnetic field, are relevant to magnetic reconnection and transport of magnetic flux to cause current disruption/dipolarization in the near-Earth region, only the convective flow components are examined here. Figure 1, B to G, shows the X component of the convective plasma flows V_x and the magnetic field elevation angles λ_B from probes P1, P3, and P4 near the substorm onset time on 26 February 2008 identified in (*1*). The inner satellites P3 and P4 detected Earthward flows ahead of tailward flows at the outer satellite P1 and before the onset (04:54:00 UT) of the THEMIS auroral electrojet index (AE_{TH}), an AE index constructed from THEMIS ground magnetic stations. Current disruption/dipolarization signifies magnetospheric current change and should be matched with ionospheric current change, that is, AE activity. If one attributes the appearance of tailward flows at P1 as reconnection onset, then it occurred after substorm disturbances close to the Earth. This time sequence is consistent with the near-Earth current disruption (CD) activated before tail reconnection further downstream, suggesting substorm onset triggered by CD and not tail reconnection. Examination on the change of λ_B at these satellites reveals a similar time sequence. Appreciable magnetic field configuration changes (current disruption/dipolarization)

The Johns Hopkins University Applied Physics Laboratory, 11100 Johns Hopkins Road, Laurel, MD 20723–6099, USA.
E-mail: Tony.Lui@jhuapl.edu

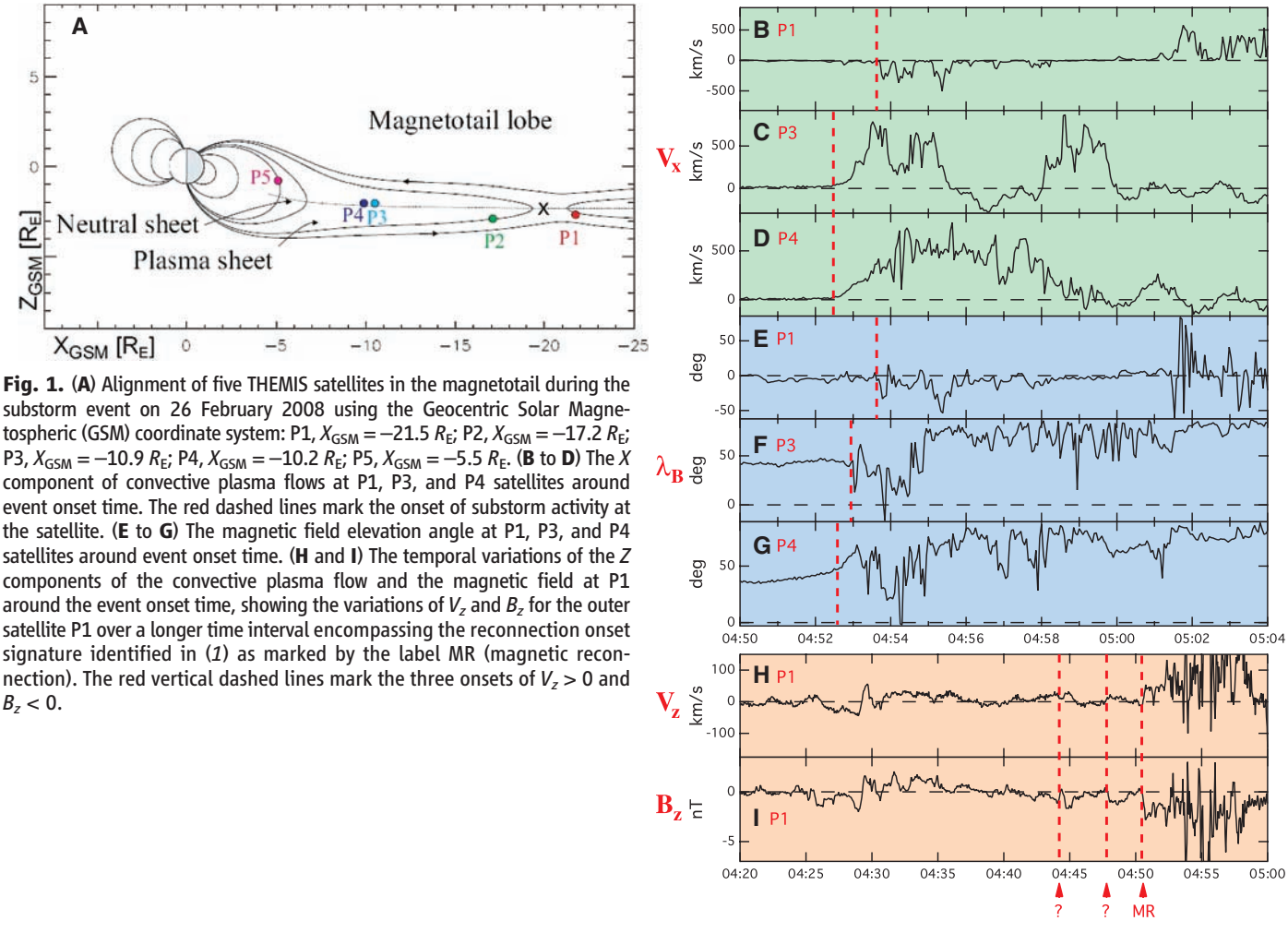

Fig. 1. (**A**) Alignment of five THEMIS satellites in the magnetotail during the substorm event on 26 February 2008 using the Geocentric Solar Magnetospheric (GSM) coordinate system: P1, $X_{GSM} = -21.5\ R_E$; P2, $X_{GSM} = -17.2\ R_E$; P3, $X_{GSM} = -10.9\ R_E$; P4, $X_{GSM} = -10.2\ R_E$; P5, $X_{GSM} = -5.5\ R_E$. (**B** to **D**) The X component of convective plasma flows at P1, P3, and P4 satellites around event onset time. The red dashed lines mark the onset of substorm activity at the satellite. (**E** to **G**) The magnetic field elevation angle at P1, P3, and P4 satellites around event onset time. (**H** and **I**) The temporal variations of the Z components of the convective plasma flow and the magnetic field at P1 around the event onset time, showing the variations of V_z and B_z for the outer satellite P1 over a longer time interval encompassing the reconnection onset signature identified in (*1*) as marked by the label MR (magnetic reconnection). The red vertical dashed lines mark the three onsets of $V_z > 0$ and $B_z < 0$.

associated with the appearance of discernible plasma flows occurred first near P4 and P3, before P1.

The features at P1 adopted by Angelopoulos *et al.* (*1*) as the first sign of reconnection at 04:50:28 UT are $V_z > 0$ and $B_z < 0$, which are not the conventional signatures. The justification is that the plasma was moving to the neutral sheet concurrent with the negative B_z development, which is interpreted as the occurrence of reconnection Earthward of P1. However, an equally likely alternative interpretation is that these are signatures of plasma sheet thinning at P1 concurrent with an even thinner near-Earth plasma sheet, producing southward dipping of the magnetic field, as documented previously (*2*). Figure 1, H and I, show that there were at least two other similar changes at P1 shortly before 04:50:28 UT, namely, at 04:44:19 and 04:47:16 UT. These earlier occurrences of the same features raise doubt on the causality of tail reconnection onset and auroral intensification onset at 04:51:39 UT. It is quite likely that reconnection onset and substorm onset are not causally related in this event, that is, that they are independent phenomena. This assessment is reinforced by noting that the required communication time (96 s) is shorter than the Alfvén transit time between the P1 location and the ionosphere, ruling out the possibility of field-aligned current connecting the two phenomena. The difficulty with assuming that electrons from reconnection are responsible for the connection is that the observed electron flux presumably ejected from reconnection shown in figure 4, C and D, in (*1*) is far too low [< 0.02 erg/(cm^2·s·sr)] by two orders of magnitude to account for the observed auroral intensity. Finally, current disruption/dipolarization associated with substorm current wedge (SCW) development occurred at P3 and P4, ~10 R_E (Earth radius) Earthward of the reconnection site. This implies that the SCW would occur considerably equatorward of the brightening auroral arc, a feature that has never been seen in an isolated substorm.

The reconnection signatures presented in (*1*) are not compelling. Although there was a positive excursion of the B_z component at P2 around that time, an expected feature Earthward of the reconnection site, there was a persistent tailward plasma flow unaffected by the positive excursion of the B_z component. This is inconsistent with the expected plasma flow signature for reconnection. This discrepancy from the expected reconnection signatures at P2 is shown with the corresponding P1 observations (Fig. 2, A to D).

Moreover, there is evidence that the substorm onset identified in (*1*) is simply an intensification of a substorm that started earlier. Figure 2, E to H, shows plasma flow activities at THEMIS satellites, whereas Fig. 2, I and J, show the official auroral indices *AU*/*AL* and Leirvogur magnetic activities. There were two temporally separated plasma flow activities at P1, P3, and P4, which were parts of a continuous substorm interval, as indicated by the ground magnetic activities, particularly the *z* component at Leirvogur. Therefore, the 04:51:39 UT onset time inferred in (*1*) from the Gilliam all-sky imager (ASI) was not an onset time of an isolated substorm. Intensification activity is often disconnected in longitude from the substorm onset longitude (*3*, *4*), and Gilliam was probably not at the right local time to detect the auroral activity at substorm onset. For this earlier substorm onset, close examination indicates that the onset of convective plasma flow also started at P3 and P4 before P1 and P2.

In summary, we have pointed to several potential shortcomings of the conclusion reported by Angelopoulos *et al.* (*1*). First, based on the conventional reconnection signatures observed

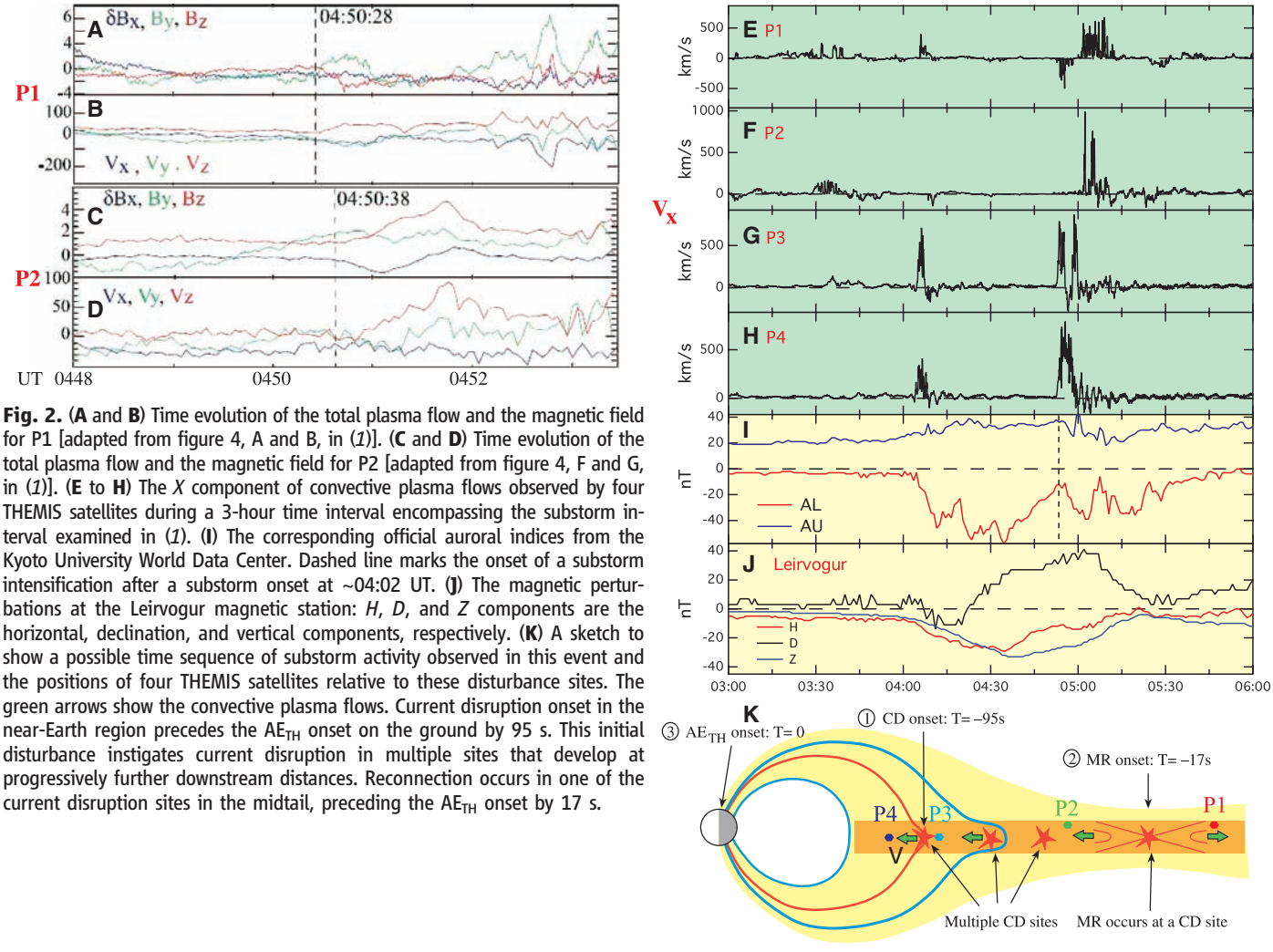

Fig. 2. (**A** and **B**) Time evolution of the total plasma flow and the magnetic field for P1 [adapted from figure 4, A and B, in (*1*)]. (**C** and **D**) Time evolution of the total plasma flow and the magnetic field for P2 [adapted from figure 4, F and G, in (*1*)]. (**E** to **H**) The *X* component of convective plasma flows observed by four THEMIS satellites during a 3-hour time interval encompassing the substorm interval examined in (*1*). (**I**) The corresponding official auroral indices from the Kyoto University World Data Center. Dashed line marks the onset of a substorm intensification after a substorm onset at ~04:02 UT. (**J**) The magnetic perturbations at the Leirvogur magnetic station: *H*, *D*, and *Z* components are the horizontal, declination, and vertical components, respectively. (**K**) A sketch to show a possible time sequence of substorm activity observed in this event and the positions of four THEMIS satellites relative to these disturbance sites. The green arrows show the convective plasma flows. Current disruption onset in the near-Earth region precedes the AE_{TH} onset on the ground by 95 s. This initial disturbance instigates current disruption in multiple sites that develop at progressively further downstream distances. Reconnection occurs in one of the current disruption sites in the midtail, preceding the AE_{TH} onset by 17 s.

by THEMIS satellites, substorm disturbances occurred in the near-Earth region before the tail reconnection. Second, the unconventional signatures used in (*1*) to identify reconnection onset can be interpreted alternatively as plasma sheet thinning, with the inner tail being thinner than the midtail. Third, the direct connection between tail reconnection onset and auroral intensification has difficulties in establishing a credible physical link, suggesting that the two phenomena are possibly not causally related. Overall, we infer the following time history of events. Near-Earth CD triggers the substorm onset, leading to the formation of a SCW. This initial disturbance instigates CD in multiple sites that develop at progressively further downstream distances. Reconnection occurs at one of the CD sites in the midtail (Fig. 2K). This sequence is in agreement with several previous studies and the inside-out model of substorm onset (*4*–*15*).

References and Notes

1. V. Angelopoulos *et al.*, *Science* **321**, 931 (2008).
2. A. T. Y. Lui, C.-I. Meng, S.-I. Akasofu, *J. Geophys. Res.* **82**, 1547 (1977).
3. R. G. Wiens, G. Rostoker, *J. Geophys. Res.* **80**, 2109 (1975).
4. S. B. Mende *et al.*, *Space Sci. Rev.* **141**, 357 (2008).
5. A. T. Y. Lui *et al.*, *J. Geophys. Res.* **113**, A00C04 (2008).
6. S.-I. Akasofu, *Physics of Magnetospheric Substorms* (Reidel, Hingham, MD, 1977).
7. A. T. Y. Lui, *J. Geophys. Res.* **96**, 1849 (1991).
8. A. Roux *et al.*, *J. Geophys. Res.* **96**, 17697 (1991).
9. L. C. Lee, L. Zhang, A. Otto, G. S. Choe, H. J. Chai, *J. Geophys. Res.* **103**, 29419 (1998).
10. Z. Y. Pu, *J. Geophys. Res.* **104**, 10235 (1999).
11. M. El-Alaoui, *J. Geophys. Res.* **106**, 6229 (2001).
12. P. Dobias, I. O. Voronkov, J. C. Samson, *Phys. Plasmas* **11**, 2046 (2004).
13. W. W. Liu *et al.*, *Geophys. Res. Lett.* **35**, L04104 (2008).
14. E. Donovan *et al.*, *Geophys. Res. Lett.* **35**, L17S18 (2008).
15. M. G. Henderson, *Ann. Geophys.* **27**, 2129 (2009).

16. This work was supported by NSF grant ATM-0630912 and NASA grant NNX07AU74G to The Johns Hopkins University Applied Physics Laboratory.

27 October 2008; accepted 11 May 2009
10.1126/science.1167726

Response to Comment on "Tail Reconnection Triggering Substorm Onset"

Vassilis Angelopoulos,[1]* James P. McFadden,[2] Davin Larson,[2] Charles W. Carlson,[2] Stephen B. Mende,[2] Harald Frey,[2] Tai Phan,[2] David G. Sibeck,[3] Karl-Heinz Glassmeier,[4] Uli Auster,[4] Eric Donovan,[5] Ian R. Mann,[6] I. Jonathan Rae,[6] Christopher T. Russell,[1] Andrei Runov,[1] Xu-Zhi Zhou,[1] Larry Kepko[7]

Lui challenges our conclusion that magnetic reconnection triggered the onset of a magnetospheric substorm. However, Lui incorrectly uses the auroral electrojet index instead of ground auroral and magnetic field pulsation signatures to determine substorm onset; single velocity and magnetic field components instead of full vectors and particle distributions to identify reconnection onset; and preliminary auroral electrojet–low index (AL) instead of ground magnometer, auroral, and magnetotail data to claim pre-existing activity.

We used data from NASA's Time History of Events and Macroscale Interactions during Substorms (THEMIS) mission to analyze the development of three magnetospheric substorms and identified reconnection as the trigger mechanism of substorm onset (*1*). Lui (*2*) challenges our conclusion for one event on several grounds, which we address here. We stand by our original interpretation of a reconnection-initiated substorm.

To argue that substorm onset took place after the onset of near-Earth current disruption, Lui equates substorm onset with an 04:54:00 UT increase in the THEMIS auroral electrojet (AE) index [see table 1 in (*1*)] despite the 04:51:39 UT auroral intensification, the 04:52:00 UT onset of Pi2 pulsations (irregular pulsations in the 40- to 150-s range), and the 04:52:21 UT poleward expansion of the aurora. All of these events occurred before the 04:52:27 UT onset of near-Earth activity at probe P3 and are therefore inconsistent with the current disruption model of substorms (*3*, *4*). Although often used as a proxy, the AE index is ill suited to identifying localized onsets.

Lui (*2*) further reports that the "conventional" signatures of reconnection, namely southward deflections of the magnetic field ($B_z < 0$, where B_z is the Z-directed component of the magnetic field in Geocentric Solar Magnetospheric coordinates) and the increase of the convective flows in the tailward direction, were not observed until after

[1]Institute of Geophysics and Planetary Physics, Department of Earth and Space Sciences, University of California at Los Angeles, Los Angeles, CA 90095, USA. [2]Space Sciences Laboratory, University of California at Berkeley, Berkeley, CA 94729, USA. [3]Code 674, NASA/Goddard Space Flight Center, Greenbelt, MD 20771, USA. [4]Technical University of Braunschweig, Braunschweig, D-38106, Germany. [5]Department of Physics and Astronomy, University of Calgary, Calgary, Alberta T2N 1N4, Canada. [6]Department of Physics, University of Alberta, Edmonton, Alberta T6G 2M7, Canada. [7]Space Science Center, University of New Hampshire, Durham, NH 03824, USA.

*To whom correspondence should be addressed. E-mail: vassilis@ucla.edu

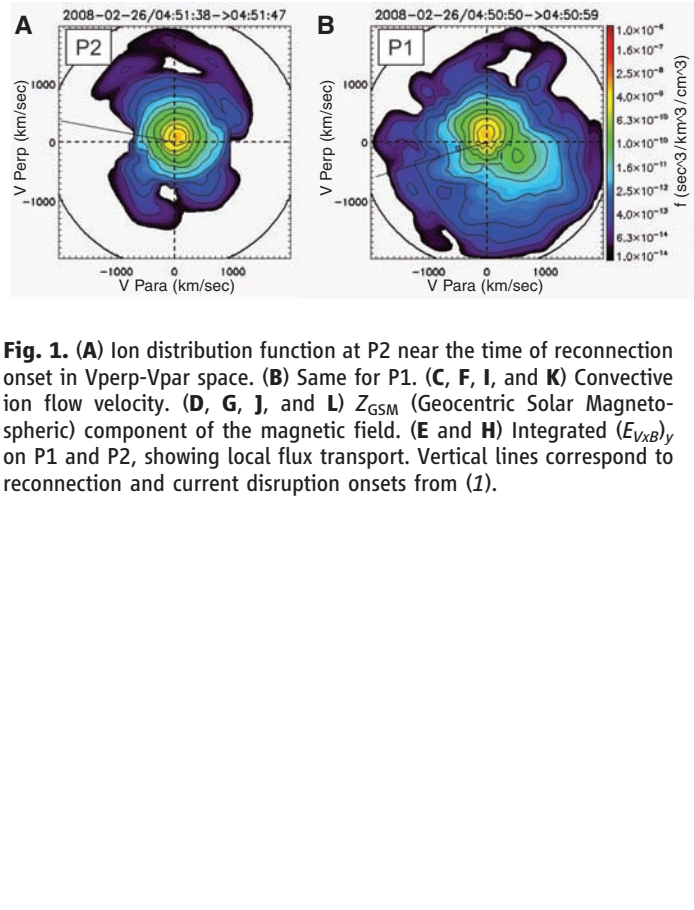

Fig. 1. (**A**) Ion distribution function at P2 near the time of reconnection onset in Vperp-Vpar space. (**B**) Same for P1. (**C**, **F**, **I**, and **K**) Convective ion flow velocity. (**D**, **G**, **J**, and **L**) Z_{GSM} (Geocentric Solar Magnetospheric) component of the magnetic field. (**E** and **H**) Integrated $(E_{VxB})_y$ on P1 and P2, showing local flux transport. Vertical lines correspond to reconnection and current disruption onsets from (*1*).

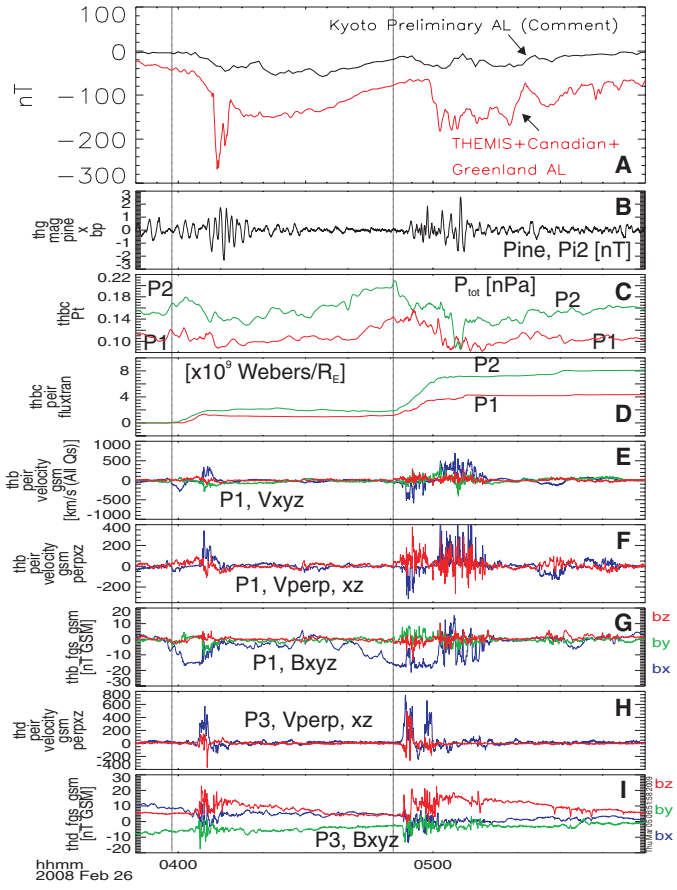

Fig. 2. (**A**) Kyoto Provisional AL index, used in (*2*), and THEMIS AL index, including additional Canadian stations. (**B**) Mid-latitude Pi2 pulsation data from Pine Ridge, used in (*1*). (**C**) Total lobe pressure determined from low-energy plasma and magnetic field data on P1 and P2 satellites. (**D**) Same as in Fig. 1, E and H, but for a longer interval. (**E** and **H**) Ion partial flow velocity from the ESA instruments on P1 and P3, respectively. (**F** and **H**) Same as Fig. 1, C and I, but for a longer interval. (**G** and **I**) Magnetic field on P1 and P3. All vectors are in GSM coordinates; *X* component is blue, *Y* component is green, and *Z* component is red. Vertical lines correspond to tail reconnection onset for the two substorms, based on the times of tailward or equatorward flow.

04:53 UT. Reconnection models indeed predict these signatures, but only in the neutral sheet. Further from the neutral sheet, models predict cold ions convecting inward toward the neutral sheet superimposed upon ion beams streaming away from the reconnection site. Near the boundary separating reconnected and unreconnected magnetic field lines, reconnection models predict antiparallel beams of field-aligned low-energy electrons streaming toward, and high-energy electrons streaming away, from the reconnection site (*5*–*7*).

Because our study (*1*) established that probes P1 and P2 were not in the neutral sheet at 04:50:28 UT reconnection onset, reconnection must be identified on the basis of signatures expected outside the neutral sheet. First, P1 observed a negative, excursion of B_z ($dB_z < 0$), P2 a positive B_z excursion ($dB_z > 0$), and P3 no excursion—a combination that demands a reconnection topology and precludes the near-Earth plasma sheet thinning scenario. Second, the northward flow velocities dV_z seen by P1 and P2 provide evidence for local reconnection inflow near these spacecraft, and their absence at P3 also excludes the near-Earth plasma sheet thinning interpretation. Third, as seen in figure 4C in (*1*), P1 observed the predicted tailward ion beam superimposed on a cold ion component. Fourth, as seen in figure 4E in (*1*), P1 observed the predicted bidirectional electron anisotropy.

Before 04:54 UT, P1 and P2 were near the separatrices within an extremely thin current sheet embedded deep within the plasma sheet. Figure 1, A and B, show the convective displacement of the dominant cold ion distributions. Because the ~20 nT magnetic field pointed Earthward along *X*, the dominant northward and *Z*-directed velocity shown in Fig. 1, C and F, was convective and consistent with the expected reconnection inflow. At P1 and P2, significant flux transport only started at 04:51 UT (Fig. 2, E and H). Figure 1B illustrates the hot, 600 km/s tailward-streaming beam expected tailward from reconnection. Cold plasma streaming anti-Sunward along the magnetic field dominated the plasma velocity moment at both spacecraft for several minutes before onset. It contributed nothing to the flux transport and is likely related to tailward motion of mantle/ionospheric plasma.

Lui (*2*) points to V_z and B_z fluctuations at P1 before the 04:51:39 UT onset to refute the reconnection timing scenario. However, these fluctuations were unaccompanied by other reconnection signatures at P1 or P2 and provide negligible flux transport toward the equator (Fig. 1, E and H).

Figure 1H in (*2*) presents the dominant (*Z*) component of the convective flow at P1 on a timeline that differs from that for the other spacecraft. Figure 1 presented here shows all components together with the timing established by (*1*). The current disruption onset timing in (*1*) was based on the abrupt increases in B_z at P3 and P4, which were accompanied by high-frequency noise, consistent with (*3*, *4*). Lui (*2*) defines current disruption on the basis of increases in V_x or slow changes in elevation angle, but neither is consistent with previous definitions (*3*, *4*).

Lui employed the Kyoto Provisional AL index to imply a link between the 04:51:39 UT substorm onset and earlier activity. The THEMIS AL index, revised to include Eastern Canadian and Greenland stations and shown in Fig. 2A, shows that the earlier activity had already subsided by 04:40 UT. Neither AL index can be used to time growth phases or onset times because baseline determination requires subtraction of the monthly quiet days. Instead, we note that no mid-latitude Pi2 pulsations occurred during the 30 min before the onset (Fig. 2B). Neither P1 nor P2 observed any significant flux transport for 40 min before onset (Fig. 2D). Increasing lobe pressures inferred from the total plasma sheet pressure at P1 and P2 (Fig. 2C) during the 20 min before onset indicate growth phase flux increases, which came to an abrupt end at P2 at onset. At P3, the B_z component of P3 (Fig. 2I) decreased for 40 min before onset, the classic signature of growth phase plasma sheet thinning. Finally, the two substorms were evident in the THEMIS imager array. Aurora associated with the earlier activity had subsided to lower magnetic latitudes (~67°) and decreased in intensity (see movie S1) at least 10 min before the 04:51:39 UT onset, as expected during the substorm growth phase. All observations therefore indicate that the growth phase of the 04:51:39 UT substorm had started by 04:40 UT, and thus its onset was not due to lingering activity.

Finally, Lui (*2*) omits evidence for reconnection before the earlier substorm's auroral intensification and expansion. P1 observed tailward flows at ~03:58 UT (Fig. 2E), ~6 min before the 04:04:51 UT dipolarization onset at P3 (Fig. 2I). The flows had a significant (>40 km/s) tailward convective component (Fig. 2F), followed by northward flows toward the neutral sheet, demonstrating reconnection inflow as in the 04:51:39 UT event. The images in movie S1 show auroral brightenings at 04:00:21 and 04:03:30 UT, both followed by expansions and both before current disruption at P3. These observations indicate that reconnection also triggered the earlier substorm.

In conclusion, we argue that Lui employs an antiquated substorm definition using the AE index to support a current disruption scenario. It focuses on dB_z and V_x signatures at P1 to time reconnection onset, ignoring correlated signatures from two spacecraft that indicate earlier reconnection onset. Lui also presents a current disruption timing analysis that is inconsistent with previously reported definitions and employs a geomagnetic index inappropriate for studies of localized small substorms to suggest that earlier activity was responsible for the 04:51:39 UT onset. A more comprehensive index, THEMIS auroral images, and spacecraft observations reveal that reconnection-triggered earlier activity had subsided at least 10 min before the 04:51:39 UT

onset, by which time the growth phase of the new substorm was well under way.

References and Notes

1. V. Angelopoulos *et al*., *Science* **321**, 931 (2008).
2. A. T. Y. Lui, *Science* **324**, 1391 (2009); www.sciencemag.org/cgi/content/full/324/5933/1391-b.
3. A. T. Y. Lui, *AGU Monogr. Ser* **64**, 43 (1991).
4. A. T. Y. Lui, *J. Geophys. Res.* **101**, 13067 (1996).
5. T. Nagai *et al*., *J. Geophys. Res.* **106**, 25929 (2001).
6. T. Nagai, S. Machida, *Geoph. Monogr. Ser* **105**, 211 (1998).
7. M. Hoshino, T. Mukai, T. Terasawa, I. Shinohara, *J. Geophys. Res.* **106**, 25979 (2001).

8. This work was supported by NASA contract NAS5-02099. The work of K.H.G. was financially supported by the German Ministerium für Wirtschaft und Technologie and the German Zentrum für Luft- und Raumfahrt under grant 50QP0402.

Supporting Online Material

www.sciencemag.org/cgi/content/full/324/5933/1391-c/DC1
Movie S1

8 December 2008; accepted 18 May 2009
10.1126/science.1168045

PSYCHOLOGY

Mr. Armstrong's Jersey and Mr. Rogers's Sweater

Michael Shermer

During a recent trip to Austin, Texas, for a debate with Old Earth creationists, I paid a visit to Lance Armstrong's famous bike shop Mellow Johnny's (so named because Americans butcher the pronunciation of maille jaune, French for yellow jersey). In addition to numerous yellow jerseys hanging on the walls, on the showroom floor were several of the bikes that Armstrong rode while winning seven Tours de France. "People think these are replica bikes," the shop manager told me. "When I explain that these are the actual bikes on which Lance won the tour, they touch them like holy relics."

Why people imbue physical artifacts with an almost mystical force that can transmit its power to the contactee is the subject of Bruce M. Hood's marvelous new book, *SuperSense: Why We Believe in the Unbelievable*. In an account chock full of real-world examples reinforced by experimental research, Hood (a cognitive psychologist at the University of Bristol) builds a theoretical model to explain how the mind comes to sense that there is something beyond the natural world, something supernatural. He calls this phenomenon our "supersense." Our supersense underlies our tendency to believe that objects, animals, and people contain an essence (something at the core of their being that makes them what they are) and that this essence may be transmitted from objects to people and from people to people. There may be evolutionary reasons for this tendency, rooted in fears about diseases and contagions that contain all-too-natural essences that can be deadly (and hence should be avoided). But we now generalize the supersense to any and all objects, seen and unseen, and assume that those seen and unseen objects have agency and intention.

Imbued with goodness? Mr. Rogers wearing his trademark cardigan.

SuperSense
Why We Believe in the Unbelievable / From Superstition to Religion—the Brain Science of Belief

by Bruce M. Hood

HarperOne, San Francisco, 2009. 320 pp. $25.99. ISBN 9780061452642. Constable, London. 330 pp. Paper, £8.99. ISBN 9781849010306.

The supersense is not restricted to the uneducated or unintelligent. "Many highly educated and intelligent individuals experience a powerful sense that there are patterns, forces, energies, and entities operating in the world that are denied by science because they go beyond the boundaries of natural phenomena we currently understand," Hood notes. "More importantly, such experiences are not substantiated by a body of reliable evidence, which is why they are *super*natural and unscientific. The inclination or sense that they may be real is our supersense."

In other words, even smart people believe weird things. Why? I have argued that it is because we all have to believe things—whether they are weird things or nonweird things (*1*). The process by which we come to believe things is called learning. We connect A to B to C, and often A really is connected to B, and B really is connected to C. But we do not have a false-pattern-detection device in our brains to help us discriminate between valid and misleading patterns, and so we make errors in our thinking: type I errors in believing patterns are real when they are not (false positives) and type II errors in not believing patterns are real when they are (false negatives). Imagine that you are a hominid on the plains of Africa and you hear a rustle in the grass. Is that the sound of a dangerous predator or just the wind? If you assume it is a dangerous predator and it is just the wind, you have made a type I error, but to no harm. But if you believe the rustle in the grass is just the wind when it is actually a dangerous predator, there is a good chance you'll be removed from your species' gene pool. Thus, I argued, there would have been natural selection for those hominids who tended to believe that all patterns are real and potentially dangerous. I called the resulting processes patternicity (the tendency to find meaningful patterns in random noise) and agenticity (the tendency to believe that the world is controlled by invisible intentional agents who may mean us harm) (*2*, *3*).

Hood's supersense is a superstructure that incorporates both of these processes. It is the basis of superstition and magical thinking. "If essences are thought to be transferable, we will not consider ourselves isolated individuals but rather members of a tribe potentially joined to each other through beliefs in supernatural connectedness," Hood explains. "We will see others in terms of the properties that make them essentially different from us. Such an idea suggests that some essential qualities are more likely to be transmitted than others." He includes among these qualities "youth, energy, beauty, temperament, strength, and even sexual preference." Many transplant patients suspect that certain aspects of the personality of the donor will be incorporated into their own essence. Along with hoping that some object will convey the force of good, we fear the transmission of evil. Studies discussed by Hood show, for example, that most people say that they would never wear the sweater of a murderer. The possibility fills them with disgust, probably an evolved emotion selected to avoid rotting food and disease-carrying substances. They would, however, happily wear the cardigan sweater of the children's television host Mr. Rogers, which they believe makes them better persons.

The supersense is so powerful, in fact, that it can influence even the most rational of skeptics. At Mellow Johnny's, I purchased an array of Lance Armstrong cycling gear (I ride bikes regularly). During my debate with the creationists that night, I was secretly wearing a pair of Lance Armstrong yellow-rimmed black socks and a "Livestrong" T-shirt underneath my suit. My rational brain does not for a moment believe that the essence of Armstrong's celebrated strength and endurance powered me through the three-hour event. Yet, for some odd reason I felt more confident, and

The reviewer, the author of *The Mind of the Market*, is at the Skeptics Society, 2761 North Marengo Avenue, Altadena, CA 91001, USA. E-mail: mshermer@skeptic.com

perhaps—given the influence of belief and the power of placebo—I was a better debater that night. I don't know. But Hood knows that the supersense is all pervasive. For that reason, his book is an important contribution to the psychological literature that is revealing the actuality of our very irrational human nature.

References

1. M. Shermer, *Why People Believe Weird Things* (Henry Holt, New York, 1997).
2. M. Shermer, *Sci. Am.* **299** (6), 46 (2008).
3. M. Shermer, *Sci. Am.* **300** (6), 36 (2009).

10.1126/science.1175719

EPIDEMIOLOGY

Epidemics of Fear

Kenneth R. Foster

Epidemics, in the usual image, are produced by invading enemies, and physicians and scientists protect us by battling against those pathogens. But sometimes, Philip Alcabes insists in *Dread*, epidemics are the product of imagination, fueled by people's anxieties and prejudices instead of germs.

The strongest chapters in this provocative but flawed polemic describe epidemics of the past in the context of changing views about the nature of disease. Between 1347 and 1351, plague killed at least a quarter of the European population. Many citizens viewed it as "an opportunity to confess sins and seek forgiveness." Others launched pogroms against Jews, blaming them for the tragedy. When cholera arrived in England in the early 1830s, it struck hardest at the poor who lived in overcrowded and unsanitary cities. Fearing social unrest and begrudging the costs of poorhouses and lazarettos (in which the victims were quarantined), the moneyed classes supported efforts to clean up the cities. Others instead blamed the moral turpitude of the victims. Alcabes (an epidemiologist in the Department of Urban Public Health at Hunter College, City University of New York) calls AIDS the first "postmodern epidemic": the infection itself became the illness. The early victims in the United States were sexually promiscuous gay men, prompting bluenoses to blame the disease "on homosexuality and, sometimes, sexual license in general."

The final chapters of *Dread* are a jeremiad against "imagined epidemics," overblown health problems that give "those who have power more reason to wield it." Some of these are real health problems in other countries that are unlikely to affect an average U.S. citizen (for example, AIDS). Others are "fall guys] for modern fears," as Alcabes says about obesity: health issues that grow in the public's mind into "epidemics" as a result of social anxieties or political manipulation, leading to overreaction by health agencies.

Alcabes's contrarian views about these health issues will infuriate many readers. He considers autism to be the "postmodern epidemic of nothing" that "became an epidemic only once policy guidelines in the United States required that public schools make accommodations for autistic children." He views influenza as another overblown threat: "There is no particular reason to think that there will ever be another epidemic of flu to equal the 1918 outbreak" and "no reason to think that if any flu strain does manage to go global it will be any worse than the garden-variety strains that come around every winter." He claims that the worries are being kept alive by "the people who make a living studying the virus and who need to attract continued grant funding to keep studying it."

Dread
How Fear and Fantasy Have Fueled Epidemics from the Black Death to Avian Flu

by Philip Alcabes

PublicAffairs, New York, 2009. 322 pp. $26.95, C$31. ISBN 9781586486181.

If "imagined epidemics" such as obesity and autism are not substantial health threats to American citizens, then perhaps the health agencies involved with them are moralistic busybodies. Some libertarian writers have made this point—for example, Jacob Sullum in "An epidemic of meddling: The totalitarian implications of public health" (*1*)—and it seems to be Alcabes's view as well. However, his arguments suffer from two major weaknesses.

The first is naked opinion. It may be, as he says, that smallpox is "defunct" and germ-warfare stocks of the virus were not worth worrying about, that drug-resistant tuberculosis in the United States was never a major health threat to its citizens, or that we have little to fear in a future flu pandemic. But if he wishes readers to accept his position, he needs to present a persuasive case for his views and not simply state them.

The second is loose editorializing. At one point, Alcabes attacks a 1994 U.S. Centers for Disease Control and Prevention (CDC) report that enrollment in day care centers is increasing as more mothers have entered the workforce (*2*). This is, he says, "a subtle form of the customary accusation that women are failing in their duty to marry and stay home." That clearly was not CDC's point at all. Elsewhere, he comments that "[t]oday, black Americans are said to be at higher risk of prostate cancer, infection with hepatitis B virus and HIV, and infant mortality, to name only a few health problems of concern"—citing a CDC Web site on racial disparities in health measures (*3*). He then complains, "Claiming that people of African descent are predisposed to such conditions explicitly attributes disease risk to genetics and implicitly attributes health to a person's fitness. And it ties fitness to race." Whom, exactly, is he criticizing?

Nonetheless, Alcabes has a point. The public is easily scared and can be manipulated to further political agendas unrelated to health and safety. The United States has a moralistic streak, and one can always find prominent individuals to blame victims for their own disease. In either case, the result can be corrosive to setting wise public policy. Unfortunately, *Dread* provides no solutions to the problems Alcabes raises.

CREDIT: HISTORY OF MEDICINE/NATIONAL LIBRARY OF MEDICINE

Seventeenth-century plague doctor.

References

1. J. Sullum, *Reason* **39**, 22 (May 2007); www.reason.com/news/show/119236.html.
2. Centers for Disease Control and Prevention, *Addressing Emerging Infectious Disease Threats: A Prevention Strategy for the United States* (U.S. Department of Health and Human Services, Atlanta, GA, 1994).
3. www.cdc.gov/omhd/Populations/BAA/BAA.htm#Disparities.

The reviewer is at the Department of Bioengineering, University of Pennsylvania, Philadelphia, PA 19104, USA. E-mail: kfoster@seas.upenn.edu

10.1126/science.1175732

DRUG DISCOVERY

Repurposing with a Difference

Consumer activism, genetic information, and social networking technologies are creating many opportunities for drug repurposing.

Mark S. Boguski,[1]* Kenneth D. Mandl,[2] Vikas P. Sukhatme[3]

There is widespread belief that current models of drug discovery and development need revamping and reinvention in order to make pharmaceutical research and development (R&D) more predictable, reliable, and less costly. We suggest a novel approach to this challenge that involves profound changes in the way postmarketing surveillance data are gathered and used. This approach capitalizes on recent advances in molecular medicine, human genomics, and information technology, as well as an increasingly sophisticated public eager for solutions to their unmet medical needs. Novel business models and imaginative legal and regulatory reforms will be critical to fulfill this promise and to maximize its impact.

Despite enormous investments in basic science, technology development, and experimentation with new organizational and management structures, pharmaceutical product development still requires at least 10 to 15 years and costs between $500 million and $2 billion (*1*, *2*). Furthermore, there is a widening productivity gap: Research and development spending continues to increase, yet the number of new therapeutic chemical and biological entities approved by the U.S. Food and Drug Administration (FDA) has been declining since the late 1990s (*3*). Overcoming these and other obstacles to increased productivity may require an overhaul of the R&D paradigm (*4*); some have called for a "disruptive" transformation of the industry (*5*).

One response to the productivity gap is drug "repurposing" (*6*, *7*) or "repositioning" (*8*)—terms that refer to the identification and development of new uses for existing or abandoned pharmacotherapies. New uses of existing drugs cost much less to develop compared with de novo drug discovery and development (*8*). There are a number of remarkable examples of repurposed drugs whose additional indications were discovered serendipitously (*8*). For instance, buproprion (Wellbutrin) was originally developed to treat depression but found another use in smoking cessation (marketed as Zyban for this indication). Duloxetine (Cymbalta) was also developed to treat depression, but was hypothesized—based on mechanism of action, not serendipity—as a treatment for stress urinary incontinence. It was successfully developed and marketed for both indications.

A very unusual case of repurposing (the rescue of an abandoned drug) is thalidomide. Originally developed as a treatment for morning sickness during pregnancy, its dangerous side effects became tragically evident in the late 1950s and early 1960s only after an epidemic of severe birth defects occurred in children exposed to the drug in utero (*9*). Thalidomide was withdrawn from the market but, several years later, was accidentally discovered to be uniquely effective in treating severe complications of leprosy. It is now marketed for this use under the trade name Thalomid. Twenty years later, Thalomid's use was granted a new method-of-use (MOU) patent (see below) as a treatment for a type of cancer (multiple myeloma).

Another form of repurposing is the off-label use of prescription medications to treat a condition other than that for which the drug was approved by the FDA (*10*). This is possible and common, because the FDA regulates how drugs are approved but not how medicine is practiced; physicians are free to prescribe approved drugs for any uses they see fit, provided they have exhausted "standard-of-care" approaches and have reason to believe that the off-label use will be of clinical benefit. Because of our increasingly sophisticated understanding of human biology and the molecular pathways of disease, one would expect there to be increasing opportunities for expanding off-label use based on fully elucidated pathways and mechanisms of action, a situation that has been called a "new grammar of drug discovery" (*11*). A classic example of this phenomenon is imatinib (Gleevec and Glivec), a drug originally developed to treat chronic myelogenous leukemia whose indications were expanded to other cancers on the basis of common underlying molecular pathways (*11*, *12*).

A more systematic way to explore the potential of existing drugs for repurposing would involve a new use of postmarketing surveillance information. Postmarketing safety monitoring (*13*) is regulated by the FDA in the United States and the European Medicines Agency in Europe (*14*, *15*). The detection of potential adverse drug reactions has traditionally depended on voluntary and spontaneous reporting by individual patients and physicians, using the FDA's Adverse Events Reporting Systems (AERS). Also, pharmaceutical companies monitor the literature for case reports that may indicate a safety problem with their medicines. In addi-

More than one use. Prior examples of repurposed drugs include bupoprion and thalidomide (*8*). A more systematic approach involving postclinical-trial patient data could yield many more repurposed drugs.

CREDITS (TOP TO BOTTOM): NEWSCOM

[1]Department of Pathology, Beth Israel Deaconess Medical Center and Center for Biomedical Informatics, Harvard Medical School, 10 Shattuck Street, Boston, MA 02115, USA. [2]Children's Hospital Informatics Program at Harvard-MIT, Division of Health Sciences and Technology and Center for Biomedical Informatics, Harvard Medical School, Boston, MA 02115, USA. [3]Beth Israel Deaconess Medical Center and Department of Medicine, Harvard Medical School, Boston, MA 02115, USA.

*To whom correspondence should be addressed. E-mail: mark_boguski@hms.harvard.edu

Published by AAAS

tion, more proactive approaches, such as statistical data-mining of hospital records, are beginning to emerge (*16*–*19*).

An increasingly important and influential resource is groups of patients who can access medical information on the Internet and see themselves as equal partners with—if not the primary drivers of—the medical profession in managing their health (*20*). Special online resources, such as Resounding Health, have recently been developed to serve this population. In a growing number of cases, patients or their relatives not only initiate, but also design and carry out, research programs that have, for example, advanced understanding and treatment of gastrointestinal stromal tumor, gastroesophageal reflux disease, autism, and the genetic disorder pseudoxanthoma elasticum (*20*). Most such efforts to date have been carried out as part of a "gift economy," in which patients and their families volunteer time and effort to bypass what they consider the "lethal lag time" of professional research processes and formalisms (*20*).

Such efforts are aided by the fact that consumers can now have their genomes typed for disease associations for as little as $399 and can share these data electronically with their families, friends, or self-defined networks of individuals (*21*). A notable recent case is that of Google cofounder Sergey Brin, whose commercial genome scan revealed a high risk of developing Parkinson's disease. Brin is personally funding a study of 10,000 patients through two nonprofit companies, including the Michael J. Fox Foundation for Parkinson's Research (*22*).

Disease-oriented social networks, such as Genetic Alliance, PatientsLikeMe, and MyDaughtersDNA, have created online communities to advance the translation of research into new treatments. Google Health, Microsoft HealthVault, and Indivo (deployed by the Dossia consortium of employers) have created personally controlled, electronic health records for individuals or groups to share their medical conditions with health care providers, researchers, and others (*23*). This convergence of increasing consumer activism, along with access to genetic information services and sophisticated, advanced, and accessible information technologies, has created unprecedented opportunities to bring worldwide human resources and data to bear on biomedical research problems.

Whereas the purpose of classical pharmacovigilance is to identify adverse side effects of drugs (*13*), the new kind of pharmacovigilance we envision aims to detect, assess, and understand beneficial drug side effects (or expanded drug indications) that may become apparent during their development or use. This "type 2" pharmacovigilance could be carried out, for example, by professionals using data-mining methods to look for potential beneficial events in electronic health records (*16*). However, we also anticipate another approach, in which potential beneficial side effects of existing drugs are identified by online communities of drug consumers using social networking technologies in a process that has been called "crowdsourcing" (*24*, *25*). Potential beneficial side effects (or new indications) for existing drugs identified in this way could be assessed in a manner conceptually similar to the formal methods by which causality criteria are applied to adverse events (*15*). Following initial assessment, candidates would be prioritized for further investigation, including some form of clinical trials. Validation would be most straightforward for those phenomena that could be rationalized on the basis of known disease pathways or mechanisms of action. Potential new uses that are not consistent with known disease mechanisms might generate hypotheses that could lead to the discovery of new biological processes or disease pathways.

Definitive clinical trials for novel uses of existing drugs will remain costly, and pharmaceutical companies are reluctant to invest in such efforts without patent protection. New information about the uses of existing drugs may create intellectual property in the form of MOU patents as opposed to composition-of-matter (COM) patents. COM patents are generally considered to be more valuable than MOU patents, but this differential valuation may be changing because, as Eisenberg points out, "Drugs are information-rich chemicals that in many respects are more akin to other information products (such as databases) than they are to other chemicals" (*26*).

Classical pharmacovigilance, which is exclusively focused on safety issues, can produce information that is of considerable social value for patients, physicians, and insurers at the expense of economic value to pharmaceutical companies (*26*). Thus, repurposed pharmacovigilance that is focused on beneficial new uses will need to be based on new business models [such as open-sourcing (*27*)] apart from the traditional, vertically integrated R&D enterprise (*5*). It would also be enabled by either patent reform by Congress or new doctrinal interpretations of current law by the FDA and the courts, as has already been suggested (*28*).

Our proposal, to repurpose pharmacovigilance, outlines a new approach to drug and biomarker discovery and suggests ways of overcoming the inadequate incentives of current business models and regulatory regimes that contribute to the productivity gap in pharmaceutical R&D. This approach leverages the talents, motivations, and resources of individuals and groups whose unmet medical needs are the fundamental goals of developing new therapies.

References and Notes

1. C. P. Adams, V. V. Brantner, *Health Aff. (Millwood)* **25,** 420 (2006).
2. J. A. DiMasi, R. W. Hansen, H. G. Grabowski, *J. Health Econ.* **22**, 151 (2003).
3. H. Grabowski, *Pharmacoeconomics* **22**, 15 (2004).
4. K. I. Kaitin, *Clin. Pharmacol. Ther*. **83**, 210 (2008).
5. C. M. Christensen, J. H. Grossman, J. Hwang, *The Innovator's Prescription: A Disruptive Solution for Health Care* (McGraw-Hill, New York, 2009).
6. D. W. Carley, *IDrugs* **8**, 306 (2005).
7. D. W. Carley, *IDrugs* **8**, 310 (2005).
8. T. T. Ashburn, K. B. Thor, *Nat. Rev. Drug Discov.* **3**, 673 (2004).
9. W. G. McBride, *Lancet* **278**, 1358 (1961).
10. K. R. Loughlin, J. A. Generali, *The Guide to Off-Label Prescription Drugs: New Uses for FDA-Approved Prescription Drugs* (Simon & Schuster, New York, 2006).
11. M. C. Fishman, J. A. Porter, *Nature* **437**, 491 (2005).
12. D. Vasella, R. Slater, *Magic Cancer Bullet: How a Tiny Orange Pill May Rewrite Medical History* (HarperCollins, New York, 2003).
13. World Health Organization (WHO), *The Importance of Pharmacovigilance: Safety Monitoring of Medicinal Products* (WHO, Geneva, 2002); http://apps.who.int/medicinedocs/en/d/Js4893e.
14. E. G. Brown, L. Wood, S. Wood, *Drug Saf*. **20**, 109 (1999).
15. H. S. Rehan, D. Chopra, A. K. Kakkar, *Eur. J. Intern. Med.* **20**, 3 (2009).
16. J. S. Brownstein *et al.*, *PLoS One* **2**, e840 (2007).
17. L. Harmark, A. C. van Grootheest, *Eur. J. Clin. Pharmacol*. **64**, 743 (2008).
18. M. Hauben, A. Bate, *Drug Discov. Today* **14**, 343 (2009).
19. J. Weaver, M. Willy, M. Avigan, *AAPS J*. **10**, 35 (2008).
20. T. Ferguson, *e-Patients: How They Can Help Us Heal Healthcare* (2007); www.e-patients.net/e-Patients_White_Paper.pdf.
21. M. S. Boguski, in *Genomic and Personalized Medicine*, H. F. Willard, G. S. Ginsberg, Eds. (Elsevier, San Diego, CA 2009), pp. 252–257.
22. A. Pollack, *New York Times*, 12 March 2009; www.nytimes.com/2009/03/12/business/12gene.html?emc=eta1.
23. K. D. Mandl, I. S. Kohane, *N. Engl. J. Med*. **358**, 1732 (2008).
24. J. Howe, *Crowdsourcing: Why the Power of the Crowd Is Driving the Future of Business* (Crown Business, New York, 2008).
25. C. Li, J. Bernoff, *Groundswell: Winning in a World Transformed by Social Technologies* (Harvard Business, Boston, 2008).
26. R. S. Eisenberg, *Yale J. Health Policy Law Ethics* **5**(2), 717 (2005).
27. B. Munos, *Nature Rev. Drug Discov.* **5**, 723 (2006).
28. B. N. Roin, *Texas Law Rev.* **87**, 503 (2009).

29. M.S.B. is a former vice president of the Novartis Institutes for Biomedical Research and the founder of Resounding Health Inc. K.D.M. is a principal developer of Indivo, an open-source, personally controlled health record that has been deployed through Dossia, Inc. V.P.S. is a cofounder of GlobalCures Inc.

10.1126/science.1169920

ASTRONOMY

Extreme Spinning Tops

Observations of the same binary star system over 10 years confirm a scenario of how pulsars form and evolve.

Michael Kramer[1,2]

Neutron stars are among the fastest rotating objects in the universe. They have diameters of about 20 km, yet can rotate at up to 43,000 times per second, resulting in speeds at the equator that exceed 10% of the speed of light. On page 1411 of this issue, Archibald *et al.* (*1*) provide evidence in support of a long-suspected evolutionary scenario in the formation of such extreme objects. They report observations on a binary neutron star consisting of a "millisecond radio pulsar" with a period of only 1.69 ms and an optically identified low-mass companion. The intriguing and important detail about this binary system is that only a few years ago, it had been identified as a low-mass x-ray binary (LMXB)—a member of the class of systems that were long-believed to be the progenitors of millisecond radio pulsars. The reported observations represent the final link in a chain of evidence, which was pieced together over the past 35 years. Moreover, it is one of the rare occasions in which an evolutionary scenario is being played out on a human time scale.

This remarkable story begins with the discovery of the first binary pulsar, PSR B1913+16, by Hulse and Taylor in 1974 (*2*). While this pulsar provided the first evidence for the existence of gravitational radiation, earning the discoverers the Nobel Prize for physics in 1993, it also sparked an intense interest in the evolution of such systems. Not only was this pulsar in a binary system, but its rotation period (59 ms), old age (100 million years), and rather low magnetic field strength (10^{10} G) also meant that it stood out from the known pulsar population at the time. It was soon proposed (*3*) that these properties could be explained by an evolutionary history during which the pulsar had been spun to its fast period by mass transfer from its companion (*4*). Then, an even more rapidly rotating millisecond pulsar was found (*5*). This one was more radical because it had a period of only 1.56 ms and showed no evidence of a companion. However, it was suggested that it had followed a similar evolutionary path, but that its companion had been destroyed in the process (*6*). This scenario was further supported with the subsequent discovery of about 100 ms pulsars of which more than two-thirds were in binary systems. Most of the companion stars are white dwarfs with a mass of about 0.2 solar masses ($0.2M_{\odot}$).

In the proposed standard evolutionary scenario for the a millisecond pulsar system (*7*, *8*) (see the figure), a main-sequence star with a mass exceeding $8M_{\odot}$ is in orbit with a low-mass ~$1M_{\odot}$ star (see the figure, panel A) and evolves into a supergiant star before exploding in a supernova and forming a neutron star that is visible as a radio pulsar (see the figure, panel B). This pulsar would then be a member of the standard population before finally ceasing to emit radio waves after tens of millions of years. The low-mass companion evolves much more slowly but will also expand and reach a point when its mass escapes its gravitational pull and is attracted to the now radio-quiet pulsar. The mass accumulates into an accretion disk and possibly reaches the neutron star surface. These systems are characterized by strong x-ray emission, predominantly in bursts (*9*), as the matter falls from the disk onto the neutron star, and they are detectable as LMXBs. In this process, mass and angular momentum are transferred to the neutron star, reducing its magnetic field while increasing its spin rate to millisecond periods (see the figure, panel C). Once accretion has stopped, the radio emission is reignited (under some as yet unknown conditions) and the neutron star becomes visible as a radio millisecond pulsar (see the figure, panel D).

A key piece of this evolutionary jigsaw was found when phase-coherent millisecond x-ray pulsations were observed in another LMXB (*10*, *11*). In this and a number of subsequently observed sources, the pulsation frequency could be linked to the rotation frequency of the neutron star, indicating that an accretion process can spin-up a neutron star to millisecond periods. The fact that a transition to radio emission, once the x-ray emission had stopped, had not been seen in any of the dozen or so known LMXBs with millisecond periods raised doubts that further new evidence of this evolutionary chain could still be found. However, the discovery by Archibald *et al.* closes the chain with a final piece of evidence—a radio millisecond pulsar that was, less than a decade ago, identified as a LMXB and where observational evidence for a recent accretion disk can still be found. Besides confirming the standard scenario, there are also some interesting implications: The pulsar is

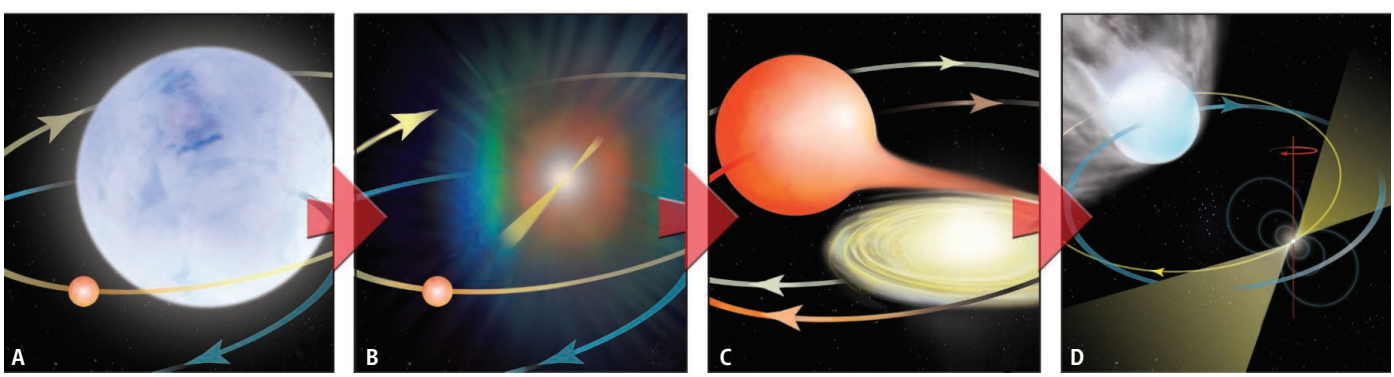

Evolving/revolving. Panels (**A**) to (**D**) describe the standard evolutionary scenario for the formation of a pulsar binary system (see text for details). Archibald *et al.* find the missing link, a binary system that evolves from x-ray–emitting to radio-emitting over a 10-year time scale, confirming the scenario proposed 35 years ago.

CREDIT: BILL SAXTON/NATIONAL RADIO ASTRONOMY OBSERVATORY/ASSOCIATED UNIVERSITIES, INC./NATIONAL SCIENCE FOUNDATION

[1]Max-Planck Institut für Radioastronomie Auf dem Hügel 69, 53121 Bonn, Germany. [2]Jodrell Bank Centre for Astrophysics, University of Manchester, Manchester M13 9PL, UK. E-mail: mkramer@mpifr-bonn.mpg.de

Published by AAAS

located less than 1.6 kpc from Earth, and the transition from LMXB to millisecond pulsar happened within the past 10 years. Both of these facts suggest that many more, similar systems remain to be identified. Furthermore, having archival observations about the state of the system in its x-ray–emitting phase and the distinct possibility that the system may revert to an active LMXB allow one to learn more about conditions that have to be met to enable the onset of radio emission.

It is intriguing that the system parameters studied by Archibald *et al.* appear as textbook values: The orbit has a very small eccentricity, indicating that during the accretion period the expected tidal interactions circularized the orbit and aligned all spin vectors in the system. The mass of the companion lies between 0.14 and 0.42$M_{\odot}$, a range that is typical for millisecond pulsar companions. The observations suggest that the companion is also being irradiated by the emission and wind from the pulsar, as for several other radio millisecond pulsars. Every little detail of the system seems so far to confirm the scenario that was boldly put forward by theoreticians 35 years ago.

However, there remain some blanks to fill in. We still do not know how fast a millisecond pulsar can be spun-up by an accretion process, i.e., what is the smallest spin period of neutron stars? The present record for the smallest spin period is 1.39 ms (*12*), but how far can we go? There will be a limit given by the properties of superdense matter, but other processes such as gravitational radiation losses may also limit accretion torques and hence the maximum spin frequency (*13*). The hunt for submillisecond pulsars is certainly on, both in electromagnetic as well as gravitational wave windows to the universe. At least now we can be sure that our basic model is correct.

References

1. A. M. Archibald *et al.*, *Science* **324**, 1411 (2009); published online 21 May 2009 (10.1126/science.1172740).
2. R. A. Hulse, J. H. Taylor, *Astrophys J.* **195**, L51 (1975).
3. L. L. Smarr, R. Blandford, *Astrophys J.* **207**, 574 (1976).
4. G. S. Bisnovatyi-Kogan, B. V. Komberg, *Sov. Astron.* **18**, 217 (1974).
5. D. C. Backer, S. R. Kulkarni, C. Heiles, M. M. Davis, W. M. Goss, *Nature* **300**, 615 (1982).
6. M. A. Alpar, A. F. Cheng, M. A. Ruderman, J. Shaham, *Nature* **300**, 728 (1982).
7. D. Bhattacharya, E. P. J. van den Heuvel, *Phys. Rep.* **203**, 1 (1991).
8. I. H. Stairs *et al.*, *Phys. Rev. Lett.* **93**, 141101 (2004).
9. M. van der Klis, *Annu. Rev. Astron. Astrophys.* **38**, 717 (2000).
10. R. Wijnands, M. van der Klis, *Nature* **394**, 344 (1998).
11. D. Chakrabarty, E. H. Morgan, *Nature* **394**, 346 (1998).
12. J. W. T. Hessels *et al.*, *Science* **311**, 1901 (2006).
13. D. Chakrabarty *et al.*, *Nature* **424**, 42 (2003).

10.1126/science.1175012

APPLIED PHYSICS

Novel Probes for Molecular Electronics

An extension of noncontact atomic force microscopy allows detection and manipulation of the charge states of individual atoms.

Ernst Meyer and Thilo Glatzel

In molecular electronics, interactions between the molecules and the underlying substrate must be minimized to ensure that their electronic properties are not disturbed. Insulating films or bulk insulators are ideal substrates in this regard. However, insulating substrates require characterization tools that do not depend on conductivity. One possibility is to probe molecules on ultrathin insulating films with low-current scanning tunneling microscopy (STM) (*1*). Alternatively, noncontact atomic force microscopy (AFM) (*2*) can be used to image molecules on insulating films or bulk insulators. On page 1428 of this issue, Gross *et al.* (*3*) use an extension of the latter technique to image adatoms on thin insulating films and to probe the charge state of these adatoms. This powerful tool may find applications well beyond molecular electronics.

Orbital imaging of molecules on thin insulating films by STM was an important milestone, where the influence of the substrate on the molecular wave functions was found to be negligible, in contrast to the situation on metallic substrates (*4*). Recently, immobilized molecules were imaged on bulk insulators at room temperature by noncontact AFM with submolecular resolution (*5*). However, the electronic properties of single molecules or atoms, such as the charge state, were not yet accessible.

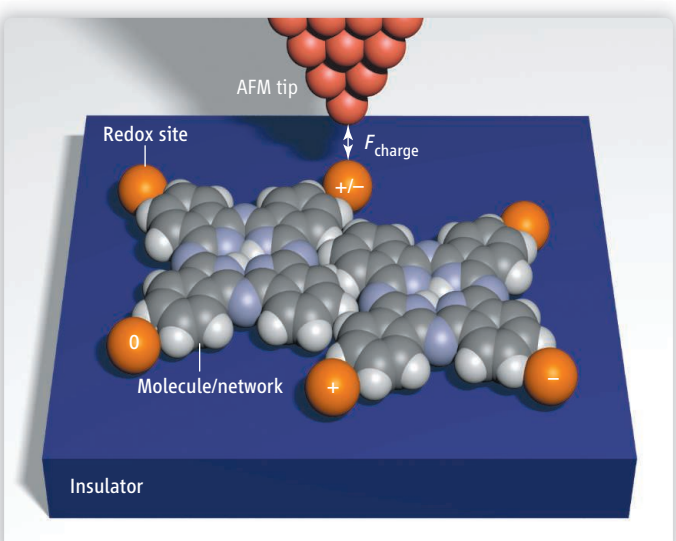

CREDIT: L. GROSS/IBM ZÜRICH RESEARCH LABORATORY

Gross *et al.* now show that noncontact AFM not only allows single atoms or molecules to be imaged, but can also be used to detect the charge state of adatoms on thin insulating films. For this purpose, the authors have implemented an extension of noncontact AFM—called Kelvin probe force microscopy—at low temperatures. In Kelvin probe force microscopy, the electrostatic force is measured separately as a function of voltage (*6*, *7*). Under appropriate measurement conditions, this method allows the local work function of the substrate to be determined with nanometer resolu-

Measuring charge transport in single molecules. Gross *et al.* show that a single molecule or molecular network on an insulator can be probed by attaching metallic adatoms, allowing single electron charges to be injected with a noncontact AFM tip. Subsequently, the charge transport can be investigated by measuring the charge states of all terminal adatoms with Kelvin probe force microscopy. F_{charge} is the force between the charge and the AFM tip.

Department of Physics, University of Basel, Klingelbergstrasse 82, 4056 Basel, Switzerland. E-mail: ernst.meyer@unibas.ch

Published by AAAS

tion. Gross *et al.* show that the method is sufficiently sensitive to distinguish the charge states of individual adatoms decoupled from the substrate by an ultrathin insulating ionic layer. Therefore, the authors can distinguish a neutral from a positively or negatively charged atom.

This achievement has tremendous consequences for the field of molecular electronics. It remains extremely difficult to electrically connect single molecules and to measure their electrical conductance. Most current lithography methods (*8*) yield metallic wires some tens of nanometers in diameter, much larger than the diameter of the molecules (typically on the order of 1 nm). This problem can be overcome by using geometries such as break junction experiments (*9*) and lifting up molecular or metallic wires by an STM tip (*10*). However, these methods do not allow spatial and electrical information to be obtained simultaneously without destroying the molecular structure. The crucial advance of Gross *et al*. is to perform their experiments without wiring the object of interest. This approach allows individual charges to be added to or removed from an atom and furthermore enables the direct measurement of the charge state.

The method of Gross *et al.* can be extended to molecules or molecular networks, where charges can be added or removed at specific sites of the molecules (redox sites). Subsequently, the whole molecule or molecular network can be characterized by Kelvin probe force microscopy or optical techniques to investigate the charge transport or conformation changes. In a recent study, Glatzel *et al.* demonstrated the contacting of single molecular structures assembled on insulating surfaces by metal clusters as well as their distinction by local Kelvin probe force microscopy measurements (*11*). By combining this approach with single atoms connected directly to the molecular structure, the charge transport can in principle be investigated without applying an external electrical current. The AFM tip can alter the charge state of one of the metallic terminals (see the figure). Afterward, the change of the charge states of the other terminals can be measured by Kelvin probe force microscopy, elucidating the propagation of charges in the molecule or molecular network. Comparison with theoretical models will give the opportunity to learn more about the energy landscape of the molecules, which is probed by single injected electrons.

A change of atomic or molecular charge state is a central feature in many chemical reactions. Combining the redox sites—that is, the metal atoms or clusters connected to the molecular structures—with probe microscopy therefore provides a novel tool for manipulating individual molecules and for performing chemical, electrochemical, or photochemical reactions with a high degree of control. In combination with optical excitation (*12*), it will allow absorption and charge generation to be measured at the molecular scale. This method is thus not only of interest for molecular electronics, but also for catalysis, material synthesis, and photovoltaics.

References

1. G. Binnig, H. Rohrer, C. Gerber, E. Weibel, *Appl. Phys. Lett*. **40**, 178 (1982).
2. S. Morita, R. Wiesendanger, E. Meyer, Eds., *Noncontact Atomic Force Microscopy* (Springer, Berlin 2002).
3. L. Gross *et al*., *Science* **324**, 1428 (2009).
4. J. Repp, G. Meyer, S. Paavilainen, F. E. Olsson, M. Persson, *Science* **312**, 1196 (2006).
5. S. Maier *et al*., *Small* **4**, 1115 (2008).
6. G. Enevoldsen *et al*., *Phys. Rev. Lett.* **100**, 236104 (2008).
7. F. Bocquet, L. Nony, C. Loppacher, Th. Glatzel, *Phys. Rev. B* **78**, 035410 (2008).
8. P. Zahl, M. Bammerlin, G. Meyer, R. R. Schlittler, *Rev. Sci. Instrum.* **76**, 023707 (2005).
9. M. A. Reed, C. Zhou, C. J. Muller, T. P. Burgin, J. M. Tour, *Science* **278**, 252 (1997).
10. L. Lafferentz *et al*., *Science* **323**, 1193 (2009).
11. Th. Glatzel *et al*., *Appl. Phys. Lett*. **94**, 063303 (2009).
12. S. A. Burke *et al*., *Adv. Mater*. **21**, 1 (2009).

10.1126/science.1175869

MATERIALS SCIENCE

Silicon Carbide as a Platform for Power Electronics

Methods for growing large, defect-free silicon carbide crystals have enabled the fabrication of devices that can operate at high power.

C. R. Eddy Jr. and D. K. Gaskill

For high-voltage, high-current devices that can be operated at elevated temperatures, silicon carbide (SiC) has been the material of choice. Efforts to produce single-crystal SiC began 30 years ago, but intrinsic problems in growing high-quality single-crystal boules free of micropipe defects—micrometer-scale pinholes created by dislocations—have only recently been overcome. A series of developments in crystal growth have made large-area, high-quality SiC substrates readily available for applications such as high-frequency transmitters and solid-state white lighting. Additional reductions in defects in the active region of devices have been achieved through epitaxial approaches, in which single-crystal layers are grown on the substrate. SiC is now poised as the linchpin to "green energy" that will replace less energy-efficient switches now based on silicon technology.

The choice of a semiconductor for switching electrical currents on and off depends on the operating voltage and how much current must be controlled. Silicon is an excellent material for the low-power transistors used in microelectronics, but for high currents and voltages, its implementation becomes complex and thermal management issues arise. The fundamental properties of SiC make it a better choice under these conditions.

One reason why SiC has been of fundamental interest to materials scientists is that it exists in more than 200 stacking modifications (polytypes) (*1*). With the advent of the vapor-phase Lely growth process in 1955, small, high-quality SiC single-crystal platelets (about 1 cm^2 in area) could be made (*2*). The most readily synthesized hexagonal polytypes, 4H and 6H, have a large indirect band gap (~3.2 eV) and a large breakdown electric field (2 MV cm^{-1}), as well as high electron mobility (900 $cm^2\ V^{-1}\ s^{-1}$) and thermal conductivity (400 $W\ m^{-1}\ K^{-1}$). Given these properties, SiC power switches should have performance figures of merit 10 to 100 times those of silicon switches.

The growth of SiC crystals presents many challenges. A SiC boule is typically grown by transporting its physical vapor to a seed crystal chosen to be as defect-free as possible. This

U.S. Naval Research Laboratory, 4555 Overlook Avenue SW, Washington, DC 20375, USA. E-mail: david.gaskill@nrl.navy.mil; charles.eddy@nrl.navy.mil

process requires extremely high temperatures (~2200°C) (*3*). Furthermore, impurities must be avoided both in the SiC feedstock and in the graphite insulation used in the growth reactor. Variations in the atomic ratio of Si to C in the vapor phase that arise from feedstock granularity must be minimized during growth. Radial and axial thermal profiles in the reactor and boule must be controlled to avoid polycrystallinity, grain boundary formation, and other defects in the lattice. Because the understanding of materials properties at these extreme temperatures is incomplete, boule growth modeling efforts must be based on extrapolated parameters. Last, all of the challenges of growing good-quality SiC boules increase as the diameter of the substrate increases.

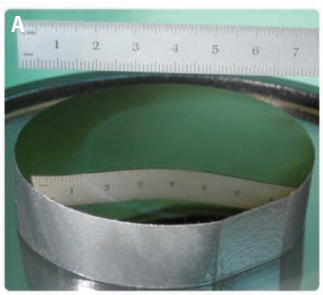

The challenges do not end once the single crystal is grown, because the lattice structure of the boule tends to replicate any defects in the starting seed crystal. Defects include basal plane dislocations (BPDs) that shift atom locations within that plane, and threading screw dislocations (TSDs) that shift atoms out of the basal plane and stack them in a spiral arrangement. Micropipes are larger-scale screw dislocations that create a pinhole through the substrate. These extended defects can occur with such high densities (up to 10,000 per square centimeter) that there is no usable area on the crystal surface to fabricate a working device.

Fortunately, at the high growth temperatures used, most dislocations have some mobility, and their interactions can cause them to cancel or "annihilate." The higher-quality part of the boules can then be used as better seed crystals. This slow but steady improvement in seed crystals and boule growth control has made larger-diameter, higher-quality wafers commercially available. Five years ago, only 50-mm-diameter SiC substrates were available, and today, 100-mm-diameter wafers are available (*4*). Expansion to 150-mm diameter would lead to substantial cost reductions because modern compound semiconductor processing equipment is designed for these larger wafers.

The bigger payoff that has occurred during this evolution in size has been a reduction in defects. In particular, the "killer defect" that has hampered the development of SiC devices, the micropipe, has been practically eliminated (*5*); commercially available wafers now have micropipe densities less than 1 cm^{-2} and are, in some cases, "micropipe free."

The current focus is on the reduction of BPDs, which are now the most important defects to eliminate, as well as TSDs. BPDs have deleterious effects on device performance, particularly for high-voltage bipolar devices. The 1c type of TSD has been linked to leakage in the common vertical device structures used in high-voltage power switches and diodes.

The BPDs propagate from the substrate into the epitaxial layers because the substrates must be offcut from the basal plane in order to maintain polytype control. The TSDs will propagate into the epitaxial device region independent of any offcut. In either case, it is highly desirable to reduce the densities of the extended defects in the active epitaxial layers. Reducing BPDs and TSDs to the desired level through boule manufacture alone will require extremely tight control on thermal gradients over larger dimensions at these extreme growth temperatures. Complementary approaches to develop epitaxial methods that can reduce BPD and TSD densities early in the growth process, and keep them out of the active regions of power devices, have shown considerable promise.

Using two epitaxial methods compatible with the manufacturing process (*6*, *7*), BPD densities have been reduced to the desired level of <1 cm^{-2}, although epitaxial approaches have not yet been implemented in the fabrication of device structures. Epitaxial approaches can also reduce propagation of TSDs from the substrate to the epilayers (*8*) and can keep such defects out of the active region of devices. Current efforts aim to reduce BPDs and TSDs to densities at or below 1 cm^{-2} both in boule manufacture and in epitaxial growth.

With the recent advances in SiC substrate quality, high-performance radio-frequency

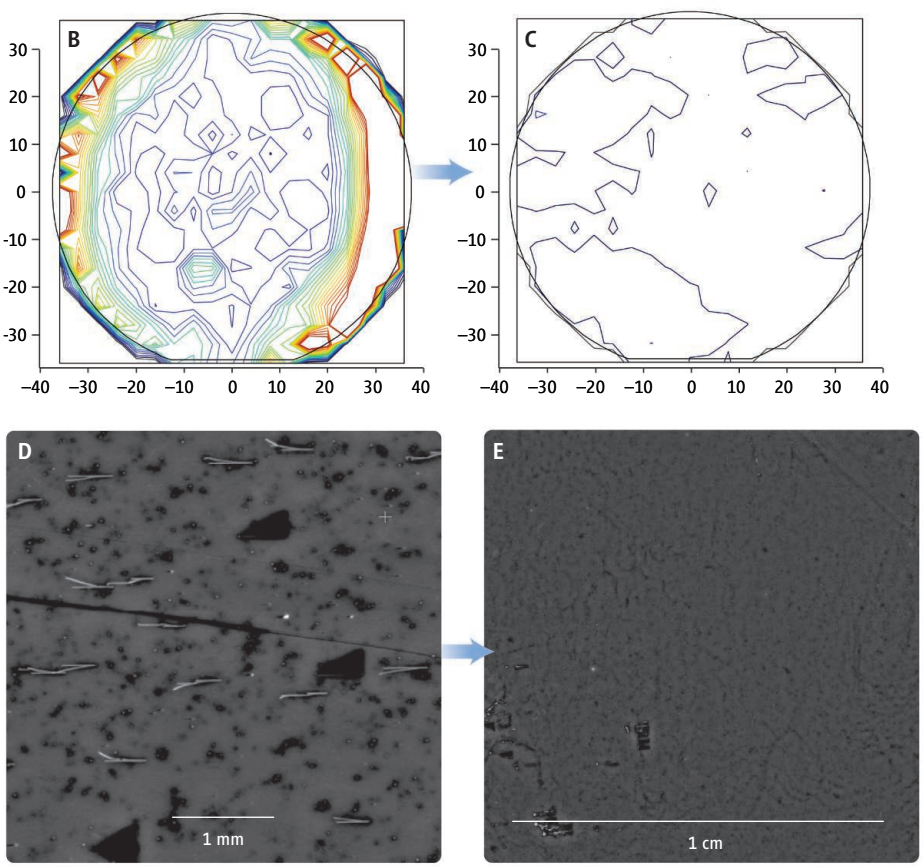

Progress in the development of SiC substrates. (**A**) SiC boule growth has advanced during the past 5 years to permit larger-diameter wafers with vastly improved quality [a 3-inch (76-mm) boule is shown]. (**B** and **C**) X-ray diffraction symmetric reflection peak width maps, ranging from 12 (black) to 120 arc sec (red) are shown in millimeters from the wafer center. Reduced peak widths in (C) demonstrate recent improvements in crystalline quality and uniformity. (**D**) Basal plane and threading screw dislocation reduction (white lines and dots, respectively, in the ultraviolet photoluminescence image) are detrimental to electronic device performance. (**E**) Recent bulk and epitaxial growth approaches have combined to yield sufficiently large (1 cm^2) areas free of basal plane dislocations (*6*, *7*).

CREDIT: BOULE PHOTO COURTESY OF II-VI INC.

Published by AAAS

devices, based either on SiC or on gallium nitride grown epitaxially on SiC, have become practical for use in advanced communications and radar systems. In addition, SiC wafers have been shown to be an effective vehicle for realizing large-area graphene films that may find application in terahertz devices and next-generation microprocessors.

The elimination of micropipes, when accompanied by reductions in BPDs and TSDs, suggests that high-voltage, high-current SiC electronic switches with increased efficiencies may be on the horizon. These types of devices will have a direct impact on energy conversion and distribution systems, as well as on electromechanical conversion processes that now rely on less efficient technologies.

References and Notes

1. N. W. Jepps, T. F. Page, *Prog. Cryst. Growth Charact.* **7**, 259 (1983).
2. J. A. Lely, *Ber. Dtsch. Keram. Ges*. **32**, 229 (1955).
3. Yu. M. Tairov, V. F. Tsvetkov, *J. Cryst. Growth* **43**, 209 (1978).
4. Current commercial 100-mm wafer suppliers: www.cree.com, www.ii-vi.com.
5. D. Cummings, *III-Vs Rev.* **18**, 18 (2005).
6. B. L. VanMil *et al.*, *Mater. Sci. Forum* **615–617**, 61 (2009).
7. R. L. Myers-Ward *et al.*, *Mater. Sci. Forum* **615–617**, 105 (2009).
8. G. Dhanaraj *et al.*, *J. Electron. Mater.* **36**, 332 (2007).

10.1126/science.1168704

CANCER

Breaching the Cancer Fortress

Pancreatic tumors are poorly vascularized, suggesting that new therapeutic strategies are needed.

Peter Olson and Douglas Hanahan

The predominant and invariably lethal form of pancreatic cancer—ductal adenocarcinoma—is characterized by an enveloping fibrotic stroma of excessive connective tissue and cells that forges rock-hard tumors. These tumors are refractory to essentially all therapies; gemcitabine, the standard-of-care chemotherapeutic drug, extends survival by only a few weeks. It has long been surmised that these pathological and clinical features are interconnected. On page 1457 in this issue, Olive *et al.* (*1*) confirm this notion, showing that cancer-associated fibroblasts in pancreatic ductal adenocarcinoma are responsible for a poorly vascularized architecture that imposes a barrier to drug delivery. Removing these fibroblasts stimulated the formation of new blood vessels (angiogenesis), improved drug delivery, and extended life span in a de novo mouse model of the disease. This study defines biophysical properties endowed by the tumor microenvironment that contribute to its therapeutic intractability and raises new questions about the role of the microenvironment in the development of this uncontrollable cancer.

Olive *et al.* noted that tumors from a de novo mouse model of pancreatic ductal adenocarcinoma responded poorly to gemcitabine, mimicking the clinical experience. However, transplanted tumors that were generated from cell lines derived from these tumors were remarkably sensitive to the drug. Transplanted tumors lacked the abundant fibrotic response present in human and de novo mouse tumors, in which epithelial cancer cells are surrounded by large swathes of activated fibroblasts, immune cells, blood vessels, and extracellular matrix components—a "fortress" collectively referred to as the desmoplastic stroma (see the figure) (*2*). The tumor microenvironment is thought to promote an ample vasculature to fuel tumor growth. However, in the de novo mouse model, blood vessels were sparse, only partially functional, and were physically separated from the epithelia by stroma. Two imaging techniques confirmed that blood flow was low in these tumors, and delivery of the naturally autofluorescent anticancer drug doxorubicin was decreased compared with delivery to transplanted tumors or normal tissue.

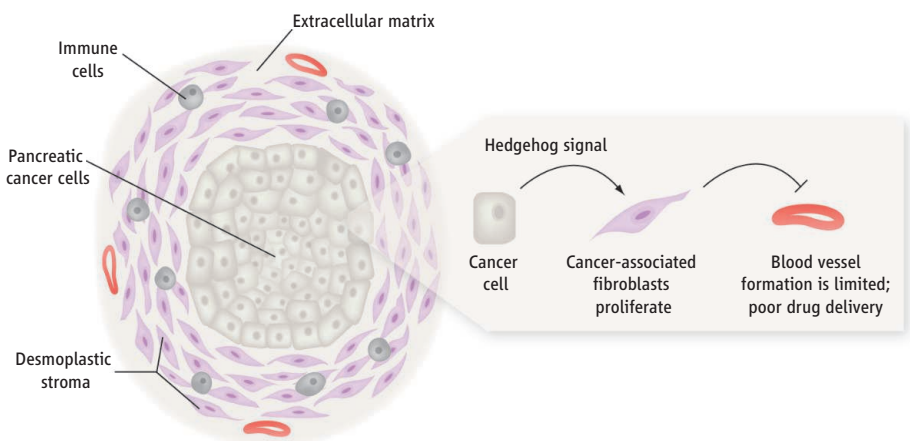

CREDIT: N. KEVITIYAGALA/*SCIENCE*

Barrier to drug delivery. In pancreatic ductal adenocarcinoma, cancer cells are surrounded by a fortress of desmoplastic stroma composed of cancer-associated fibroblasts and inflammatory cells along with copious amounts of extracellular matrix components. This assemblage impedes angiogenesis, limiting drug delivery. **(Inset)** The secreted factor Hedgehog sustains this stromal environment. Inhibition of Hedgehog signaling eliminates cancer-associated fibroblasts, thus increasing angiogenesis and vascular delivery of chemotherapeutic drugs.

Cancer-associated fibroblasts promote tumor growth and angiogenesis in other tumor types (*3*–*5*). Surprisingly, cancer-associated fibroblasts in pancreatic ductal adenocarcinoma were responsible for the sparse vasculature and poor drug delivery. These cancer cells signal in a paracrine fashion to fibroblasts via the secreted factor Hedgehog. Olive *et al*. treated mice with de novo tumors with a pharmacological Hedgehog inhibitor alone and in combination with gemcitabine. There was equivocal survival benefit with Hedgehog inhibitor therapy, and only a few weeks of added survival with the combination. Nevertheless, the Hedgehog inhibitor largely eliminated fibroblasts, while vascular endothelial and other cell types proliferated. The results suggest that cancer-associated fibroblasts in pancreatic ductal adenocarcinoma limit the formation of new blood vessels, with

Comprehensive Cancer Center, Diabetes Center, and Department of Biochemistry and Biophysics, University of California, San Francisco, San Francisco, CA 94143–0534, USA. E-mail: polson@diabetes.ucsf.edu; dh@ucsf.edu

poor drug delivery an unfortunate but incidental consequence.

Is it possible being poorly vascularized is advantageous for tumor growth? Though it is not obvious why a tumor would prefer to be starved for oxygen and nutrients, clues are emerging that this environment can promote malignant phenotypes. Hypoxia can drive genomic instability and lead to a more aggressive tumor phenotype (*6*, *7*), which may explain the highly metastatic nature of pancreatic ductal adenocarcinoma. Additionally, low blood-vessel density and high interstitial pressure may prevent host-derived factors (e.g., cells and/or molecules, akin, in principle to anticancer drugs) from reaching the tumor in sufficient quantities to exert an antitumor effect (*8*, *9*). Notably, the effects of the Hedgehog inhibitor proved transitory, followed by restoration of the hypovascular state, suggesting that the hypovascular, stromal-rich microenvironment is functionally important for the biology of pancreatic ductal adenocarcinoma.

Stimulating angiogenesis to treat pancreatic cancer, in the context of disrupting the desmoplastic fortress, is seemingly counterintuitive. Targeting tumor vasculature to improve blood flow and drug delivery is not new (*10*). However, previous theories posited that angiogenesis inhibitors can "normalize" tumor vasculature by pruning back immature vessels, thereby improving delivery of anticancer drugs to the tumor. By contrast, Olive *et al.* show that Hedgehog inhibition actually induced angiogenesis to improve drug delivery.

The predominant stroma and sparse vasculature in pancreatic ductal adenocarcinoma could be envisioned as a barrier to metastasis; hence the increased vascularization consequent to Hedgehog inhibitor therapy might be expected to spur metastasis. On the contrary, however, Hedgehog inhibition decreased metastatic frequency (*11*). Notably, a minority of pancreatic cancer cells express much higher amounts of Hedgehog and are 100 times more tumorigenic than the majority population (*12*–*14*). Perhaps these rare pancreatic cancer cells engage Hedgehog signaling as part of a metastatic program and, thus, are impaired by Hedgehog inhibition.

A somber lesson from this study is the eventual failure of the combined gemcitabine plus Hedgehog inhibitor therapy, which extended life span by only 2 weeks. The hypovascular state was restored upon relapse, although the effects on the stroma are unclear. Multiple cell signaling pathways have been implicated in orchestrating the desmoplastic stroma, including transforming growth factor–β, platelet-derived growth factor, and various cytokines (*13*, *15*). Thus, Hedgehog inhibition may transiently eliminate pancreatic cancer–associated fibroblasts until alternative signaling pathways are activated to restore the desmoplastic stroma, reflecting another form of adaptive resistance to targeted therapies (*16*).

Numerous conventional clinical trials with a variety of anticancer drugs have failed to make substantial inroads in treating pancreatic ductal adenocarcinoma. There is reason to hope that authentic mouse models of this cancer could provide a more effective means to define mechanisms and flight test new therapeutic strategies involving mechanism-based drugs in different sequences, and layered combinations. The approach taken by Olive *et al*. represents a step in the right direction.

References

1. K. P. Olive *et al*., *Science* **324**, 1457 (2009); published online 21 May 2009 (10.1126/science.1171362).
2. G. C. Chu, A. C. Kimmelman, A. F. Hezel, R. A. DePinho, *J. Cell Biochem.* **101**, 887 (2007).
3. R. Kalluri, M. Zeisberg, *Nat. Rev. Cancer* **6**, 392 (2006).
4. A. Orimo *et al.*, *Cell* **121**, 335 (2005).
5. K. Pietras, J. Pahler, G. Bergers, D. Hanahan, *PLoS Med.* **5**, e19 (2008).
6. B. Keith, M. C. Simon, *Cell* **129**, 465 (2007).
7. D. A. Nelson *et al.*, *Genes Dev.* **18**, 2095 (2004).
8. C. H. Heldin, K. Rubin, K. Pietras, A. Ostman, *Nat. Rev. Cancer* **4**, 806 (2004).
9. R. K. Jain, *Annu. Rev. Biomed. Eng.* **1**, 241 (1999).
10. R. K. Jain, *Nat. Med.* **7**, 987 (2001).
11. G. Feldmann *et al.*, *Cancer Res.* **67**, 2187 (2007).
12. O. Nolan-Stevaux *et al.*, *Genes Dev.* **23**, 24 (2009).
13. R. L. Yauch *et al.*, *Nature* **455**, 406 (2008).
14. C. Li *et al.*, *Cancer Res.* **67**, 1030 (2007).
15. R. Jaster, *Mol. Cancer* **3**, 26 (2004).
16. G. Bergers, D. Hanahan, *Nat. Rev. Cancer* **8**, 592 (2008).

10.1126/science.1175940

MATERIALS SCIENCE

Yield Stress Fluids Slowly Yield to Analysis

The behavior of a type of complex fluid (exemplified by mayonnaise and concrete) can depend on the sample's flow history.

Daniel Bonn[1,2] and Morton M. Denn[3]

We are surrounded in everyday life by yield stress fluids: materials that behave as solids under small stresses but flow like liquids beyond a critical stress. For example, paint must flow under the brush, but remain fixed in a vertical film despite the force of gravity. Food products (such as mayonnaise), other consumer products (such as toothpaste), concrete, and even radioactive nuclear waste sludge exhibit yield stresses. The yield stress may serve to keep particulate fillers from settling, as in many consumer products and gelled propellants, or determine whether bubbles remain trapped in cement. For handling and using these materials, it is paramount to know the stress at which the material starts to flow, but a consensus on the mechanical behavior of these materials is only slowly emerging.

Yield stress materials have been studied for nearly a century (*1*). In the classical description, initiated by Bingham, there is no flow (infinite viscosity) if the shear stress is less than a critical value (the yield stress), and the stress is a monotonically increasing function of the shear rate above that value. In practice, however, measurement of the shear stress as a function of shear rate is fraught with difficulty (*2*, *3*). Apparent wall slip due to heterogeneity and the contribution of nondissipative elastic stresses are obvious and well-known experimental problems (although the latter is rarely considered), but they do not explain why different measurements often give very different yield stresses for the same material. Despite the practical importance, there is no reliable way at present to predict the onset of flow. Indeed, there has been a discussion in the rheological literature for two decades as to whether a "true" yield stress even exists.

Perhaps the main difficulty with much of the literature on yield stress fluids is the prevail-

[1]WZI, University of Amsterdam, Valckenierstraat 65, Amsterdam 1018XE, Netherlands. [2]LPS de l'ENS, 24 Rue Lhomond, F-75231 Paris cedex 05, France. [3]Benjamin Levich Institute, City College of New York, New York, NY 10031, USA. E-mail: bonn@science.uva.nl, denn@ccny.cuny.edu

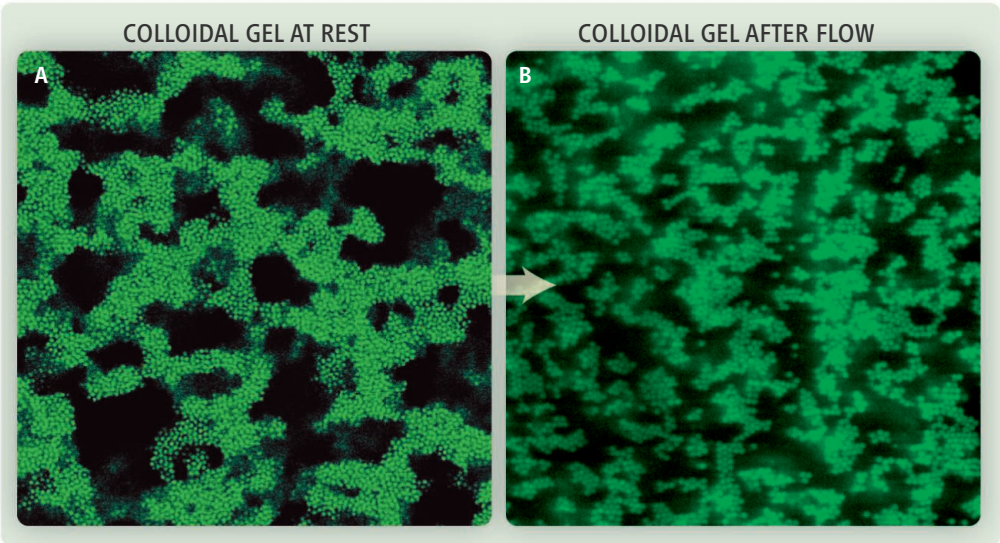

Watching the yield stress disappear in a "thixotropic" system. The same colloidal gel is shown at rest (**A**) and just after flow (**B**). In (A), a clear percolated structure can be observed. This material has a yield stress of ~5 Pa. In (B), the gel has broken into many smaller flocs. The material no longer has a measurable yield stress. Particle diameter, 1.3 μm.

ing presumption that the solid-liquid transition occurs at a single invariant stress. This assumption ignores the fact that the microstructure may adjust dynamically when flow begins. In many systems, such as clay suspensions, the yield stress is due to an internal (percolated) structure that is broken down by the flow (see the figure). As the microstructure is degraded, the viscosity may drop rapidly, and the stress required to initiate flow may then be much higher than that required to maintain it.

Such a "thixotropic" response, in which the viscosity decreases monotonically with time under shear, can lead to avalanche behavior at high imposed stresses, as observed, for example, in colloidal gels (*4*). Conversely, at low flow stresses the structure may rebuild, leading to an increase in both viscosity and yield stress. These competing processes are seen in many other soft materials, including pastes, colloidal glasses, and polymer gels, and are commonly referred to in the soft condensed-matter literature as shear rejuvenation and aging, respectively. The competition between aging and rejuvenation depends on stress; in a bentonite clay suspension, for example, there is unbounded growth in the viscosity below a critical stress (aging beats rejuvenation) but an asymptotic approach to a low viscosity above the critical stress (rejuvenation wins). This phenomenon has been dubbed viscosity bifurcation (*4*).

What does this mean for the debate whether true yield stress materials exist? Is the viscosity really infinite below the yield stress, or just very high? Foams, emulsions, and Carbopol gels (such as hair gel) are probably closest to "ideal" yield stress materials, because they do not usually show measurable rejuvenation or aging; in these cases, a yield stress may be a material property. In contrast to thixotropic systems like the clay suspension, these systems are made up of very dense packings of soft particles (bubbles in foams, drops in emulsions, and microgels in Carbopol gels).

Carbopol gels have been cited as examples of apparent yield stress materials that flow with a very high viscosity at low stresses and never become true solids—and hence are not "true" yield stress fluids (*1*). However, recent careful measurements on Carbopol gels, foams, and emulsions show that the apparent high viscosity reported at low stresses is an experimental artifact resulting from the transient viscoelastic response of the materials (*5*).

The distinction between thixotropic and ideal yield stress materials thus resolves the engineering problem of the yield stress: Reproducible experimental determination is feasible, but requires taking the shear history of the sample into account if the material is thixotropic. Ideal yield stress materials do not flow at all below a critical applied stress.

The remaining fundamental issue about the flow properties of these materials has to do with the homogeneity of flow. For ideal yield stress fluids, the classical Bingham description predicts "shear banding" when a stress gradient is present: There should be a region of sheared liquid where the stress exceeds the yield stress, and a solid layer where the stress is at or below the critical value. In contrast, in thixotropic yield stress materials shear banding is observed below a critical shear rate even in a homogeneous stress field (*6*). Due to the competition between aging and rejuvenation, the transition from flow to rest happens discontinuously. This observation implies the existence of not only a critical stress, but also a critical shear rate: the lowest shear rate for which rejuvenation wins out over aging (*6*).

Most fundamental and engineering problems for yield stress materials thus seem to be resolved by distinguishing between thixotropic and ideal materials, and it should in principle be possible to predict velocity and stress distributions in flows that are more complex than simple one-dimensional shear. Such prediction may, for example, help to determine whether air bubbles will be trapped in poured concrete or will rise (*7*, *8*), an important factor in the structural integrity of buildings.

However, in practice, it is very difficult to model even the generic example of flow about a solid sphere falling in an ideal yield stress fluid (*9*, *10*). The location of the yield surface where flow can occur is not known a priori. Therefore, numerical schemes are difficult to implement (*10*–*12*), and conventional approximations used in classical fluid mechanics may break down (*13*). In the few direct comparisons between computed and experimental velocity fields for the falling sphere, the agreement is poor (*14*), probably because the yielding process in the experimental fluids is not adequately described by the models. Much fundamental work thus remains to be done.

References

1. H. A. Barnes, *J. Non-Newtonian Fluid Mech*. **81**, 133 (1999).
2. Q. D. Nguyen, D. V. Boger, *Annu. Rev. Fluid Mech.* **24**, 47 (1992).
3. H. A. Barnes, Q. D. Nguyen, *J. Non-Newtonian Fluid Mech*. **98**, 1 (2001).
4. P. Coussot, Q. D. Nguyen, H. T. Huynh, D. Bonn, *Phys. Rev. Lett*. **88**, 175501 (2002).
5. P. C. F. Moller, A. Fall, D. Bonn, http://arxiv.org/abs/0904.1467v1.
6. P. C. F. Moller, S. Rodts, M. A. J. Michels, D. Bonn, *Phys. Rev. E* **77**, 041507 (2008).
7. J. P. Singh, M. M. Denn, *Phys. Fluids* **20**, 040901 (2008).
8. J. Tsamopoulos, Y. Dimakopoulos, N. Chatzidai, G. Karapetsas, M. Pavlidis, *J. Fluid Mech*. **601**, 123 (2008)
9. A. N. Beris, J. A. Tsamopoulos, R. C. Armstrong, R. A. Brown, *J. Fluid Mech*. **158**, 219 (1985).
10. B. T. Liu, S. J. Muller, M. M. Denn, *J. Non-Newtonian Fluid Mech*. **102** 179 (2002).
11. I. A. Frigaard, C. Nouar, *J. Non-Newtonian Fluid Mech*. **127** 1 (2005).
12. E. Mitsoulis, in *Rheology Reviews 2007*, D. M. Binding, N. E. Hudson, R. Keunings, Eds. (British Society of Rheology, Glasgow, UK, 2008), pp. 135–178.
13. G. G. Lipscomb, M. M. Denn, *J. Non-Newtonian Fluid Mech*. **14**, 337 (1984).
14. B. Gueslin, L. Talini, B. Herzhaft, Y. Peysson, C. Allain, *Phys. Fluids* **18**, 103101 (2006).

10.1126/science.1174217

Comprehensive Control of Atomic Motion

Mark G. Raizen

Recent work provides a general two-step solution to trapping and cooling of atoms. The first step is magnetic stopping of paramagnetic atoms with the use of a sequence of pulsed fields. The second step is single-photon cooling, which is based on a one-way barrier. This cooling method is related intimately to the historic problem of "Maxwell's Demon" and subsequent work by L. Szilard. Here, I discuss the connections between single-photon cooling and information entropy. I also outline future application of these methods to fundamental tests with hydrogen isotopes.

Trapping and cooling of atoms in the gas phase has been a major area of research for over 30 years, motivated by the possibility of more precise spectroscopy, tests of fundamental symmetries, and the study of many-body physics. To date, the standard method has been laser cooling, which relies on momentum kicks that are imparted to atoms by repeated cycles of photon absorption followed by spontaneous decay (*1*). Despite the enormous success of laser cooling, it has been limited to a rather small set of atoms in the periodic table because of two constraints. First, a simple two-level transition is required so that an atom can absorb a resonant photon and spontaneously decay back to the same state, enabling many cycles of the process. Second, the transition must be accessible with tunable lasers. These two constraints exclude most of the periodic table, as well as any molecules, because of the generally complicated multi-level energy structure. To sharpen this point, the simplest atom in the periodic table, hydrogen, is not amenable to laser cooling because of the lack of appropriate lasers in the far-ultraviolet region of the spectrum. The case of hydrogen is already compelling for fundamental physics: Precision spectroscopy of hydrogen isotopes (H, D, and T) would benefit enormously from trapping and cooling methods. Such methods would also enable precision measurement of beta decay of atomic tritium and would enable a breakthrough in the long-standing quest to study anti-hydrogen. Why should we be interested in general methods beyond hydrogen? One reason is that they could be an attractive alternative to standard laser cooling, especially for light alkalis such as lithium or sodium. Another reason is that there is a growing list of atoms that have been proposed for fundamental tests or applications (several examples are As, Co, Dy, Fe, Ga, In, and Ra). One thing is clear: Comprehensive methods of cooling and trapping will stimulate the scientific community to study other atoms, and it is very likely that these will lead to new discoveries. In this article, I review recent results that provide a comprehensive two-step solution to trapping and cooling of almost any atom in the periodic table. I then describe how these methods will be applied to the special case of hydrogen isotopes.

Center for Nonlinear Dynamics and Department of Physics, The University of Texas at Austin, Austin, TX 78712, USA. E-mail: raizen@physics.utexas.edu

From Room Temperature to Sub-Kelvin

The starting point for atoms in the laboratory is typically room temperature, where they are often in the solid phase. They can be converted to the gas phase either by heating in an oven or by laser ablation. The first question is how to cool the atoms from room temperature to a fraction of a degree Kelvin without the advantage of laser cooling. Rather than answer that directly, I follow with another question: What is the one property of atoms that is nearly universal? The answer is magnetism. Nearly all atoms (in their ground or first metastable electronic state) exhibit paramagnetism due to an unpaired electron in the outer orbital. This has led to cooling of atoms by using helium as a cryogenic buffer gas and then

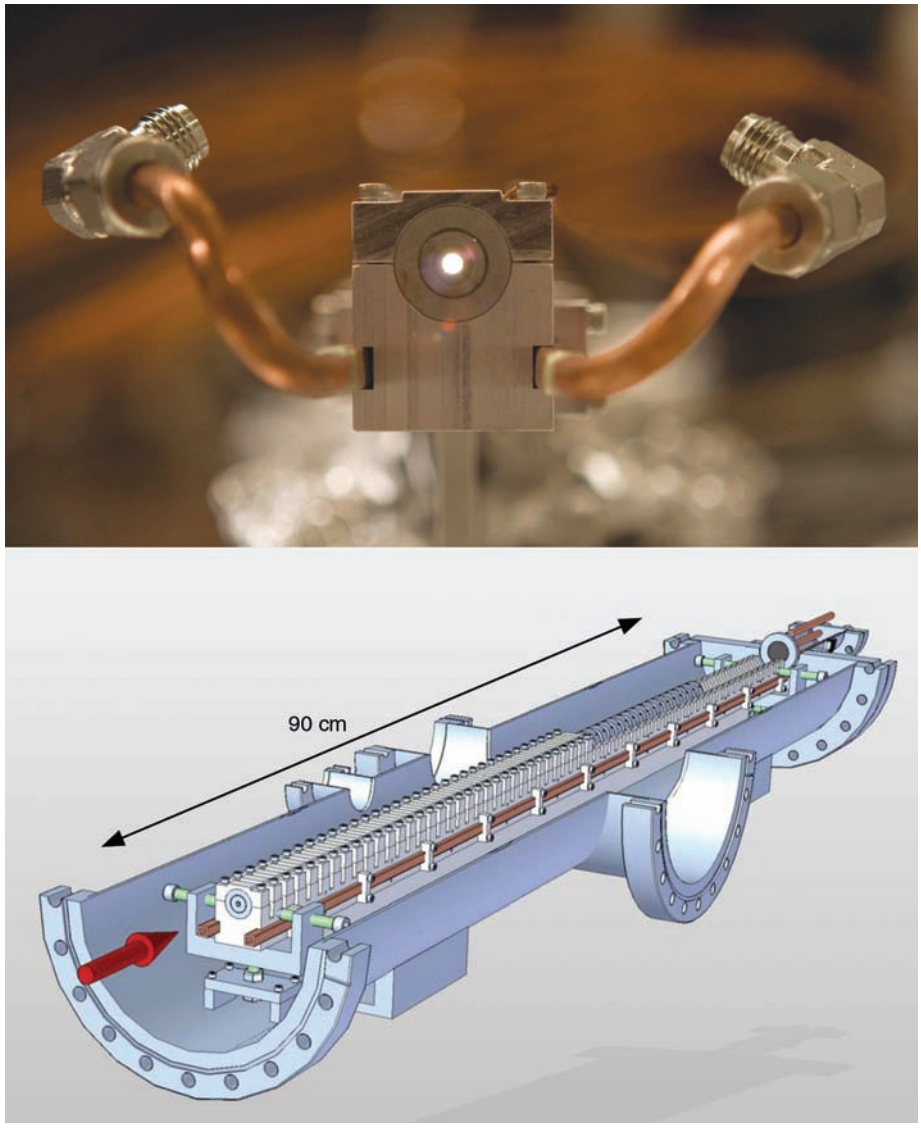

Fig. 1. Experimental set-up for the atomic coilgun. (**Top**) Photo of the assembled coilgun, head on and illuminated from the back. (**Bottom**) Schematic of the 64-stage coilgun.

trapping them magnetically at a field minimum created inside the cryostat. This method, known as buffer gas cooling, can work on any paramagnetic atom or molecule and has been used in a range of experiments over the past decade (*2*–*4*). The drawbacks of this method are the high cost and complexity of cryogenic methods and the limited optical access. It has been recognized that it would be extremely valuable to be able to trap atoms at similar temperatures, but in a simple vacuum chamber that can afford better optical access.

The starting point for these experiments is the supersonic molecular beam, which has been the workhorse of physical chemistry for many years (*5*). In these devices, a high-pressure (multi-atmosphere) inert gas expands through a small aperture into vacuum and undergoes adiabatic cooling. The properties of such beams are notable, as they are nearly monoenergetic, with a relative velocity spread of less than 1% of the mean velocity. In the co-moving frame, the temperature of the gas is in the range of tens of millikelvin. This distribution is clearly nonthermal, as it has a large forward velocity. Supersonic beams are typically operated in a pulsed mode with an actuated valve so that vacuum can be maintained without too large a gas load. The pulsed source is therefore a "bullet" of gas-phase atoms traveling down the chamber at a very well-defined velocity, launched at the precise opening time of the valve. The supersonic beam serves as a universal platform for cold but fast atoms or molecules: The carrier gas can be "seeded" with another species if it is already in the gas phase. Alternatively, atoms or molecules can be entrained into the flow near the output of the supersonic valve by laser ablation of a nearby target. Further downstream (typically 10 cm or more), the two species decouple collisionally as they expand, and the density drops. This led us to propose that paramagnetic atoms could be stopped with the use of a series of pulsed electromagnetic coils (*6*). The principle of magnetic deceleration is conceptually simple and bears close resemblance to a coilgun, which is used to launch macroscopic ferromagnetic projectiles by fast switching of electromagnetic coils. The atomic coilgun also has some similarities to the Stark decelerator, which uses pulsed electric fields to stop supersonic beams of polar molecules (*7*–*9*).

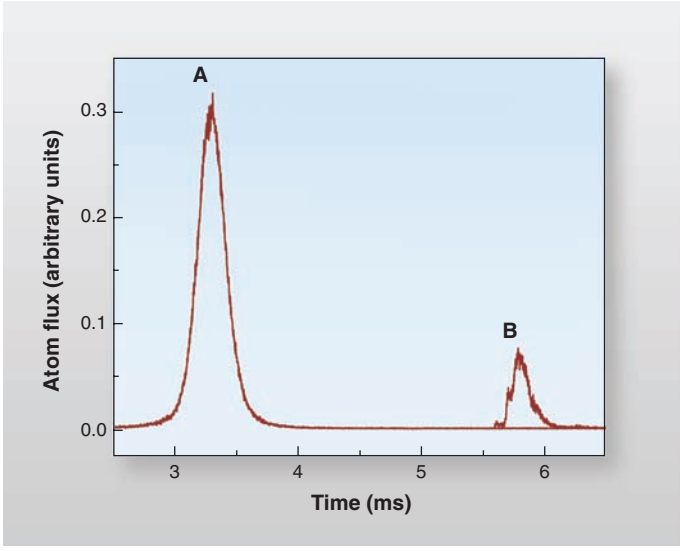

Fig. 2. Magnetic stopping of a supersonic beam of metastable neon with an atomic coilgun. The metastable atoms are detected in time-of-flight, and their delay after the firing of the valve is measured in milliseconds. The initial distribution (**A**) had a velocity of 447 m/s. The final distribution (**B**) had a velocity of 56 m/s that was required to direct the atoms to the detector (*13*).

For the case of atoms, they can be classified in terms of their response to external magnetic fields. Atoms in low-field–seeking states minimize their potential energy by going to a lower magnetic field. Consider an atom entering an electromagnetic coil, climbing a potential hill and slowing down. When the atom reaches the top of the magnetic hill, the magnetic field is suddenly switched off. Due to conservation of energy, the amount of the kinetic energy lost is equal to the energy shift, induced by the magnetic field. In the ideal operation of the atomic coilgun, the width of the velocity distribution is not changed, but the mean velocity in the laboratory frame is removed. This is not a cooling process but simply a translation in velocity space. After stopping the atoms, they can be confined in a magnetic trap. The timing of the coils can be optimized following the method of phase stability, as first developed for synchrotrons (*10*, *11*). There is a trade-off between the number of stages in the coilgun and the total flux of atoms that can be stopped. In general, a low phase angle corresponds to turning off the coils before the atoms reach the peak magnetic field, making the process more stable. Following the conceptual development and design stage, the coilgun was constructed, and the experimental set-up is shown (Fig. 1). A beam of metastable neon, as well as a beam of molecular oxygen, were stopped (*12*–*14*), and representative data with neon is displayed (Fig. 2). Parallel and independent work demonstrated stopping of atomic hydrogen (*15*–*17*).

Once the atoms are stopped, they can be trapped in static magnetic fields that create a field minimum. Such coils are used to store ultracold atoms after laser cooling and are the typical starting point for Bose-Einstein condensation experiments. The simplest configuration is to have two coils with currents running in opposite directions, known as an anti-Helmholz pair. This creates a point in the center where the magnetic field is zero and increases in all directions.

Single-Photon Cooling

After the atoms are magnetically trapped, the next question is how to cool them further, from

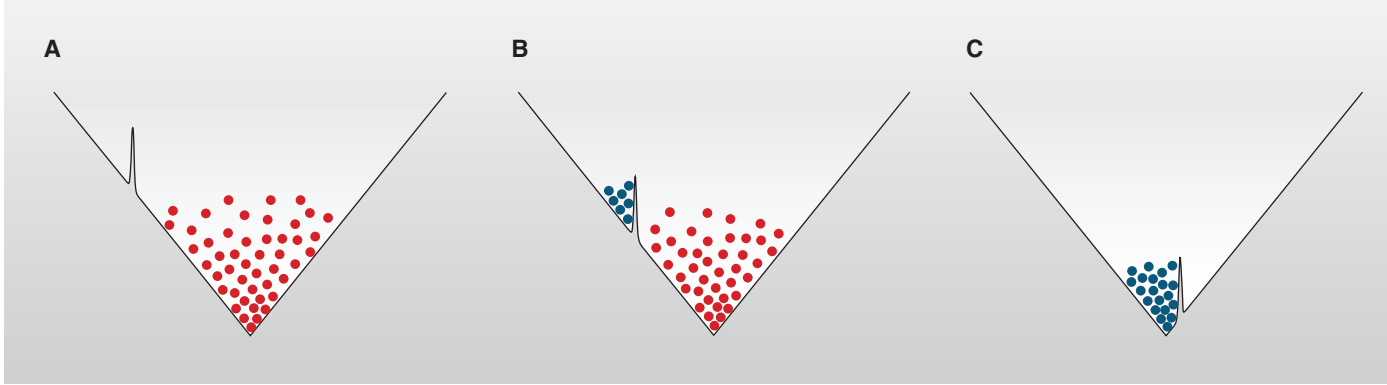

Fig. 3. Illustration of single-photon cooling in one dimension. The potential is from a magnetic trap. The one-way wall is swept from the left, catching atoms near their classical turning points. As they cross the wall, the atoms change state, as indicated by the change in color from red to blue. In (**A**), the wall is to the left of all of the particles, in (**B**), some particles are captured, and in (**C**), all of the particles are captured.

tens of millikelvin. This temperature is still very far from the limits reached by laser cooling and would not be very interesting without a way to go lower. One possible approach is to use evaporative cooling, whereby the hottest atoms are ejected from the trap, and the remaining atoms reequilibrate by collisions. However, in most cases, the initial density produced with this method is small, resulting in very long re-equilibration times and making it impractical to realize evaporative cooling during the trap lifetime. The other potential problem with evaporative cooling is that the trapped, low-field–seeking atoms can collide and change to high-field seekers that are ejected from the trap.

The approach I took was inspired by a seemingly unrelated question: Is it possible to make a barrier or wall for atoms that is "one-way"? In other words, atoms impinging from one direction can pass through, whereas atoms coming from the other directions are turned back. This one-way operation occurs in nature; for example, ion channels in cell membranes that regulate flow and maintain osmotic pressure. The question is posed here with respect to atoms in gas inside a vacuum chamber, which is quite different than anything that occurs in biology. Surprisingly, the answer is yes, as was shown in a series of papers four years ago (*18*–*21*). The basic construction is to combine a conservative potential with an irreversible step. The conservative potential is, in general, created by electromagnetic fields, which hold the atoms away from the walls of the vacuum chamber. The two viable possibilities are magnetic fields or light. The former was discussed earlier in the context of the atomic coilgun. The latter is most familiar in the context of optical tweezers. These are focused beams of light that create an attractive or repulsive potential for atoms, depending on whether they are tuned to the red or blue of an atomic transition. The irreversible step for an atom is absorption of light at a specific wavelength, followed by spontaneous decay to a different internal state.

Showing how the one-way wall can be used to cool translational motion is interesting. The principle of operation is best illustrated for a one-dimensional (1D) central potential (such as a magnetic trap) (Fig. 3). Initially, particles are contained in the main trap, and a one-way wall is placed in the wings. Atoms reaching that region are at their classical turning points where they have converted all their kinetic energy into potential energy. After passing through the one-way wall, they are trapped by scattering a single photon that changes the internal state. As the one-way wall is swept from the left, all of the atoms are captured. This method is called single-photon cooling, because the trapping process is accomplished via a single-photon scattering event. Laser cooling, in contrast, entails multiple cycles of scattering. A three-level model is the simplest example where single-photon cooling works; however, any multi-level structure is possible. Ironically, the only case that cannot work is a two-level atom, which is the prerequisite for laser cooling. Another point to emphasize is that although particle motion is in three dimensions, trap ergodicity can couple these degrees of freedom so that cooling in one direction can be sufficient.

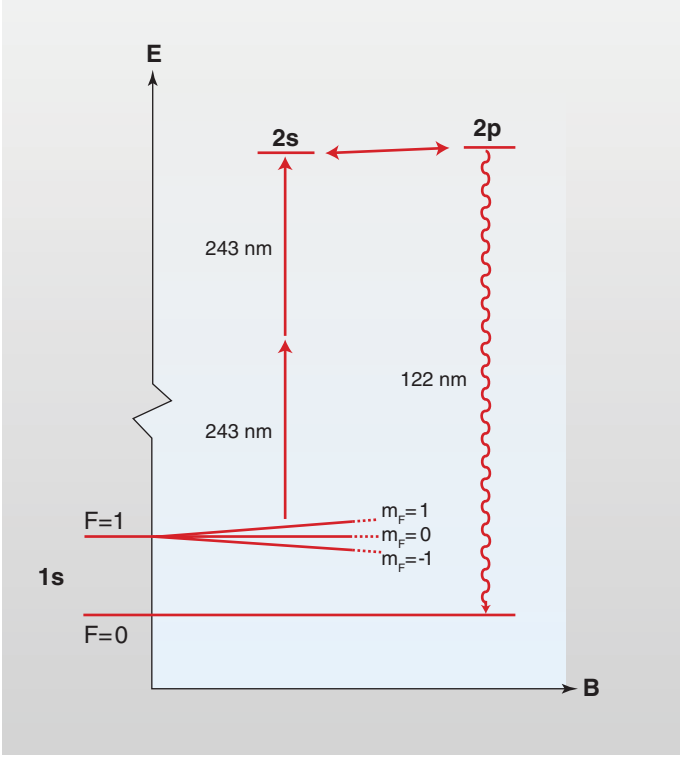

Fig. 4. Schematic of transitions in atomic hydrogen. The 1S ground state is split into two hyperfine states ($F = 1$ and $F = 0$), separated by 1.42 GHz. The $F = 1$ state is split into three states as a function of magnetic field, denoted with "B." A two-photon transition near 243 nm excites the atoms to the 2S state. This state is coupled to the 2P state, which decays by emitting a Lyman alpha photon near 121 nm. The energy axis is not to scale.

One proposal for the one-way barrier was a hybrid magnetic/optical approach, and this method led to efficient cooling of atoms (*22*–*24*). Subsequently, an all-optical method following the original proposal was demonstrated, although it could not be used for cooling due to the lasers being close to atomic resonance where heating dominates (*25*).

An all-magnetic approach can improve the cooling effect by providing a 2D trapping surface that catches nearly all the atoms near their turning points (*26*). Although these experiments prove the viability of single-photon cooling, they were still performed on rubidium atoms where standard laser is possible. The next step is to implement single-photon cooling for atoms that are not amenable to laser cooling. Atomic hydrogen is the most compelling case. Before describing these future directions, I make a historical digression to understand the fundamental nature of single-photon cooling in terms of information entropy.

Maxwell's Demon and the Szilard Engine

In 1871, James Clerk Maxwell proposed a thought experiment that is still a topic of controversy and discussion today (*27*, *28*). He considered a chamber with gas particles separated by a wall with a trap door. Maxwell envisaged an "intelligent being with deft hands" who could see the coming and going of particles and open or close the trap door appropriately. This creature became known as "Maxwell's Demon" and appeared to violate the second law of thermodynamics, as the Demon could lower the entropy of the gas without doing any work. The resolution to this paradox took many years to evolve, and the most important contribution was by L. Szilard (*29*). He first proposed an engine that could run from a single heat bath using the Demon, in clear violation of the second law (*30*, *31*). The resolution Szilard proposed was that the Demon collects information every time that the trap door is opened. This information, he argued, carries entropy that exactly balances the entropy decrease of the gas, thereby saving the second law. The concept that information has real physical meaning was arguably the start of modern information science. The role of information in cooling has been the topic of much discussion over the years and was the basis for stochastic cooling of charged particles in accelerators (*32*). However, the information content and overall efficiency in that case is extremely small, as only a small pick-up coil is used to detect the particle motion and a fast electronic feedback loop was required.

I now return to single-photon cooling and examine its connection with Maxwell's Demon. A theoretical analysis shows that, as each atom scatters one photon, information is provided about the turning point and the energy of that particle. A calculation of the entropy increase of the radiation field scattered from a directional laser into a random direction shows that, in fact, it exactly balances the entropy reduction of the atoms as they are trapped with the one-way wall (*33*, *34*). Therefore, single-photon cooling is a physical realization of Maxwell's Demon. The demon, in this case, is particularly simple and efficient: a laser beam that induces an irreversible process and scatters one photon from the beam. Such a demon is certainly not an intelligent being, yet it does not need an active

feedback loop. The fact that the information is available and can in principle be collected is enough.

Future Directions

The possibility of trapping and cooling almost any atom in the periodic table will undoubtedly open new areas of research. The same methods should also work on any paramagnetic molecule, which will enable the study of ultracold chemistry (*26*). Here I concentrate on the simplest atom in the periodic table, hydrogen, and show that new tests of fundamental physics become possible.

Hydrogen is the most abundant element in the universe and serves as the Rosetta Stone of physics. The two other isotopes of hydrogen are deuterium, with one neutron, and tritium, with two neutrons. There is a long and rich history of experiments on atomic hydrogen and related theory. The story starts with the measurement and explanation of hydrogen spectra, one of the first major successes of quantum mechanics. The story continues with the Lamb shift and the triumph of quantum electrodynamics, still the best tested theory today. In recent years, trapping and cooling of hydrogen was accomplished with heroic efforts using a dilution refrigerator and evaporative cooling (*35*). The pinnacle of quantum control, Bose-Einstein condensation, was even achieved with hydrogen (*36*). These trapping methods have not been extended to deuterium or tritium and have now been discontinued. Further progress hinges on new methods to trap and cool hydrogen isotopes in a simple room temperature apparatus. In parallel, ultrasensitive spectroscopy on hydrogen and deuterium beams has reached an exquisite level of precision due to the advent of the frequency comb (*37*, *38*).

The methods described above are perfectly suited to trapping and cooling of all three isotopes of hydrogen. The starting point will be a supersonic beam of molecular hydrogen in a neon carrier gas. The molecules will be dissociated with a discharge near the nozzle, and the atomic coilgun will stop the atoms and confine them in a magnetic trap. In fact, hydrogen has already been stopped and trapped with a coilgun (*17*). The structure of hydrogen is ideally suited to single-photon cooling, although it requires a laser near 243 nm to drive a two-photon transition to a metastable 2S state (Fig. 4). The atoms in the $F = 0$, $m = 0$ state will be optically trapped in a standing wave of light inside a build-up cavity.

One of the first goals with trapped hydrogen isotopes will be to push the current limits of ultrahigh precision spectroscopy, especially needed for tritium. More importantly, trapping and cooling of atomic tritium may hold the key to the determination of the neutrino rest mass, one of the most pressing questions in modern physics. A recent concept paper showed how a sample of trapped ultracold tritium serves as an ideal system for neutrino mass measurement by kinematic reconstruction of the recoiling electron in coincidence with the recoiling helium ion (*39*).

The same methods will also work for trapping and cooling of anti-hydrogen (*40*, *41*). In this case, the supersonic beam method cannot be used as the starting point. Instead, a beam of anti-hydrogen could be generated by launching anti-protons through a positron cloud and then stopped and cooled with our methods. Experiments with anti-hydrogen will be able to answer the simple question: Does anti-matter fall the same way as matter? Such experiments can also test charge-parity-time reversal invariance, believed to be a fundamental symmetry of nature. These examples illustrate that hydrogen and its isotopes hold the key to many unanswered questions about the universe.

In the short term, work will concentrate on optimizing the efficiency of the atomic coilgun. The first possible improvement is to mode-match the incident beam to the coilgun by magnetic focusing. I am also investigating the possibility of an adiabatic magnetic slower in which the atoms would be trapped in three dimensions throughout the entire stopping process. This would then preserve the initial phase space density, translating the atoms to rest in the laboratory frame. The case of single-photon cooling must be further developed, and the limitations of the method have to be studied. For example, the density limit has not been reached and must be studied further. A quantum analysis of single-photon cooling has not yet been developed. The temperature that can be reached is limited to the photon recoil, as opposed to evaporative cooling that has no such limit. I envisage that single-photon cooling is most suitable as the first stage, followed by evaporation in an optical trap to reach quantum degeneracy.

References and Notes

1. H. J. Metcalf, P. van der Straten, *Laser Cooling and Trapping* (Springer, New York, 1999).
2. J. D. Weinstein, R. deCarvalho, T. Guillet, B. Friedrich, J. M. Doyle, *Nature* **395**, 148 (1998).
3. C. I. Hancox, S. C. Doret, M. T. Hummon, L. Luo, J. M. Doyle, *Nature* **431**, 281 (2004).
4. W. C. Campbell, E. Tsikata, H. Lu, L. D. van Buuren, J. M. Doyle, *Phys. Rev. Lett.* **98**, 213001 (2007).
5. G. Scoles, Ed., *Atomic and Molecular Beam Methods*, vols. 1 and 2 (Oxford Univ. Press, New York, 2000).
6. E. Narevicius *et al.*, *New J. Phys.* **9**, 96 (2007).
7. H. L. Bethlem, G. Berden, G. Meijer, *Phys. Rev. Lett.* **83**, 1558 (1999).
8. S. Y. T. van de Meerakker, P. H. M. Smeets, N. Vanhaecke, R. T. Jongma, G. Meijer, *Phys. Rev. Lett.* **94**, 023004 (2005).
9. B. C. Sawyer *et al.*, *Phys. Rev. Lett.* **98**, 253002 (2007).
10. E. M. McMillan, *Phys. Rev.* **68**, 143 (1945).
11. V. Veksler, *J. Phys. (USSR)* **9**, 153 (1945).
12. E. Narevicius *et al.*, *New J. Phys.* **9**, 358 (2007).
13. E. Narevicius *et al.*, *Phys. Rev. Lett.* **100**, 093003 (2008).
14. E. Narevicius *et al.*, *Phys. Rev. A* **77**, 051401 (2008).
15. N. Vanhaecke, U. Meier, M. Andrist, B. H. Meier, F. Merkt, *Phys. Rev. A* **75**, 031402 (2007).
16. S. D. Hogan, D. Sprecher, M. Andrist, N. Vanhaecke, F. Merkt, *Phys. Rev. A* **76**, 023412 (2007).
17. S. D. Hogan, A. W. Wiederkehr, H. Schmutz, F. Merkt, *Phys. Rev. Lett.* **101**, 143001 (2008).
18. M. G. Raizen, A. M. Dudarev, Q. Niu, N. Fisch, *Phys. Rev. Lett.* **94**, 053003 (2005).
19. A. Ruschhaupt, J. G. Muga, *Phys. Rev. A* **70**, 061604 (2004).
20. Reference (*19*) was submitted shortly after (*18*), but the work cited in (*19*) was independent.
21. A. M. Dudarev, M. Marder, Q. Niu, N. Fisch, M. G. Raizen, *Europhys. Lett.* **70**, 761 (2005).
22. G. N. Price, S. T. Bannerman, E. Narevicius, M. G. Raizen, *Laser Phys.* **17**, 965 (2007).
23. G. N. Price, S. T. Bannerman, K. Viering, E. Narevicius, M. G. Raizen, *Phys. Rev. Lett.* **100**, 093004 (2008).
24. S. T. Bannerman, G. N. Price, K. Viering, M. G. Raizen, *New J. Phys.*, in press; preprint available at http://arXiv.org/abs/0810.2239.
25. J. J. Thorn, E. A. Schoene, T. Li, D. A. Steck, *Phys. Rev. Lett.* **100**, 240407 (2008).
26. E. Narevicius, S. T. Bannerman, M. G. Raizen, *New J. Phys.*, **11**, 055046 (2009).
27. J. C. Maxwell, in *Theory of Heat* (Longmans, Green, London, 1871), pp. 308–309.
28. H. S. Leff, A. Rex, Eds., *Maxwell's Demon: Entropy, Information, Computing* (Princeton Univ. Press, Princeton, NJ, 1990).
29. L. Szilard, *Z. Phys.* **53**, 840 (1929).
30. R. J. Scully, M. O. Scully, *The Demon and the Quantum* (Wiley-VCH, Weinheim, Germany, 2007).
31. P. A. Skordos, W. H. Zurek, *Am. J. Phys.* **60**, 876 (1992).
32. S. Van der Meer, *Rev. Mod. Phys.* **57**, 689 (1985).
33. A. Ruschhaupt, J. G. Muga, M. G. Raizen, *J. Phys. At. Mol. Opt. Phys.* **39**, 3833 (2006).
34. P.-M. Binder, *Science* **322**, 1334 (2008).
35. H. Hess *et al.*, *Phys. Rev. Lett.* **59**, 672 (1987).
36. D. G. Fried *et al.*, *Phys. Rev. Lett.* **81**, 3811 (1998).
37. J. L. Hall, *Rev. Mod. Phys.* **78**, 1279 (2006).
38. T. Hänsch, *Rev. Mod. Phys.* **78**, 1297 (2006).
39. M. Jerkins, J. Majors, J. R. Klein, M. G. Raizen, preprint available at http://arXiv.org/abs/0901.3111.
40. M. Amoretti *et al.*, *Nature* **419**, 456 (2002).
41. G. Gabrielse *et al.*, *Phys. Rev. Lett.* **89**, 213401 (2002).

42. This work is supported by NSF, the Army Research Office, the R. A. Welch Foundation, the State of Texas Advanced Research Program, and the Sid W. Richardson Foundation.

10.1126/science.1171506

Herapathite

Bart Kahr,* John Freudenthal, Shane Phillips, Werner Kaminsky

Few crystalline substances are as celebrated in the history of optics as is herapathite, first prepared when an assistant to the toxicologist William Bird Herapath precipitated metallic-reflecting, needle-shaped crystals upon dropping tincture of iodine into the urine of a dog that had been fed quinine (*1*). Herapath reported that, when the transparent crystals sat one upon the other at right angles, the overlap was "black as midnight." He recognized that his crystals functioned as excellent linear light polarizers absorbing virtually all the light polarized along the shorter axis of the best-developed face [supporting online material (SOM) text] (fig. S4) and declared that "there is no doubt" herapathite, the name coined by Haidinger (*2*), will soon replace costly tourmaline polarizers and Nichol prisms (*3*). Sir David Brewster wished for crystals large enough to add special effects to his invention, the kaleidoscope (*4*). Herapathite captured the attention of Stokes; he analyzed its remarkable reflectivity (*5*, *6*).

Applications of herapathite were not forthcoming for 75 years when Land oriented fragile microcrystals of herapathite in extruded polymers, a process that produced the first large-aperture light polarizers (*7*, *8*) and launched the Polaroid empire. Curiously, despite the widespread use of herapathite polarizers in goggles, as photographic filters, and for stereoscopic imaging, as well as their role as the progenitors of the many polarizing plastics prepared subsequently, the structure of herapathite has never been established.

The composition of Herapath's salt was established by Jörgensen as $4\mathbf{Q}H_2^{2+} \cdot 3SO_4^{2-} \cdot 2I_3^- \cdot 6H_2O$, where **Q** is quinine, $C_{20}H_{24}N_2O_2$ (*9*, *10*). In 1896, herapathite was used to study x-rays rather than vice versa as in this study. Just 7 months after the discovery of a new kind of radiation by Röntgen, Mayer (*11*) failed to polarize x-rays with herapathite. West (*12*) established that the herapathite crystals belong to the orthorhombic system.

The curious absence of a crystal structure of herapathite has been expressed (*13*). Past difficulties in its determination presumably arose from lamellar twinning and the complexity of the formula unit. In the absence of a crystal structure, we are not certain how herapathite functions as a dichroic polarizer. This is a vexing and remarkably long-standing (>150 years) question. West and others (*13*–*15*) speculated that a linear arrangement of the iodides might explain the enormous dichroic ratio. Spectra in polarized light were given by Land and West (*16*).

Crystals of herapathite were grown from quinine, concentrated sulfuric acid, and I_2 in 1:1 ethanol:acetic acid (*3*). Herapath-like needles ripened on standing in the mother liquor such that the absorbing axis became more elongated (*12*) (figs. S4 and S5). The crystals were analyzed with an x-ray diffractometer at room temperature. The orthorhombic cell parameters were a = 15.2471(3) (estimated standard deviations) Å, b = 18.8854(4) Å, and c = 36.1826(9) Å. The crystal structure was solved and refined in the space group $P22_12_1$. Crystallographic data are summarized in table S1. The quinine configuration established the absolute structure. The asymmetric unit (fig. S1) of our crystals has an acetic acid molecule not captured in Jörgensen's formula (*9*). Smirnov argued that herapathite is not one substance but a family of related solvates and salts with varying component stochiometries (*15*).

The crystal structure is shown in Fig. 1. The six water molecules are distributed over eight sites, and the acetic acid molecule is distributed over two sites associated with disorder in the quinine vinyl group. The ensemble has a diad axis along a and an approximate diad within the asymmetric unit broken by the dissymmetry in the positions of the iodine atoms. The two triiodide ions lie roughly parallel to the b axis, a feature apparently deduced from powder data (*17*). Our data give intertriiodide bond lengths of 3.74 and 3.81 Å and intratriiodide distances from 2.89 to 3.01 Å.

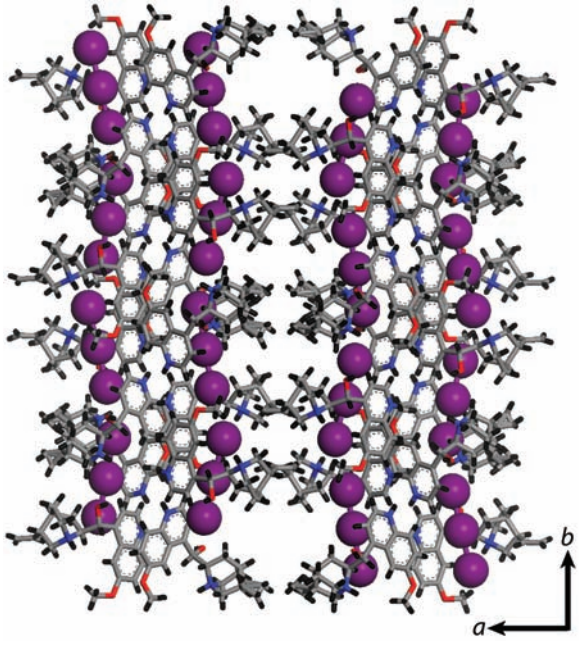

Fig. 1. The crystal structure of herapathite. Iodine atoms are purple spheres. The absorbing axis is vertical. Solvent molecules and sulfate ions have been removed for clarity. See also figs. S2 and S3.

In all crystals examined, the b axis is the most absorbing direction. Even though herapathite does not have an obvious visible chromophore, triiodide salts are often richly colored (*18*). This is a consequence of the association of triiodide ions in extended chains (*19*) with exciton interactions along the chain length that significantly shift the absorption bands to lower energy, as in model starch-iodine complexes (*20*). Likewise, delocalized, excitations among many I_3^- ions, polarized along b rather than along the I_3^- ions themselves, account for the remarkable light-absorbing properties of herapthite, confirming the speculation of others (*12*, *14*, *15*).

The papers of Herapath (*1*, *3*) and Jörgensen (*9*) cited herein indicate many related dichroic substances that comprise a rich clathrate chemistry.

References and Notes

1. W. B. Herapath, *Phil. Mag.* **3**, 161 (1852)
2. W. Haidinger, *Phil. Mag.* **6**, 284 (1853).
3. W. B. Herapath, *Phil. Mag*. **6**, 346 (1853).
4. D. Brewster, *The Kaleidoscope* (Van Cort, Mount Holyoke, MA, 1987).
5. G. G. Stokes, *Rep. Brit. Assoc.* **22**, 15 (1852).
6. G. G. Stokes, *Phil. Mag.* **6**, 393 (1853).
7. E. D. Land, *J. Opt. Soc. Am.* **41**, 957 (1951).
8. See also F. Bernauer, *Fortschr. Mineral. Kristallogr. Petrogr.* **19**, 22 (1935).
9. S. M. Jörgensen, *J. Prakt. Chem.* **14**, 215 (1877).
10. S. M. Jörgensen, *J. Prakt. Chem.* **15**, 65 (1877).
11. A. M. Mayer, *Am. J. Sci.* **151**, 467 (1896).
12. C. D. West, *Am. Mineral.* **22**, 731 (1937).
13. F. H. Herbstein, G. M. Reisner, W. Schwotzer, *Acta Crystallogr. Sect. C Cryst. Struct. Commun.* **41**, 510 (1985).
14. Y. Hoshino, *J. Phys. Math. Soc. Jpn.* **17**, 265 (1943).
15. L. V. Smirnov, *Tr. Leningr. Tekhnol. Inst. Pishch. Prom.* **1**, 112 (1949).
16. E. H. Land, C. D. West, in *Colloid Chemistry*, J. Alexander, Ed. (Van Nostrand, New York, 1900), vol. 6, pp. 160–190.
17. K. Tojima *et al*., U.S. Patent 5368780 (1994).
18. M. Mizuno, J. Tanaka, I. J. Harada, *J. Phys. Chem.* **85**, 1789 (1981).
19. P. H. Svensson, L. Kloo, *Chem. Rev.* **103**, 1649 (2003).
20. M. B. Robin, *J. Chem. Phys.* **40**, 3369 (1964).
21. We thank NSF and the donors to the American Chemical Society Petroleum Research Fund.

Supporting Online Material

www.sciencemag.org/cgi/content/full/324/5933/1407/DC1
Materials and Methods
SOM Text
Figs. S1 to S5
Table S1
References

16 March 2009; accepted 21 April 2009
10.1126/science.1173605

Department of Chemistry, Box 351700, University of Washington, Seattle, WA 98195–1700, USA.

*To whom correspondence should be addressed. Department of Chemistry, New York University, 100 Washington Square East, New York, NY 10003, USA. E-mail: bart.kahr@nyu.edu

Magnetic Fields in the Formation of Massive Stars

Josep M. Girart,[1]* Maria T. Beltrán,[2]† Qizhou Zhang,[3] Ramprasad Rao,[4] Robert Estalella[2]

Massive stars play a crucial role in the production of heavy elements and in the evolution of the interstellar medium, yet how they form is still a matter of debate. We report high-angular-resolution submillimeter observations toward the massive hot molecular core (HMC) in the high-mass star-forming region G31.41+0.31. We find that the evolution of the gravitational collapse of the HMC is controlled by the magnetic field. The HMC is simultaneously contracting and rotating, and the magnetic field lines threading the HMC are deformed along its major axis, acquiring an hourglass shape. The magnetic energy dominates over the centrifugal and turbulence energies, and there is evidence of magnetic braking in the contracting core.

Stars more massive than 8 $M_\odot$ (where $M_\odot$ is the mass of the Sun) account for only 1% of the stellar population in our Galaxy. Nevertheless they dominate the appearance and evolution of its interstellar medium and are responsible for the production of heavy elements.

The formation of massive stars is not completely understood. Stars form when dense molecular clouds collapse as a result of gravity. But as the mass of a young star reaches 8 $M_\odot$, its own radiation can exert enough outward pressure to halt infall, inhibiting further stellar growth (*1*). The presence of a flattened accretion disk surrounding the protostar (*2*) can alleviate this inhibition by shielding the infalling material from stellar radiation and by creating a lower density section along the rotation axis of the disk and a molecular outflow, which helps by channeling the radiation out, allowing the formation of stars more massive than 40 $M_\odot$ (*3*–*5*). Massive stars may also form through mergers of smaller stars (*6*).

The scenario whereby massive stars form through disk-assisted accretion resembles the way stars like the Sun form. Both processes involve accretion through a flattened disk and molecular outflows. The magnetic field is thought to play an important role in the formation of Sun-like stars by shaping cloud collapse, removing excess angular momentum, and thus allowing continuous accretion (*7*–*9*), even in the case of an originally weak magnetic field (*10*). High-angular-resolution polarimetric observations of the low-mass protostellar system NGC 1333 IRAS 4A (IRAS 4A) showed a magnetic field with a clear hourglass morphology at scales of a few hundred astronomical units (AU) around the collapsing molecular core surrounding the protostars (*11*), a configuration that was shown to be consistent with theoretical models for the formation of solar-type stars, where well-ordered, large-scale, rather than turbulent, magnetic fields control the evolution and collapse of the molecular cores from which stars form (*12*).

We investigated the hot molecular core (HMC) in G31.41+0.31 (G31.41), a massive star-forming region [~500 to 1500 $M_\odot$ (*13*, *14*)] located 7900 parsecs (pc) away (*15*). G31.41 has a luminosity

[1]Institut de Ciències de l'Espai [Consejo Superior de Investigaciones Científicas (CSIC)–Institut d'Estudis de Catalunya (IEEC)], Campus Universitat Autònoma de Barcelona (UAB)–Facultat de Ciències, Torre C5 - parell 2[a], 08193 Bellaterra, Catalunya, Spain. [2]Departament d'Astronomia i Meteorologia (IEEC-UB). Institut de Ciencies del Cosmos y Unitat Associada a CSIC, Universitat de Barcelona, Martí i Franquès 1, 08028 Barcelona, Catalunya, Spain. [3]Harvard-Smithsonian Center for Astrophysics, 60 Garden Street, Cambridge, MA 02138, USA. [4]Academia Sinica, Institute of Astronomy and Astrophysics, 645 North Aohoku Place, Hilo, HI 96720, USA.

*To whom correspondence should be addressed. E-mail: girart@ieec.cat

†Present address: Osservatorio Astrofisico di Arcetri, Largo Enrico Fermi 5, 50125 Firenze, Italy.

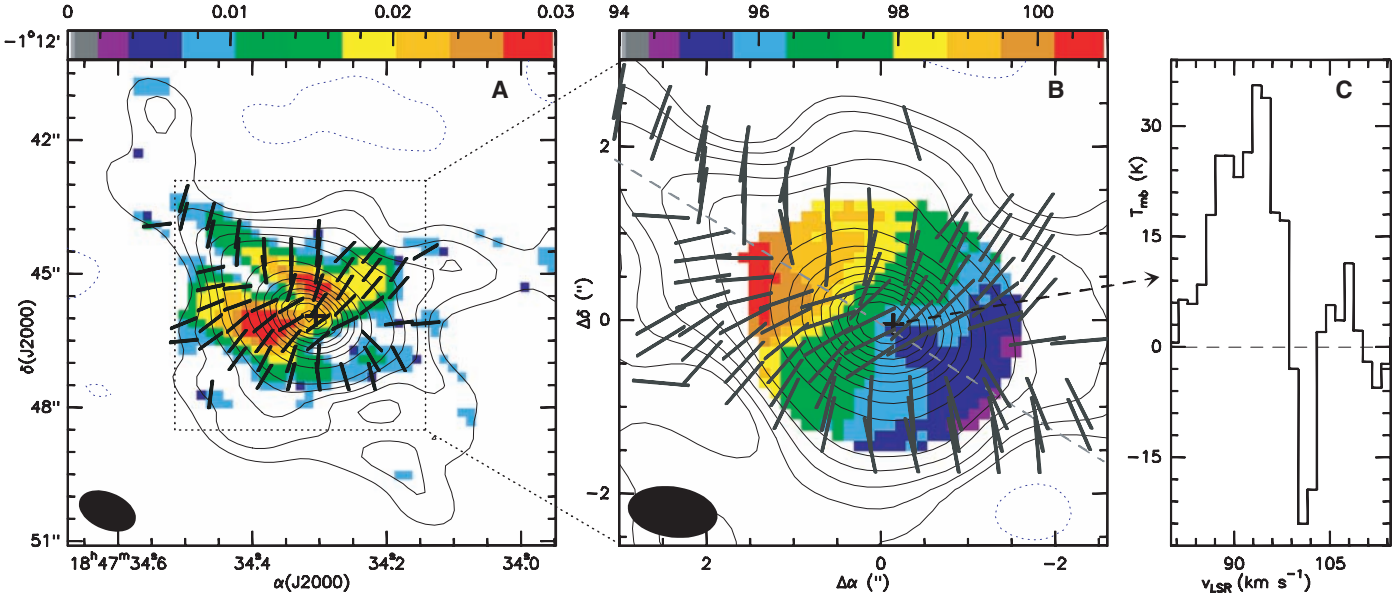

Fig. 1. (**A**) Contour map of the 879-μm dust emission superposed on the color image of the polarized flux intensity in units of Jy per beam. Black thick bars indicate the position angle of the magnetic field. These maps were obtained by using a natural weighting to the visibility data, which yielded to a full width at half maximum synthesized beam of 1.34″ × 0.83″ with a position angle of 67° (shown in the bottom left corner). Contour levels are 0.8, 1.5, 2.5, 4, 6, 16, 26, 36…96% of the peak intensity, 9.13 Jy per beam. (**B**) Contour map of the 879 μm dust emission superposed on the color image of the flux weighted velocity map of the CH_3OH 14_7-15_6 A. Black thick bars indicate the direction of the magnetic field. These maps were obtained by using a robust weighting of 0 to the visibility data, which yielded to a full width at half maximum synthesized beam of 1.04″ × 0.59″ with a position angle of 82° (shown in the bottom left corner). Contour levels are the same as in the previous panel, with a peak intensity of 6.55 Jy per beam. (**C**) Spectrum of the $C^{34}S$ 7-6 line at the position of the dust emission peak. The continuum has been subtracted from the line emission (this is valid for all the molecular line data presented here).

of 3×10^5 $L_\odot$ (where $L_\odot$ is the luminosity of the Sun), suggesting that the core's center harbors O-type hydrogen-burning stars (*14*, *15*). It is associated with very weak free-free emission (*16*), implying that an ultracompact HII region has not yet developed and therefore that the embedded young stellar objects are in a very early stage of their evolution. High-angular-resolution observations of methyl cyanide toward the HMC reveal a massive toroid (*13*, *17*) rotating about the axis of a bipolar outflow (*18*), the direction of which is controversial (*16*). The mass of the toroid is much larger than the dynamical mass required for equilibrium (~87 $M_\odot$) (*13*), which suggests that the toroid may be gravitationally unstable and undergoing collapse, unless a strong (20 to 40 mG) magnetic field is present. The physical properties of the HMC have been modeled recently, with an infall radius smaller than $\sim 2 \times 10^4$ AU and a high accretion rate of 3×10^{-3} $M_\odot$ year^{-1} (*14*).

We observed G31.41 at 879 μm with use of the Submillimeter Array (SMA) (*19*) in its compact and extended configurations (which provides an angular resolution slightly below 1 arc sec: see Fig. 1) and with use of the SMA polarimetry system (*20*). The continuum emission, which traces the dust in the HMC, is resolved in a slightly elongated compact component with a size of 1.16″ by 0.93″ (8100 AU by 6500 AU) and a position angle (PA) of 56°, surrounded by a weaker component extending to the northeast and reaching an ultracompact HII region located 5″ northeast of the HMC (*15*). The total flux measured in our 879-μm observations is 21.2 ± 1.0 janskys (Jy, 1 Jy = 10^{-26} W m^{-2} Hz^{-1}) over an area of 15.9 square arc sec, where there is adequate sensitivity to measure the polarization. For an optically thin emission, a temperature of 164 K (*15*), a gas-to-dust ratio of 100, and a dust opacity of 1.9 cm^2 g^{-1} (*21*), the total mass traced by the dust is 577 $d_{7.9}$ $M_\odot$ [$d_{7.9} \equiv (d/7.9\ \text{kpc})$, where d is the adopted distance to the G31.41 cloud], in the range of previous estimations (*13*, *14*). We can estimate the averaged column and volume density of the region traced by the dust: $\langle N(H_2) \rangle = M/(A\mu_m)$ and $\langle n(H_2) \rangle = M/(V\mu_m)$, where M is the dust mass, μ_m is the average mass per particle, A is the area of the dust emission, and $V = (4/3)\pi^{-1/2}A^{3/2}$ is the volume. For a helium-to-hydrogen mass ratio of 30%, the mean column density is $\langle N(H_2) \rangle = 3.5 \times 10^{24}$ cm^{-2}, and the mean volume density is $\langle n(H_2) \rangle = 3.1 \times 10^6 d_{7.9}^{-1}$ cm^{-3}.

We detected linearly polarized dust emission in the HMC, mainly along the major axis of the dust emission (color scale in Fig. 1A), with a maximum polarized flux of 30 mJy per beam. At the position of the maximum polarized flux, the polarization fraction is at a 4% level. The position angle of the dust polarization allows us to examine the magnetic field. Thus, at the spatial scale of the SMA angular resolution, ~6000 AU, the magnetic field lines are deformed along the major axis of the HMC (Fig. 1, A and B), providing evidence of an hourglass magnetic field configuration in a high-mass star-forming region. An hourglass configuration was also found in the OMC-1 (*22*), but it was at much larger scales (~0.5 pc) and in a more-complex and -evolved high-mass star-forming region.

The 4 GHz of bandwidth available for the SMA allowed us to detect a large number of spectral lines. The myriad of lines is dominated by CH_3OH, with more than 30 lines, but also by $HCOOCH_3$, CH_3OCH_3, and SO_2. Many of the lines show a similar morphological and kinematical pattern in the HMC. There is a broad range of excitation conditions among the molecular lines detected, with upper energy levels going from a few tens up to more than 1000 K. In general, the emission is more compact for the lines with a higher excitation energy level, showing a velocity gradient along the major axis (Fig. 1B), which is suggestive of rotation, as previously found for CH_3CN (*13*). One of the lowest excitation lines, $C^{34}S$ 7-6, shows a clear inverse P-Cygni profile in its spectrum (Fig. 1C). The emission feature peaks at about 93.5 km s^{-1} and the absorption feature at about 100.5 km s^{-1}, whereas the cloud velocity, V_{LSR}, is ≈97.4 km s^{-1} (*14*). The colder molecular gas from the circumstellar envelope absorbs the bright continuum emission. The absorption at positive velocities (i.e., redshifted because of the Doppler effect) relative to the cloud velocity and the presence of the blueshifted emission imply that the circumstellar envelope at scales of a few thousand AUs is infalling. The infall velocity, which has been estimated as $|V_{LSR} - V_{redshifted}|$, is ~3.1 km s^{-1}.

We proceeded, similarly to (*11*), to derive the magnetic field properties by first fitting its morphology with a family of exponential functions. We find that the center of symmetry of the magnetic field coincides within the measured uncertainty, ~0.2", with the center of the core (i.e., the position of the dust emission peak). The position angle of the magnetic field axis, ≈–27°, is almost perpendicular to the major axis of the envelope (Fig. 2). There are some discrepancies southwest of the center where the measured field directions suggest a small tilt of the major axis westward of the center. The observed dispersion in the residuals (fig. S1), $\delta\theta_{obs}$, is 13.6 ± 1.0°. Because the measurement uncertainty of the polarization angle (σ_θ) is 9.5 ± 3.3°, the intrinsic dispersion, $\delta\theta_{int} = (\delta\theta_{obs}^2 - \sigma_\theta^2)^{1/2}$, is $\delta\theta_{int}$ = 9.8 ± 3.5°. The magnetic field strength can be estimated from the dispersion in polarization angles (which is a consequence of the perturbation by Alfvén waves or turbulence in the field lines). With use of the value of the volume density derived from our data, $n(H_2) = 3.1 \times 10^6$ cm^{-3}, and a turbulent velocity dispersion of $\delta v_{los} \approx 2.7$ km s^{-1}, the expected value from the Osorio *et al.* modeling (*14*) at the scale of $\approx 1.5 \times 10^4$ AU, which is the scale of the observed polarized emission—we calculated

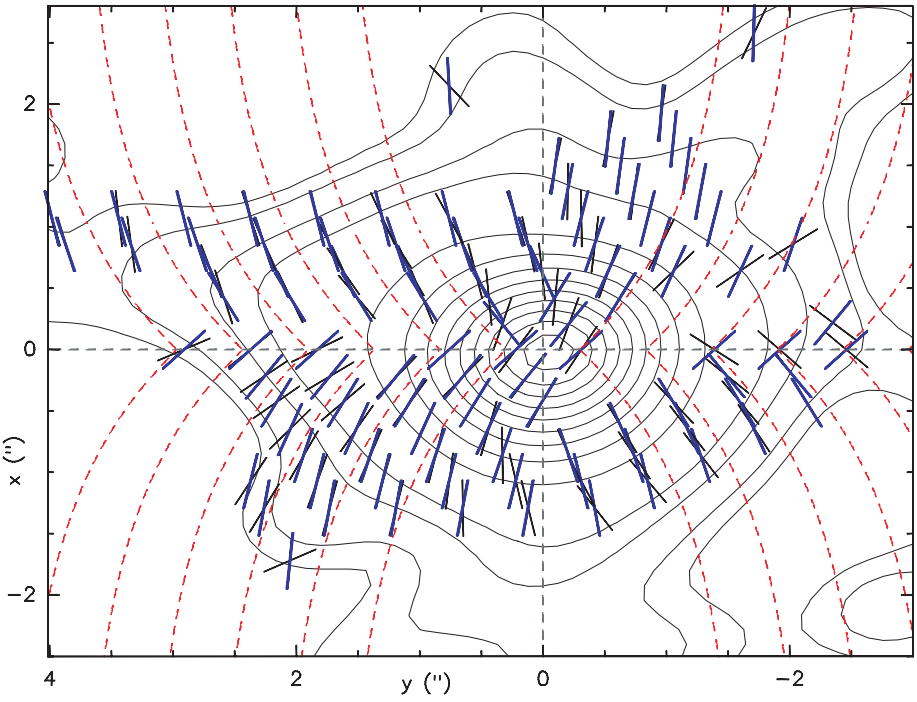

Fig. 2. Magnetic field directions superposed on the contour map of the dust emission. The map has been rotated by 27° to the east with respect to the one shown in Fig. 1. Contour levels are at 0.9, 1.4, 3, 5, 15, … 95% of the intensity peak. The black bars show the vectors of the measured magnetic fields. The blue bars correspond to the best fit to the magnetic field lines assuming an exponential form of $y = y_0 - C_1\exp(-C_2 x)$, where the x is the distance from the center of the symmetry along the magnetic field axis. The fit was done by using a χ^2 analysis with the following free parameters: $\langle_0$ and $_0$, the center of symmetry; χ_{PA}, the position angle of the field axis, C_1 and C_2. The best fit is obtained when χ_{PA} = –27° ± 1°, $\langle_0(J2000) = 18^h47^m34.31^s \pm 0.02^s$, $_0(J2000) = -1°12'46.0'' \pm 0.2''$, $C_1 = 0.8 \pm 0.2$, and $C_2 = 1.4 \pm 0.4$. The red dashed lines show the exponential shape of the best-fit field.

the magnetic field strength in the plane of the sky to be $B_{pos} \approx 9.7 d_{7.9}^{-1/2}$ mG. This value is a factor of ~2 higher that an earlier value derived by the Osorio *et al*. (*14*) assuming equipartition between the magnetic and turbulent energy. The magnetic field strength in G31.41 is also higher than those in other massive star-forming cores (*23*, *24*). The derived value of the magnetic field strength implies an Alfvenic velocity of $v_A = \sqrt{B/(4\pi\rho)} =$ 7.9 km s^{-1}, which is larger than the infall velocity, so the collapse is sub-Alfvenic. The key parameter that determines whether magnetic fields provide support against gravitational collapse is the mass–to–magnetic flux ratio. With use of the standard formula (*25*), we find that the mass–to–magnetic flux ratio is $\approx 2.7 d_{7.9}^{1/2}$ times the critical value for collapse. The ratio of the turbulent to magnetic energy, $\beta_{turb} = 3(\delta v_{los}/v_A)^2 = 3.64 \times 10^{-3} (\delta\theta_{int}/^\circ)^2$, is $\beta_{turb} = 0.35^{+0.29}_{-0.20}$, indicating that the magnetic energy dominates over the turbulent energy. This ratio is a lower limit, and the mass-to-flux ratio is an upper limit because what is measured is the component on the plane of the sky of the magnetic field strength. However, the deprojected values are likely not too different because, first, the clear hourglass morphology suggests that the HMC is not close from the pole-on configuration and, second, the size of the major and minor axes are similar, so it is reasonable to use the estimated column density to derive the mass–to–magnetic flux ratio.

The mass accretion rate can be estimated from the infall velocity derived from the inverse P-Cygni profile. Although the associated infall radius is uncertain, we have chosen a lower limit of 4080 AU, which corresponds to the source radius obtained from Gaussian deconvolution of the continuum image, and an upper limit of 12,640 AU, which corresponds to the radius of the emission at 5% of the peak emission, which includes most of the dust emission. Following Beltrán *et al*. (*26*), the mass accretion rate onto the star ($4\pi R^2 m H_2 n V_{infall}$) inside a solid angle Ω is $M_{acc} = \Omega/(4\pi)(3 \times 10^{-3}$ to $3 \times 10^{-2}) M_\odot$ year^{-1}, which is in agreement with the estimate from modeling G31.41 (*14*). Such a high value of the infall rate has also been estimated for other O-type (proto)stars (*26*–*28*), supporting the nonspherical accretion scenario for the formation of massive stars, which is expected in the presence of a substantial magnetic field, as observed here.

Here on, we study the kinematical behavior resulting from the velocity gradient along the major axis of the HMC, which is indicative of rotation (this is supported by the fact that this velocity gradient is perpendicular to the hourglass magnetic field shape). To avoid chemical effects that could affect the interpretation, we used only methanol transitions, which is the most populated species within the observed bandwidth. Of these lines, we selected only those with upper excitation energy levels that range from 60 to 1020 K and appear clean of interlopers (Fig. 3). The lower excitation lines (top graphs of Fig. 3) show a relative minimum at redshifted velocities toward the center, which is indicative of infall, as found more clearly in the even lower excitation $C^{34}S$ line. The position-velocity maps reveal a smaller velocity gradient, that is, a smaller rotation velocity, in the more spatially compact lines (typically the higher excitation ones) (Fig. 4). For a collapsing core with angular momentum conservation and with a very weak magnetic field, the rotation velocity is expected to be inversely proportional to the radius (*10*). This is the opposite of what is observed in the HMC, in which the rotation velocity decreases for decreasing radius, indicating that the angular momentum is not conserved during the collapse. Given the hourglass magnetic field morphology in the HMC, this spin-down in the HMC suggests magnetic braking, a process proposed to remove the excess of angular momentum. Theoretical models of magnetic braking predict a spin-down qualitatively in agreement with what is shown in Fig. 4 (*7*, *10*). Depending on the value of the rotation velocity and the magnetic field, the evolution of a collapsing core is regulated either by the centrifugal forces or by the magnetic forces (*29*). If the measured (ω/*B*) value is larger than

$$\left(\frac{\omega_{st}}{B}\right)_{crit} = 1.69 \times 10^{-7} \times \left(\frac{c_s}{0.19 \mathrm{km/s}}\right)^{-1} \mathrm{year}^{-1}\,\mu\mathrm{G}^{-1},$$

where c_s is the sound speed and ω is the angular velocity, the centrifugal forces dominate the dynamics. Otherwise the magnetic forces regulate the dynamics. For c_s=0.93 km s^{-1}, we found that the measured ratio, 6.6×10^{-9} year^{-1} μG^{-1}, is smaller than the critical value, 3.5×10^{-8} year^{-1} μG^{-1}. Thus, the magnetic field dominates energetically (with respect to centrifugal and turbulence forces) the dynamics of the collapse.

The HMC in G31.41 is much larger (by a factor of 20) and more massive (by a factor of 200) and luminous (by five orders of magnitudes) than the Sun-like IRAS 4A. However, both sources show an inverse P-Cygni profile, indicative of

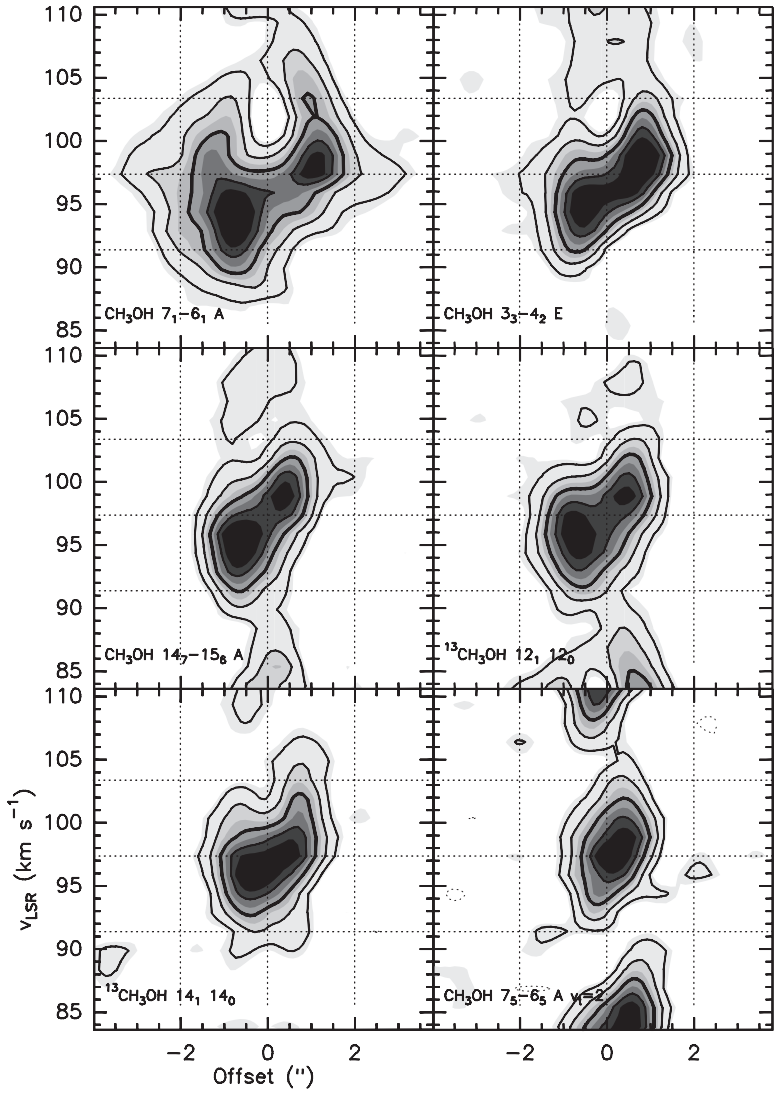

Fig. 3. Position-velocity cuts along a position angle of 65° (close to the major axis of the HMC) for six methanol lines (their transitions are labeled in the lower left part of each graph). The zero offset position is located at the position of the Very Large Array 7-mm source A (*16*). Contour levels are the 15, 30, 50 (thicker contour), 70, and 90% of the peak intensity of each transition. The central horizontal dotted line shows the cloud velocity.

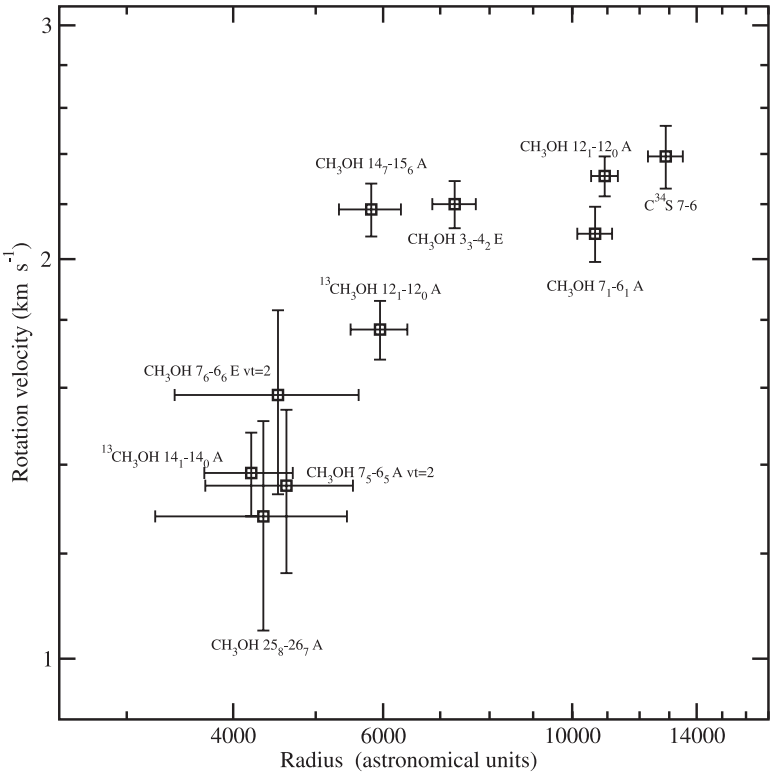

Fig. 4. The distribution of the rotation velocity as a function of the radius. These values were derived from the integrated intensity and the intensity weighted mean velocity maps at the position where the dust major axis intersects the half maximum contour level from the integrated emission (the velocity gradient is observed along the major axis; see Fig. 1).

infall motions (*30*), and have similar magnetic field properties (a hourglass configuration approximately along the major axis and a similar mass-to-flux ratio). The energetic relations do not differ too much, either: Both cores are collapsing because gravity has overcome pressure forces, but the collapsing dynamics are controlled by the magnetic energy rather than by turbulence. This similarity suggests that the role of the magnetic field in the early stages of the formation of high- and low-mass stars may not be too different. However, once the massive stars turn on an ultracompact HII, the feedback from the massive stars (radiation and ionization pressure, turbulence, and outflows) becomes energetically more important than the magnetic fields (*31*).

References and Notes

1. M. G. Wolfire, J. P. Cassinelli, *Astrophys. J.* **319**, 850 (1987).
2. T. Nakano, *Astrophys. J.* **345**, 464 (1989).
3. H. W. Yorke, C. Sonnhalter, *Astrophys. J.* **569**, 846 (2002).
4. M. R. Krumholz, C. F. McKee, R. I. Klein, *Astrophys. J.* **618**, L33 (2005).
5. M. R. Krumholz, R. I. Klein, C. F. McKee, S. S. R. Offner, A. J. Cunningham, *Science* **323**, 754 (2009); published online 15 January 2009 (10.1126/science.1165857).
6. I. A. Bonnell, M. R. Bate, *Mon. Not. R. Astron. Soc.* **362**, 915 (2005).
7. S. Basu, T. Ch. Mouschovias, *Astrophys. J.* **432**, 720 (1994).
8. A. P. Boss, *Astrophys. J.* **658**, 1136 (2007).
9. D. Galli, S. Lizano, F. H. Shu, A. Allen, *Astrophys. J.* **647**, 374 (2006).
10. R. Mellon, Z.-Y. Li, *Astrophys. J.* **681**, 1356 (2008).
11. J. M. Girart, R. Rao, D. P. Marrone, *Science* **313**, 812 (2006).
12. J. Gonçalves, D. Galli, J. M. Girart, *Astron. Astrophys.* **490**, L39 (2008).
13. M. T. Beltrán *et al.*, *Astrophys. J.* **601**, L187 (2004).
14. M. Osorio, G. Anglada, S. Lizano, P. D'Alessio, *Astrophys. J.* **694**, 29 (2009).
15. R. Cesaroni, E. Churchwell, P. Hofner, C. M. Walmsley, S. Kurtz, *Astron. Astrophys.* **288**, 903 (1994).
16. E. Araya, P. Hofner, S. Kurtz, L. Olmi, H. Linz, *Astrophys. J.* **675**, 420 (2008).
17. M. T. Beltrán *et al.*, *Astron. Astrophys.* **435**, 901 (2005).
18. L. Olmi, R. Cesaroni, C. M. Walmsley, *Astron. Astrophys.* **307**, 599 (1996).
19. P. T. P. Ho, J. M. Moran, K. Y. Lo, *Astrophys. J.* **616**, L1 (2004).
20. D. P. Marrone, J. M. Moran, J.-H. Zhao, R. Rao, *Astrophys. J.* **640**, 308 (2006).
21. V. Ossenkopf, T. Henning, *Astron. Astrophys.* **291**, 943 (1994).
22. D. A. Schleuning, *Astrophys. J.* **493**, 811 (1998).
23. S.-P. Lai, R. M. Crutcher, J. M. Girart, R. Rao, *Astrophys. J.* **561**, 864 (2001).
24. P. Cortes, R. M. Crutcher, *Astrophys. J.* **639**, 965 (2006).
25. T. C. Mouschovias, L. Spitzer Jr., *Astrophys. J.* **210**, 326 (1976).
26. M. T. Beltrán *et al.*, *Nature* **443**, 427 (2006).
27. E. R. Keto, P. T. P. Ho, A. D. Haschick, *Astrophys. J.* **318**, 712 (1987).
28. L. A. Zapata *et al.*, *Astron. Astrophys.* **479**, L25 (2008).
29. M. N. Machida, T. Matsumoto, K. Tomisaka, T. Hanawa, *Mon. Not. R. Astron. Soc.* **362**, 369 (2005).
30. J. Di Francesco, P. C. Myers, D. J. Wilner, N. Ohashi, D. Mardones, *Astrophys. J.* **562**, 770 (2001).
31. Y. W. Tang *et al.*, *Astrophys. J.* **695**, 1399 (2009).

32. The Submillimeter Array is a joint project between the Smithsonian Astrophysical Observatory and the Academia Sinica Institute of Astronomy and Astrophysics and is funded by the Smithsonian Institution and the Academia Sinica. We thank D. Galli, R. R. Cesaroni, and J. M. Torrelles for helpful comments. J.M.G., M.T.B., and R.E. acknowledge Ministerio de Ciencia e Innovación (Spain) for support through grants AYA2005-08523-C03 and AYA2008-06189-C03. J.M.G. also acknowledges support from Agència de Gestió d'Ajuts Universitaris i de Recerca 2005-SGR00489 grant.

Supporting Online Material

www.sciencemag.org/cgi/content/full/324/5933/1408/DC1
Fig. S1

3 February 2009; accepted 30 April 2009
10.1126/science.1171807

A Radio Pulsar/X-ray Binary Link

Anne M. Archibald,[1]* Ingrid H. Stairs,[2,3,4] Scott M. Ransom,[5] Victoria M. Kaspi,[1] Vladislav I. Kondratiev,[6,5,7] Duncan R. Lorimer,[6,8] Maura A. McLaughlin,[6,8] Jason Boyles,[6,8] Jason W. T. Hessels,[9,10] Ryan Lynch,[11] Joeri van Leeuwen,[9,10] Mallory S. E. Roberts,[12] Frederick Jenet,[13] David J. Champion,[3] Rachel Rosen,[8] Brad N. Barlow,[14] Bart H. Dunlap,[14] Ronald A. Remillard[15]

Radio pulsars with millisecond spin periods are thought to have been spun up by the transfer of matter and angular momentum from a low-mass companion star during an x-ray–emitting phase. The spin periods of the neutron stars in several such low-mass x-ray binary (LMXB) systems have been shown to be in the millisecond regime, but no radio pulsations have been detected. Here we report on detection and follow-up observations of a nearby radio millisecond pulsar (MSP) in a circular binary orbit with an optically identified companion star. Optical observations indicate that an accretion disk was present in this system within the past decade. Our optical data show no evidence that one exists today, suggesting that the radio MSP has turned on after a recent LMXB phase.

The fastest-spinning radio millisecond pulsars (MSPs) are thought to be formed in systems containing a neutron star (NS) and a low-mass [$\lesssim$1 solar mass ($M_\odot$)] companion star (*1*). Mass transfer occurs when matter overflows the companion's Roche lobe (*2*), forms an accretion disk around the NS, and eventually falls onto its surface, producing bright x-ray emission (*1*, *3*).

Radio emission that would otherwise be produced by a rapidly rotating magnetic NS is thought to be quenched during active accretion by the presence of ionized material within the pulsar's light cylinder. However, at a sufficiently low accretion rate, infalling material may be halted outside the light cylinder by magnetic pressure, presumably allowing the MSP's radio emission to turn on. At this point, the MSP's electromagnetic emission and particle wind should irradiate the disk and companion, driving mass out of the system. This activation as a radio pulsar, a possible

end to the accretion phase, is poorly understood, in part because no radio MSP has yet been observed to turn on in such a system, although there is indirect evidence that this may occur (*4*–*6*).

The radio source FIRST J102347.67+003841.2 (hereafter J1023) appears optically as a star with visual magnitude in the V band ~ 17.5, with a mid-G (solar-type) spectrum and mild 0.198-day orbital variability (*7*) However, in observations from May 2000 to December 2001, J1023 had a blue spectrum with prominent emission lines (*8*, *9*) (absent in quiescence) and exhibited rapid flickering by ~1 magnitude (*8*), This optical behavior is typical of an accretion flow, and the double-peaked nature of the lines (*9*) suggests an accretion disk specifically. This history led to the system's classification as an accreting white dwarf (*8*) or NS (*7*) binary. For a more detailed history, see the supporting online material (SOM). Since 2002, the system has shown no further sign of accretion, and our optical spectroscopic observations of 23 and 25 December 2008 (SOM) confirm the continued absence of emission lines. Thus, J1023 is currently in a quiescent state.

We found PSR J1023+0038, a bright MSP with a spin period of 1.69 ms at a dispersion measure (DM) of 14.33 pc cm^{-3}, as part of a 350-MHz pulsar survey carried out with the Robert C. Byrd Green Bank Telescope (GBT) in 2007 (see SOM for details).

Phase-coherent timing of the radio pulsations at the GBT, the Arecibo Observatory, and Parkes Observatory has allowed high-precision measurements of the binary parameters (Table 1 and SOM). Together with the much smaller position uncertainties implied by the telescope beam sizes of the timing observations, these binary parameters unambiguously place this pulsar in the J1023 system, confirming the prediction of (*7*) that J1023 has a NS primary.

Combining these parameters with optical radial velocity measurements (*7*), we find that the pulsar is a factor of 7.1 ± 0.1 more massive than its companion. The determination of the individual masses depends only on the inclination angle i of the orbital plane from the plane of the sky. The pulsar's Keplerian mass function $(m_c \sin i)^3/(m_p + m_c)^2$ is $1.1 \times 10^{-3}\ M_\odot$, where m_c and m_p are the masses of the companion and the pulsar, respectively. For a NS mass in the range from ~1.0 to ~3.0 $M_\odot$ (*10*), i is restricted to the range from ~53° to ~34°, and the companion mass is restricted to ~0.14 to ~0.42 $M_\odot$.

Stellar models, based on the assumption (reasonable in light of the evidence for a recent accretion flow) that the companion is filling its Roche lobe, show that it is possible for the companion star to exhibit the observed orbital modulation of color, magnitude, and radial velocity if the primary has an isotropic luminosity of ~2 solar luminosities (*7*). These models also imply $i < 55°$, which is compatible with the range obtained from theoretical NS mass limits. Similar models account for the light-curve modulation during quiescence of the low-mass companion to SAX J1808.4−3658 (*6*), an accreting x-ray pulsar in a 2-hour orbit [e.g., (*11*, *12*)], which has been suspected of harboring an MSP when in quiescence (*4*, *5*, *13*).

The brightness, radial velocities, and presumed Roche lobe–filling companion of J1023 imply that the distance to the system is 0.9 kpc/sin i; for the allowed range of i, the distance is between ~1.1 and ~1.6 kpc. A pulsar mass of 1.4 $M_\odot$ implies a distance of 1.3 kpc. For comparison, given the observed DM of 14.325 pc cm^{-3}, the standard Galactic free-electron density model (*14*) predicts a distance of 0.6 kpc, which is consistent with our range, given its known uncertainties.

Ordinarily one can estimate a pulsar's spin-down luminosity from its observed pulsar period derivative ($\dot{P}$), but for MSPs this is subject to contamination by several factors, including accelerations of J1023 and the solar system barycenter in the Galactic gravitational potential. From the measured optical proper motion μ of J1023 (Table 1), we expect a significant positive contribution to $\dot{P} = P d\mu^2/c \simeq 1.8 \times 10^{-21}$ (d/1.3 kpc) due to the Shklovskii effect (*15*) (P, pulsar period; d, distance; μ, proper motion; c, the speed of light). Although in some binary systems the accelerations can be constrained independently with the use of orbital period variations, in J1023 we

Table 1. Pulsar parameters. Parameters listed in the top section are held fixed in the timing fit that produces the parameters listed in the middle section (SOM). The position and proper motion values are from the U.S. Naval Observatory NOMAD optical catalog (*25*). With the exceptions of DM, P, and eccentricity, uncertainties on timing quantities are twice the formal 1σ errors returned by the pulsar timing analysis program. The DM of the source varies substantially: Around orbital phase 0.3, it occasionally increases by ~0.15 pc cm^{-3}, and we observe apparent orbit-to-orbit variations as large as ~0.01 pc cm^{-3}. Our estimate of the eccentricity is approximate because DM variations limit the orbital coverage of usable timing data. Our estimate for $\dot{P}$ is approximate because it is highly covariant with pulsar position; it was estimated by fitting for $\dot{P}$ while varying the position according to the optical uncertainties listed above. We have not subtracted Shklovskii or galactic accelerations. The flux density and spectral index are estimated using standard system temperature and gain values for the GBT and the Parkes telescope. The flux density is subject to substantial variability intrinsic to the pulsar (we have observed brightening by a factor of ~4 within minutes), as well as interstellar scintillation; for this reason, we estimated the spectral index using the simultaneous 600-MHz and 3000-MHz Parkes observations. Spin-down luminosity and magnetic field upper limits are calculated from the 3σ upper limit on $\dot{P}$ using the standard formulas $\dot{E} = 3.95 \times 10^{31}$ erg s^{-1} ($\dot{P}/10^{-15}$) (P/1 s)$^{-3}$ and $B = 3.2 \times 10^{19}$ G $\sqrt{P\dot{P}}$.

Parameter	Value
Right ascension (α; J2000)	10 hours 23 min 47.687(3) s
Declination (δ; J2000)	00°38′41.15(7)″
Proper motion in α (μ_α)	10(1) milli–arc sec year^{-1}
Proper motion in δ (μ_δ)	−16(2) milli–arc sec year^{-1}
Epoch [modified Julian date (MJD)]	54802
Dispersion measure	14.325(10) pc cm^{-3}
Pulsar period (P)	1.6879874440059(4) ms
Pulsar period derivative ($\dot{P}$)	$1.2(8) \times 10^{-20}$
Orbital period (P_b)	0.1980962019(6) days
Orbital period derivative ($\dot{P}_b$)	$2.5(4) \times 10^{-10}$
Orbital period second derivative ($\ddot{P}_b$)	$-5.21(14) \times 10^{-11}$ s^{-1}
Time of ascending node (MJD)	54801.97065348(9)
a sin i	0.3433494(3) light-seconds
Eccentricity	$\lesssim 2 \times 10^{-5}$
1600-MHz flux density	~14 mJy
Spectral index (α; $S \propto \nu^{-\alpha}$)	~ −2.8
Surface magnetic field	$<3 \times 10^8$ G
Spin-down luminosity	$<3 \times 10^{35}$ erg s^{-1}

[1]Department of Physics, McGill University, 3600 Rue University, Montréal, Quebec, H3A 2T8, Canada. [2]Department of Physics and Astronomy, University of British Columbia, 6224 Agricultural Road, Vancouver, British Columbia V6T 1Z1, Canada. [3]Australia Telescope National Facility, Commonwealth Scientific and Industrial Research Organisation (CSIRO), Post Office Box 76, Epping, New South Wales 1710, Australia. [4]Centre for Astrophysics and Supercomputing, Swinburne University of Technology, Mail 39, Post Office Box 218, Hawthorn Vic 3122, Australia. [5]National Radio Astronomy Observatory (NRAO), 520 Edgemont Road, Charlottesville, VA 22901, USA. [6]Department of Physics, West Virginia University, 210 Hodges Hall, Morgantown, WV 26506, USA. [7]Astro Space Center of the Lebedev Physical Institute, Profsoyuznaya 84/32, Moscow 117997, Russia. [8]National Radio Astronomy Observatory, Green Bank, WV 24944, USA. [9]Netherlands Institute for Radio Astronomy, Postbus 2, 7990 AA Dwingeloo, Netherlands. [10]Astronomical Institute Anton Pannekoek, University of Amsterdam, Kruislaan 403, 1098 SJ, Amsterdam, Netherlands. [11]Department of Astronomy, University of Virginia, Charlottesville, VA 22904–4325, USA. [12]Eureka Scientific, 2452 Delmer Street, Suite 100, Oakland, CA 94602-3017, USA. [13]Department of Physics and Astronomy, University of Texas at Brownsville, 80 Fort Brown, Brownsville, TX 78520, USA. [14]Department of Physics and Astronomy, University of North Carolina at Chapel Hill, CB 3255, Phillips Hall, Chapel Hill, NC 27599–3255, USA. [15]Massachusetts Institute of Technology Kavli Institute for Astrophysics and Space Research, 77 Massachusetts Avenue, 37-287, Cambridge, MA 02139, USA.

*To whom correspondence should be addressed. E-mail: aarchiba@physics.mcgill.ca

observe very large orbital period variability (binary period derivative ~3×10^{-10}), almost certainly due to classical tidal torquing from gas motion in the extended envelope of the companion star. The near-zero eccentricity of the pulsar's orbit (Table 1) also suggests that the system has undergone tidal circularization.

This picture of a Roche lobe–filling companion is supported by evidence for the presence of ionized material in the system. Our broadband radio observations reveal substantial DM variations at certain orbital phases (Fig. 1G), as well as smaller DM variations on time scales of minutes throughout the orbit. Moreover, we observe regular eclipses ranging from very brief at 3000 MHz to covering most of the orbit in our 150-MHz observations with the Westerbork Synthesis Radio Telescope (WSRT) (Fig. 1, A to F). We also see very brief eclipses at all orbital phases (Fig. 1E in particular). Given the established range of i, the line of sight between the pulsar and Earth will not intersect the Roche lobe of the companion at any point in the orbit. If we assume that during the DM variations near orbital phase 0.4 (Fig. 1, ii and iii) the obstructing plasma is uniform, has a plasma frequency of 700 MHz (based on the loss of the 700-MHz signal at this phase), and contributes the excess DM of 0.15 pc cm^{-3}, we predict a thickness of 3×10^4 km (thin compared to the companion's size of ~3×10^5 km). This suggests that a thin but dense layer of material, perhaps a shock due to the pulsar wind meeting either winds from the companion or material overflowing the companion's Roche lobe, crosses the line of sight at this orbital phase.

Similar eclipses and DM variations have been seen in the Galactic "black widow" systems: tight NS binary systems in the Galactic field with companions an order of magnitude less massive than that of J1023 (*16*). Such eclipses have also been seen in several radio MSPs in globular clusters (*17*, *18*). In both cases, they have been attributed to the presence of gas flowing out from the irradiated companion, as is probably the case for J1023. However, J1023 differs from all other known radio MSPs in that there is evidence for a recent accretion disk.

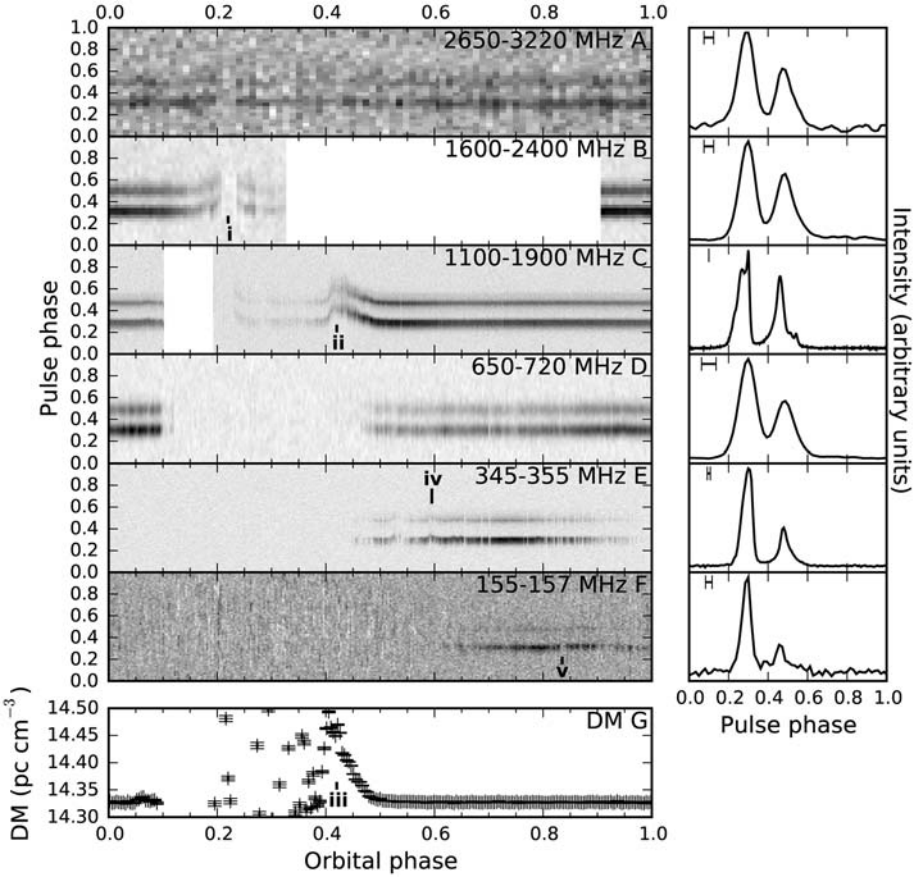

Fig. 1. Frequency dependence of eclipses, DM variations, and pulse profiles. (**A** to **F**) Flux density as a function of pulse phase and orbital phase at 3000, 2000, 1600, 700, 350, and 156 MHz, respectively. (**G**) DM, as estimated from the 1600-MHz observations (SOM). Orbital phase is defined to be zero at the pulsar's ascending node, so that the companion passes closest to our line of sight at orbital phase 0.25. To the right of (A) through (F) are pulse profiles at the respective bands; the instrumental smearing time is indicated with a horizontal bar in each panel except (C), which is instead based on a 1410-MHz observation with higher time resolution. The eclipse is nearly absent at 3000 MHz but is longer at 700 MHz than at 1600 MHz. At low frequencies, random short eclipses, indicated by (iv) and (v), are also visible. Pulse phase is as predicted by a phase-coherent timing solution, so that large short-term timing variations are visible as vertical motions of the pulse peak. Note in particular the pulse arrival time variations at eclipse ingress (i) and egress (ii); the variation at egress appears to be due to the substantial DM variation (iii) visible in (G).

For an accreting NS, the accretion luminosity is proportional to the accretion rate, which is unknown for J1023. But if the matter is to reach the NS surface, it must overcome magnetic pressure at the Keplerian corotation radius, so there is a minimum accretion rate and hence a minimum luminosity for a given NS magnetic field (*19*). For a magnetic field equal to our timing-derived upper limit (Table 1), this minimum luminosity for J1023 is 1.1×10^{37} erg s^{-1} [using formulas from (*19*)]. Such a high luminosity can be clearly ruled out by our analysis of archival Rossi X-ray Timing Explorer all-sky monitor data (SOM): The average annual x-ray luminosity for each year from 1996 to 2008 was less than 4.8×10^{33} erg s^{-1} (d/1.3 kpc)^2. The variable nature of low-mass x-ray binary (LMXB) x-ray emission cannot explain this low luminosity: On 1 February 2001, when an optical emission line spectrum was observed (*9*), the average flux was less than 2.4×10^{34} erg s^{-1} (d/1.3 kpc)^2. If accretion occurred during the active phase, the annual upper limit would imply that the magnetic field of the NS in J1023 was less than 6×10^6 G, smaller than that of any known MSP.

It therefore seems more likely that infalling matter did not reach the NS surface, but instead underwent what is known as "propeller-mode accretion" (*20*): Infalling matter entered the light cylinder but was stopped by magnetic pressure outside the corotation radius, which prevented it from falling further inward. This process also has a minimum accretion rate and minimum luminosity: If the infalling matter does not reach the light cylinder, the radio pulsar mechanism will presumably become active. If this occurs, no stable balance exists between outward radiation and the wind pressure and ram pressure of infalling material, and the disk will be cleared from the system (*19*). The minimum luminosity for propeller-mode accretion is substantially lower than that for standard accretion; our timing-derived upper limit on the magnetic field (Table 1) implies a minimum luminosity of just 2.7×10^{32} erg s^{-1} [using formulas from (*19*)]. Thus, it seems likely that during J1023's active phase, the mass transfer rate was high enough for propeller-mode accretion but not high enough for material to reach the NS surface.

In this scenario, a small drop in the mass transfer rate would clear the disk from the system and return J1023 to its current quiescent state. Overflowing matter from the companion would then encounter a shock near the inner Lagrange point and be carried out of the system (*19*), possibly explaining the observed variable hard power-law x-ray spectrum of J1023 (*21*) and the presence of gas in the system. Such shocks have been suggested to explain the variable power-law x-ray emission in 47 Tuc W (*22*) and PSR J1740−5340 in NGC 6397 (*23*), which also have low-mass companions and have previously been compared with SAX J1808.4−3658, though with no evidence for the recent presence of an accretion disk.

Despite the apparent resemblance of J1023 to 47 Tuc W and PSR J1740−5340, the latter two systems (and indeed all other currently known eclipsing pulsars with companions of several-tenths $M_\odot$) reside in globular clusters and are likely to have acquired their current companions in exchange interactions after the pulsars were "recycled" (*24*). J1023 is the only known highly recycled (the fifth fastest known) MSP in the field of the Galaxy with both a nondegenerate companion and an orbit that has been circularized through tidal interactions. A globular cluster origin for J1023 is extremely unlikely because of its large distance from the nearest globular cluster as well as from the Galactic bulge. The evidence points to J1023's having been recycled by its current companion, which has not yet completed the transformation to a white dwarf.

The observed transition of J1023 suggests that it is in a bistable state: For certain rates of Roche lobe overflow, if the radio pulsar mechanism is quenched, propeller-mode accretion can occur, but if the radio pulsar mechanism is active, that same mass accretion rate cannot overcome the radiation pressure and no accretion occurs. Should the mass transfer rate of J1023 rise sufficiently, then it may enter another LMXB phase: A disk will form, the radio emission may be quenched, and the x-ray luminosity may increase dramatically, due to either propeller-mode accretion, with a net spin-down of the pulsar, or even brighter accretion onto the surface, with a net spin-up.

References and Notes

1. D. Bhattacharya, E. P. J. van den Heuvel, *Phys. Rep.* **203**, 1 (1991).
2. In a circular binary system, a star's Roche lobe is that volume in which matter corotating with the system is gravitationally bound to that star.
3. T. M. Tauris, E. P. J. van den Heuvel, *Formation and Evolution of Compact Stellar X-ray Sources* (Cambridge Univ. Press, Cambridge, 2006), pp. 623–665.
4. L. Burderi, T. Di Salvo, F. D'Antona, N. R. Robba, V. Testa, *Astron. Astrophys.* **404**, L43 (2003).
5. J. M. Hartman *et al*., *Astrophys. J.* **675**, 1468 (2008).
6. C. J. Deloye, C. O. Heinke, R. E. Taam, P. G. Jonker, *Mon. Not. R. Astron. Soc.* **391**, 1619 (2008).
7. J. R. Thorstensen, E. Armstrong, *Astron. J.* **130**, 759 (2005).
8. H. E. Bond, R. L. White, R. H. Becker, M. S. O'Brien, *Proc. Astron. Soc. Pac.* **114**, 1359 (2002).
9. P. Szkody *et al*., *Astron. J.* **126**, 1499 (2003).
10. J. M. Lattimer, M. Prakash, *Science* **304**, 536 (2004).
11. R. Wijnands, M. van der Klis, *Nature* **394**, 344 (1998).
12. D. Chakrabarty, E. H. Morgan, *Nature* **394**, 346 (1998).
13. C. O. Heinke, P. G. Jonker, R. Wijnands, C. J. Deloye, R. E. Taam, *Astrophys. J.* **691**, 1035 (2009).
14. J. M. Cordes, T. J. W. Lazio, preprint available at http://arxiv.org/abs/astro-ph/0207156 (2002).
15. I. S. Shklovskii, *Sov. Astron.* **13**, 562 (1970).
16. A. S. Fruchter, J. E. Gunn, T. R. Lauer, A. Dressler, *Nature* **334**, 686 (1988).
17. N. D'Amico *et al*., *Astrophys. J.* **561**, L89 (2001).
18. B. W. Stappers *et al*., *Astrophys. J.* **465**, L119 (1996).
19. S. Campana, M. Colpi, S. Mereghetti, L. Stella, M. Tavani, *Astron. Astrophys. Rev.* **8**, 279 (1998).
20. A. F. Illarionov, R. A. Sunyaev, *Astron. Astrophys.* **39**, 185 (1975).
21. L. Homer *et al*., *Astron. J.* **131**, 562 (2006).
22. S. Bogdanov, J. E. Grindlay, M. van den Berg, *Astrophys. J.* **630**, 1029 (2005).
23. J. E. Grindlay *et al*., *Astrophys. J.* **581**, 470 (2002).
24. F. Camilo, F. A. Rasio, in *Binary Radio Pulsars*, vol. 328 of *Astronomical Society of the Pacific Conference Series*, F. A. Rasio, I. H. Stairs, Eds. (Astronomical Society of the Pacific, San Francisco, 2005), pp. 147–170.
25. N. Zacharias *et al*., *Bull. Am. Astron. Soc.* **36**, 1418 (2004).

26. We thank J. Condon of the NRAO for pointing out that J1023 lay within our survey beam; B. Stappers for help with WSRT observations and analysis; and S. Bogdanov, J. Thorstensen, and Z. Wang for useful discussions. The Robert C. Byrd GBT is operated by the NRAO, which is a facility of the U.S. NSF operated under cooperative agreement by Associated Universities, Inc. The Arecibo Observatory is part of the National Astronomy and Ionosphere Center, which is operated by Cornell University under a cooperative agreement with NSF. The Parkes Observatory radio telescope is part of the Australia Telescope, which is funded by the Commonwealth of Australia for operation as a National Facility managed by CSIRO. The WSRT is operated by the Netherlands Institute for Radio Astronomy, with support from the Netherlands Foundation for Scientific Research (NWO). We thank the directors of all four facilities for their generous allocation of exploratory time to this project. ASP and GASP are collaborations funded by the Natural Sciences and Engineering Research Council of Canada (NSERC) and NSF; I.H.S. and J.v.L. thank their co-developers D. Backer, D. Nice, P. Demorest, R. Ferdman, I. Cognard, and R. Ramachandran for their hardware and/or software contributions, and P. Demorest and W. van Straten for making the PSRCHIVE software compatible with ASP/GASP data. We further thank M. Bailes, S. Kulkarni, and the others in the Caltech–Green-Bank–Swinburne-Recorder collaboration for the use of some of their computer nodes during GASP observations. J.R.B., V.I.K., D.R.L., and M.A.M. are supported by a West Virginia Experimental Program to Stimulate Competitive Research (EPSCoR) Research Challenge Grant. M.A.M. is an Alfred P. Sloan fellow. J.W.T.H. is an NWO Veni Fellow. V.M.K. is supported via the Lorne Trottier Chair in Astrophysics and Cosmology, the Canada Research Chair program, an NSERC Discovery Grant, the Fonds Québécois de la Recherche sur la Nature et les Technologies, the Canadian Institute for Advanced Research, and the Canada Foundation for Innovation (CFI). I.H.S. received support from NSERC, the CFI, the Australia Telescope National Facility Distinguished Visitor program, and the Swinburne University of Technology Visiting Distinguished Researcher Scheme.

Supporting Online Material

www.sciencemag.org/cgi/content/full/1172740/DC1
SOM Text
Fig. S1
Tables S1 and S2
References

25 February 2009; accepted 12 May 2009
Published online 21 May 2009;
10.1126/science.1172740
Include this information when citing this paper.

Determining the Dynamics of Entanglement

O. Jiménez Farías,[1,2] C. Lombard Latune,[1,3] S. P. Walborn,[1] L. Davidovich,[1] P. H. Souto Ribeiro[1]*

The estimation of the entanglement of multipartite systems undergoing decoherence is important for assessing the robustness of quantum information processes. It usually requires access to the final state and its full reconstruction through quantum tomography. General dynamical laws may simplify this task. We found that when one of the parties of an initially entangled two-qubit system is subject to a noisy channel, a single universal curve describes the dynamics of entanglement for both pure and mixed states, including those for which entanglement suddenly disappears. Our result, which is experimentally demonstrated using a linear optics setup, leads to a direct and efficient determination of entanglement through the knowledge of the initial state and single-party process tomography alone, foregoing the need to reconstruct the final state.

The environment-induced dynamics of entanglement presents surprising features and challenging problems. For instance, when the parts of an entangled system interact with independent environments, entanglement may disappear at a finite time, before coherence decays (*1*–*7*). Understanding the dynamics and how it scales with the size of the system is of central relevance to quantum computing and quantum communication (*8*–*10*), as the viability of complex quantum information tasks involving many qubits (quantum bits) is intimately related to the robustness of entanglement. However, its assessment is still an open problem, especially for multipartite systems. Even for the simplest entangled systems, composed of just two qubits, subtle dynamical features have been revealed (*1*, *3*, *5*–*7*). Therefore, uncovering basic dynamical laws is an appealing task that might shed some light on entanglement and the feasibility of its applications.

The marked differences between the dynamics of entanglement and the individual evolution of the components of a physical system are consequences of the nonlinear dependence of entanglement measures on the state of the system. The concurrence, for instance, introduced as a quantifier of entanglement (*11*), is given for a two-qubit system described by the density matrix ρ_{12} by $C = \max\{0,\Lambda\}$, where $\Lambda = \sqrt{\lambda_1} - \sqrt{\lambda_2} - \sqrt{\lambda_3} - \sqrt{\lambda_4}$. The quantities λ_i are the positive eigenvalues of the matrix $\rho_{12}(\sigma_{y1}\otimes\sigma_{y2})\,\rho^*_{12}\rho(\sigma_{y1}\otimes\sigma_{y2})$ in decreasing order, where σ_{yi} is the second Pauli matrix corresponding to qubit i and the conjugation occurs in the computational basis $\{|00\rangle, |01\rangle, |10\rangle, |11\rangle\}$. The symbol $\otimes$ stands for the direct product of operators corre-

[1]Instituto de Física, Universidade Federal do Rio de Janeiro, Caixa Postal 68528, Rio de Janeiro RJ 21941-972, Brazil. [2]Instituto de Ciencias Nucleares, Universidad Nacional Autónoma de México (UNAM), Apdo. Postal 70-543, México 04510 D.F. [3]École Normale Supérieure, 24 rue Lhomond, 75005 Paris, France.

*To whom correspondence should be addressed. E-mail: phsr@if.ufrj.br

sponding to different qubits. C takes values between 0 (separable states) and 1 (maximal entanglement). The calculation of entanglement through this procedure requires knowledge of the density matrix that characterizes the system. The dynamics of entanglement is thus usually obtained from the evolved state, reconstructed through quantum tomography or calculated by considering the interaction between the entangled system and the environment, which can be represented by a "quantum channel" $ that transforms the initial density matrix ρ into $(ρ).

An alternative to these tomographic procedures that does not require the determination of the final state was recently derived (*12*). When one of the parts of an initially pure bipartite system interacts with a noisy environment, the evolution of entanglement can be simply described by the product of two factors that depend on the environment and the initial state, respectively. Explicitly, when a quantum channel $ acts on only one qubit of a two-qubit state described by the density matrix ρ, the concurrence satisfies

$$C[(\mathrm{I}\otimes\$)\rho] \le C[(\mathrm{I}\otimes\$)|\varphi_+\rangle\langle\varphi_+|]C(\rho) \quad (1)$$

where $|\varphi_+\rangle$ is the Bell state $(|00\rangle + |11\rangle)/\sqrt{2}$. The quantity $C[(\mathrm{I}\otimes\$)|\varphi_+\rangle\langle\varphi_+|]$ is the concurrence of the state that evolves from $|\varphi_+\rangle$ when channel $ acts on the second qubit, and $C(\rho)$ is the concurrence of the initial state. The equality in Eq. 1 is valid for pure initial states. In this case, knowledge of the initial concurrence plus the characterization of the environment through its action on the state $|\varphi_+\rangle$ are enough to determine the final concurrence. If the initial state is mixed, Eq. 1 provides an upper bound for the final entanglement.

The experimental demonstration of the above equality requires (i) the production of quasi-pure quantum states, and (ii) a precise control of the quantum channel, which should act on only one of the two qubits. Both conditions are fulfilled in the experiment reported here, which leads to a clear-cut demonstration of Eq. 1. Furthermore, we show that the factorization relation in Eq. 1 can be used to estimate the entanglement of the final state through single-qubit channel tomography, which is faster and more accurate than the full reconstruction of the final state. In addition, we propose and demonstrate experimentally an extended version of the factorization relation in Eq. 1, in which the equality also applies to mixed states. We show that a universal curve describes the evolution of entanglement for arbitrary initial states.

The evolution of a density matrix under the action of a quantum channel $ can be written as $(ρ) = $\sum_i K_i \rho K_i^\dagger$, where K_i are the Kraus operators (*8*). For a qubit, there can be at most four independent Kraus operators, which can be written as linear combinations of the identity and the Pauli matrices. The possible actions of the environment can then be reduced to a finite number of typical quantum channels. The set of Kraus operators completely characterizes the quantum channel. They can be obtained from the unitary evolution of the system plus environment by tracing out the environment degrees of freedom.

A paradigmatic example of a quantum channel is the amplitude channel:

$$|0\rangle_S|0\rangle_E \rightarrow |0\rangle_S|0\rangle_E$$

$$|1\rangle_S|0\rangle_E \rightarrow \sqrt{1-p}|1\rangle_S|0\rangle_E + \sqrt{p}|0\rangle_S|1\rangle_E \quad (2)$$

where the subindex S denotes states of the system and the subindex E those of the environment. This equation describes, for instance, the spontaneous decay of a two-level atom interacting with a zero-temperature environment (no initial excitation in the environment). If the atom is initially in the ground state, the global state does not evolve. If the atom is excited, it has a probability p of decaying and exciting the environment. Complete decay corresponds to $p = 1$. With $p = 1 - \exp(-\Gamma t)$, where Γ is the excited-state decay rate, Eq. 2 is essentially the one derived by Weisskopf and Wigner in 1930 (*13*). The corresponding Kraus operators can be calculated directly from Eq. 2. We have, in this case,

$$K_1 = \begin{pmatrix} 1 & 0 \\ 0 & \sqrt{1-p} \end{pmatrix}, K_2 = \begin{pmatrix} 0 & \sqrt{p} \\ 0 & 0 \end{pmatrix},$$
$$K_3 = K_4 = \hat{0} \quad (3)$$

In our experiment, the amplitude decay channel displayed in Eq. 2 is implemented by the modified Sagnac interferometer in Fig. 1. The operation of the interferometer as a quantum channel is described in detail in (*1*, *3*). The system states $|0\rangle_S$ and $|1\rangle_S$ correspond respectively to the horizontal (H) and the vertical (V) polarizations of a photon; the environment states correspond to different propagation modes. A single input photon is split into H and V polarization components at the polarizing beam splitter (PBS) of the Sagnac interferometer. This amounts to coupling the photon momentum and polarization degrees of freedom, as different polarizations travel in different directions after the PBS. The H component remains untouched after propagation through the half-wave plate HWP(0) inside the interferometer, while the V component propagates through a half-wave plate HWP(θ_V) that can change the polarization state. HWP(0) is used only as a path length compensator, but, depending on the setting of the HWP(θ_V), the V component is rotated. The two paths are recombined at another point of the same polarizing beam splitter. When $\theta_V = 0$, the polarization state of the field at the output in mode 0 of Fig. 1 is essentially the same as at the input. However, if $\theta_V \neq 0$, part of the V component will rotate to H and leak to mode 1. The probability that an initially V-polarized photon is flipped to H and leaks to mode 1 is $p = \sin^2 \theta_V$. This implements the quantum channel given by Eq. 2. Modes 0 and 1 are then incoherently recombined using a HWP and a PBS and sent to detection, in order to implement the experimental equivalent of performing the partial trace over the environment degrees of freedom. The final polarization state is analyzed with quantum tomography. This procedure is repeated for several values of $p = \sin^2 \theta_V$.

The initial entangled bipartite state is produced in the polarization degrees of freedom of two photons generated by spontaneous parametric down-conversion (*14*, *15*). Quantum state tomography is performed, through an arrangement of

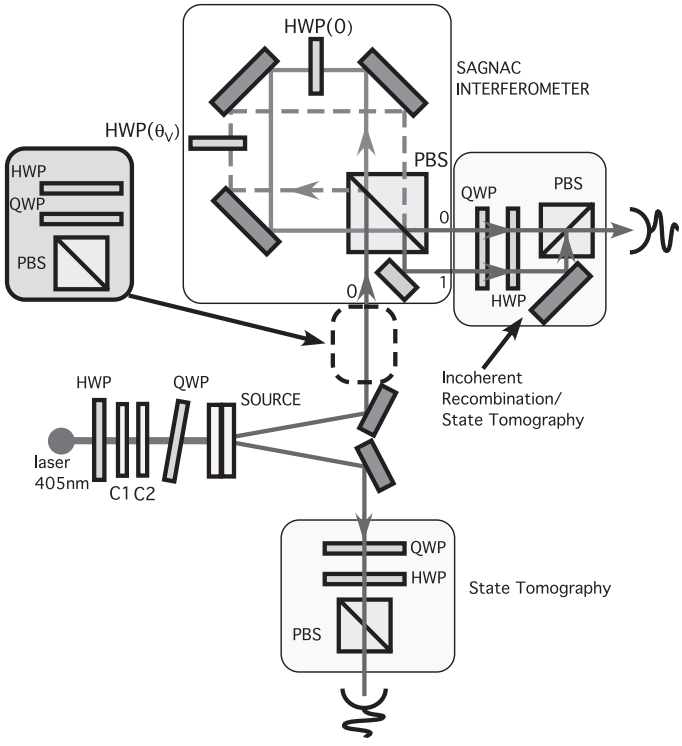

Fig. 1. Experimental setup. The elements in the gray box to the left are inserted when quantum process tomography is performed (*15*).

wave plates and PBSs (*16*), in order to characterize the initial state.

For each setting of p, we perform quantum process tomography (QPT) to experimentally characterize the quantum channel (*15*). This leads to the reconstruction of the corresponding Kraus operators (*8*, *17*). Figure 2 shows the Kraus operators K_i (i = 1, ..., 4) reconstructed from QPT measurements for different values of p. One can see that the matrix elements closely follow those in Eq. 3, implying that our setup leads to a very good implementation of the amplitude channel. The characterization of the quantum channel through QPT allows the calculation of the first factor on the right side of Eq. 1. The concurrence obtained from quantum state tomography of the final state is then compared with the one given by the factorization relation.

We study two quite different types of entanglement dynamics, corresponding to an initial quasi-pure state (for which entanglement vanishes only when $p = 1$) and to an initial highly mixed state (which leads to the vanishing of entanglement for $p < 1$). The quasi-pure state is close to $|\psi\rangle = \alpha|HH\rangle + \beta|VV\rangle$ with $\alpha \approx 0.46$, $\beta \approx 0.88$, and concurrence $C \approx 0.69$. This choice provides a more interesting scenario than a maximally entangled state, for which Eq. 1 is trivially satisfied. Mixed states are produced by letting the photon that does not interact with the environment pass through another Sagnac interferometer similar to the one in Fig. 1. The results (Fig. 3) correspond to the quasi-pure and the highly mixed state. The measured concurrence of the final state $C[(I\otimes\$)\rho]$ is plotted versus the product $C(I\otimes\$|\phi_+\rangle\langle\phi_+|)C[\rho]$, where $C[\rho]$ is the measured concurrence of the initial state and $C(I\otimes\$|\phi_+\rangle\langle\phi_+|)$ is obtained from the reconstruction of the channel through QPT. The different points correspond to several values of $p = \sin^2\theta_V$, which increase in the direction of the origin ($p = 1$ corresponds to the origin in Fig. 3 where the final state becomes completely separable). Error bars were obtained from Monte Carlo simulations of experimental runs (*18*). Ideally, the circles indicating the quasi-pure state should stand on a linear function with a unit slope (dashed line). The linear fit of the circles has a slope of 0.87 (solid line). The slope is not exactly equal to 1 because the initial state is not perfectly pure. Mixed states lead to the inequality in Eq. 1. This is clearly demonstrated by the squares in Fig. 3, which correspond to an initial mixed state with initial concurrence $C = 0.5$ and purity 0.53. Because in Fig. 3 the parameter p of the signal interferometer increases in the direction of the origin, we note that this state leads to "sudden death" of the entanglement (*1*); that is, the concurrence vanishes for $p < 1$.

The characterization of the channel through QPT is made with local measurements, which are generally less demanding than the two-qubit measurements involved in bipartite quantum state tomography. Furthermore, in most real-world situations, the signal-to-noise ratio is much better for the initial state than for the final state because of unavoidable losses in the evolution process. Therefore, as compared to the full reconstruction of the bipartite state, our method provides for a more efficient determination of the final entanglement.

Our setup can be easily adjusted to implement a wide variety of channels (*3*), allowing, in all cases, the characterization of the channel through QPT. In fact, this setup allows for a textbook demonstration of quantum channels (*1*, *3*). The dashed line in Fig. 3 represents the equality in Eq. 1 and is therefore the same for all kinds of quantum channels, providing the final concurrence for initially pure states and an upper bound for initial mixed states.

It is possible, however, to extend Eq. 1 so as to always obtain the actual value of the final concurrence, irrespective of the purity of the initial state. The final concurrence is also obtained, in this generalized version, from the knowledge of the initial state and the characterization of the channel.

The basis of this result is the duality between channels and bipartite states, which implies (*19*, *20*) that there always exists a one-qubit channel $\$'$ such that any bipartite density matrix ρ can be written as $\rho = (I\otimes\$')\sigma$, where σ is a pure-state density matrix determined in the following way. The reduced density matrix corresponding to qubit 1, $\rho_1 = Tr_2(\rho)$, is written in terms of its diagonalizing basis, $\rho_1 = \sum_{i=1}^{2} r_i|e_i\rangle\langle e_i|$. One then defines a pure state that yields the same reduced density matrix as the original state: $|\Psi\rangle = \sum_{i=1}^{2}\sqrt{r_i}|e_i\rangle\otimes|f_i\rangle$. Then $\sigma = |\Psi\rangle\langle\Psi|$. Replacing

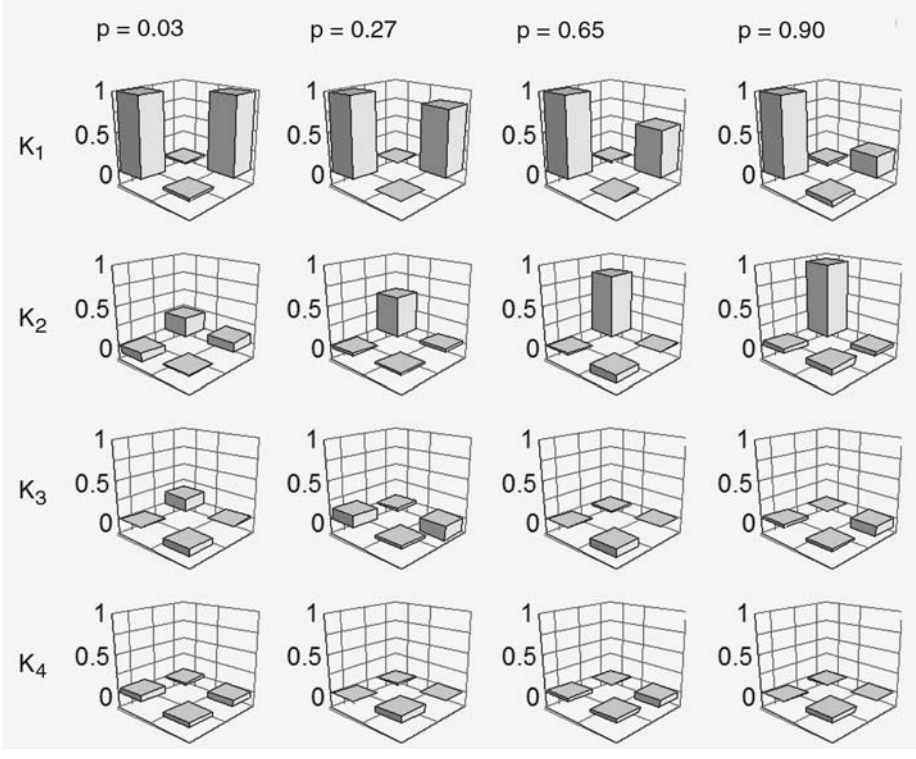

Fig. 2. Experimental Kraus operators for several values of p. Average fidelity with respect to the ideal amplitude channel given by Eq. 2 is 0.95.

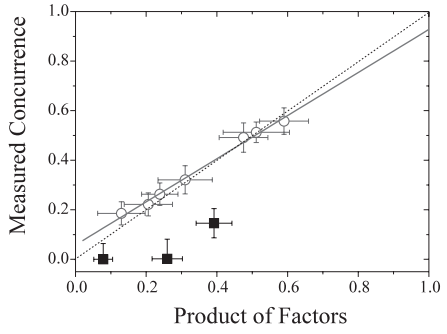

Fig. 3. Comparison between measured concurrence and the product of factors on the right side of Eq. 1. The circles and squares correspond respectively to quasi-pure and mixed initial states. The dashed line is a linear function with unit slope and the solid line is a linear fit to the circles, with slope of ~0.87.

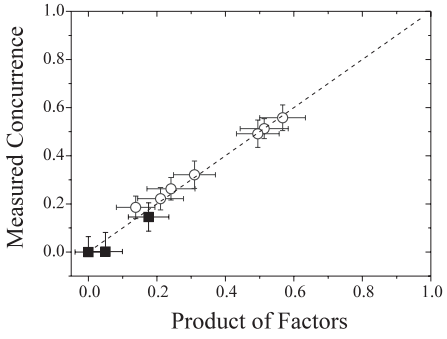

Fig. 4. Comparison between measured concurrence and the product of factors on the right side of Eq. 5. The circles and squares correspond to those displayed in Fig. 3. The dashed line is a linear function with unit slope. A linear fit to the set of all data points results in a slope of ~0.97.

this into $\rho = (I\otimes\$')\sigma$, the channel $\$'$ should satisfy the equation $\rho_1 = \sum_{i,j}\sqrt{r_i r_j}|e_i\rangle\langle e_j|\otimes\$'(|f_i\rangle\langle f_j|)$, which determines the matrix elements (indexed by a, b) of the channel $\$'$:

$$[\$'(|f_i\rangle\langle f_j|)]_{ab} = (r_i r_j)^{-1/2}\langle f_a|\langle e_i|\rho|e_j\rangle|f_b\rangle \quad (4)$$

Because $C[(I\otimes\$)\rho] = C[(I\otimes\$)(I\otimes\$')\sigma]$, and σ is a pure state, it follows from Eq. 1 that

$$C[(I\otimes\$)\rho] = C[(I\otimes\$\$')|\varphi_+\rangle\langle\varphi_+|]C(\sigma) \quad (5)$$

This is the extended version of the equality in Eq. 1. It shows that even if the input state is mixed, the final concurrence is given by the product of two factors. The first factor is the concurrence of an initial Bell state evolving under the action of the product of two channels, $\$\$'$, acting on the second qubit, and the second factor is the concurrence of a pure state, $C(\sigma)$. Both the channel $\$'$ and $C(\sigma) = 2\sqrt{r_1 r_2}$ are obtained from the initial mixed state.

Figure 4 compares the concurrence obtained from the tomography of the final state with the product on the right side of Eq. 5, both for the quasi-pure and the mixed states considered before. The channel $\$'$ and $C(\sigma)$ are determined from the initial state, using the procedure described above. All the points are very close to the dashed line with unit slope, which is now a universal curve for both pure and mixed states. Therefore, the benefit of obtaining the final concurrence from single-qubit QPT and the knowledge of the initial state, rather than the costlier final-state tomography, is now extended to initial mixed states.

References and Notes

1. M. P. Almeida *et al.*, *Science* **316**, 579 (2007).
2. L. Aolita, R. Chaves, D. Cavalcanti, A. Acín, L. Davidovich, *Phys. Rev. Lett.* **100**, 080501 (2008).
3. A. Salles *et al.*, *Phys. Rev. A* **78**, 022322 (2008).
4. C. Simon, J. Kempe, *Phys. Rev. A* **65**, 052327 (2002).
5. T. Yu, J. H. Eberly, *Phys. Rev. Lett.* **93**, 140404 (2004).
6. M. F. Santos, P. Milman, L. Davidovich, N. Zagury, *Phys. Rev. A* **73**, 040305(R) (2006).
7. T. Yu, J. H. Eberly, *Science* **323**, 598 (2009).
8. M. A. Nielsen, I. Chuang, *Quantum Computation and Quantum Information* (Cambridge Univ. Press, Cambridge, 2000).
9. E. Knill, R. Laflamme, G. J. Milburn, *Nature* **409**, 46 (2001).
10. P. Walther *et al.*, *Nature* **434**, 169 (2005).
11. W. K. Wootters, *Phys. Rev. Lett.* **80**, 2245 (1998).
12. T. Konrad *et al.*, *Nat. Phys.* **4**, 99 (2008).
13. V. Weisskopf, E. Wigner, *Z. Phys.* **63**, 54 (1930).
14. P. G. Kwiat, E. Waks, A. G. White, I. Applebaum, P. H. Eberhard, *Phys. Rev. A* **60**, R773 (1999).
15. See supporting material on *Science* Online.
16. D. V. James, P. G. Kwiat, W. J. Munro, A. G. White, *Phys. Rev. A* **64**, 052312 (2001).
17. J. B. Altepeter *et al.*, *Phys. Rev. Lett.* **90**, 193601 (2003).
18. J. B. Altepeter, E. R. Jeffrey, P. G. Kwiat, *Adv. At. Mol. Opt. Phys.* **52**, 107 (2005).
19. A. Jamiołkowski, *Rep. Math. Phys.* **3**, 275 (1972).
20. R. F. Werner, in *Quantum Information—An Introduction to Basic Theoretical Concepts and Experiments*, G. Alber *et al.*, Eds. (Springer, Berlin, 2002), pp. 14–57.

21. We thank A. Buchleitner, M. Hor-Meyll, F. de Melo, and M. Tiersch for helpful discussions. Supported by a graduate fellowship from Consejo Nacional de Ciencia y Tecnología and Instituto de Ciencias Nucleares–UNAM (O.J.F.) and by the Brazilian funding agencies CNPq, CAPES, PRONEX, FUJB, and FAPERJ. This work was performed as part of the Brazilian National Institute of Science and Technology for Quantum Information.

Supporting Online Material

www.sciencemag.org/cgi/content/full/1171544/DC1
SOM Text
References

28 January 2009; accepted 16 April 2009
Published online 14 May 2009;
10.1126/science.1171544
Include this information when citing this paper.

Colloidal Nanocrystals with Molecular Metal Chalcogenide Surface Ligands

Maksym V. Kovalenko,[1] Marcus Scheele,[2] Dmitri V. Talapin[1,3]*

Similar to the way that atoms bond to form molecules and crystalline structures, colloidal nanocrystals can be combined together to form larger assemblies. The properties of these structures are determined by the properties of individual nanocrystals and by their interactions. The insulating nature of organic ligands typically used in nanocrystal synthesis results in very poor interparticle coupling. We found that various molecular metal chalcogenide complexes can serve as convenient ligands for colloidal nanocrystals and nanowires. These ligands can be converted into semiconducting phases upon gentle heat treatment, generating inorganic nanocrystal solids. The utility of the inorganic ligands is demonstrated for model systems, including highly conductive arrays of gold nanocrystals capped with $Sn_2S_6^{4-}$ ions and field-effect transistors on cadmium selenide nanocrystals.

Inorganic colloidal nanocrystals (NCs) with precisely controlled compositions and morphologies have shown useful physical and chemical properties (*1*) and have found applications in light-emitting devices (*2*), photodetectors (*3*), solar cells (*4*), and other devices. Despite progress in NC synthesis, fabrication of competitive solid-state devices from solution-processed colloidal building blocks remains challenging. In a NC solid, where each individual NC carries size-dependent properties of the respective metal, semiconductor, or magnet, the transport of charges is dominated by the interparticle medium. The most successful synthetic methodologies developed for colloidal nanomaterials use surface ligands to stabilize the particles with long (C_8 to C_{18}) hydrocarbon chains (*5*) or bulky organometallic molecules (*6*). These large molecules create highly insulating barriers around each NC. Complete removal of surface ligands has proven to be difficult and can create surface dangling bonds and charge-trapping centers (*7*). In a few successful examples, ligand exchange by mild chemical treatment of PbSe NC films with dilute hydrazine solutions (*8*, *9*) or by linking CdSe NCs with 1,4-phenylenediamine (*10*) yielded conductive NC solids with carrier mobilities comparable to those of solution-processed organic semiconductors. At the same time, dynamic changes of volatile, easily oxidizable small linking molecules impart instabilities in the electronic properties of conductive NC solids.

It would be beneficial to design surface ligands for colloidal nanostructures that (i) adhere to the NC surface and provide colloidal stabilization, (ii) provide stable and facile electronic communication between the NCs, and (iii) constructively supplement the properties of the NC solid. We propose a generalized approach that is compatible with existing methodology for NC synthesis and is based on exchange of the original organic ligands with molecular metal chalcogenide complexes (MCCs). MCCs provide colloidal stabilization of various nanostructures while enabling strong electronic coupling in the NC solids.

Some molecular MCCs are known as precursors for mesoporous metal chalcogenides (*11*–*13*) and semiconducting films with high carrier mobility (*14*, *15*). Many MCCs can be synthesized by dissolution of bulk main group or transition metal chalcogenides in hydrazine (*14*). Excess chalcogen is usually added to form soluble anionic species such as $Sn_2S_6^{4-}$ (*14*) with hydrazinium ($N_2H_5^+$) as the counterion. Various structures including covalent $(N_2H_4)_2ZnTe$ (*16*), layered $N_4H_9Cu_7S_4$ (*17*), and mixed-metal $(N_2H_4)_5SnS_4Mn_2$ (*18*) are accessible by this approach. Hydrazine-stabilized MCCs, whose exact molecular structure in soluble form has yet to be identified, can be prepared for many other metal chalcogenides including Ga_2Se_3, Sb_2Se_3, Sb_2Te_3, $CuInSe_2$, $CuIn_xGa_{1-x}Se_2$, and HgSe (*19*).

To prepare MCC-capped NCs (Fig. 1A), we developed a simple ligand-exchange procedure based on phase transfer of NCs from a nonpolar organic medium into a polar solvent such as hydrazine or dimethyl sulfoxide (DMSO) (*19*). Typically, a solution of MCC in anhydrous hydrazine (~1 to 5 μmol/ml) was stirred with NCs dissolved in hexane (1 to 20 mg/ml) until the organic phase turned colorless and a stable colloidal solution of NCs in hydrazine was formed. The ligand-

[1]Department of Chemistry, University of Chicago, Chicago, IL 60637, USA. [2]Molecular Foundry, Lawrence Berkeley National Laboratory, Berkeley, CA 94720, USA. [3]Center for Nanoscale Materials, Argonne National Laboratory, Argonne, IL 60439, USA.

*To whom correspondence should be addressed. E-mail: dvtalapin@uchicago.edu

exchange process was greatly facilitated by the nucleophilic nature of MCCs, the electrophilicity of undercoordinated metal atoms at the NC surface, and the ability of hydrazine to efficiently strip off the hydrocarbon ligands (*8*). Infrared (IR) spectroscopy, elemental analysis, and nuclear magnetic resonance spectroscopy revealed the absence of hydrocarbon species in MCC-capped NCs, suggesting complete exchange of original ligands during the phase transfer (*19*). The generality of this approach is illustrated by capping 3.6-nm CdSe NCs with various MCCs (Fig. 1B) as well as by combining a given MCC ligand, $Sn_2S_6^{4-}$, with various NCs (Fig. 1C). Notably, nanomaterials of virtually any shape (dots, rods, tetrapods, nanowires) and size (from dots 1.5 nm in diameter to wires 25 nm in diameter and 5 μm in length) could be solubilized by MCCs to form stable colloidal solutions. Below we report characteristic features of MCC-capped NCs, using Au and CdSe as representative examples of metal and semiconductor NCs.

Measurements of electrophoretic mobility and ζ-potential indicated that in the presence of $(N_2H_5)_4Sn_2S_6$, both CdSe and Au NCs are negatively charged (Fig. 1F and fig. S4) as a result of bonding of negatively charged MCC ions to the NC surface. The charging prevents aggregation of NCs and stabilizes the colloidal solutions. Dynamic light scattering revealed single-particle populations in colloidal solutions (Fig. 1G and fig. S4). Solvents other than hydrazine can be used for handling MCC-capped NCs in applications where chemical compatibility or toxicity of hydrazine is a concern. Figure 1D shows colloidal solutions of $Sn_2S_6^{4-}$-capped CdSe NCs in water, DMSO, formamide, or ethanolamine (*19*). ζ-Potential measurements carried out for various NCs dispersed in different solvents and stabilized with different MCCs suggest that negative charging of the NC surface is a general phenomenon responsible for colloidal stabilization of MCC-capped NCs (fig. S4).

Transmission electron microscopy (TEM) showed that MCC-capped NCs retain their size and shape in hydrazine phase (Fig. 2 and fig. S5). The ability of monodisperse NCs to form periodic structures (superlattices) was also preserved, as shown for two- and three-dimensional superlattices of 5-nm Au NCs capped with $Sn_2S_6^{4-}$ (Fig. 2B and fig. S6). Typically, the assembly of MCC-capped particles requires rigorous control of the surface charges through adjustment of ionic strength and pH and may potentially lead to the design of binary superlattices stabilized by electrostatic interactions (*20*).

Both CdSe and Au NCs capped with $Sn_2S_6^{4-}$ preserved their size-dependent optical absorption features (figs. S7 and S8). In polar organic solvents such as DMSO, formamide, and ethanolamine, $Sn_2S_6^{4-}$-capped CdSe NCs exhibited size-dependent excitonic photoluminescence with a quantum efficiency of several percent, comparable to that of as-prepared organics-capped NCs (Fig. 1E and figs. S9 and S10), indicative of a good passivation of surface states by MCC ligands. In neat hydrazine, the luminescence of CdSe NCs was quenched, whereas CdSe-CdS core-shell nanorods and tetrapods exhibited ~10% quantum yields (Fig. 1E).

An important feature of MCCs is their transformation into amorphous or crystalline metal chalcogenides upon mild thermal treatment (*14*–*18*). For example, $Sn_2S_6^{4-}$ neutralized by volatile hydrazinium counterions decomposes at 180°C: $(N_2H_5)_4Sn_2S_6 \rightarrow SnS_2 + 4N_2H_4 + 2H_2S$ (*14*). Because of the absence of any nonvolatile or carbon-containing impurities, the SnS_2 phase crystallizes into pure electronic-grade semiconductor (*14*). The thermogravimetric scans for 3.6-nm CdSe NCs capped with $Sn_2S_6^{4-}$ ions generally follow thermogravimetric scans for pure $(N_2H_5)_4Sn_2S_6$ but reach the plateau at slightly lower temperatures, about 160°C (Fig. 3A). The ligand conversion process involves a total weight loss of only 3.8%, favorable for producing continuous crack-free NC solids. The elemental analysis (fig. S11) is consistent with thermogravimetric data and confirms that typically 2 to 10 weight % of MCCs is sufficient to stabilize colloidal NCs in solution (*19*). After heating to 180°C, we observed complete disappearance of absorption features in IR spectra, confirming the absence of entities containing C–H, S–H, and N–H bonds (Fig. 3B and figs. S12 and S13). In control experiments on Au and CdSe NCs prepared using dodecanethiol and ODPA-HDA-TOPO (octadecylphosphonic acid, hexadecylamine, and trioctylphosphine oxide), correspondingly, the IR spectra remained nearly unaltered after 180°C annealing (fig. S14). X-ray diffraction and TEM studies re-

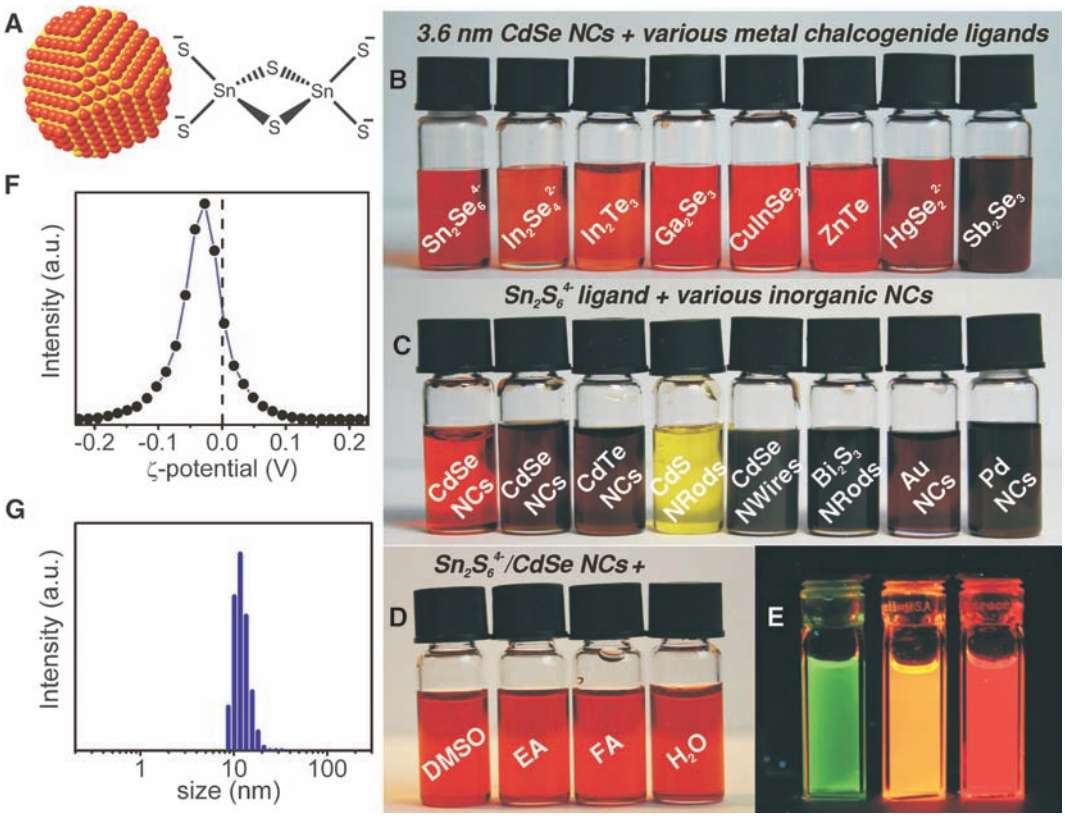

Fig. 1. (**A**) Sketch of a CdSe NC capped with $Sn_2S_6^{4-}$ ions. (**B**) Stable colloidal solutions of 3.6-nm CdSe NCs capped with various metal chalcogenide complexes in hydrazine. (**C**) From left to right: stable colloidal solutions obtained by combining $(N_2H_5)_4Sn_2S_6$ with 3.6- and 5.8-nm CdSe NCs, 9-nm CdTe NCs, CdS nanorods (NRods; ~60 nm wide, 5 nm long), CdSe nanowires (NWires; ~25 nm wide, 2 to 5 μm long), Bi_2S_3 NRods (~25 nm wide, 6 nm long), 5-nm Au NCs, and 3-nm Pd NCs. (**D**) From left to right: CdSe-$Sn_2S_6^{4-}$ NCs dispersed in DMSO, ethanolamine (EA), formamide (FA), and water. (**E**) Photograph of NC photoluminescence excited by an ultraviolet lamp. From left to right: 2.9-nm CdSe-$Sn_2S_6^{4-}$ NCs in ethanolamine [green emission, quantum yield (QY) ≈ 2%], 3.6-nm CdSe-$Sn_2S_6^{4-}$ in DMSO (yellow emission, QY ≈ 3%), and $Sn_2S_6^{4-}$-capped CdSe-CdS core-shell NRods in hydrazine (red emission, QY = 10%). (**F**) ζ-Potential measured for $Sn_2S_6^{4-}$-capped 8-nm CdSe NCs in hydrazine. (**G**) Size histogram obtained from dynamic light scattering for 8-nm CdSe-$Sn_2S_6^{4-}$ NCs in hydrazine.

vealed substantial stability of MCC-capped CdSe and Au NCs against sintering into a bulk phase (fig. S15).

When two or more metallic or semiconducting nanoparticles are in close proximity to each other, their wave functions can couple forming states delocalized over several NCs or propagating throughout the entire NC solid. The quantum mechanical coupling energy can be approximated as $\beta \approx h\Gamma \approx \exp[-(2m^*\Delta E/\hbar^2)^{1/2}\Delta x]$, where h is Planck's constant, Γ is the tunneling rate between two NC neighbors, m^* is the carrier effective mass, $\hbar$ is Planck's constant divided by 2π, and ΔE and Δx are the height of the tunneling barrier and the shortest edge-to-edge distance between the NCs, respectively (*21*, *22*). Replacement of bulky insulating hydrocarbon chains with much smaller and more conductive MCCs should strongly reduce both ΔE and Δx, thereby facilitating electronic communication between the NCs. We probed the coupling between MCC-capped NCs by optical absorption and charge transport measurements. Thus, for 4.6-nm CdSe NCs capped with conventional hydrocarbon ligands, the absorption spectra of colloidal solution and close-packed films are very similar to each other, indicative of strong localization of electron and hole wave functions on individual NCs (Fig. 3C and fig. S16). In contrast, the excitonic features in close-packed films of CdSe NCs capped with $Sn_2S_6^{4-}$ showed a pronounced 46-meV red shift relative to individual NCs in solution (Fig. 3C and fig. S16). Such a shift implies partial leakage of the wave functions into neighboring NCs that relaxes the quantum confinement. Conversion of the $Sn_2S_6^{4-}$ ligands to SnS_2 at 180°C lowers the barrier height ΔE, leading to an additional 34-meV red shift of the optical transitions in the NC solid while maintaining the excitonic features and quantum confinement (Fig. 3C). Similarly, Au NCs capped with $Sn_2S_6^{4-}$ showed a pronounced plasmonic absorption peak around 535 nm in solution, which completely disappeared in NC films (fig. S17A), indicating strong delocalization of the electronic states (*23*). Note that all observed spectral changes were reversible; the plasmonic peak appeared again after redissolution of the NC film. The reference samples of dodecanethiol-capped Au NCs showed strong plasmonic absorption in solutions and in close-packed films (fig. S17B).

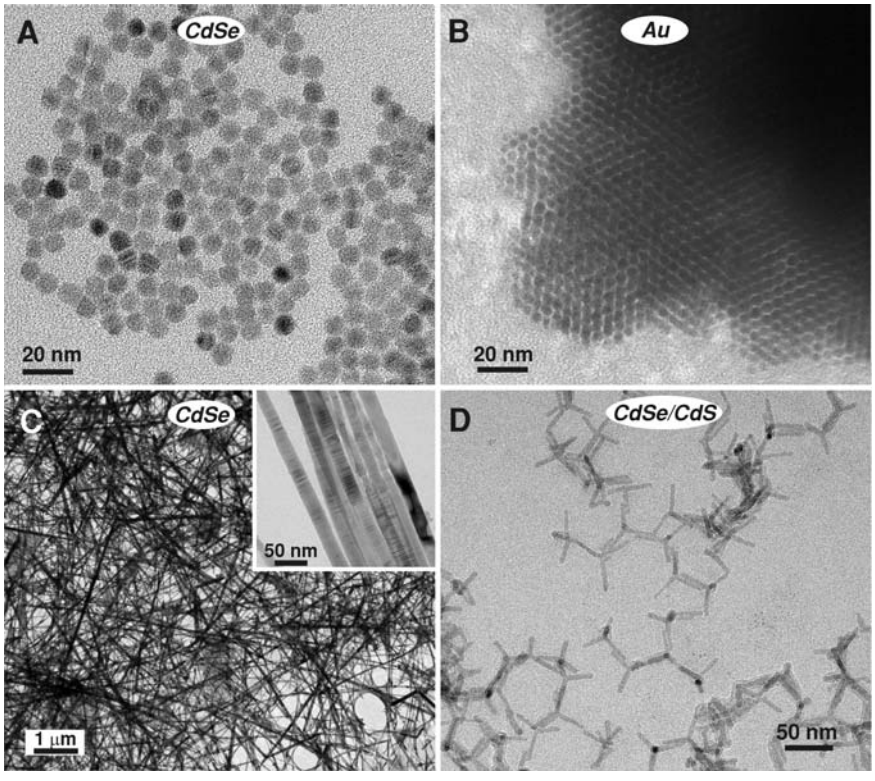

Fig. 2. TEM images of selected examples of NCs capped with $Sn_2S_6^{4-}$ ligands: (**A**) 8.1-nm CdSe NCs, (**B**) face-centered cubic superlattice of ~5-nm Au NCs, and (**C**) CdSe nanowires ~25 nm wide and 2 to 5 μm long. Inset shows a magnified view of a single bundle of CdSe nanowires. (**D**) CdSe-CdS nanotetrapods.

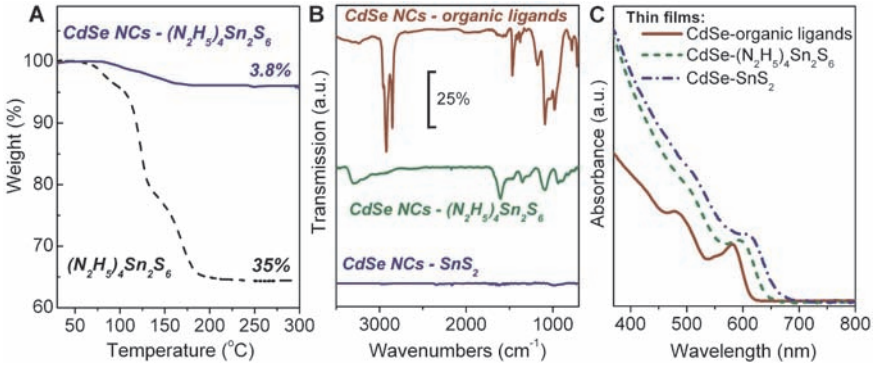

Fig. 3. (**A**) Thermogravimetric scans for $(N_2H_5)_4Sn_2S_6$ (dashed line) and for 3.6-nm $(N_2H_5)_4Sn_2S_6$-capped CdSe NCs (solid line). (**B**) Fourier-transform infrared spectra for 3.6-nm CdSe NCs capped with long-chain organic ligands (red line) and with $(N_2H_5)_4Sn_2S_6$ ligands before (blue line) and after (green line) annealing at 180°C. The IR spectra were normalized to the amount of absorbing material (*19*) and are vertically shifted for clarity. The assignment of peaks is given in (*19*). (**C**) Absorption spectra collected using an integrating sphere for thin films composed of 4.6-nm CdSe NCs capped with original organic ligands (red line) and with $(N_2H_5)_4Sn_2S_6$ ligands before (blue line) and after (green line) annealing at 180°C.

For charge transport studies, we used highly doped Si wafers with a 110-nm layer of thermal oxide and lithographically patterned Ti-Au electrode structures (*19*). The Si substrate was used as the back gate electrode for field-effect transistor (FET) measurements. Close-packed NC films were deposited on these substrates by spin coating or dropcasting. The film thickness was measured using atomic force microscopy profiles and cross-sectional scanning electron microscopy (SEM) studies. The amount of MCC ligands was kept below 10 weight %, sufficient to provide colloidal stabilization but insufficient to form any continuous conductive channels of phase-separated metal chalcogenide, as discussed below.

The original organic ligands rendered NC films highly insulating, with conductivities (σ) on the order of ~10^{-9} S cm^{-1} for 5-nm Au NCs (Fig. 4D) and less than 10^{-12} S cm^{-1} for 5.5-nm CdSe NCs. Replacing dodecanethiol ligands with $Sn_2S_6^{4-}$ increased the conductivity of Au NC solids by ~11 orders of magnitude, approaching σ values of ~200 S cm^{-1} (Fig. 4D). $(N_2H_5)_4Sn_2S_6$ films could not support efficient charge transport (fig. S18), indicating that high conductivity resulted from the NCs. After electrical measurements, the film could be easily dissolved in hydrazine or H_2O, disassembling into individual NCs. Comparison of TEM images before and after electrical measurements revealed no changes in NC size and shape, ruling out sintering as a possible reason for the observed very high conductivity. To the best of our knowledge, the highest conductivity reported for Au NC solids with short-chain organic capping (e.g., *n*-ethyl or *n*-butanethiol) was less than 10^{-1} S cm^{-1} (*24*). The disappearance of the plasmonic absorption peak strongly

supports the metallic nature of $Sn_2S_6^{4-}$-capped Au NC solids. A Mott-type metal-insulator transition was predicted to occur in the Au NC solids when the interparticle spacing is reduced below ~1.1 nm (*24*). Our TEM studies revealed a strong decrease in the mean interparticle distance from ~1.6 nm for dodecanethiol-capped Au NCs to less than 0.5 nm for $Sn_2S_6^{4-}$-capped Au NCs (Fig. 4, A to C). Relative to other prospective solution-processable materials, the conductivity of $Sn_2S_6^{4-}$-capped Au NC solids is much higher than the conductivities of solution-cast conducting polymers (*25*) and graphene-based composites (*26*) and is lower than the conductivity reported for a dense network of single-walled carbon nanotubes (*27*).

MCC capping of colloidal NCs is a promising approach to designing solution-processed inorganic semiconductors. Figure 4E and fig. S19 show characteristics of a field-effect transistor with a channel assembled of 4.5-nm CdSe NCs capped with $Sn_2S_6^{4-}$ and annealed for a short time at 200°C. We observed an n-type gate effect with current modulation $I_{on}/I_{off} \approx 10^5$ and electron mobility $\mu \approx 3 \times 10^{-2}$ cm^2 V^{-1} s^{-1} in the saturation regime (*19*). Similar results were obtained for CdSe NCs capped by $Sn_2Se_6^{4-}$ ions (fig. S20). Higher mobilities should be achievable by replacing Au electrodes by a metal with lower work function and by using FETs with top-electrode configuration (*14*, *19*). For reference, $\mu \approx 10^{-2}$ cm^2 V^{-1} s^{-1} has been previously achieved for CdSe NC films at very high doping densities by means of electrochemical gating (*10*, *28*). Melting and sintering pyridine-capped CdSe NCs into a polycrystalline film by high-temperature anneal yielded $\mu \approx 1$ cm^2 V^{-1} s^{-1} (*29*). Relative to those results, MCC-capped CdSe NCs enabled good performance of solid-state FETs while retaining optical and electronic tunability provided by the quantum confinement. Illumination of MCC-capped CdSe NCs increased their conductivity by several orders of magnitude, as shown for $Sn_2Se_6^{4-}$-capped CdSe NCs (fig. S21). We used small concentrations of MCCs to observe transport through "pure" quantum dot solids. At high concentrations of MCC component, highly conductive continuous channels of metal chalcogenide can form between the NCs. Indeed, we observed an abrupt increase of conductivity in composite materials made of CdSe NCs and $(N_2H_5)_4Sn_2Se_6$ when the CdSe-to-$SnSe_2$ ratio approached 1:1 by weight (fig. S20). Complementary x-ray diffraction studies revealed the appearance of the $SnSe_2$ phase at this composition (fig. S22).

In the previous examples, MCC ligands behaved as electronically transparent "glue" for NCs. However, they can be used for creating composite materials where the properties of MCC and NC components complement each other. Thermal decomposition of the hydrazinium-based MCCs can generate various chalcogenide phases with n- and p-type conductivity, phase-change properties (*15*), etc. (fig. S23). For example, combining electron-conducting nanowires (e.g., CdS) with hole-conducting hosts (e.g., $CuIn_{1-x}Ga_xSe_2$) will form materials with distributed networks of p-n junctions. Future work can certainly benefit from rational design and optimization of MCC-NC pairs. The possibility of all-solution device fabrication makes this approach appealing for large-area, roll-to-roll applications such as manufacture of thin-film solar cells.

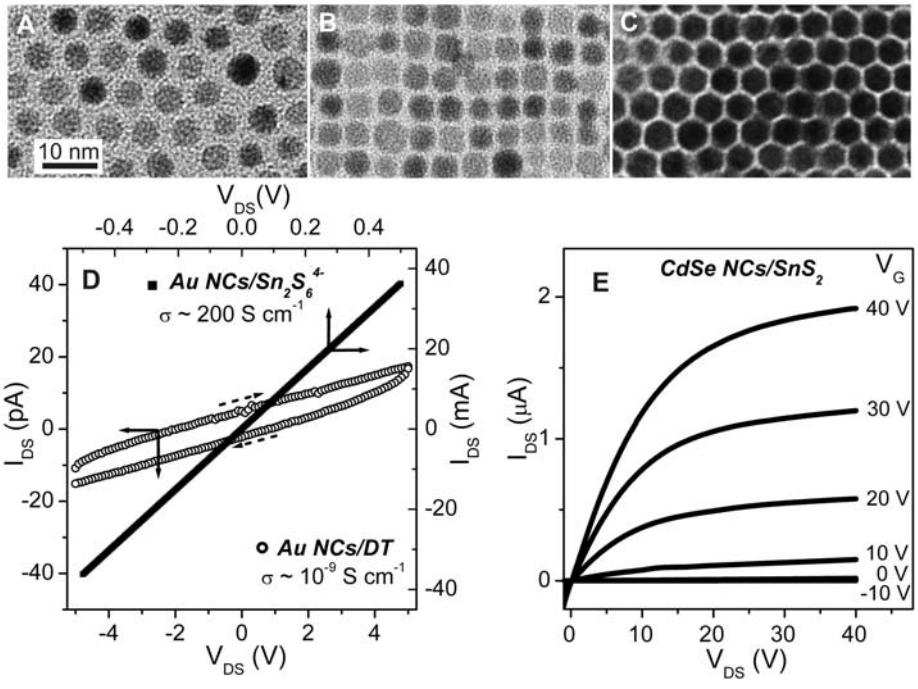

Fig. 4. (**A**) TEM image of an array of ~5-nm Au NCs capped with dodecanethiol. (**B**) TEM image of a layer of ~5-nm Au NCs capped with $(N_2H_5)_4Sn_2S_6$. (**C**) TEM image of a three-dimensional superlattice of ~5-nm Au NCs capped with $(N_2H_5)_4Sn_2S_6$. (**D**) Current-voltage (*I-V*) scans for a film of dodecanethiol-capped 5-nm Au NCs (open circles) and for a film of the same Au NCs capped with $(N_2H_5)_4Sn_2S_6$ (black squares). Dashed arrows show the voltage scan direction. (**E**) Plot of drain current I_D versus drain-source voltage V_{DS} for a NC FET with a channel composed of 4.5-nm CdSe NCs capped with $(N_2H_5)_4Sn_2S_6$ and annealed at 200°C (channel length 10 μm, width 3800 μm, 110-nm-thick SiO_2 gate dielectric).

References and Notes

1. A. P. Alivisatos, *Science* **271**, 933 (1996).
2. J. M. Caruge, J. E. Halpert, V. Wood, V. Bulovic, M. G. Bawendi, *Nat. Photonics* **2**, 247 (2008).
3. G. Konstantatos *et al.*, *Nature* **442**, 180 (2006).
4. I. Gur, N. A. Fromer, M. L. Geier, A. P. Alivisatos, *Science* **310**, 462 (2005).
5. C. B. Murray, C. R. Kagan, M. G. Bawendi, *Annu. Rev. Mater. Sci.* **30**, 545 (2000).
6. T. Ni *et al.*, *J. Am. Chem. Soc.* **124**, 3980 (2002).
7. M. Kuno, J. K. Lee, B. O. Dabbousi, F. V. Mikulec, M. G. Bawendi, *J. Chem. Phys.* **106**, 9869 (1997).
8. D. V. Talapin, C. B. Murray, *Science* **310**, 86 (2005).
9. M. Law *et al.*, *J. Am. Chem. Soc.* **130**, 5974 (2008).
10. D. Yu, C. Wang, P. Guyot-Sionnest, *Science* **300**, 1277 (2003).
11. S. Bag, P. N. Trikalitis, P. J. Chupas, G. S. Armatas, M. G. Kanatzidis, *Science* **317**, 490 (2007).
12. M. J. MacLachlan, N. Coombs, G. A. Ozin, *Nature* **397**, 681 (1999).
13. A. E. Riley, S. D. Korlann, E. K. Richman, S. H. Tolbert, *Angew. Chem. Int. Ed.* **45**, 235 (2006).
14. D. B. Mitzi, L. L. Kosbar, C. E. Murray, M. Copel, A. Afzali, *Nature* **428**, 299 (2004).
15. D. J. Milliron, S. Raoux, R. M. Shelby, J. Jordan-Sweet, *Nat. Mater.* **6**, 352 (2007).
16. D. B. Mitzi, *Inorg. Chem.* **44**, 7078 (2005).
17. D. B. Mitzi, *Inorg. Chem.* **46**, 926 (2007).
18. M. Yuan *et al.*, *Inorg. Chem.* **46**, 7238 (2007).
19. See supporting material on *Science* Online.
20. A. M. Kalsin *et al.*, *Science* **312**, 420 (2006); published online 22 February 2006 (10.1126/science.1125124).
21. I. S. Beloborodov, A. V. Lopatin, V. M. Vinokur, K. B. Efetov, *Rev. Mod. Phys.* **79**, 469 (2007).
22. D. Vanmaekelbergh, P. Liljeroth, *Chem. Soc. Rev.* **34**, 299 (2005).
23. C. P. Collier, R. J. Saykally, J. J. Shiang, S. E. Henrichs, J. R. Heath, *Science* **277**, 1978 (1997).
24. A. Zabet-Khosousi, A.-A. Dhirani, *Chem. Rev.* **108**, 4072 (2008).
25. S. Kirchmeyer, K. Reuter, *J. Mater. Chem.* **15**, 2077 (2005).
26. S. Stankovich *et al.*, *Nature* **442**, 282 (2006).
27. D. S. Hecht, L. Hu, G. Grüner, *Curr. Appl. Phys.* **7**, 60 (2007).
28. D. Yu, B. L. Wehrenberg, P. Jha, J. Ma, P. Guyot-Sionnest, *J. Appl. Phys.* **99**, 104315 (2006).
29. B. A. Ridley, B. Nivi, J. M. Jacobson, *Science* **286**, 746 (1999).

30. We thank D. B. Mitzi and P. Guyot-Sionnest for stimulating discussions, M. Bodnarchuk and J. Huang for synthesis of Au nanoparticles and CdSe/CdS tetrapods, E. Shevchenko and I. Steele for help with energy-dispersive x-ray and SEM measurements, J.-S. Lee and R. Divan for help with electrical measurements, the Analytical Chemistry Laboratory at Argonne National Laboratory for elemental analysis, and F. Stafford for reading the manuscript. Supported by Deutsche Studienstiftung (M.S.), American Chemical Society Petroleum Research Fund grant 48636-G10, the Chicago Energy Initiative, and Evident Technologies Inc. Work at the Center for Nanoscale Materials, Argonne National Laboratory, was supported by the U.S. Department of Energy under contract DE-AC02-05CH11357.

Supporting Online Material

www.sciencemag.org/cgi/content/full/324/5933/1417/DC1
Materials and Methods
Figs. S1 to S23
Tables S1 and S2
References

5 January 2009; accepted 27 April 2009
10.1126/science.1170524

Polarization Control of Electron Tunneling into Ferroelectric Surfaces

Peter Maksymovych,[1]* Stephen Jesse,[1] Pu Yu,[2] Ramamoorthy Ramesh,[2] Arthur P. Baddorf,[1] Sergei V. Kalinin[1]

We demonstrate a highly reproducible control of local electron transport through a ferroelectric oxide via its spontaneous polarization. Electrons are injected from the tip of an atomic force microscope into a thin film of lead-zirconate titanate, $Pb(Zr_{0.2}Ti_{0.8})O_3$, in the regime of electron tunneling assisted by a high electric field (Fowler-Nordheim tunneling). The tunneling current exhibits a pronounced hysteresis with abrupt switching events that coincide, within experimental resolution, with the local switching of ferroelectric polarization. The large spontaneous polarization of the PZT film results in up to 500-fold amplification of the tunneling current upon ferroelectric switching. The magnitude of the effect is subject to electrostatic control via ferroelectric switching, suggesting possible applications in ultrahigh-density data storage and spintronics.

In quantum mechanics, a particle can tunnel through a potential barrier that exceeds the particle's energy. Tunneling underlies the operation of the resonant tunneling diode (*1*) and flash memory (*2*), enables atomically resolved imaging in scanning tunneling microscopy (*3*), and holds promise for quantum computing based on superconducting quantum interference device magnetometers and quantum dots (*4*, *5*). Replacing a conventional insulator in the tunnel junction with electronically correlated materials can modify existing devices and yield new types of electronic functionality. In one of the earliest such concepts proposed by Esaki (*6*), dubbed a "polar switch," the tunneling barrier was composed of a ferroelectric oxide, which would have spontaneous, nonvolatile polarization that could be switched in direction with an applied electric field. In a number of recent theoretical papers (*7*–*9*), including first-principles studies, the spontaneous polarization was predicted to modulate the height of the tunneling barrier, which would yield distinct nonvolatile conductance states that could subsequently be used to encode information. The density of the recorded informa-

[1]Center for Nanophase Materials Science, Oak Ridge National Laboratory, Oak Ridge, TN 37831, USA. [2]Department of Materials Science and Engineering and Department of Physics, University of California, Berkeley, CA 94720, USA.

*To whom correspondence should be addressed. E-mail: maksymovychp@ornl.gov

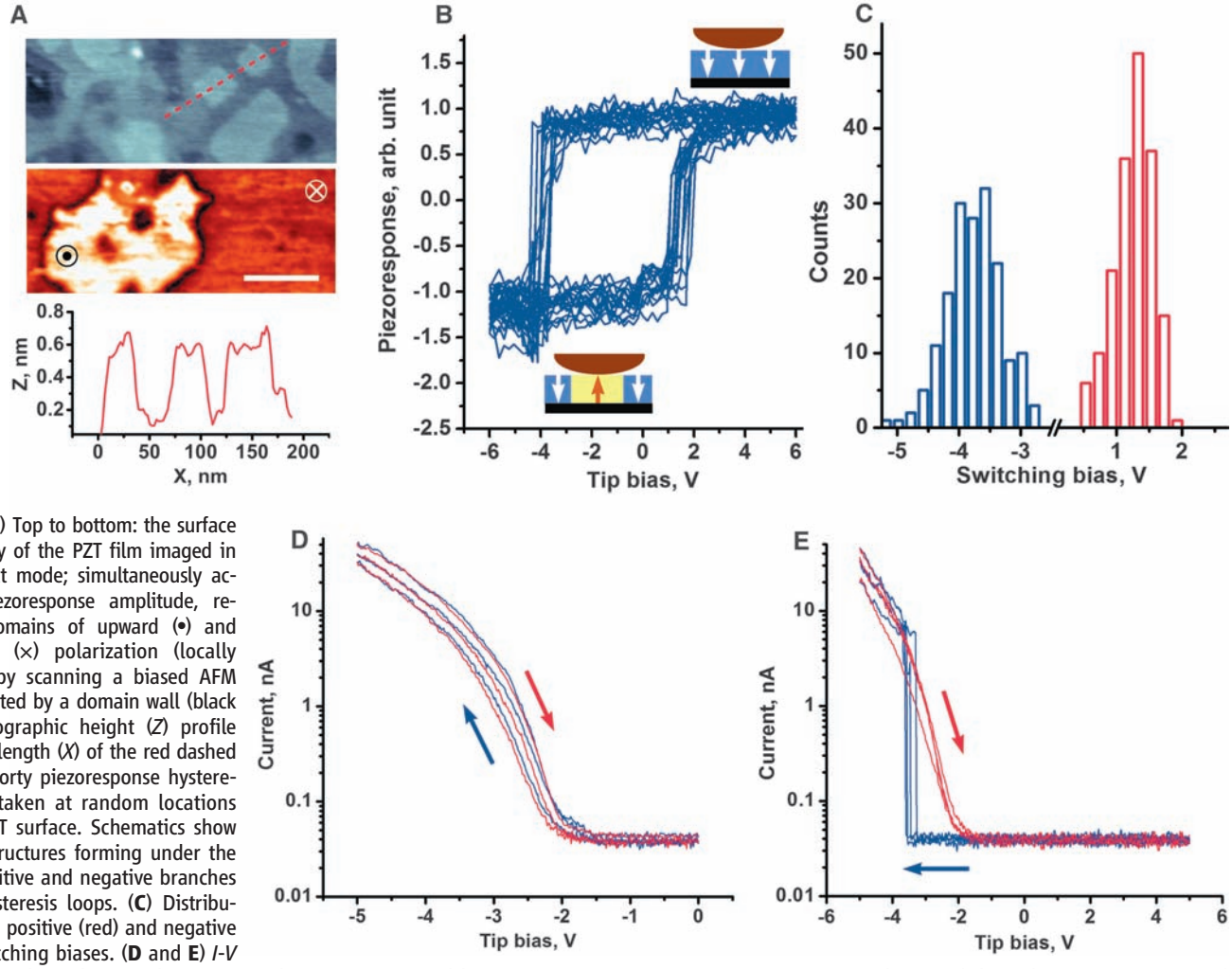

Fig. 1. (**A**) Top to bottom: the surface topography of the PZT film imaged in the contact mode; simultaneously acquired piezoresponse amplitude, revealing domains of upward (•) and downward (×) polarization (locally recorded by scanning a biased AFM tip) separated by a domain wall (black line); topographic height (*Z*) profile along the length (*X*) of the red dashed line. (**B**) Forty piezoresponse hysteresis loops taken at random locations on the PZT surface. Schematics show domain structures forming under the tip on positive and negative branches of the hysteresis loops. (**C**) Distribution of the positive (red) and negative (blue) switching biases. (**D** and **E**) *I*-*V* curves from three different locations on the surface acquired by using a triangular ramp of tip bias from 0 V to −5 V (D) and from 5 V to −5 V in (E). The blue curves were acquired during the forward branch of the bias ramp from positive to negative values, and the red curves were acquired during the reverse branch of the bias ramp from negative to positive values.

tion can potentially approach near-atomic limit because the width of polarization domains in nanoscale ferroelectric oxides can be as small as several nanometers (*10*, *11*).

It has proven difficult to find a material system that would simultaneously satisfy the dimensional constraints for tunneling and ferroelectricity. Ferroelectricity vanishes below a critical thickness, varying from 1 to 10 nm (*12*, *13*), whereas direct tunneling is only feasible across a wide band-gap oxide thinner than ~2 nm. Although the polar distortion in perovskite oxides leading to ferroelectricity was recently reported even in three unit-cell (~1.2 nm) films (*11*), the presence of switchable polarization at this ultrathin limit has not yet been confirmed. Switching could be hindered by the formation of lamellar domain structures and a strong preference of the polarization to remain in the as-grown state (*14*). Gajek *et al.* (*15*) recently demonstrated hysteresis of tunneling conductance through a 2-nm multiferroic film, albeit with a very small magnitude of <15%, as expected for the diminishing spontaneous polarization in such thin films (*12*). In addition to these fundamental physical constraints, the defect-rich nature of transition metal oxides often favors filamentary and defect-mediated conduction mechanisms over intrinsic tunneling (*16*, *17*).

To demonstrate the polarization control of electron transport through a ferroelectric oxide, we used the tunneling barrier electronically defined at the junction between a sharp metal tip and the ferroelectric surface. We could thus avoid the necessity to reduce the oxide width and were able to work with relatively thick ferroelectric films (30 nm) with large spontaneous polarization. The electrons were injected into the oxide from the metal tip in the regime of Fowler-Nordheim (FN) tunneling (*18*) across an effectively triangular-shaped barrier. The FN conductance was found to be strongly dependent on the polarization direction, which resulted in abrupt enhancement of current (up to 500-fold) at ferroelectric switching events.

We studied the local transport properties of the (100)-oriented 30-nm ferroelectric film of tetragonal $Pb(Zr_{0.2}Ti_{0.8})O_3$ (PZT) by using atomic force microscopy (AFM) in ultrahigh vacuum (UHV). The surface of the film was flat with well-defined unit-cell steps (Fig. 1A). The preferred direction of spontaneous polarization is toward the bottom metallic $La_{0.7}Sr_{0.3}MnO_3$ (LSMO) electrode. The polarization could be readily switched in UHV (Fig. 1B) by biasing the AFM tip relative to the bottom electrode. The switching bias, determined from the piezoresponse hysteresis loops (*19*), varied across the surface because of the inherent disorder in the film with averages of 1.3 ± 0.6 V and –3.7 ± 0.8 V for the positive and the negative nucleation bias, respectively (Fig. 1C). The hysteresis loops also revealed a ~1.2-V built-in potential across the film.

Local current-voltage (*I-V*) characteristics (Fig. 1, D and E) were highly rectifying with no current above the noise floor (~40 pA) observed at positive tip bias. The shape of the *I-V* curve, however, depended strongly on the probed range of the tip bias. The onset of current was smooth, and the *I-V* curve exhibited little or no hysteresis between forward (increasing negative tip bias) and backward bias ramps if the positive bias was limited to <0 V (Fig. 1D). In contrast, increasing the upper limit to >2 V yielded an abrupt current jump in the forward direction, followed by a continuous region and a smooth reverse curve (Fig. 1E). The tip bias at the current discontinuity varied across the surface with an average value of –3.3 ± 1.1 V. Because this voltage variation is well within the range of ferroelectric switching (Fig. 1C), the observed current hysteresis may be related to the ferroelectric polarization of the surface. However, a rigorous correlation can be established only in a simultaneous measurement of the ferroelectric and conducting properties because transition metal oxides can exhibit defect-mediated resistive switching (*16*, *20*, *21*) and charge injection from the AFM tip was previously shown to induce local conducting states in lead-zirconate films (*22*).

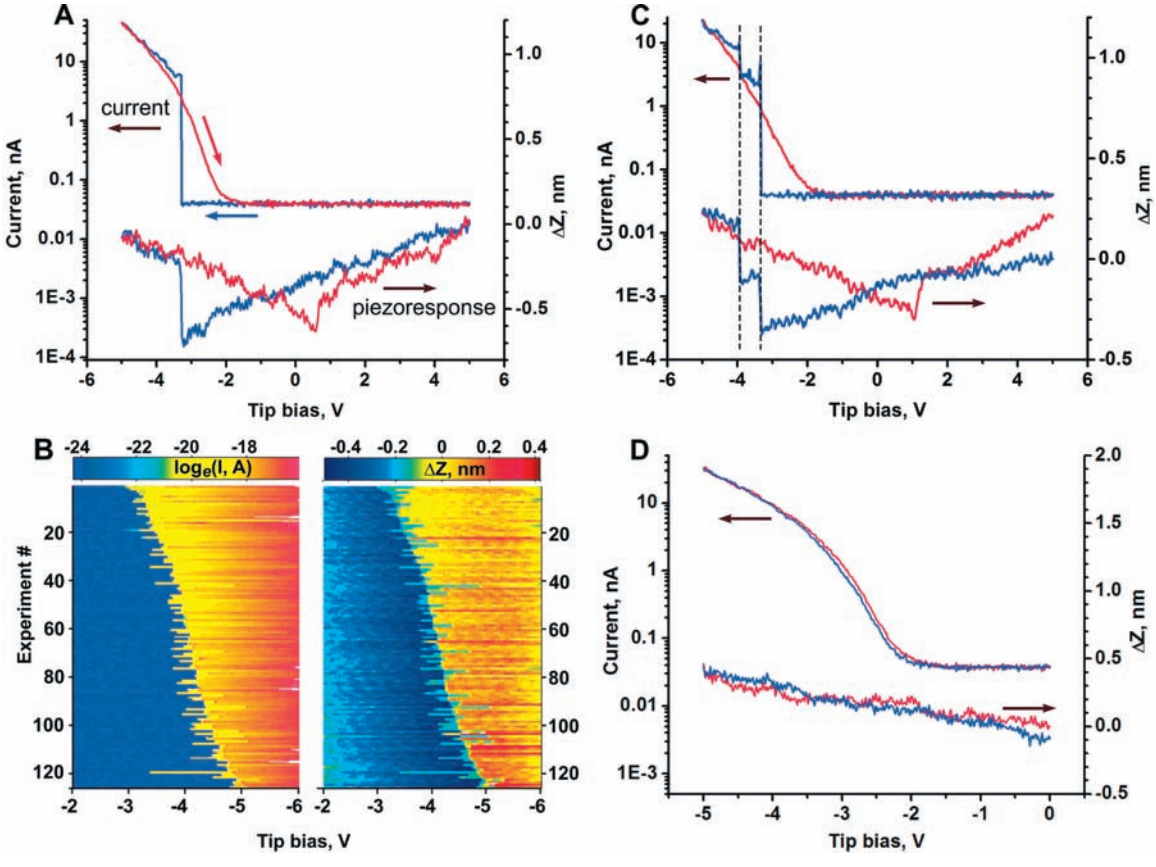

Fig. 2. Simultaneous measurements of local conductance and piezoresponse on the surface of a 30-nm PZT film. The bias ranged from 5 V to −5 V for *I-V* curves in (**A**) and (**C**) and from 0 V to −5 V for that in (**D**). (**B**) Correlation between current and strain curves based on 126 measurements acquired on a 6400-nm^2 grid with a lateral resolution of 20 nm. Each horizontal line in the images corresponds to one forward *I-V* (left) and its matching strain (right) curve. Both *I-V* and strain curves in the data set were sorted according to the negative tip bias at the largest current discontinuity. The discontinuities lie along the boundary of the blue and yellow regions. The boundaries are identical in the current and strain measurements, revealing the coincidence of the respective switching events. Streaks in the images correspond to double jumps as in (C).

To acquire local piezoresponse hysteresis loops (Fig. 1B), we applied an ac bias to the AFM tip after subsequent dc-poling cycles (*19*). A typical ac bias amplitude of >0.5 V tended to smooth the observed ferroelectric switching event and also interfered with the conductance measurements. Thus, we acquired local strain loops via a static displacement of the AFM tip during the dc-bias ramp (*23*). As seen in Fig. 2A, the strain loop in a symmetric bias window (+5 V to –5V) had a clear butterfly shape because the direction of local surface deformation changed sign (discontinuity in strain curves) at the ferroelectric switching events. The statistical distributions of the switching bias from the strain and ac-piezoresponse measurements were similar (Fig. 3A), although the former yielded slightly smaller average values. This difference was likely caused by a relaxation effect, in that the occurrence of a stable reverse-polarity domain was detected at zero tip bias in the ac technique and at a nonzero value in the strain-loop measurements.

The discontinuities in the strain loop and the simultaneously acquired current hysteresis coincide at negative tip bias (Fig. 2A). This behavior was reproduced in all of ~600 hysteretic *I-V* curves acquired in different places on the PZT surface, a subset of which is shown in Fig. 2B. About 10% of the measured points displayed matching patterns of several discontinuities in the *I-V* and strain curves (Fig. 2C). This response may be indicative of defect-mediated pinning of the reversed-polarization domain growth. At the same time, smooth *I-V* curves correlated only with continuous strain loops, where no ferroelectric switching occured (Fig. 2D). Lastly, the transition between smooth (Fig. 2D) and hysteretic *I-V* characteristics (Fig. 2A) occurs at the minimal positive bias required to open the butterfly-shaped strain loop (fig. S1). These measurements rigorously establish the correlation between switching of ferroelectric polarization and electronic conductance.

To rule out a possible involvement of residual adsorbates in the observed effects, we carried out a control experiment on a similarly grown 50-nm PZT-LSMO film and found that annealing the film in 20 mTorr oxygen atmosphere at $T = 600$ K for 20 min had no observable effect on the polarization-dependent electron transport through the film (fig. S2). At the same time, the reproducibility of *I-V* curves across the surface distinguishes our results from those of filamentary conduction because the spatial distribution of conducting filaments was shown to be very nonuniform (*17*). Also, highly rectifying *I-V* characteristics (Fig. 2, A and C) are distinct from a previous study of a macroscopic ferroelectric capacitor, where the *I-V* curves became ohmic after polarization switching (*24*).

Smooth *I-V* curves can be linearized in the coordinates $\log(I/V^2) = f(V^{-1})$, which is a signature of FN tunneling through a triangular potential barrier. The FN tunneling current (*18*),

$$I = A_{\mathrm{eff}} \frac{e^3 m_{\mathrm{Pt}}}{8\pi\, hm_{\mathrm{PZT}}\phi_{\mathrm{B}}} \times E^2 \exp\left(-\frac{8\pi\sqrt{2m_{\mathrm{PZT}}}}{3he}\frac{\phi_{\mathrm{B}}^{3/2}}{E}\right) \quad (1)$$

is a function of the barrier height, ϕ_{B}; electric field, E; effective tunneling area, A_{eff}; and the effective electron mass in the tip (m_{Pt}, assumed ~m_e) and in the PZT (m_{PZT}, assumed here ~$3m_e$). The observed current hysteresis implies that the FN-tunneling conductance is drastically reduced when the polarization vector is antiparallel to the applied electric field. Polarization switching is accompanied by the changes in local strain and electrostatics in the material, both of which can be the source of hysteresis.

We can rule out nanomechanical origins, such as the local expansion of the material and the change of the tip-surface contact area, A_{eff}. Indeed, this piezoelectric effect would increase the width of the tunneling barrier upon switching (*7*), leading to a drop in the tunneling conductance, opposite to the observed trend (Fig. 2, A to C). The changes in the tip-surface contact area were ascertained to be insignificant by measuring the bias dependence of the contact resonance of the cantilever (Fig. 3B). The frequency varied by only ~300 Hz across the whole bias range, corresponding to at most a twofold change in the contact area (*25*).The current, however, increased by several orders of magnitude upon switching. Furthermore, the resonance frequency decreased at negative tip bias, indicating that the contact area slightly decreases too. The FN-current hysteresis must therefore arise from electrostatic effects, originating from the screening of the bound polarization charge on ferroelectric surfaces (*7*, *9*).

The barrier height in Eq. 1 corresponds to the height of the Schottky barrier at the metal-ferroelectric interface. The interfacial band alignment is influenced by the presence of bound dipoles (*26*). These dipoles may originate from dangling bonds or polar terminations in conven-

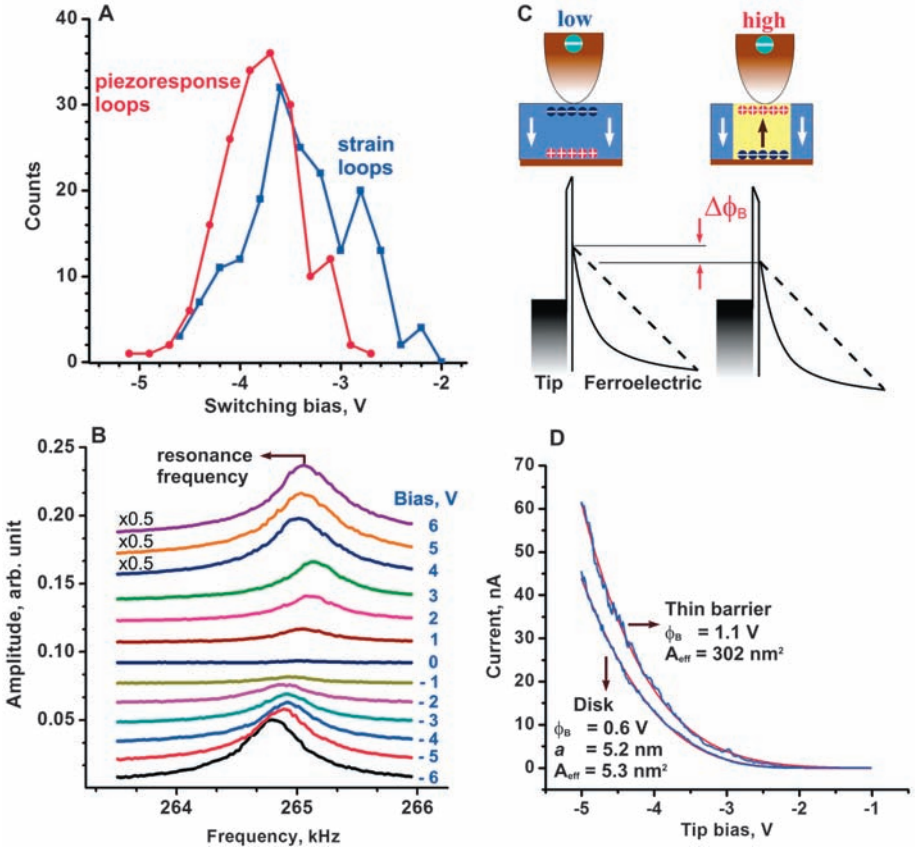

Fig. 3. (**A**) Distribution of the switching bias was determined from strain loops (blue) and ac-piezoresponse loops (red). (**B**) The measurement of the first contact resonance of the cantilever as a function of dc bias. The amplitude of the oscillation varies because of nonlocal electrostatic effects (*36*). (**C**) Schematic polarization domain structure and interfacial band alignment for low- and high-conducting states of the PZT film. Only the conduction band profile of the ferroelectric is shown. The dashed line corresponds to a uniform potential in the film, whereas the solid line is the schematic nonuniform distribution in the disk and in thin Schottky barrier models. (**D**) Fitting of a smooth *I-V* curves (blue) to the modified FN equation in the framework of the disk potential and thin Schottky barrier models (blue curve, data; red curve, fit; *a*, disk radius).

tional semiconductors, whereas in ferroelectrics there is an additional strong component caused by the bound polarization charge. In the simplest one-dimensional model, the metal and ferroelectric are separated by an ultrathin insulating layer that could arise from a nonepitaxial contact (between the tip and the surface in our case), the reacted surface layer, or the formation of an intrinsic dielectric dead layer (*27*). The potential drop across the dielectric gap rigidly shifts the electronic bands of the ferroelectric relative to the Fermi level of the tip (Fig. 3C). The change of the barrier height can be estimated as $\Delta\phi_B = \frac{e\delta_I}{\varepsilon_I}\sigma_s$ (*26*), where δ_I is the width of the dielectric gap, ε_I its dielectric constant, and σ_s is the surface charge density. The magnitude of σ_s is determined by the competition between internal and external screening of the polarization charge, as well as a possible suppression of the polarization charge in the vicinity of the interface (*27*). $\Delta\phi_B$ is ~0.7 eV for an estimated δ_I = 0.06 nm, $\varepsilon_I = \varepsilon_0$, and σ_s = 0.1 C* m^{-2}. This difference is large enough to fully suppress FN electron tunneling into an oppositely polarized film, as observed experimentally.

Because the accumulation of positive surface charge on an upward polarized surface will shift the ferroelectric bands down in energy (Fig. 3C), the Schottky barrier for electron tunneling into the conduction band of the ferroelectric (n-type band alignment) will decrease in height. The n-type band alignment in the tip-surface junction is consistent with the observation of current at negative tip polarity. Therefore the external screening model predicts the right sign of the effect irrespective of the detailed mechanisms. Our estimate also agrees with recent ab initio calculations of an epitaxial $SrRuO_3$-$BaTiO_3$-$SrRuO_3$ capacitor, where the barrier height decreases by ~0.4 eV for upward polarization because of combined effects of electrostatics and local chemical bonding (*9*).

Fitting of Eq. 1 to the experimental *I-V* curves with the assumption of a 300-nm^2 contact area (20-nm tip diameter) reveals that the electric field has to exceed 5 × 10^6 V* cm^{-1} to allow tunneling across a realistic potential barrier of 0.8 to 1.0 eV between Pt (the tip coating) and PZT (*28*). This value is at least five times higher than what would be achieved if the potential drop were uniform across the PZT film. The required nonuniformity can be produced by the sharpness of the metal tip producing a localized electric field in the vicinity of the surface or by a relatively large total density of deep and shallow levels in the band gap of the ferroelectric that yield narrow Schottky barriers via effective screening.

To assess the strength of a localized field, we have modeled the tip-surface junction as a disk in contact with a dielectric surface (*29*). Although the model fits the data very well (Fig. 3D), sufficiently localized fields in a dielectric substrate (or a fully depleted film) are produced if the tip diameter is less than 5 nm (*25*), whereas the effective tunneling area is ~4 nm^2. These values are less than the expected tip diameter of >20 nm in contact-mode AFM. Thus, the localized field enhancement can take place if there is a sharp asperity on the tip surface that dominates the tunneling transport. Notably, although the potential drop across the film is nonuniform, it is almost identically linear several nanometers under the tip (fig. S4), creating a narrow triangular potential barrier where the FN-tunneling equation applies.

The second possibility of thin Schottky barriers was previously invoked to rationalize the occurrence of FN tunneling in capacitor experiments with macroscopic electrodes (*30*, *31*). Several works (*30*, *32*) have reported a relatively high total density of rechargeable levels in $Pb(Zr_{0.2}Ti_{0.8})O_3$ films, up to 10^{20} cm^{-3}. The ferroelectric film can then be treated as a doped semiconductor, where the polarization charge is screened by charged and ionized defects (*33*). The depletion width and the corresponding maximum electric field (E_m) at the interface become polarization dependent. E_m can exceed 4 MV cm^{-1} already at a tip bias of 2 V (*25*). Substituting the bias-dependent E_m into the Eq. 1 also yields a good fit to the measured *I-V* curves (Fig. 3D), with an average barrier height of 1.1 ± 0.1 eV,

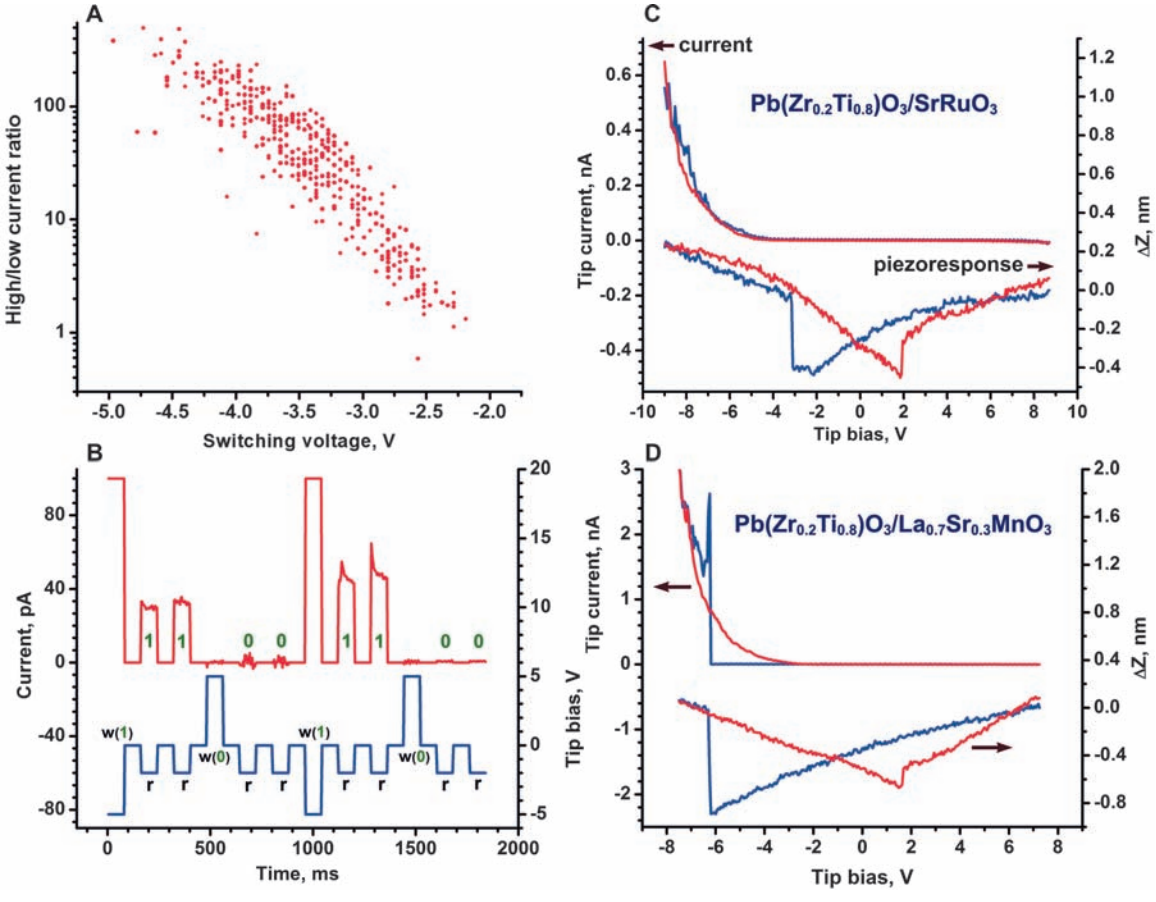

Fig. 4. (**A**) High-to-low ratio of conductance as a function of the tip bias corresponding to ferroelectric switching from the analysis of 400 hysteretic *I-V* curves. (**B**) Prototypical memory action based on the ferroelectric control of FN tunneling. The blue curve is a pulse sequence that records (w) and reads out (r) high (logical 1) and low (logical 0) conductance states. The red curve is a current readout. (**C** and **D**) Local *I-V* (top) and strain (bottom) curves on 50-nm PZT films with SRO (C) and LSMO (D) bottom electrodes.

a realistic tunneling area of 300 ± 6 nm^2 (tip diameter ~ 20 nm), and a spontaneous polarization of 0.4 ± 0.1 C cm^{-2}. The depletion width in this model is polarization dependent, which will introduce strong current hysteresis in addition to that from the change of the barrier height.

Although we cannot determine which of the above models is dominant, we have observed similar local transport through 50-nm PZT films (fig. S2) and 5-nm $BiFeO_3$ films (fig. S3). The barrier narrowing thus appears to be an intrinsic property of high-field transport in perovskite ferroelectrics, in agreement with a number of capacitor measurements (*30*). The polarization dependence of the Schottky barrier height will have an equally pronounced effect on local conductance independently of the model, and it will also produce strong conductance hysteresis in the Schottky emission (*34*), another interface-limited conduction mechanism that exhibits exponential dependence on the barrier height.

The pronounced coupling between ferroelectricity and FN tunneling results in high-to-low conductance ratios up to 500:1 in the region of the current hysteresis (Fig. 4A). The conductance ratio grows exponentially with decreasing ferroelectric switching voltage because the downward-polarized surface shows no detectable conductance (Fig. 2, A and D). The hysteresis observed in our measurements was already sufficient to demonstrate a prototype resistive memory action. Figure 4B shows a series of consecutive write (±5 V) and read (–2 V) bias pulses, where the read voltage was chosen to yield measurable current on the upward polarized surface. The memory effect is manifested in the ability to read out high (30 to 50 pA) and low (noise limited to ~1 pA) conductance states and to do so nondestructively (Fig. 4B) because the read bias was at least 1 V below the onset of ferroelectric switching. Theoretically, the FN-conductance ratio can exceed five orders of magnitude, depending on the polarization-induced change of the barrier height, tip bias, size, and material properties (fig. S6). The hysteresis window can be optimized through the built-in field across the ferroelectric film by varying its dimensions, doping, and the choice of the bottom electrode and tip materials. This is exemplified in Fig. 4, C and D, for 50-nm PZT films grown on $SrRuO_3$ (SRO) and LSMO electrodes. The *I-V* curve on the PZT-SRO film revealed negligible hysteresis because ferroelectric switching occurred in the bias range where the film was insulating (Fig. 4C). Substituting SRO with LSMO produced a strong built-in field, overlapping the bias range of conductance and polarization switching events and creating a very pronounced conductance hysteresis (Fig. 4D).

The large magnitude of the conductance hysteresis, its tunability via ferroelectric switching, and the ability to implement nondestructive resistive (rather than capacitive) read-out of polarization direction indicate the promise of ferroelectric FN tunneling in the development of ultrahigh-density information storage. According to a recent theoretical study, the minimum recordable domain size decreases with thickness but passes through a minimum, increasing again for the thinnest films (*35*). A relatively weak thickness dependence of FN tunneling will thus be critical in achieving the highest density of resistively readable information on a ferroelectric surface. The compatibility of FN tunneling with multiferroic oxides (such as $BiFeO_3$) also poses a possibility of implementing multiferroic control of this transport regime for spintronic applications. Lastly, polarization-dependent transport can be used to study the ferroelectric property itself in an attempt to reveal the switching mechanisms in nanoscale systems and explore the role of defects.

References and Notes

1. R. Tsu, L. Esaki, *Appl. Phys. Lett.* **22**, 562 (1973).
2. R. Bez, E. Camerlenghi, A. Modelli, A. Visconti, *Proc. IEEE* **91**, 489 (2003).
3. G. Binnig, H. Rohrer, *IBM J. Res. Dev.* **30**, 4 (1986).
4. J. Majer *et al.*, *Nature* **449**, 443 (2007).
5. J. M. Elzerman *et al.*, *Nature* **430**, 431 (2004).
6. L. Esaki, R. B. Laibowitz, P. J. Stiles, *IBM Tech. Discl. Bull.* **13**, 2161 (1971).
7. H. Kohlstedt, N. A. Pertsev, J. R. Contreras, R. Waser, *Phys. Rev. B* **72**, 125341 (2005).
8. E. Y. Tsymbal, H. Kohlstedt, *Science* **313**, 181 (2006).
9. J. P. Velev *et al.*, *Nano Lett.* **9**, 427 (2009).
10. P. Aguado-Puente, J. Junquera, *Phys. Rev. Lett.* **100**, 177601 (2008).
11. D. D. Fong *et al.*, *Science* **304**, 1650 (2004).
12. J. Junquera, P. Ghosez, *Nature* **422**, 506 (2003).
13. C. H. Ahn, K. M. Rabe, J.-M. Triscone, *Science* **303**, 488 (2004).
14. V. Nagarajan *et al.*, *J. Appl. Phys.* **100**, 051609 (2006).
15. M. Gajek *et al.*, *Nat. Mater.* **6**, 296 (2007).
16. H. Kohlstedt *et al.*, *Appl. Phys. Lett.* **92**, 062907 (2008).
17. K. Szot, W. Speier, G. Bihlmayer, R. Waser, *Nat. Mater.* **5**, 312 (2006).
18. R. H. Fowler, L. W. Nordheim, *Proc. R. Soc. London Ser. A* **119**, 173 (1928).
19. S. Jesse *et al.*, *Nat. Mater.* **7**, 209 (2008).
20. R. Waser, M. Aono, *Nat. Mater.* **6**, 833 (2007).
21. Y. Watanabe, *Ferroelectrics* **349**, 190 (2007).
22. C. Yoshida, A. Yoshida, H. Tamura, *Appl. Phys. Lett.* **75**, 1449 (1999).
23. S. Wicks, V. Anbusathiah, V. Nagarajan, *Nanotechnology* **18**, 465502 (2007).
24. P. W. M. Blom, R. M. Wolf, J. F. M. Cillessen, M. P. C. M. Krijn, *Phys. Rev. Lett.* **73**, 2107 (1994).
25. Materials and methods are available as supporting material on *Science* Online.
26. R. T. Tung, *Phys. Rev. B* **64**, 205310 (2001).
27. A. K. Tagantsev, G. Gerra, *J. Appl. Phys.* **100**, 051607 (2006).
28. I. Stolichnov, A. Tagantsev, N. Setter, J. S. Cross, M. Tsukada, *Appl. Phys. Lett.* **75**, 1790 (1999).
29. A. N. Morozovska, S. V. Kalinin, E. A. Eliseev, S. V. Svechnikov, *Ferroelectrics* **354**, 198 (2007).
30. J. F. Scott, *Ferroelectric Memories* (Springer, New York, 2000).
31. I. Stolichnov, A. K. Tagantsev, E. L. Colla, N. Setter, *Appl. Phys. Lett.* **73**, 1361 (1998).
32. L. Pintilie *et al.*, *J. Appl. Phys.* **98**, 124104 (2005).
33. L. Pintilie, M. Alexe, *J. Appl. Phys.* **98**, 124103 (2005).
34. S. M. Sze, *Semiconductor Devices: Physics and Technology, 2nd Ed.* (Wiley, New York, 2001).
35. A. N. Morozovska, E. A. Eliseev, *Physica B* **373**, 54 (2006).
36. S. Jesse, A. P. Baddorf, S. V. Kalinin, *Nanotechnology* **17**, 1615 (2006).

37. Experiments were done at the Center for Nanophase Materials Sciences, Office of Basic Energy Sciences, U.S. Department of Energy. P.M.'s research performed as a Eugene P. Wigner Fellow and staff member at the Oak Ridge National Laboratory. The work at Berkeley is partially supported by the Semiconductor Research Corporation–Nanoelectronics Research Initiative–Western Institute of Nanoelectrics program as well as by the Director, Office of Science, Office of Basic Energy Sciences, Materials Sciences Division of the U.S. Department of Energy under contract no. DE-AC02-05CH1123.

Supporting Online Material

www.sciencemag.org/cgi/content/full/324/5933/1421/DC1
Materials and Methods
Figs. S1 to S6
References

21 January 2009; accepted 12 May 2009
10.1126/science.1171200

Isotopic Homojunction Band Engineering from Diamond

H. Watanabe,* C. E. Nebel,† S. Shikata

Confinement of charge carriers in semiconductors by quantum wells is usually accomplished with layers that vary in elemental composition, such as aluminum gallium arsenide and gallium arsenide. We fabricated diamond superlattices by creating multilayer structures of isotopically pure carbon isotopes carbon-12 (^{12}C) and carbon-13 (^{13}C), which confine electrons by a difference in band-gap energy of 17 millielectron volts. Cathodoluminescence experiments performed at 80 kelvin showed that excitonic recombination in the higher-energy band of ^{13}C vanishes in favor of increased recombination in the lower-energy ^{12}C material. Carrier confinement was achieved in diamond superlattices made up of both thinner (30 nanometers) and thicker (up to 350 nanometers) layers.

In semiconductor applications, superlattice architectures (periodic layers of materials with different band gaps) play an important role in creating quantum wells. These low-dimensional structures can exhibit high electron and hole mobilities, and they can be used to tune the emission properties of light-emitting diodes and lasers, to realize optical gratings for dielectric resonator struc-

tures, or simply to confine electrons and holes in well-defined volume fractions of hetero-junction devices. Superlattice structures are usually engineered by using different material compositions, most prominently III/V semiconductor junctions such as AlGaAs/GaAs high-electron mobility transistors (HEMTs), in which the variation of Al content gives rise to a variation of the electronic band gap (*1*). For diamond, a "wide–band-gap" semiconductor (5.48 eV), superlattice structures have not been realized as yet, because diamond cannot be alloyed with other elements (admixtures to the diamond lattice cause defect formation).

However, isotopic compositions can alter the electronic structure through electron-phonon coupling and through the change of volume with isotopic mass. These effects can be applied to realize low-dimensional superlattices from diamond. The excitonic band gap of diamond as a function of mass decreases from ^{13}C to ^{12}C by 19 meV, which is about one order of magnitude greater than for the heavier elements Si or Ge (*2*–*5*). This strong variation can be used to create a type of superlattice, based on isotope variations, that could be and will allow fabrication of two-dimensional electronic devices, such as HEMTs from diamond. In addition, atomically controlled arrangements of spatially nuclear spins (^{13}C) in combination with zero nuclear spin ^{12}C atoms are required for diamond quantum computing application (*6*–*13*).

Compositional impurities of isotopes with different masses are a common issue inherent in almost all semiconductor materials (*3*, *4*, *14*–*16*). Isotopic control is, however, an undeveloped field in semiconductor device applications, even for silicon. Hence, a control of isotope compositions in diamond offers new routes to applications far beyond conventional approaches.

Recently, we successfully used microwave plasma-assisted chemical vapor deposition to synthesize high-quality single-crystalline diamonds with controlled carbon isotope compositions (*17*). Advanced research focusing on controlled isotope composition of diamonds was performed by A. T. Collins *et al.* in 1990 (*18*). For isotopic defined diamond grown by high-pressure and high-temperature (HPHT) methods, they discovered that diamonds enriched by ^{13}C have a band gap that is 13.6 meV greater than diamonds enriched by ^{12}C. The theoretical prediction for this value is 16.5 meV (*18*). Furthermore, an energy gap of 14.6 meV was observed by T. Ruf *et al.* in 1998 (*19*). They also found that the band gap depends linearly on the ^{13}C isotopic content. In 2004, an energy gap of 18 meV for ^{13}C diamond was reported by R. Sauer *et al.* (*20*). However, any verification relating to isotopic effects in diamonds has mostly been limited to diamonds synthesized by HPHT from carbon raw materials that include a metal catalyst, which limits the purity and size of the product. The actual variation of band-gap energies and their accurate detection depends ultimately on the quality of the isotopic films and on the temperature during measurement. More recently, we revealed a band-gap shift of 19 meV (*5*) by measurements of ultraclean diamonds, and this value is greater than the theoretical prediction from (*18*).

Here we present the use of highly purified ^{12}C and ^{13}C diamond superlattices to control electron confinement, an effect not yet detected in Si (*21*) and other materials (*22*–*25*). These results indicate the use of band-gap engineering, which will allow the development of high-mobility devices using diamond quantum-well structures, an increase in light emission, and the realization of well-defined stacked isotope arrangements for quantum computing applications.

Diamond superlattice structures have been realized by homoepitaxial growth on single-crystalline diamonds substrates with alternating layers of ^{12}C and ^{13}C diamond (Fig. 1A) (*26*). Two types of layered structures were grown on synthetic diamond substrates by switching between different supply lines of isotopically enriched methane gas (either $^{12}CH_4$ or $^{13}CH_4$) and setting a fixed-growth time window. In one case, a ~870-nm-thick film of ^{12}C diamond (Fig. 1A, also shown in cross section in Fig. 2A) was grown, followed by 13 repeating cycles of ^{13}C and ^{12}C diamonds of films measuring 30 nm in thickness. The results of compositional depth profile analysis, based on secondary ion mass spectrometry (SIMS) of the derived $^{13}C/^{12}C$ diamond multilayer film (Fig. 1B) and the distribution of compositionally controlled ^{12}C and ^{13}C diamond, shows uniform layers with sharp boundaries.

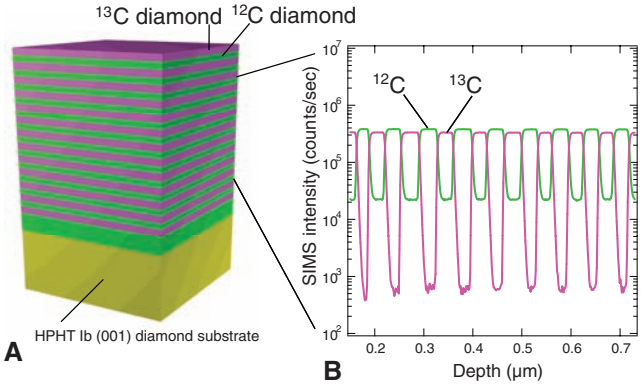

Fig. 1. (**A**) Schematic sketch of the periodic layered structures of isotopically enriched diamond films grown in this work. (**B**) Depth profiles measured by SIMS. Green represents ^{12}C diamond layers; purple represents ^{13}C layers.

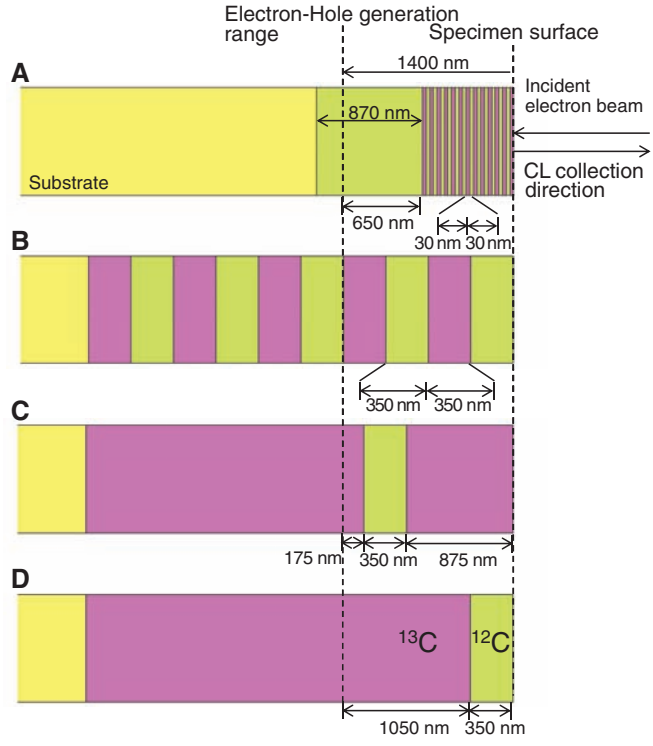

Fig. 2. (**A** to **D**) Schematic cross-sectional structures of the periodic layer of isotopically enriched diamond films used in our experiment. Green represents ^{12}C diamond layers; purple represents ^{13}C layers. Further details of the structure are provided in the text. An electron beam is incident on the sample, generating electron-hole pairs. CL are collected under 180° from the incident electron beam.

Diamond Research Center, National Institute of Advanced Industrial Science and Technology (AIST), Tsukuba Central 2-13, 1-1-1, Umezono, Tsukuba, Ibaraki 305-8568, Japan.

*To whom correspondence should be addressed. E-mail: hideyuki-watanabe@aist.go.jp

†Present address: Fraunhofer Institut für Angewandte Festkörperphysik, Tullastrasse 72, 79108 Freiburg, Germany.

We used the free-exciton emission properties to investigate the cathodoluminescence (CL) signal at 80 K from the above-described structure (Fig. 1A, also shown in cross section in Fig. 2A) and, in addition, from a superlattice consisting of only 5 repeating cycles that are ~10 times thicker (350 nm) than the 13 repeating cycles that we used previously (Fig. 2B). For comparison, we also grew a single layer of ^{12}C that was ~350 nm thick, either embedded in a thick ^{13}C film (Fig. 2C) or on top of the ^{13}C film (Fig. 2D). The electron-beam penetration depth shown in the figure was determined by the Kanaya-Okayama model (*27*). This electron-beam penetration depth is approximately equal to the range in which electron-hole pairs are generated, and it can be controlled by electron-beam accelerating voltage. We can estimate a penetration depth of ~1400 nm, based on the electron-beam accelerating voltage of 13 kV. The electrons and holes generated within the diamond form excitons (electron-hole pairs). If the crystal is of sufficiently high quality with low extrinsic purities, free-exciton recombination can be detected with a peak energy at 5.27 eV (*28*).

Figure 3 shows CL spectra taken at 80 K from the samples shown in Fig. 2. To determine the peak positions, we used one asymmetric function to fit the spectra. As shown in Fig. 3A, a single peak was observed at 5.281 eV. This spectrum can be explained as the free-exciton emission from the ^{12}C diamond with transverse optical phonons. No peak was detected for ^{13}C. In contrast, in Fig. 3, C and D, this spectrum consists of two components with peaks at 5.280 and 5.297 eV, respectively, with the expected energy difference of 17 meV.

We can account for these results with the use of a simple energy diagram of the superlattice (Fig. 4A) to explain the exciton emission spectrum observed from the layered structures shown in Fig. 3, A and B. Here, the band-gap energy difference is fixed at the experimental value of 17 meV, but the relation between E_c and E_V is only speculative (E_c is conduction band-edge and E_V is valence band-edge). Excitonic emission is not observed from the higher-energy band gap of ^{13}C, but it was observed from the ^{12}C layer, which is lower in energy. The carriers that form in the ^{13}C layer migrate by carrier diffusion into the lower-energy ^{12}C layers. This result suggests that carrier confinement is possible for diamond by means of potential set up by layers of different isotopic composition. In comparison, the energy difference in the heavier elements is much less: In silicon (^{30}Si to ^{28}Si), it is only 1 meV (*16*), and in germanium (^{76}Ge to ^{70}Ge), it is even less (0.36 meV) (*16*). Comparable results for superlattices have not been reported in these materials.

In conventional abrupt heterojunction structures, carriers recombine at the junction interface, and graded structures are adopted to minimize the recombination. However, in our structure, relatively high emission efficiency from the ^{12}C layer is observed, as shown for the 30-nm multilayers with 25 junction interfaces, as well as for the 350-nm multilayers with only 3 interfaces. This similarity indicates that the recombination at the homojunction interface is rather low and the junction quality high, and also that the excess carriers in isotopically pure diamond have long lifetimes and long diffusion lengths (at least 175 nm). Thus, high-quality homojunction band engineering can be achieved with the use of isotopically well-defined diamond.

We assume that the CL signal originates only from the recombination of excess carriers distributed in the crystal as a result of electron-beam excitation. The exciton emission intensity generated by CL excitation is proportional to the integral of

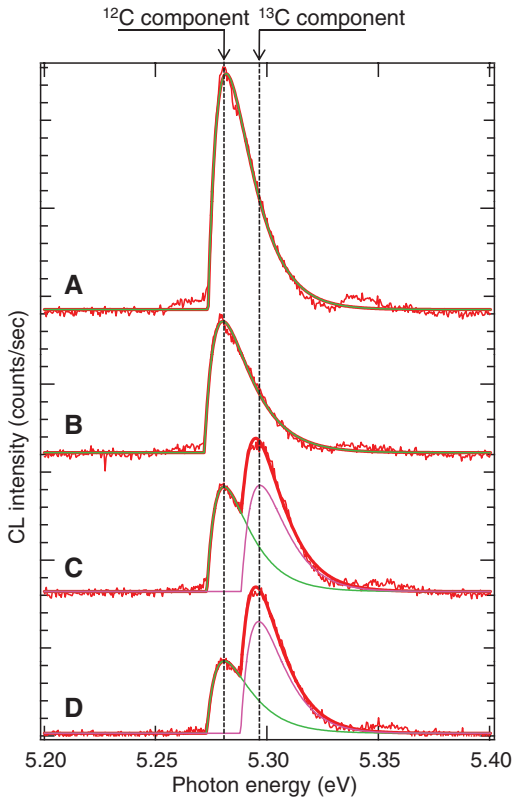

Fig. 3. (**A** to **D**) Spectra correspond respectively to layered structures [(A) to (D)] shown in Fig. 2. The thick red line shows one fitting of an experimental spectrum. The observation temperature was 80 K.

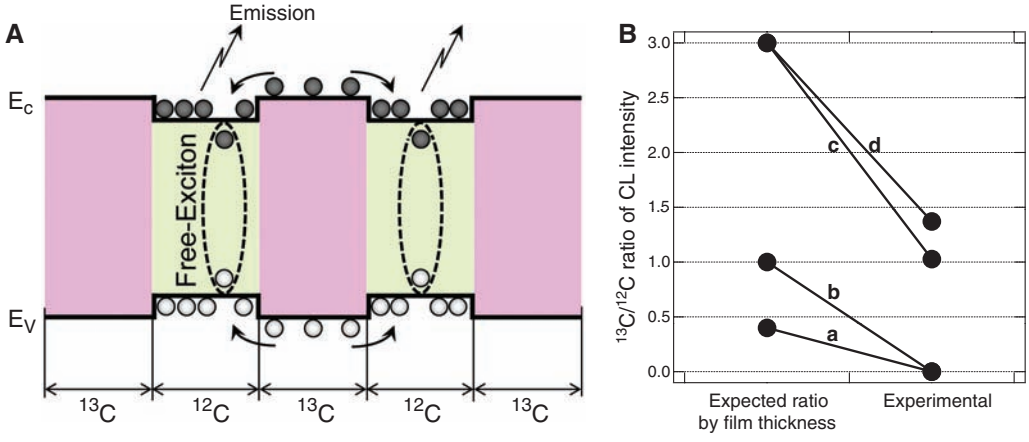

Fig. 4. (**A**) Energy band diagram. Simplified schematic diagram of arrangements of the confinement of electrons and holes in the periodic layered structures of isotopically enriched diamond films (Fig. 3, A and B) showing the observed excitonic spectra. E_c and E_V are conduction band-edge and valence band-edge, respectively. (**B**) Changes in $^{13}C/^{12}C$ ratio of CL integrated luminescence intensity. The behaviors of "a" to "d" correspond, respectively, to the (A) to (D) spectra results shown in Fig. 3.

the concentration of carriers distributed throughout the generating range of the electron beam [$\Delta n(z)$].

$$I_{CL} \propto \int_V \frac{\Delta n(z)}{\tau_r} dz \quad (1)$$

In this formula, τ_r is the life of the carriers that contribute to radiative recombination, V is the generation volume, and z is a depth. On the basis of this assumption, the CL intensity (I_{CL}) is simply proportional to the film thickness. The expected CL intensity ratios of ^{13}C to ^{12}C, calculated from the thicknesses of the multilayer structures, are shown in Fig. 4B. All of the experimental data show dramatic decreases, accompanied by a decrease of emission from ^{13}C layers and the related increase from ^{12}C layers. Even for the structures in Fig. 2, C and D, which consist of a ^{12}C single layer in ^{13}C, the intensity (I) ratio $I[^{13}C]/I[^{12}C]$ decreases from 1/2 to 1/3, with respect to the expected ratio. These phenomena indicate that a large diffusion length of the excited carriers plays an important role. Several studies have reported diffusion lengths in natural isotopic mixtures of diamond that range from 500 nm to 250 μm (*29*–*31*). Our results indicate that almost all carriers generated in our samples diffuse at least 175 nm and may diffuse up to several hundred nanometers.

References and Notes

1. H. Ehrenreich, D. Turnbull, Eds., *Solid State Physics: Advances in Research Applications,* vol. 44 (Academic Press, New York, 1991).
2. J. W. Ager III, E. E. Haller, *Phys. Stat. Sol. A* **203**, 3550 (2006).
3. E. E. Haller, *Solid State Commun.* **133**, 693 (2005).
4. K. M. Itoh, E. E. Haller, *Phys. E* **10**, 463 (2001).
5. H. Watanabe, C. E. Nebel, S. Shikata, *Proc. New Diamond Nano Carbons* **2**, 202 (2008).
6. L. Childress *et al*., *Science* **314**, 281 (2006); published online 13 September 2006 (10.1126/science.1131871).
7. S. Prawer, A. D. Greentree, *Science* **320**, 1601 (2008).
8. Z. Yuan *et al*., *Science* **295**, 102 (2002); published online 13 December 2001 (10.1126/science.1066790).
9. J. J. L. Morton, *Nat. Phys.* **2**, 365 (2006).
10. T. Gaebel *et al*., *Nat. Phys.* **2**, 408 (2006).
11. J. R. Maze *et al*., *Nature* **455**, 644 (2008).
12. J. M. Taylor *et al*., *Nat. Phys.* **4**, 810 (2008).
13. P. Neumann *et al*., *Science* **320**, 1326 (2008).
14. V. G. Plekhanov, *Prog. Mater. Sci.* **51**, 287 (2006).
15. F. Widulle *et al*., *Solid State Commun.* **118**, 1 (2001).
16. M. Cardona, M. L. W. Thewalt, *Rev. Mod. Phys.* **77**, 1173 (2005).
17. H. Watanabe, C. E. Nebel, *Diamond Relat. Mater.* **17**, 511 (2008).
18. A. T. Collins, S. C. Lawson, G. Davies, H. Kanda, *Phys. Rev. Lett.* **65**, 891 (1990).
19. T. Ruf *et al*., *Solid State Commun.* **105**, 311 (1998).
20. R. Sauer, N. Teofilov, K. Thonke, *Diamond Relat. Mater.* **13**, 691 (2004).
21. T. Kojima, R. Nebashi, K. M. Itoh, Y. Shiraki, *Appl. Phys. Lett.* **83**, 2318 (2003).
22. T. Y. Tan *et al*., *J. Appl. Phys.* **72**, 5206 (1992).
23. J. Spitzer *et al*., *Phys. Rev. Lett.* **72**, 1565 (1994).
24. K. Morita *et al*., *Thin Solid Films* **369**, 405 (2000).
25. M. Nakajima *et al*., *Phys. Rev. B* **63**, 161304 (2001).
26. Materials and methods are available as supporting material on *Science* Online.
27. K. Kanaya, S. Okayama, *J. Phys. D* **5**, 43 (1972).
28. H. Watanabe *et al*., *Appl. Phys. Lett.* **73**, 981 (1998).
29. T. Malinauskas *et al*., *Diamond Relat. Mater.* **17**, 1212 (2008).
30. T. Teraji, S. Yoshizaki, S. Mitani, T. Watanabe, T. Ito, *J. Appl. Phys.* **96**, 7300 (2004).
31. J. Ristein, W. Stein, L. Ley, *Phys. Rev. Lett.* **78**, 1803 (1997).

32. The authors thank N. Fujimori (Diamond Research Center, AIST) and K. Kajimura (Technical Research Institute, Japan Society for the Promotion of Machine Industry) for their support and encouragement during the early days of the study.

Supporting Online Material

www.sciencemag.org/cgi/content/full/324/5933/1425/DC1
Materials and Methods

17 February 2009; accepted 20 April 2009
10.1126/science.1172419

Measuring the Charge State of an Adatom with Noncontact Atomic Force Microscopy

Leo Gross,[1]* Fabian Mohn,[1] Peter Liljeroth,[1,2] Jascha Repp,[1,3] Franz J. Giessibl,[3] Gerhard Meyer[1]

Charge states of atoms can be investigated with scanning tunneling microscopy, but this method requires a conducting substrate. We investigated the charge-switching of individual adsorbed gold and silver atoms (adatoms) on ultrathin NaCl films on Cu(111) using a qPlus tuning fork atomic force microscope (AFM) operated at 5 kelvin with oscillation amplitudes in the subangstrom regime. Charging of a gold atom by one electron charge increases the force on the AFM tip by a few piconewtons. Moreover, the local contact potential difference is shifted depending on the sign of the charge and allows the discrimination of positively charged, neutral, and negatively charged atoms. The combination of single-electron charge sensitivity and atomic lateral resolution should foster investigations of molecular electronics, photonics, catalysis, and solar photoconversion.

Recently, tremendous progress has been made in atomic force microscopy (AFM). For example, chemical sensitivity on the atomic scale (*1*), manipulation of atoms laterally (*2*) and vertically (*3*), and the measurement of lateral forces during atomic manipulation (*4*) have been demonstrated. The resolution of local contact potential difference (LCPD) maps acquired with kelvin probe force microscopy (KPFM) (*5*) has also been pushed to the atomic scale (*6*–*10*).

In this paper, we present the measurement of single-electron charges with atomic resolution by use of AFM. The charge state and charge distribution of adsorbates are an important property that governs many physical and chemical processes and moreover can be exploited in single-electron devices (*11*, *12*). Single-electron devices have attracted considerable attention because they exhibit interesting physical properties and functionalities, such as Coulomb blockade and the Kondo effect. To investigate such devices and the underlying physics at the ultimate spatial limit, it is essential that single-electron charges can be probed directly and with atomic resolution. For example, the ability to map the charge distribution of a single molecular charge-transfer complex will deepen the basic understanding of and advance the search for materials for molecular electronics and organic photovoltaic cells. Furthermore, important insight into catalytic processes will be gained because the charge state also governs the catalytic reactivity of adsorbates (*13*). Most of the systems of relevance in this area involve insulators as a prerequisite to separate charges.

Probing the charge state of single adatoms has recently been demonstrated with scanning tunneling microscopy (STM) (*14*–*16*). However, this indirect measurement requires a conducting tunneling junction, which is incompatible with insulators. In contrast, electrostatic force measurements performed with noncontact AFM (NC-AFM) can achieve single-electron sensitivity (*17*–*23*). In most of these studies, the micromechanical cantilevers have oscillation amplitudes in the 10 to 50 Å regime. Such large amplitudes increase the sensitivity to long-range electrostatic forces but limit the resolution of short-range chemical forces and therefore the spatial resolution. For atomic resolution, oscillation amplitudes on the order of 1 Å are desirable (*24*). In this work, we demonstrate the switching and direct measurement of the charge state of a single atom with AFM. Our approach combines electrostatic force microscopy of single-electron sensitivity with lateral atomic resolution. We image and identify differently charged individual atoms, and measure the difference in

[1]IBM Research, Zurich Research Laboratory, 8803 Rüschlikon, Switzerland. [2]Debye Institute for Nanomaterials Science, Utrecht University, Post Office Box 80000, 3508 TA Utrecht, Netherlands. [3]Institute of Experimental and Applied Physics, University of Regensburg, 93040 Regensburg, Germany.

*To whom correspondence should be addressed. E-mail: lgr@zurich.ibm.com

vertical force and LCPD caused by single-electron charging.

The low-temperature STM/AFM is based on a qPlus sensor design (*25*) operated in ultra-high vacuum at a temperature of ~5 K. A metal tip (*26*) is mounted on the free prong of the tuning fork, and a separate tip wire (that is insulated from the electrodes of the tuning fork) is installed to measure the tunneling current. The bias voltage V is applied to the sample. The high stiffness of the tuning fork [spring constant (k) = 1.8 × 10^3 N/m, resonance frequency (f_0) = 23 kHz, and mechanical quality factor (Q) = 5 × 10^4] allows stable operation at subangstrom oscillation amplitudes A (down to A = 0.2 Å) in the frequency modulation mode (*27*). As a model system, we used single Au and Ag adatoms on 2-monolayer (ML)–thick NaCl films on Cu(111) (Fig. 1A). Previous studies (*14*, *15*) have shown that the adatoms can be switched reversibly between different charge states by applying suitable bias pulses with the STM tip. The NaCl layers are thin enough to permit the tunneling of electrons but can stabilize a single charge on the metal adatom through ionic relaxation in the NaCl film. The differently charged atoms have been identified by means of STM, scanning tunneling spectroscopy (STS), as well as comparison with density functional theory (DFT) (*14*, *15*). Below, we describe how we can resolve the charge state of individual atoms directly from AFM measurements.

In a constant-current STM measurement (Fig. 1B), a negatively charged gold adatom (Au^-) is identified by its surrounding depression (sombrero-shaped) and its smaller apparent height (h) [$h(Au^-) \approx$ 1.5 Å] with respect to a neutral Au adatom Au^0 [$h(Au^0) \approx 2.0$Å] (*14*). The same atoms were then imaged in constant-height mode, and the tunneling current (Fig. 1C) as well as the frequency-shift (Δf) signal (Fig. 1D) were recorded simultaneously. The larger absolute value of the tunneling current above Au^0 than above Au^- is in agreement with its larger apparent height in constant-current STM images. In the Δf image (Fig. 1D, inset), taken with NC-AFM, the adatoms are resolved as circular depressions with a diameter (full width at half maximum) of 6.5 and 5.5 Å for Au^0 and Au^-, respectively. The peak frequency shift measured above the negatively charged Au^- [$\Delta f(Au^-) = -1.86$ Hz] is, in absolute values, greater than above Au^0 [$\Delta f(Au^0) = -1.39$ Hz]. Figure 2A shows constant-height line scans above these two adatoms recorded at decreasing tip-to-sample distances Δz.

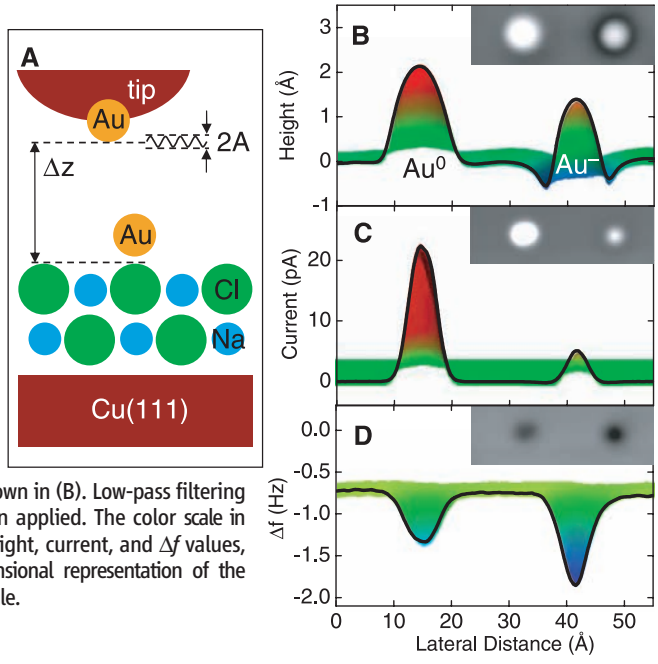

Fig. 1. (**A**) Model of the tip-sample geometry, showing the definition of the oscillation amplitude A and the tip height Δz (*26*). (**B**) Constant-current STM measurement [V = –50 mV and current (I) = 2 pA] of Au^0 (left) and Au^- (right) adsorbed on NaCl(2 ML)/Cu(111). The line scan is through the center of both atoms shown in the inset (image size of insets is 55 Å by 17 Å). (**C**) Current and (**D**) frequency shift recorded simultaneously in a constant-height measurement (Δz = 5.0 Å, V = –5 mV, and A = 0.3 Å) of the same area as shown in (B). Low-pass filtering (adjacent averaging) has been applied. The color scale in (B) to (D) corresponds to the height, current, and Δf values, respectively, in a three-dimensional representation of the images, cut along the line profile.

We used the method described by Sader and Jarvis (*28*) to deconvolve the oscillation amplitude from Δf and extract the vertical force from the constant-height line scans (*26*). In Fig. 2B, we plot the vertical force component; the background of the force from the substrate has been subtracted. The line scan at closest tip approach, corresponding to a tip height of 4.8 Å, shows an attractive force that is 11 pN greater above the negatively charged Au atom than it is above the neutral atom. The resolution in the force was better than 1 pN, and the charged atom could already be detected at a tip height of 6 Å, revealing a force that is about 2 pN greater than that above Au^0. A very high stability of the experimental system was needed for measuring forces in the piconewton regime. Charge screening by the insulating film [that is, ionic relaxations in the topmost NaCl layer as inferred from DFT calculations (*14*, *15*)] and image charges at the Cu interface make the forces so small. Approaching the tip further in order to increase the forces resulted in unintended charge switching and lateral manipulation of the adatoms.

It is known from DFT calculations that a Au adatom relaxes by about 0.4 Å toward the substrate when it becomes negatively charged (*14*). Just from this topographic difference, we would expect an effect in the direction opposite (a decrease of $|\Delta f|$) to that of the observed shift. We assigned the observed shift above the negatively charged Au^- to electrostatic interactions that overcompensate the topographic effect.

We investigated the switching event itself and its effect on the frequency shift and on the LCPD by measuring Δf with respect to the sample bias V. We specify the LCPD from measurements of V_{CPD} = (1/e) × LCPD (where e is the electron charge) by determining the peak position of the parabola obtained in a $\Delta f(V)$ measurement at a given tip position. The corresponding maximum in $\Delta f(V)$ is Δf^*, that is, Δf at compensated V_{CPD}. Without changing the tip height and position, we first (i) measured $\Delta f(V)$ above Au^-, then (ii) applied a bias voltage pulse of about –1 V so as to

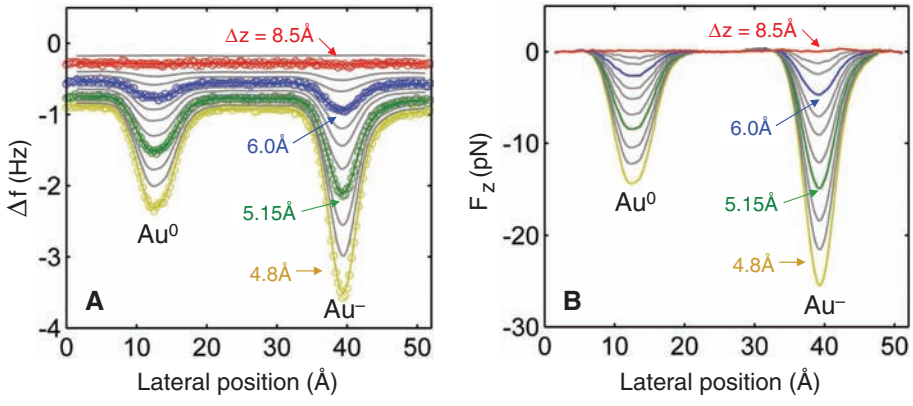

Fig. 2. (**A**) Frequency shift Δf recorded at a constant height (A = 0.22 Å and V = –2 mV) above Au^0 and Au^-. Different line scans correspond to different tip heights Δz as indicated. For some curves, every eighth point of the raw data are shown as an open circle in Fig. 2A; the solid lines correspond to the averaged data. (**B**) Vertical force F_z* extracted from the averaged data in (A) with the oscillation amplitude deconvolved and the constant background force subtracted from each curve (*26*).

switch the charge state (*14*), and finally (iii) measured $\Delta f(V)$ once more, as shown in Fig. 3A (*26*). To confirm that the switching event occurred and to verify that the switched atom did not change its lateral position, STM images were taken before and after this routine (Fig. 3, B and C). Performing the measurement under these conditions, and without moving the tip, ensured that the observed effects did not arise from tip changes, different tip heights, or spatial variations of the LCPD of the substrate. For typical experimental parameters, such as A = 0.6 Å and Δz = 5.8 Å, which result in a total frequency shift of about Δf = –3 Hz, we observed that the V_{CPD} of Au^- shifted by (+27 ± 8) mV with respect to Au^0. The corresponding Δf^* shifted by (–0.11 ± 0.03) Hz on Au^- as compared with Au^0.

Quantitatively, these values crucially depend on the exact tip shape (*9*, *29*), but we always observe a larger attractive force (a larger $|\Delta f^*|$) and a larger LCPD for Au^- than for Au^0. We attribute the shift in $|\Delta f^*|$ primarily to the interaction of the charged atom and its image charge induced in the AFM tip that was negligible in previous experiments (*19*, *23*, *26*). However, this is the main contribution to the observed contrast in Fig. 1D and Fig. 2. The shift in the LCPD can be explained by a dipole moment directed from the vacuum to the surface and induced by the negative Au^- (and its screening charge in the underlying substrate). Hence, the work function at the adatom position increases locally (*8*); the sample has to be biased more positively to compensate for the negative charge on the adatom.

To prove that positive, neutral, and negative charge states can be distinguished and determined with AFM, we included measurements of silver adatoms. For Ag, both the neutral Ag^0 and the positively charged Ag^+ adatoms are stable on NaCl(2 ML)/Cu(111) (*15*). Figure 4A shows a STM measurement of Au and Ag adatoms in their different possible charge states. Several $\Delta f(V)$ measurements were performed above these atoms at different tip-sample separations Δz, without a tip change between measurements and without switching the charge states. For each $\Delta f(V)$ measurement, we determined the peak position of the parabola, meaning the LCPD and the corresponding Δf^*. Figure 4B shows the LCPD plotted versus the tip height Δz. First, we compared the LCPD of NaCl(2 ML)/Cu(111) with that of the bare Cu(111) surface. The NaCl layer lowers the work function of the Cu surface, so we expected a decrease of the LCPD of NaCl(2 ML)/Cu(111) with respect to that of Cu(111). This is exactly what we observed, but in addition this effect increases with decreasing Δz. The latter observation is explained by an averaging effect, in which the sample area that contributes to the LCPD becomes larger with increasing Δz. The closer we approach the tip toward the NaCl island, the smaller the effect of the surrounding Cu(111) surface becomes, which explains the shift to smaller LCPD as the tip approaches the NaCl island (*26*).

For tip heights larger than 18 Å, the LCPD above the adatoms on the NaCl island are of similar value (within 100 mV). At smaller Δz, the effects arising from the adatom predominate, and the differently charged atoms can be distinguished by their LCPD for Δz < 10 Å. We observed that the LCPD of Ag^+ is smaller and that the LCPD of Au^- is larger than that of the corresponding neutral adatoms. The absolute values of these differences depend on the tip shape, but the direction of the LCPD shift is always determined by the direction of the dipole induced by the charged adatom.

In Fig. 4C, we plot the LCPD as a function of Δf^* for the same data as shown in Fig. 4B. This representation corresponds to a KPFM measurement and shows the LCPD at a given frequency shift with the contact potential compensated. Measuring these values at constant height without a feedback loop for either Δz or V (which is in contrast to usual KPFM measurements) increases the stability and sensitivity and allows the use of small oscillation amplitudes. In Fig. 4C, the contrast between the different species increases with more negative values of Δf^*. With decreasing Δz (and hence increasing $|\Delta f^*|$), the effect of the single atom becomes more pronounced as compared with the background forces from the substrate, and we observe that the LCPD shifts into different directions for the differently charged atoms. These measurements demonstrate that the charge state of neutral, positively, and negatively charged adatoms can be determined by measuring their LCPD at a certain tip height Δz or frequency shift Δf.

It should be possible to measure the transport of single-electron charges on insulating surfaces. For example, single atoms or small clusters acting as redox sites could be connected with molecules to form metal-molecular networks. By using the tip for charging the redox

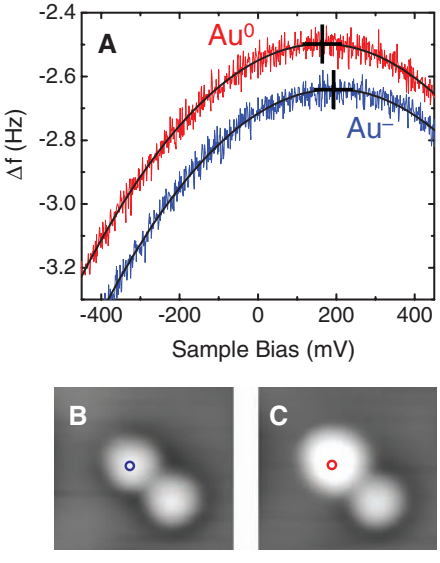

Fig. 3. (**A**) Frequency shift measured as a function of the voltage above Au^- and Au^0. Both measurements are performed without moving the tip (A = 0.6 Å and Δz = 5.8 Å; raw data). After measuring $\Delta f(V)$ above Au^-, the charge state is switched to Au^0 by applying a bias pulse of V = –1 V for a few seconds (*26*). Parabolic fits and corresponding parabola peaks are indicated. STM images (I = 7.4 pA, V = –50 mV, and size = 29 Å by 27 Å) before (**B**) and after (**C**) the $\Delta f(V)$ measurements confirm the charge-switching event and show that the switched Au atom has maintained its lateral position.

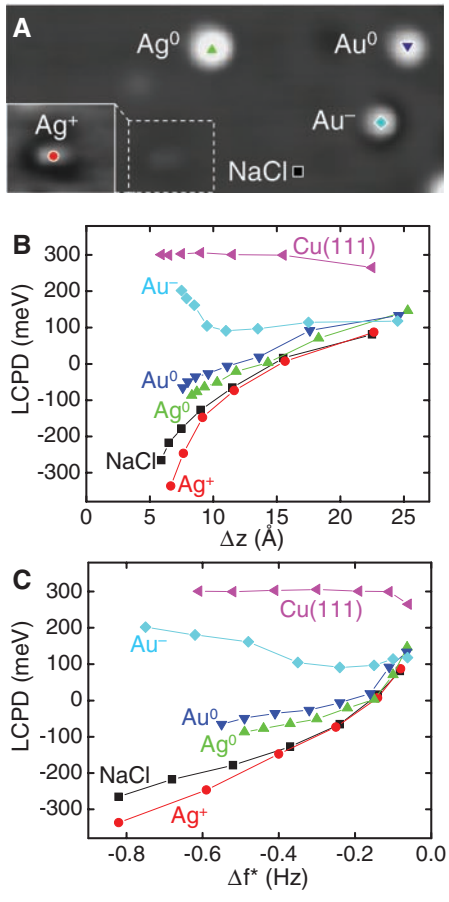

Fig. 4. (**A**) Constant-current STM image (I = 3 pA, V = 200 mV, and size = 130 Å by 60 Å) of Ag^+, Ag^0, Au^0, and Au^- on NaCl(2 ML)/Cu(111). The inset shows the Ag^+ adatom with fivefold increased z-contrast. (**B**) LCPD above atoms with different charge states and on NaCl(2 ML)/Cu(111) at the positions indicated in (A) and on Cu(111). At each site, $\Delta f(V)$ is measured for different tip heights Δz with respect to the NaCl surface [on Cu(111) with respect to point of contact with the metal]. Each $\Delta f(V)$ measurement is fitted with a parabola, yielding the LCPD and the corresponding frequency shift Δf^*. LCPD is shown as a function of Δz. (**C**) LCPD shown as a function of Δf^*; that is, corresponding to a KPFM measurement. The complete set of measurements has been performed without a tip change between measurements (*29*). Lines serve as a guide to the eye. The errors in Δz, LCPD, and Δf^* estimated from repeated measurements are ±0.2 Å, ±15 meV, and ±30 mHz, respectively.

sites, electrons can be injected into this network, and their propagation in the network could be observed with NC-AFM as described above. While STM is not ideally suited for this purpose because it relies on the tunneling of electrons (the unintended charging caused by the measurement and discharging of the structures via the substrate constitute a problem in STM experiments), we have shown that electrostatic AFM can enable the investigation of the charge landscape and of charge transport in metal-molecular nanostructures with atomic resolution.

References and Notes

1. Y. Sugimoto *et al.*, *Nature* **446**, 64 (2007).
2. Y. Sugimoto *et al.*, *Nat. Mater.* **4**, 156 (2005).
3. Y. Sugimoto *et al.*, *Science* **322**, 413 (2008).
4. M. Ternes, C. P. Lutz, C. F. Hirjibehedin, F. J. Giessibl, A. J. Heinrich, *Science* **319**, 1066 (2008).
5. M. Nonnenmacher, M. P. O'Boyle, H. K. Wickramasinghe, *Appl. Phys. Lett.* **58**, 2921 (1991).
6. S. Kitamura, K. Suzuki, M. Iwatsuki, C. B. Mooney, *Appl. Surf. Sci.* **157**, 222 (2000).
7. K. Okamoto, Y. Sugawara, S. Morita, *Appl. Surf. Sci.* **188**, 381 (2002).
8. M. Ikeda, N. Koide, L. Han, A. Sasahara, H. Onishi, *J. Phys. Chem. C* **112**, 6961 (2008).
9. G. H. Enevoldsen, T. Glatzel, M. C. Christensen, J. V. Lauritsen, F. Besenbacher, *Phys. Rev. Lett.* **100**, 236104 (2008).
10. F. Bocquet, L. Nony, C. Loppacher, T. Glatzel, *Phys. Rev. B* **78**, 035410 (2008).
11. K. Uchida, in *Nanoelectronics and Information Technology: Advanced Electronic Materials and Novel Devices*, R. Waser, Ed. (Wiley, New York, 2003), chap. 16.
12. K. K. Likharev, *IEEE Proc.* **87**, 606 (1999).
13. M. Haruta, *Catal. Today* **36**, 153 (1997).
14. J. Repp, G. Meyer, F. E. Olsson, M. Persson, *Science* **305**, 493 (2004).
15. F. E. Olsson, S. Paavilainen, M. Persson, J. Repp, G. Meyer, *Phys. Rev. Lett.* **98**, 176803 (2007).
16. M. Sterrer *et al.*, *Phys. Rev. Lett.* **98**, 096107 (2007).
17. C. Schoenenberger, S. F. Alvarado, *Phys. Rev. Lett.* **65**, 3162 (1990).
18. L. J. Klein, C. C. Williams, *Appl. Phys. Lett.* **79**, 1828 (2001).
19. R. Stomp *et al.*, *Phys. Rev. Lett.* **94**, 056802 (2005).
20. J. Zhu, M. Brink, P. L. McEuen, *Appl. Phys. Lett.* **87**, 242102 (2005).
21. E. Bussmann, N. Zheng, C. C. Williams, *Appl. Phys. Lett.* **86**, 163109 (2005).
22. E. Bussmann, C. C. Williams, *Appl. Phys. Lett.* **88**, 263108 (2006).
23. Y. Azuma, M. Kanehara, T. Teranishi, Y. Majima, *Phys. Rev. Lett.* **96**, 016108 (2006).
24. F. J. Giessibl, *Rev. Mod. Phys.* **75**, 949 (2003).
25. F. J. Giessibl, *Appl. Phys. Lett.* **76**, 1470 (2000).
26. Materials and methods are available as supporting material on *Science* Online.
27. T. Albrecht, P. Grütter, D. Horne, D. Rugar, *J. Appl. Phys.* **69**, 668 (1991).
28. J. E. Sader, S. P. Jarvis, *Appl. Phys. Lett.* **84**, 1801 (2004).

29. We observed that the LCPD and Δf^* are crucially dependent on the tip. However, the direction of the observed shifts in the LCPD and in Δf^* because of the atoms' charge state are not tip-dependent, allowing the determination of the charge states by comparison. In general, we observed higher shifts in the LCPD for smaller tip-sample separations and for tips exhibiting a small background force (that is, presumably very sharp tips).

30. We thank R. Allenspach for valuable comments. This work was supported by the Swiss National Center of Competence in Research (NCCR) "Nanoscale Science" and by the European Union project "NanoMan." P.L. and J.R. gratefully acknowledge funding by the Nederlandse Organisatie voor Wetenschappelijk Onderzoek (Chemical Sciences, Vidi-grant 700.56.423) and Volkswagen Foundation through its Lichtenberg program, respectively.

Supporting Online Material

www.sciencemag.org/cgi/content/full/324/5933/1428/DC1
Materials and Methods
SOM Text
Figs. S1 and S2
References

13 February 2009; accepted 1 May 2009
10.1126/science.1172273

Oxygen-18 of O_2 Records the Impact of Abrupt Climate Change on the Terrestrial Biosphere

Jeffrey P. Severinghaus,[1]* Ross Beaudette,[1] Melissa A. Headly,[1]† Kendrick Taylor,[2] Edward J. Brook[3]

Photosynthesis and respiration occur widely on Earth's surface, and the $^{18}O/^{16}O$ ratio of the oxygen produced and consumed varies with climatic conditions. As a consequence, the history of climate is reflected in the deviation of the $^{18}O/^{16}O$ of air ($\delta^{18}O_{atm}$) from seawater $\delta^{18}O$ (known as the Dole effect). We report variations in $\delta^{18}O_{atm}$ over the past 60,000 years related to Heinrich and Dansgaard-Oeschger events, two modes of abrupt climate change observed during the last ice age. Correlations with cave records support the hypothesis that the Dole effect is primarily governed by the strength of the Asian and North African monsoons and confirm that widespread changes in low-latitude terrestrial rainfall accompanied abrupt climate change. The rapid $\delta^{18}O_{atm}$ changes can also be used to synchronize ice records by providing global time markers.

The mechanism of abrupt climate change, in particular the Heinrich and Dansgaard-Oeschger (D/O) events of the last ice age, remains poorly understood (*1*). One barrier is the dearth of information about the spatial extent of the events, due in part to the paucity of low-latitude paleoclimate records with sufficient dating precision to establish whether events are synchronous, time-transgressive, or unrelated (*2*). Cave stalagmite $\delta^{18}O$ records with radiometric U/Th dating are a notable exception (*3*–*6*), but these are still spot records with generally unknown spatial importance. Atmospheric gas records from ice cores can help address the spatial issue because the atmosphere acts as an integrator of innumerable gas fluxes over broad spatial scales. Methane has been used in this capacity (*7*), but methane production is dominated by rather special settings (e.g., high-productivity anoxic wetland soils). Oxygen (O_2), in contrast, is produced widely in the low latitudes by photosynthesis, making it a more ideal tracer of the spatial extent and global importance of climate change. In particular, the isotopic composition of oxygen produced on land varies strongly with environmental conditions, making it a unique tracer of the impact of climate on the terrestrial biosphere (*8*–*11*).

The $^{18}O/^{16}O$ ratio of atmospheric molecular oxygen ($\delta^{18}O_{atm}$) is known to vary on orbital time scales in response to the growth of ice sheets and changes in biogeochemical fractionation (*8*–*11*), with a typical glacial-interglacial range of ~1.5 per mil (‰). The substrate for all photosynthetic oxygen production is water, and the isotopic composition of the water ($H_2{}^{18}O/H_2{}^{16}O$) in which photosynthesis occurs is transferred to O_2 (*12*). Thus, variations in water $\delta^{18}O$ at the site of photosynthesis (i.e., the chloroplast) are a primary cause of variation in $\delta^{18}O_{atm}$ (*13*). Ice sheet growth and decay, with attendant change in seawater $\delta^{18}O$ (and thus all meteoric water), causes roughly half of the variation. The balance is due to changes in hydrological cycle fractionation during condensation and evaporation that affect chloroplast water $\delta^{18}O$, and fractionation by the respiratory sink of O_2 (*10*, *11*). These fractionation processes collectively create a steady-state offset between seawater $\delta^{18}O$ and the $\delta^{18}O$ of O_2, known as the Dole effect, which today amounts to +23.88‰ (*14*).

Past variations in the Dole effect are known to occur on orbital time scales, chiefly the 23,000-year (23 ky) precession period (*10*, *11*). These variations are likely due to the Asian and African monsoon variations that occur on this time scale because of the impact of precession on summer insolation (*15*, *16*), although other factors may also contribute, and the subject is currently not well understood. Faster variations have generally not been expected because of the ~1000-year turnover time of atmospheric O_2.

[1]Scripps Institution of Oceanography, University of California, San Diego, CA 92093–0244, USA. [2]Desert Research Institute, Nevada System of Higher Education, 2215 Raggio Boulevard, Reno, NV 89512, USA. [3]Department of Geosciences, Oregon State University, Corvallis, OR 97331, USA.

*To whom correspondence should be addressed. E-mail: jseveringhaus@ucsd.edu

†Present address: The Pennington School, 112 West Delaware Avenue, Pennington, NJ 08534, USA.

This view was challenged by recent high-precision and high-resolution measurements in the North Greenland Ice Core Project (NGRIP) ice core between 60,000 and 75,000 years ago (60 to 75 ka), which showed rapid millennial-scale variations in $\delta^{18}O_{atm}$ (*17*). Here, we extend this finding to the complete 0- to 100-ka interval with a new $\delta^{18}O_{atm}$ record from the Siple Dome ice core, Antarctica, and a short record (24 to 14 ka) from the Greenland Ice Sheet Project 2 (GISP2) ice core, Greenland. We analyzed samples in duplicate for $\delta^{15}N$, $\delta^{18}O$ of O_2, $\delta O_2/N_2$, and $\delta Ar/N_2$ following established procedures (*18*–*20*). We use the customary notation $\delta^{18}O = [(^{18}O^{16}O/^{16}O_2)_{sample}/(^{18}O^{16}O/^{16}O_2)_{reference} - 1]‰$, and the reference for all four measured gases is the modern atmosphere in La Jolla in 2006.

In addition to the previously known orbital variation, the new $\delta^{18}O_{atm}$ record shows variations on the millennial scale (Fig. 1). Their appearance in multiple ice core records confirms that they are real atmospheric features and not artifacts (*19*).

Prominent cold periods in the Northern Hemisphere known as Heinrich stadials (*21*, *22*) appear as positive anomalies of ~0.15‰ in $\delta^{18}O_{atm}$, or positive changes in the derivative (Fig. 1; note that the $\delta^{18}O_{atm}$ scale is inverted, following convention). Generally, the signature of the cold stadial phases of the D/O events (termed D/O stadials) is more muted but still recognizable, especially for the longer events (Fig. 2).

To further explore the isotopic fluxes from land to atmosphere and associated climatic changes, we take the derivative of the data and account for the effects of oceanic processes. Because the ~1000-year turnover time of O_2 in the atmosphere acts as an integrator, imparting a smoothing to the record of isotopic fluxes to the atmosphere, we remove the smoothing effect with a one-box model deconvolution (*19*).

$$\Delta\varepsilon_{LAND} = \left[\tau\frac{d\delta_{atm}}{dt} + \delta_{atm} - \delta_{seawater}\right]\frac{1}{f_L} \quad (1)$$

Here, $\Delta\varepsilon_{LAND}$ is an empirical parameter that represents the lumped changes over time in the terrestrial hydrological and respiratory fractionations that create the changes in the Dole effect, τ is the turnover time of 1000 years, the derivative is calculated from a least-squares Fourier-series fit to the $\delta^{18}O_{atm}$ time series data, $\delta_{seawater}$ is an estimate of seawater $\delta^{18}O$ through time (*23*), and f_L is the fraction of total oxygenesis occurring on land (taken to be 0.65) (*19*). Although it is unlikely that f_L is constant in time, we neglect changes in f_L based on recent findings that the intrinsic fractionation of terrestrial and oceanic processes contributing to the Dole effect are more similar than previously believed (*24*–*27*), so variations in their relative oxygen production will have little influence on the Dole effect.

We urge caution in interpreting the fractionation parameter $\Delta\varepsilon_{LAND}$, because the seawater $\delta^{18}O$ curve is highly smoothed in comparison to our high-frequency $\delta^{18}O_{atm}$ curve. This could have the effect of creating spurious changes in $\Delta\varepsilon_{LAND}$ during stadials (if the smoothing has removed a positive anomaly in seawater $\delta^{18}O$) or an underestimate of the amplitude of the millennial-scale positive anomalies in $\Delta\varepsilon_{LAND}$ (if the smoothing has removed a negative anomaly in seawater $\delta^{18}O$). We argue that the latter possibility is the

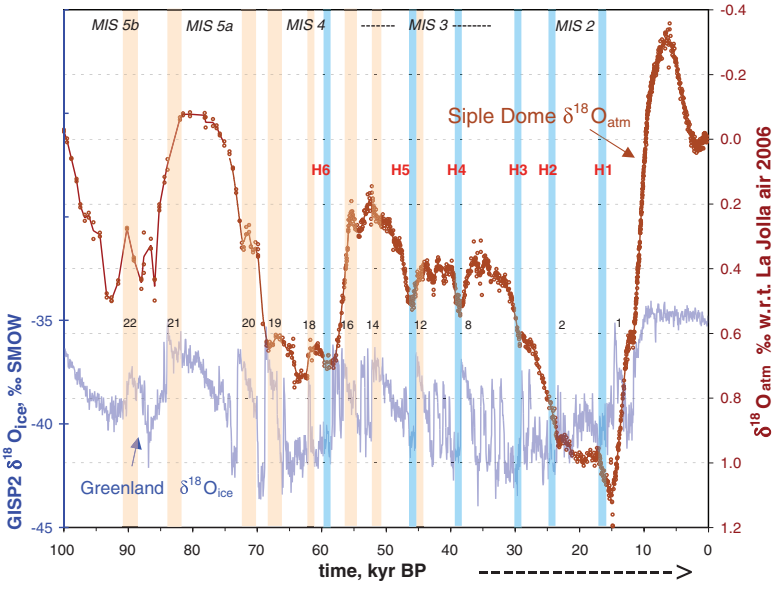

Fig. 1. Measured $^{18}O/^{16}O$ of atmospheric molecular oxygen ($\delta^{18}O_{atm}$) over the past 100 ky from the Siple Dome ice core, Antarctica (note inverted right axis). Data have been corrected for gravitational settling in the firn layer on top of the ice sheet using measured $\delta^{15}N$ and for gas-loss–induced fractionation using measured $\delta O_2/N_2$ and $\delta Ar/N_2$ (*19*). The line drawn through points from 0 to 75 ka is a least-squares fit, and the line from 75 to 100 ka connects mean values. Approximate timings of the marine isotope stages (MISs) are shown at the top. Greenland $\delta^{18}O_{ice}$ (*40*) is shown for reference, and Heinrich stadials (H1 to H6 in red numbers) and the older D/O events (small black numbers) are labeled. Time scale is synchronized to GISP2 (*41*).

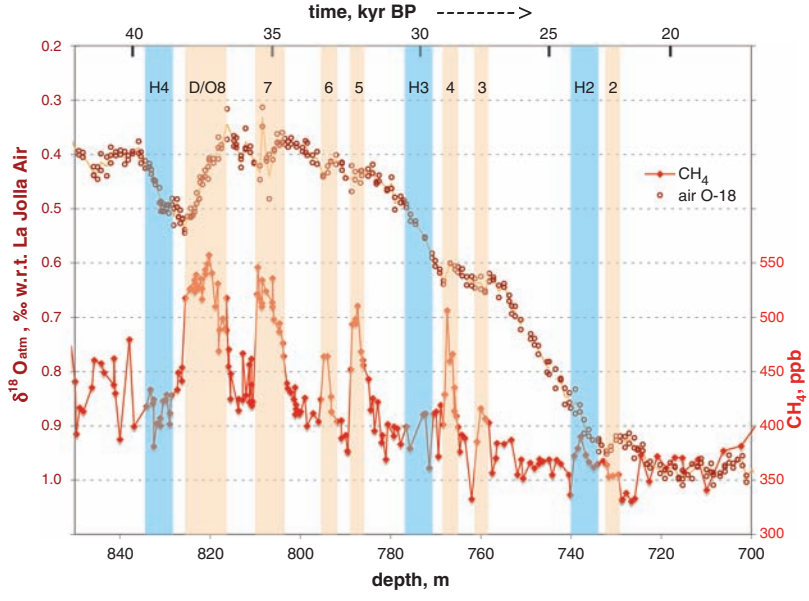

Fig. 2. Expanded view of $\delta^{18}O_{atm}$ from the Siple Dome ice core during D/O events of MIS 3, plotted versus depth to show the raw temporal relationship to methane (measured in the same ice core), without further complications from gas age assignment. Individual $\delta^{18}O_{atm}$ replicates shown, with means connected by solid line. Inferred positions of Heinrich stadials (H4 to H2) and D/O events (D/O8 to D/O2) are shown with vertical shaded bars. Approximate ages are given at top. Methane data from (*41*).

more likely one, because Heinrich stadial 1 is clearly accompanied by rising sea level, and therefore decreasing seawater $\delta^{18}O$ (*28*, *29*). By analogy to Heinrich stadial 1, we argue that all Heinrich stadials are accompanied by negative seawater $\delta^{18}O$ anomalies, making our deduced positive Dole effect anomalies at these times minimum estimates.

If respiratory fractionation were constant (not necessarily realistic), $\Delta\varepsilon_{LAND}$ would be equal to the isotopic fractionation of terrestrial chloroplast water relative to seawater (strictly, production-weighted-mean terrestrial chloroplast water $\delta^{18}O$ minus seawater $\delta^{18}O$). In this case, $\Delta\varepsilon_{LAND}$ would give globally integrated information about the hydrological cycle, in particular the $\delta^{18}O$ of precipitation over photosynthetically active land areas such as the monsoon regions, and the relative humidity in these areas [which controls the amount of evaporative enrichment of the leaf water $\delta^{18}O$ (*10*, *13*)]. Strong summer monsoons affect both mechanisms in the same sense, with less isotopic enrichment (*10*, *11*, *15*, *16*).

The good correlation between $\Delta\varepsilon_{LAND}$ and independent indicators of monsoon strength from Chinese cave records (Fig. 3) lends support to the view that the Dole effect is tightly linked to the strength of the Asian monsoon (*10*, *15*, *16*). Detailed correlations during the last deglaciation and the Holocene lend further support to this view (r = 0.95) (*30*) and even suggest coherence at centennial time scales (Fig. 4). The fact that the abrupt climate event at 8.2 ka has a visible impact on the Dole effect (Fig. 4) is noteworthy because of its short duration and lack of seawater $\delta^{18}O$ change. The rapidity of the changes in $\delta^{18}O_{atm}$ are surprising and raise the question of whether the turnover time of oxygen in the atmosphere has been overestimated, pointing to the need for further work.

Changes in respiration over time may also have contributed to the variations in the Dole effect, although understanding is limited at present. Respiration increases closely in parallel with increases in photosynthesis, and strong monsoons might be expected to increase the global proportion of weakly fractionating tropical respiration (~10‰) relative to boreal respiration (~22‰), which could be a powerful effect (*26*). Again, the fractionation change would be in the same sense (more tropical respiration causes a decrease in $\delta^{18}O_{atm}$ and $\Delta\varepsilon_{LAND}$) as that caused by precipitation. Thus, part of the correlation between $\Delta\varepsilon_{LAND}$ and monsoon strength could be due to respiration; we therefore caution against using $\Delta\varepsilon_{LAND}$ as a proxy for chloroplast water $\delta^{18}O$.

The implication of these data is that a very large, albeit poorly quantified, fraction of the photosynthetic capacity of the planet's terrestrial surface was affected by Heinrich and D/O stadials. As noted above, a similar conclusion has been drawn from the ice core methane record (*31*). However, methane production takes place in anoxic soils, prevalent only in wetland regions, whereas oxygen is produced widely over the land surface. Thus, our data strengthen conclusions about the involvement of the low-latitude hydrological cycle in abrupt climate change that were already drawn from ice core methane data (*7*, *31*) and local records (*32*).

These findings are consistent with recent speleothem records (*6*) and modeling results (*33*, *34*) that suggest that the intertropical convergence zone (ITCZ) can abruptly shift to a state in which it stays predominantly in the southern hemisphere during Heinrich and D/O stadials. Because of the paucity of land in the southern hemisphere, and the fact that rainfall on the ocean has little effect on marine chloroplast water $\delta^{18}O$ due to dilution by seawater, a southern-shifted ITCZ is expected to produce high $\Delta\varepsilon_{LAND}$ and a strong Dole effect. Also, the ITCZ stimulates vigorous plant growth on the land that does exist in the southern hemisphere. A southern-shifted locus of intense oxygenesis should strengthen the Dole effect, because the $\delta^{18}O$ of terrestrial oxygenic precipitation in the Southern Hemisphere is generally higher than in the Northern Hemisphere because of lesser continentality, lower altitude, and less intense isotopic distillation, as suggested by the fact that Southern Hemisphere Brazilian cave records are ~4‰ higher in $\delta^{18}O$ during corresponding phases than their Chinese counterparts (*6*).

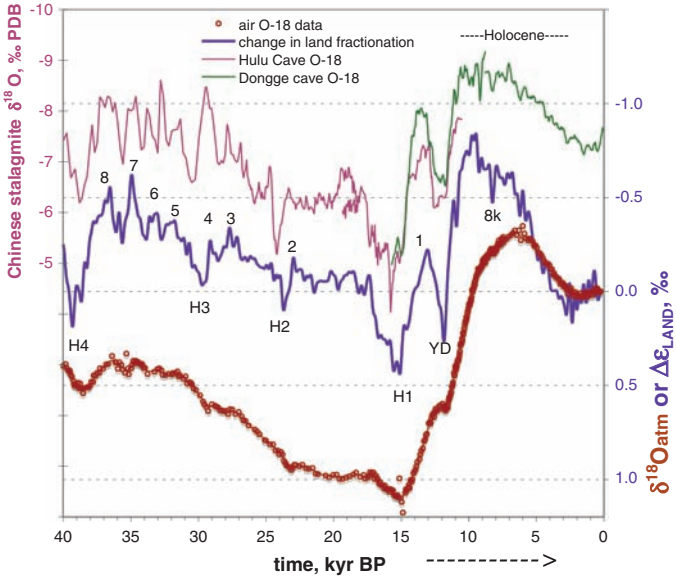

Fig. 3. Records over the past 40 ky of $^{18}O/^{16}O$ of atmospheric molecular oxygen ($\delta^{18}O_{atm}$), inferred change in terrestrial $^{18}O/^{16}O$ fractionation ($\Delta\varepsilon_{LAND}$), and Chinese cave stalagmite $^{18}O/^{16}O$ (*3*–*5*). Dongge Cave records are smoothed with a 200-year moving average for clarity (*30*). D/O events 2 to 8 and Heinrich stadials H1 to H4 are numbered, and Younger Dryas (YD) and 8.2-ka event (8k) are labeled.

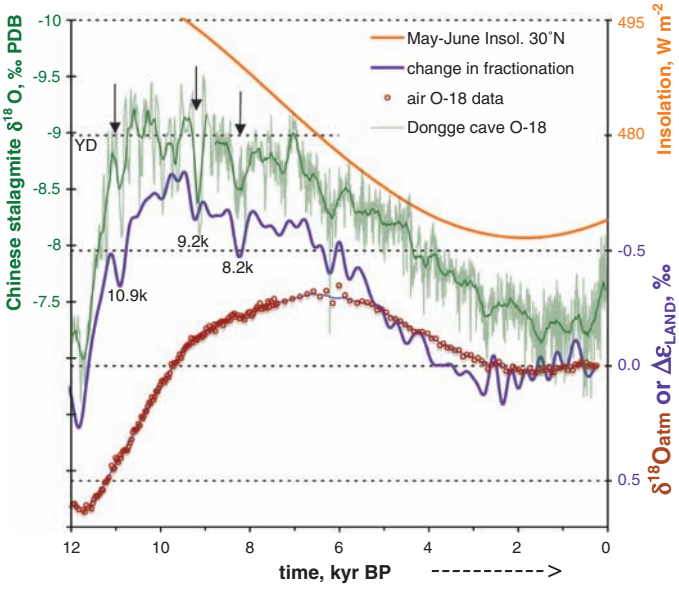

Fig. 4. Expanded view of Holocene portion of Fig. 3. Similarities between inferred global terrestrial $^{18}O/^{16}O$ fractionation ($\Delta\varepsilon_{LAND}$) and the Chinese cave $^{18}O/^{16}O$ are noted with arrows at 8.2 ka, 9.2 ka, and 10.9 ka (8.2k, 9.2k, and 10.9k, respectively). Dongge cave records (*4*, *5*) are shown raw and with a 200-year running average and have been corrected for seawater $^{18}O/^{16}O$ change (*23*) to emphasize the fractionation relative to seawater. The upturn in monsoon strength around 2 ky before the present (BP) implied by $\Delta\varepsilon_{LAND}$ could have been driven by the upturn in May and June mean insolation (*42*), suggesting that there is no need to invoke an anthropogenic cause (*43*) of the upturn in atmospheric methane concentration at that time.

We cannot rule out a small role of boreal ecosystems in shaping $\Delta\varepsilon_{LAND}$, because photosynthesis in these latitudes would be expected to produce isotopically light O_2 from snowmelt during warm phases of the D/O events. We also cannot rule out the hypothesis (*17*) that lower relative humidity over most land areas and a southward-shifted vegetation distribution explains the strong Dole effect during D/O stadials. However, the temporal pattern of $\Delta\varepsilon_{LAND}$ (strong Heinrich and weak D/O stadials, abrupt mid-Holocene change) (Figs. 3 and 4) does not match that of known boreal climate patterns (e.g., weak Heinrich and strong D/O, a steady Holocene cooling) (Fig. 1). Also, the strong boreal respiratory fractionation (*26*) should nullify the effect of boreal photosynthesis to some extent (*35*). We thus suggest that our $\delta^{18}O_{atm}$ data imply large changes in low-latitude terrestrial hydrology associated with abrupt climate change, whether (i) directly through the low $\delta^{18}O$ of heavy precipitation, (ii) indirectly through the weak evaporative enrichment of chloroplast water under conditions of high humidity, or (iii) indirectly through the weak respiratory fractionation that characterizes wet tropical biomes. These findings highlight in a general way the sensitivity of low-latitude rainfall patterns to abrupt climate change in the high-latitude north, with possible relevance for future rainfall and agriculture in the heavily populated monsoon regions.

Finally, the millennial scale oscillations in $\delta^{18}O_{atm}$ open up possibilities for improving the dating of ice cores and glacial outcrops. Because the atmosphere is well-mixed on 1-year time scales, $\delta^{18}O_{atm}$ is a global time-stratigraphic marker that has been used for synchronizing different ice core chronologies (*36*). Previous use of $\delta^{18}O_{atm}$ has been limited to the orbital scale, however, and millennial-scale dating has been done with methane concentration (*37*). During times when methane concentration varied little, such as during the last glacial maximum, the small variations in $\delta^{18}O_{atm}$ that we identify provide new tie points (e.g., fig. S5). Also, low-latitude ice cores generally do not preserve reliable atmospheric methane records because methane is a trace gas that is vulnerable to in situ production (*38*). As an abundant gas, oxygen is more resistant to in situ alteration, making $\delta^{18}O_{atm}$ useful for millennial-scale dating of low-latitude ice cores.

References and Notes

1. G. H. Denton, R. B. Alley, G. C. Comer, W. S. Broecker, *Quat. Sci. Rev.* **24**, 1159 (2005).
2. C. Wunsch, *Quat. Sci. Rev.* **22**, 1631 (2003).
3. Y. J. Wang *et al*., *Science* **294**, 2345 (2001).
4. Y. J. Wang *et al*., *Science* **308**, 854 (2005).
5. C. A. Dykoski *et al*., *Earth Planet. Sci. Lett.* **233**, 71 (2005).
6. X. Wang *et al*., *Geophys. Res. Lett.* **34**, L23701 10.1029/2007GL031149 (2007).
7. E. J. Brook, S. Harder, J. Severinghaus, E. J. Steig, C. M. Sucher, *Global Biogeochem. Cycles* **14**, 559 (2000).
8. T. Sowers, M. L. Bender, D. Raynaud, *J. Geophys. Res.* **94**, 5137 (1989).
9. M. Bender *et al*., *Nature* **372**, 663 (1994).
10. M. L. Bender, T. Sowers, L. Labeyrie, *Global Biogeochem. Cycles* **8**, 363 (1994).
11. B. Malaizé, D. Paillard, J. Jouzel, D. Raynaud, *J. Geophys. Res.-Atmos.* **104**, 14199 (1999).
12. R. D. Guy, M. L. Fogel, J. A. Berry, *Plant Physiol.* **101**, 37 (1993).
13. G. D. Farquhar, L. A. Cernusak, B. Barnes, *Plant Physiol.* **143**, 11 (2007).
14. E. Barkan, B. Luz, *Rapid Commun. Mass Spectrom.* **19**, 3737 10.1002/rcm.2250 (2005).
15. M.-A. Mélières, M. Rossignol-Strick, B. Malaizé, *Geophys. Res. Lett.* **24**, 1235 (1997).
16. V. Masson *et al*., *Geophys. Res. Lett.* **27**, 1747 (2000).
17. A. Landais *et al*., *Earth Planet. Sci. Lett.* **258**, 101 (2007).
18. V. V. Petrenko, J. P. Severinghaus, E. J. Brook, N. Reeh, H. Schaefer, *Quat. Sci. Rev.* **25**, 865 (2006).
19. Materials and methods are available as supporting material on *Science* Online.
20. Electronic archived data is available at http://gcmd.nasa.gov/getdif.htm?0440975_severinghaus.
21. S. Barker *et al*., *Nature* **457**, 1097 (2009).
22. We believe that it is useful to make a distinction between stadials with an associated Heinrich event (Heinrich stadials) and those without (D/O stadials). In the tropics, Heinrich stadials have a different character than D/O stadials, suggesting a different mechanism. The amplitude of the former in the tropics is larger than that of the D/O stadials, in contrast to high-latitude records, where all stadials seem to have a similar expression. It has been proposed (*39*) that the Heinrich stadials represent times when the Atlantic meridional overturning circulation was completely shut off, and the D/O stadials represent times when only the Greenland-Iceland-Norwegian (GIN) seas and the associated overflows on the Greenland-Scotland ridge were shut off, with the Labrador Sea continuing to produce deep water. The implication of this hypothesis is that the northward cross-equatorial flow in the Atlantic ceased during Heinrich stadials but not during the D/O stadials. This could explain why the two types of events seem so different in the low latitudes, because near-equatorial meridional sea surface temperature gradients (e.g., 20°N to 20°S) have a profound effect on the mean position of the ITCZ (*33*).
23. C. Waelbroeck *et al*., *Quat. Sci. Rev.* **21**, 295 (2002).
24. M. Hendricks, M. L. Bender, B. Barnett, *Deep Sea Res. Part I Oceanogr. Res. Pap.* **51**, 1541 (2004).
25. E. Barkan, D. Eisenstadt, A. Kaplan, B. Luz, The effect of marine photosynthesis on $^{17}O/^{16}O$ and $^{18}O/^{16}O$ of atmospheric O_2 (abstr.)., Proceedings Goldschmidt 2009, Davos, 21 to 26 June 2009.
26. A. Angert *et al*., *Global Biogeochem. Cycles* **17**, 1089 10.1029/2003GB002056 (2003).
27. The idea that the fraction of land versus ocean photosynthesis influences the Dole effect is awkward in its construction; it implicitly assumes that there is a single "land" value of fractionation, whereas in fact it is now clear that the land fractionation is extremely heterogeneous in time and space. It may be conceptually more helpful to think of the Dole effect as being the integral of competing "heavy" land isofluxes (e.g., from savannas, deserts, and well-aerated soils) and "light" land isofluxes (e.g., from humid, water-saturated biomes), against a background of relatively uniform and constant oceanic values. (Here, the concept of isofluxes subsumes the isotopic effects of both sources and sinks.)
28. G. H. Denton, W. S. Broecker, R. B. Alley, *PAGES News* **14**, 1416 (2006).
29. The view that Heinrich stadials are times of sea-level rise is supported by speleothem records (*32*) that show a consistent pattern of weak monsoons during times of sea-level rise at many glacial terminations, suggesting that there is some unifying mechanism that produces Heinrich-like stadials and weak monsoons in the presence of sea level rise. For example, such a mechanism could be the effect of meltwater injected into the North Atlantic ocean on the meridional ocean overturning circulation and winter sea ice cover in the North Atlantic (*1*).
30. A composite Dongge Cave record was constructed from the entire 8.8-ky record of Wang *et al*. (*4*) and the Dongge D4 record (*5*) from 8.8 to 15.7 ka, and was linearly interpolated and smoothed with a 200-year running average (Fig. 3). This average was resampled at 20-year intervals for comparison with $\Delta\varepsilon_{LAND}$, giving a Pearson correlation coefficient (r) of 0.95 for the 0.3- to 12-ka interval (Fig. 4). The correlation between $\Delta\varepsilon_{LAND}$ and Hulu Cave records is visually apparent but numerically limited by time scale errors (GISP2 time scale is up to 1 ky too young in the 16- to 31-ka interval).
31. J. Chappellaz *et al*., *Nature* **366**, 443 (1993).
32. Y. J. Wang *et al*., *Nature* **451**, 1090 (2008).
33. J. C. H. Chiang, C. M. Bitz, *Clim. Dyn.* 10.1007/s00382-005-0040-5 (2005).
34. J. C. H. Chiang, W. Cheng, C. M. Bitz, *Geophys. Res. Lett.* **35**, L07704 10.1029/2008GL033292 (2008).
35. The amount of photosynthesis occurring in boreal regions is known to increase during the warm phases of D/O events (from pollen records). The amount of respiration must also increase at these times, because respiration and photosynthesis are tightly coupled by the fact that organic matter is generally unstable with respect to microbial attack. Thus, the respiratory contribution to the Dole effect will increase because the boreal respiratory fractionation factor is greater than the mean global value. The same logic holds in reverse for wet tropical biomes, in the Asian and African monsoon regions. Here, weak respiratory fractionation has the effect of reducing the Dole effect when wet tropical oxygenesis/respiration increases during warm phases of D/O events, even if the magnitude of the fractionation in that biome is constant. The key point is that respiration and hydrological-fractionation-with-oxygenesis have opposing effects in boreal biomes but constructive effects in tropical biomes. Therefore, wet tropical biomes should dominate the variability in the Dole effect, rather than boreal biomes, because of this "monsoon rectifier effect."
36. M. L. Bender, B. Malaizé, J. Orchardo, T. Sowers, J. Jouzel, in *Mechanisms of Global Climate Change at Millennial Time Scales*, P. U. Clark, R. S. Webb, L. D. Keigwin, Eds., vol. 112, *Geophysical Monograph Series* (American Geophysical Union, Washington, DC, 1999), pp. 149–164.
37. T. Blunier, E. J. Brook, *Science* **291**, 109 (2001).
38. R. K. Campen, T. Sowers, R. B. Alley, *Geology* **31**, 231 (2003).
39. R. B. Alley, P. U. Clark, L. D. Keigwin, R. S. Webb, in *Mechanisms of Global Change at Millennial Time Scales*, P. U. Clark, R. S. Webb, L. D. Keigwin, Eds., vol. 112, *Geophysical Monograph Series* (American Geophysical Union, Washington, DC, 1999), pp. 385–394.
40. M. Stuiver *et al*., *Quat. Res.* **44**, 341 (1995).
41. E. J. Brook *et al*., *Quat. Sci. Rev.* **24**, 1333 (2005).
42. D. Paillard, L. Labeyrie, P. Yiou, *Eos Trans. AGU* **77**, 379 (1996).
43. W. F. Ruddiman, *Clim. Change* **61**, 261 (2003).

44. We thank B. Luz, L. Edwards, R. Keeling, M. Bender, A. Landais, K. Kawamura, C. Wunsch, G. Farquhar, and W. Broecker for helpful conversations. B. Cornuelle did the Fourier-series curve fitting. M. Henkart analyzed the tank of air from 1976 to test for anthropogenic change in the Dole effect. We thank J. Rhoades and the staff of the National Ice Core Laboratory for help in sampling the Siple Dome ice core. This work was supported by NSF-OPP 04-40975 (J.P.S), NSF-OPP 01-26057 (E.J.B), and the Gary Comer Science and Education Foundation, and recovery of the Siple Dome ice core was supported by NSF-OPP 95-26421 (K.T.).

Supporting Online Material

www.sciencemag.org/cgi/content/full/324/5933/1431/DC1
Materials and Methods
Figs. S1 to S10
References

8 December 2008; accepted 30 April 2009
10.1126/science.1169473

Boom-and-Bust Development Patterns Across the Amazon Deforestation Frontier

Ana S. L. Rodrigues,[1,2,3]* Robert M. Ewers,[4] Luke Parry,[5] Carlos Souza Jr.,[6] Adalberto Veríssimo,[6] Andrew Balmford[1]

The Brazilian Amazon is globally important for biodiversity, climate, and geochemical cycles, but is also among the least developed regions in Brazil. Economic development is often pursued through forest conversion for cattle ranching and agriculture, mediated by logging. However, on the basis of an assessment of 286 municipalities in different stages of deforestation, we found a boom-and-bust pattern in levels of human development across the deforestation frontier. Relative standards of living, literacy, and life expectancy increase as deforestation begins but then decline as the frontier evolves, so that pre- and postfrontier levels of human development are similarly low. New financial incentives and policies are creating opportunities for a more sustained development trajectory that is not based on the depletion of nature and ecosystem services.

The Brazilian Amazon harbors 40% of all remaining tropical rainforest (*1*), playing a vital role in global biodiversity conservation (*2*), climate regulation (*3*), and biogeochemical cycles (*4*). An average of 1.8 million hectares of forest has been lost annually during the 1988–2008 period as agricultural land uses expand (*5*), corresponding to nearly one-third of global tropical deforestation (*6*) and releasing about 250 million tons of carbon (*3*, *7*). Yet this is also one of the least developed regions in Brazil (*8*), and conversion of forest for agriculture and cattle ranching (typically preceded by logging and burning) is often seen as the most practical route to achieving legitimate aspirations to economic development (*9*). Here, we investigated how human development varies across the region's deforestation frontier to determine whether deforestation is associated with a sustained improvement in people's well-being.

The Brazilian Amazon is well suited to exploring trade-offs between development and conservation because habitat conversion is proceeding quickly—compressing into decades a process that took centuries or millennia in many other parts of the world—and because socioeconomic conditions are systematically documented (*8*, *10*). Furthermore, although the Brazilian Amazon is by no means a homogeneous region, it has relatively limited variation in the potentially confounding factors (such as geography, history, and governance) that have been shown to explain variation in wealth at the global scale (*11*).

One measure used to assess levels of development is the human development index (HDI), calculated following a standard procedure developed by the United Nations Development Programme (*12*). The overall HDI is calculated as the mean of three subindices: life expectancy (based on life expectancy at birth), literacy (based on literacy rate and school enrollment), and standard of living (based on per capita income); it thus offers a measure of human development that is more comprehensive than measures based solely on per capita income (*12*). We obtained HDI values from the 2000 Brazilian Atlas of Human Development for 286 municipalities in the Brazilian Amazon (*8*). Municipalities were grouped into seven classes (A to G) describing their position relative to the deforestation frontier in 2000, defined according to both deforestation activity and deforestation extent (*5*) (Fig. 1 and fig. S1). The classes range from prefrontier municipalities, with essentially intact forest cover and virtually no ongoing deforestation (A), through progressively deforested classes, with increasing (B to D) and then declining (D to F) deforestation activity, through to heavily deforested postfrontier municipalities that were again almost inactive in terms of deforestation (G) (Fig. 1). The current wave of deforestation began with government colonization schemes on the eastern and southern borders of the region in the early 1970s, extending westward and along the southern fringes through the 1980s, forming an "arc of deforestation" that is still expanding into the heart of the Amazon (*5*).

When the median HDI of each class is plotted against deforestation extent, a boom-and-bust pattern becomes apparent (*9*, *14*), which suggests that relative development levels increase rapidly in the early stages of deforestation and then decline as the frontier advances (Fig. 2A). Hence, although municipalities with active deforestation had development levels that approached the overall Brazilian median, pre- and postfrontier HDI

[1]Conservation Science Group, Department of Zoology, University of Cambridge, Cambridge CB2 3EJ, UK. [2]IN+, Center for Innovation, Technology and Policy Research, Environment and Energy Section, Mechanical Engineering Department, Instituto Superior Técnico, Portugal. [3]Centre d'Ecologie Fonctionnelle et Evolutive, CNRS UMR5175, 1919 Route de Mende, 34293 Montpellier, France. [4]Division of Biology, Imperial College London, Silwood Park Campus, Ascot SL5 7PY, UK. [5]School of Environmental Sciences, University of East Anglia, Norwich NR4 7TJ, UK. [6]IMAZON–Amazon Institute of People and the Environment, Belém, PA, Brazil.

*To whom correspondence should be addressed. E-mail: ana.rodrigues@cefe.cnrs.fr

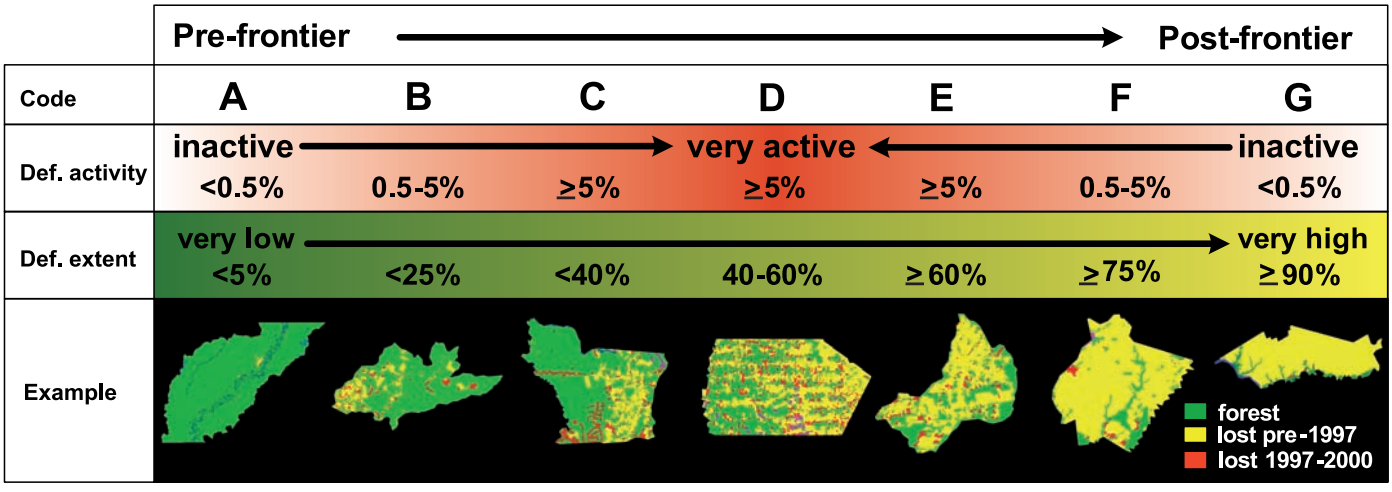

Fig. 1. Definition of frontier classes A to G according to recent deforestation activity (percentage of municipality area deforested between 1997 and 2000) and deforestation extent (percentage of the original forest that had been lost by 2000). A representative municipality is mapped as an example of each class (spatial scale variable) (*5*, *13*).

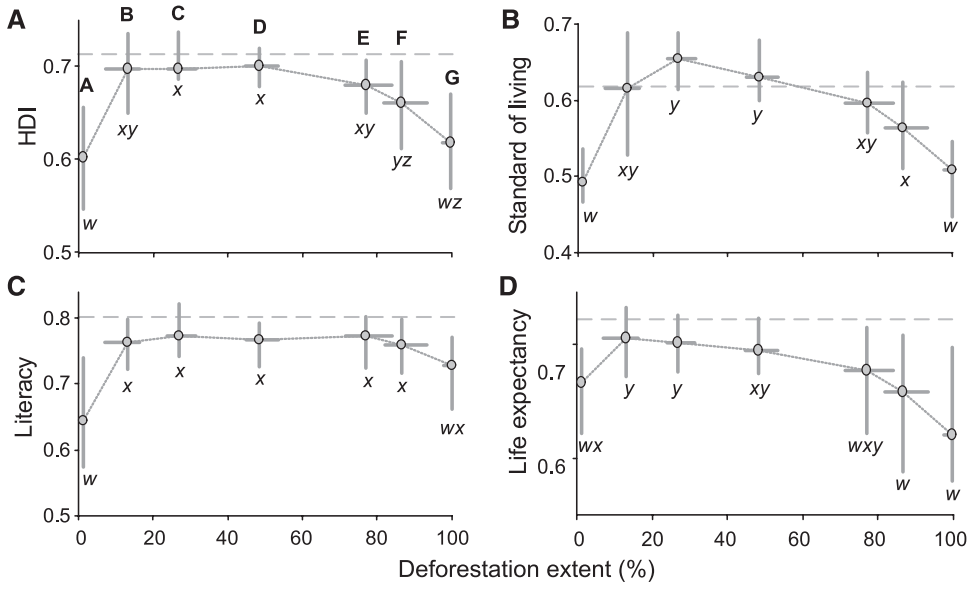

Fig. 2. Variation along a deforestation gradient (*5*) corresponding to frontier classes A to G, as defined in Fig. 1, in (**A**) the human development index (HDI, obtained by averaging the subindices on standard of living, literacy, and life expectancy); (**B**) the standard-of-living subindex (based on per capita income); (**C**) the literacy subindex (based on literacy rate and school enrollment); and (**D**) the life expectancy subindex (based on life expectancy at birth) (*8*). As labeled in (A), circles from left to right correspond to classes A to G in all panels. Circles indicate median values; bars indicate first and third quartiles; horizontal dashed line indicates the median across all Brazilian municipalities. All variables present significant variation across the frontier classes (Kruskal-Wallis: $P < 0.0001$); classes that do not have a letter (*u*, *v*, *w*, *x*, *y*, *z*) in common differ significantly (Tukey's honestly significant difference test: $P > 0.05$). Classes A and G are statistically indistinguishable in terms of HDI ($P = 0.93$), standard of living ($P = 1.00$), life expectancy ($P = 0.83$), and literacy ($P = 0.12$). All data are from the year 2000.

values were substantially lower and statistically indistinguishable from each other ($P > 0.9$) (Fig. 1A). These results are robust to the particular thresholds used to define the frontier classes (*13*) (figs. S2 and S3). A boom-and-bust pattern is also found for each of the HDI subindices: standard of living, literacy, and life expectancy (Fig. 2, B to D).

Our analysis investigated relative development patterns across space, rather than the trajectory of absolute development through time. The latter was not possible given a lack of long-term time-series data, but the former has the advantage of standardizing for temporal changes that affect the entire region (e.g., economic cycles in the Brazilian economy). Hence, the boom-and-bust pattern we report does not necessarily imply that the absolute HDI of individual municipalities has first increased and then declined as deforestation has progressed; given Brazil's overall improvement in HDI over time (e.g., median municipality HDI increased from 0.627 in 1990 to 0.713 in 2000) (*8*), it is likely that development levels have generally increased throughout the Amazon. What our results suggest is that life expectancy, literacy, and standard of living improve more quickly than the national average in municipalities at the early stages of the deforestation frontier, and at below-average rates as deforestation progresses, resulting in relative HDI values that are higher at the frontier, but lower and similar in pre- and postfrontier municipalities (fig. S4).

The immediate causes of most deforestation in the Brazilian Amazon are the expansion of mechanized agriculture and land use changes by newly arrived migrants (*15*, *16*) (fig. S5). A wide diversity of people migrate to the frontier (including capitalized ranchers and farmers, colonists, landless peasants, gold miners, loggers, and landgrabbers) (*17*), but ultimately they are all attracted by the prospect of life improvement. The increase in HDI suggests that such improvement does take place at the early stages of the frontier (Fig. 2), although an alternative explanation might be that increased HDI is "imported" by immigrants coming from regions in Brazil that have better levels of education, health, and access to capital (*14*). However, immigration alone is unlikely to explain the "boom" in HDI at the early stages of deforestation, because people moving into the frontier are generally poorer and less educated than average in their areas of origin (*15*), and also because the frontier would probably not attract large-scale investment or migrants if it did not provide real prospects of high economic return and life improvement. More likely, HDI increases as people capitalize on the newly available natural resources—including land, timber, and minerals (*15*, *17*)—and on the improved accessibility to markets promoted by the new roads (*18*) that are associated with frontier expansion (*19*). Accordingly, relative levels of income improve very quickly at the early stages of deforestation (Fig. 2B). So do levels of literacy (Fig. 2C) and life expectancy (Fig. 2D), possibly because improved income and road connections result in better living conditions and improved access to education and medical care, and because governmental investment strengthens educational and medical infrastructure.

At the frontier, development levels come close to (and income even exceeds) the median values across all Brazilian municipalities. However, our results suggest that those improvements are transitory, with municipal standard of living, literacy, and life expectancy declining in the postfrontier to levels similar to those in the prefrontier municipalities (Fig. 2). This "bust" is likely to reflect the exhaustion of the natural resources that supported the initial "boom," compounded by the increasing human population. Accordingly, per capita timber (Fig. 3A), cattle (Fig. 3B), and crop production (Fig. 3C) also exhibit boom-and-bust patterns across the deforestation frontier. Timber (Fig. 3D) and cattle (Fig. 3E) also decline on a per-area basis, indicating a reduction in overall productivity irrespective of increasing human population. The first is expected, as the very resource on which timber production relies is depleted as deforestation progresses. The second likely reflects large-scale pastureland degradation as soils lose productivity (*20*), or conversion to alternative land uses as land market conditions change. By the early 1990s, more than 75% of the land that had been deforested until then in the Amazon had been used for the development of pastures, one-third of which had already been abandoned (*21*). Although the increasing population density in the postfrontier is key to understanding the decline in HDI, such density is not particularly high within the Brazilian context; most Brazilian municipalities have much higher HDI despite similar levels of population density (fig. S5).

Our results show that, in net terms, people in municipalities that have cleared their forests are not better off than those in municipalities that have not (Fig. 2). The current development pattern in the Brazilian Amazon is therefore far from desirable in terms of either human development or the conservation of natural resources. The huge challenge facing this region is how to ensure that future development paths translate into sustained improvements in human well-being, while avoiding the depletion of nature and the services it provides (*3*). A single solution is unlikely to exist. Instead, a combined approach might include supporting the better use of areas that have already been deforested (e.g., via the intensification of ranching and agriculture) alongside restricting further deforestation [e.g., through protected areas (*22*) and appropriate land use zoning (*23*)] and promoting reforestation in degraded landscapes (*24*); direct incentives to encourage forest-based livelihoods based on the sustainable harvest of timber and nontimber forest products, within and beyond forest concessions

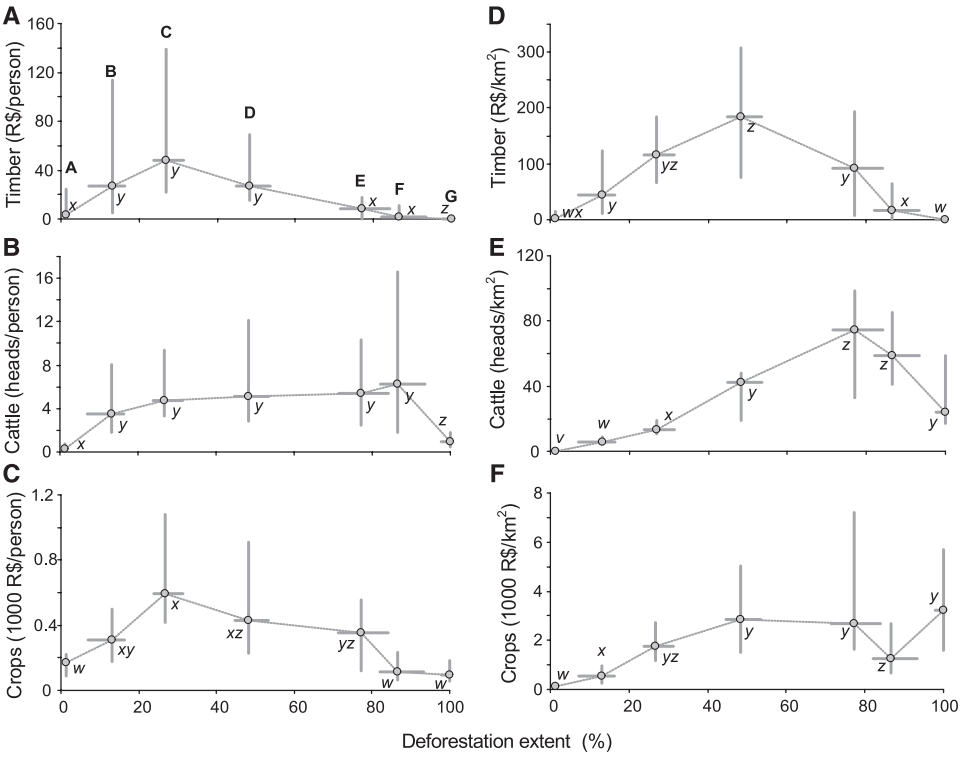

Fig. 3. Variation in the production of timber (**A** and **D**), cattle (**B** and **E**), and crops (**C** and **F**) across frontier classes A to G, either standardized by population [(A) to (C)] or by municipality area [(D) to (F)] (*10*). Timber and crop production is shown in units of Brazilian currency, the real (R$). As labeled in (A), circles from left to right correspond to classes A to G in all panels. Circles indicate median values; bars indicate first and third quartiles; horizontal dashed line indicates the median across all Brazilian municipalities. All variables present significant variation across the frontier classes (Kruskal-Wallis: $P < 0.0001$); classes that do not have a letter (*u*, *v*, *w*, *x*, *y*, *z*) in common differ significantly (Tukey's honestly significant difference test: $P > 0.05$). All data are from the year 2000.

(*25*); and targeted policies to improve literacy, health, and land tenure security (*26*).

Payments for ecosystem services, including carbon sequestration, are likely to play a key role in the financial sustainability of these approaches, by converting at least some of the wider value of Amazonian forests into local economic incentives for their long-term conservation (*27*). Such schemes are starting to be implemented in Brazil at the national (Bolsa Amazônia) and state levels (Bolsa Floresta; State of Amazonas) (*28*). Internationally, a global financial mechanism to reduce emissions from deforestation and forest degradation in developing countries is currently being negotiated under the United Nations Framework Convention on Climate Change (*7*, *29*, *30*). Brazil, with its huge carbon stocks (*31*), high technical capacity for monitoring forest changes (*32*), and improving governance (*33*), is arguably the best-positioned country for implementing and benefiting from this major new initiative. However, the long-term success of these incentives will also depend on other regional development policies, such as government incentives for agricultural expansion. For example, Amazonian "critical municipalities" with high deforestation rates now have reduced access to subsidized rural credit until targets for land tenure regularization and deforestation control are reached (*23*). Hence, although our results indicate that past development in the Brazilian Amazon has followed a boom-and-bust trajectory, future development may very well be associated with improvement in environmental quality and forest recuperation, as predicted by the environmental Kuznets hypothesis (*34*) and forest transition theory (*35*). New financial mechanisms and policies are paving the way for more sustained development trajectories and creating the conditions in which the largest tropical forest in the world can be recognized as more valuable standing than felled.

References and Notes

1. W. F. Laurance *et al.*, *Science* **291**, 438 (2001).
2. R. A. Mittermeier *et al.*, *Proc. Natl. Acad. Sci. U.S.A.* **100**, 10309 (2003).
3. J. A. Foley *et al.*, *Front. Ecol. Environ.* **5**, 25 (2007).
4. D. C. Nepstad, C. M. Stickler, B. S. Filho, F. Merry, *Philos. Trans. R. Soc. London Ser. B* **363**, 1737 (2008).
5. Instituto Nacional de Pesquisas Espaciais (INPE), *Projeto PRODES: Monitoramento da Floresta Amazônica Brasileira por Satélite*, 2008 (www.obt.inpe.br/prodes).
6. R. S. DeFries *et al.*, *Proc. Natl. Acad. Sci. U.S.A.* **99**, 14256 (2002).
7. D. Nepstad *et al.*, *The Costs and Benefits of Reducing Carbon Emissions from Deforestation and Forest Degradation in the Brazilian Amazon* (Woods Hole Research Center, Falmouth, MA, 2007).
8. United Nations Development Programme–Brazil (UNDP-Brazil), *Atlas do Desenvolvimento Humano no Brazil*, 2003 (www.pnud.org.br/atlas).
9. R. R. Schneider, E. Arima, A. Veríssimo, P. Barreto, C. Souza Jr., *Sustainable Amazon: Limitations and Opportunities for Rural Development* (World Bank and IMAZON, Brasília, 2000; www.imazon.org.br/publicacoes/publicacao.asp?id=109).
10. Instituto Brasileiro de Geografia e Estatística (IBGE), Download de Arquivos (www.ibge.gov.br/servidor_arquivos_est).
11. J. Diamond, *Nature* **429**, 616 (2004).
12. United Nations Development Programme (UNDP), *The Human Development Index*, 2008 (http://hdr.undp.org/en/statistics/indices/hdi).
13. See supporting material on *Science* Online.
14. D. Celentano, A. Veríssimo, *O Avanço da Fronteira na Amazônia: do boom ao colapso* (IMAZON, Belém, PA, Brazil, 2007; www.imazon.org.br/publicacoes/publicacao.asp?id=512).
15. D. Carr, *Prog. Hum. Geogr.* 10.1177/0309132508096031 (2008).
16. T. K. Rudel, *Tropical Forests: Regional Paths of Destruction and Regeneration in the Late Twentieth Century* (Columbia Univ. Press, New York, 2005).
17. P. M. Fearnside, *Ecol. Soc.* **13**, 23 (2008).
18. H. G. Jacoby, *Econ. J.* **110**, 713 (2000).
19. B. S. Soares-Filho *et al.*, *Nature* **440**, 520 (2006).
20. M. M. L. Müller, M. F. Guimarães, T. Desjardins, D. Mitja, *Agric. Ecosyst. Environ.* **103**, 279 (2004).
21. P. M. Fearnside, R. I. Barbosa, *For. Ecol. Manage.* **108**, 147 (1998).
22. D. White *et al.*, in *Agricultural Technologies and Tropical Deforestation*, A. Anglesen, D. Kaimowitz, Eds. (CABI, Wallingford, UK, 2001), pp. 91–111.
23. Ministério do Meio Ambiente (MMA), *Ações do MMA para os municípios*, 2009 (www.mma.gov.br/estruturas/182/_arquivos/cartilha_182.pdf).
24. R. L. Chazdon, *Science* **320**, 1458 (2008).
25. A. Veríssimo, M. A. Cochrane, C. Souza Jr., *Science* **297**, 1478 (2002).
26. A. Hall, *J. Lat. Am. Stud.* **38**, 689 (2006).
27. A. Balmford, T. Whitten, *Oryx* **37**, 238 (2003).
28. A. Hall, *J. Int. Dev.* **20**, 965 (2008).
29. Y. Malhi *et al.*, *Science* **319**, 169 (2008); published online 27 November 2007 (10.1126/science.1146961).
30. L. Miles, V. Kapos, *Science* **320**, 1454 (2008).
31. H. K. Gibbs, S. Brown, J. O. Niles, J. A. Foley, *Environ. Res. Lett.* **2**, 045023 (2007).
32. J. Tollefson, *Nature* **452**, 134 (2008).
33. D. Nepstad *et al.*, *Science* **295**, 629 (2002).
34. M. Bhattarai, M. Hammig, *World Dev.* **29**, 995 (2001).
35. T. K. Rudel *et al.*, *Glob. Environ. Change* **15**, 23 (2005).

36. Supported by a Marie Curie Intra-European Fellowship under the European Community Sixth Framework Programme and by a Fundação para a Ciência e Tecnologia Postdoctoral Fellowship (Portugal) (A.S.L.R.), the Gordon and Betty Moore Foundation (C.S. and A.V.), and the "Valuing the Arc" program of the Leverhulme Trust (A.B.). We thank J. Barlow, T. Gardner, R. Green, B. Strassburg, and three anonymous reviewers for valuable and constructive comments.

Supporting Online Material

www.sciencemag.org/cgi/content/full/324/5933/1435/DC1
Materials and Methods
SOM Text
Figs. S1 to S5
References

24 March 2009; accepted 24 April 2009
10.1126/science.1174002

Leading-Edge Vortices Elevate Lift of Autorotating Plant Seeds

D. Lentink,[1]* W. B. Dickson,[2] J. L. van Leeuwen,[1] M. H. Dickinson[2]

As they descend, the autorotating seeds of maples and some other trees generate unexpectedly high lift, but how they attain this elevated performance is unknown. To elucidate the mechanisms responsible, we measured the three-dimensional flow around dynamically scaled models of maple and hornbeam seeds. Our results indicate that these seeds attain high lift by generating a stable leading-edge vortex (LEV) as they descend. The compact LEV, which we verified on real specimens, allows maple seeds to remain in the air more effectively than do a variety of nonautorotating seeds. LEVs also explain the high lift generated by hovering insects, bats, and possibly birds, suggesting that the use of LEVs represents a convergent aerodynamic solution in the evolution of flight performance in both animals and plants.

Maples (*Acer*) are primary succession trees adapted to nutrient-poor habitats in temperate climates (*1*). Like many other pioneer trees, maples rely on wind, updrafts, and turbulent gusts to disperse their seeds over distances ranging from several meters to kilometers (*2*, *3*). Maple seeds typically disperse under windy conditions and start to autorotate within 1 m of detaching from the tree (Fig. 1, A and C). They autorotate because the heavy nut, and hence the center of gravity, is located at the base of the wing-shaped seed (*4*–*8*). The stable autorotation of maple and other rotary seeds depends on an interplay between their three-dimensional (3D) inertial and aerodynamic properties, which is not fully understood (*4*, *9*, *10*). The presumed function of autorotation is that it creates lift to prolong the descent of the seed. Detailed performance studies (*4*, *6*, *8*) revealed that autorotating seeds are able to generate unexpectedly high lift forces despite their small size and slow velocity. Like autorotating seeds, insect wings generate very high lift despite operating at angles of attack well above those that will stall conventional aircraft wings and helicopter blades (*11*) (Fig. 1D). Instead of stalling, insect wings generate a prominent leading-edge vortex (LEV), which is known to be responsible for elevating both lift and drag (*11*, *12*–*16*). Building upon these observations, we hypothesized that autorotating seeds create a LEV that enables them to generate high lift at high angles of attack during their descent.

To test if autorotating seeds generate a LEV, we built a dynamically scaled model actuated by a robotic arm in a tank of mineral oil (*17*, *18*) (fig. S1). We based the shape of the model on the planform of one individual seed ($n = 1$) and the kinematics on the average free-flight motion of 20 individuals ($n = 20$) from three species of maple (*m1: Acer diabolicum* Blume; *m2: Acer palmatum* Thunb. var. *matsumurae* Makino, and *m3: Acer palmatum* Thunb) and one species of hornbeam (*h*: *Carpinus ischonoskii* Maxim) (Fig. 1B). The seeds from all four of these species are known to generate high lift (*6*, *19*). The flight parameters and the ratio of inertial to viscous stress in the surrounding flow of the model seeds in oil were scaled such that they are identical to real seeds descending in air. This stress ratio is measured by the Reynolds number and is on the order of 1000 for autorotating seeds (*6*). We used stereo digital particle image velocimetry (DPIV) to measure the 3D velocity field at 26 equally spaced spanwise slices starting at roughly 25% span (indicated in green in Fig. 1B) and extending well beyond the wing tip so that we captured the structure of the tip vortex as well. We combined all slices to reconstruct the 3D velocity field around the model seeds (*18*, *20*) (Fig. 2).

Our measurements show that all four model seeds generate a prominent LEV near the base, which is markedly similar to the LEVs produced by insect wings. The structure of the LEV depends not only on the wing shape and Reynolds number, but also on the wing's angle of attack. Because the wing's rotation induces a radial velocity distribution as the seed descends, the angle of attack is maximal at the wing root (~90°) and minimal at the wing tip (Fig. 1D). Based on prior free-flight measurements (*6*, *19*), we calculated the angle of attack at the wing tip to be lowest for maple seed *m1* (16°), highest for hornbeam *h* (28°), and intermediate for the two other maples seeds, *m2* (25°) and *m3* (26°) (*18*). This qualitative trend can explain in part why the LEV of all three maple seeds (Fig. 2, A to C) is relatively compact and well attached to the seed's surface, whereas the LEV generated by the hornbeam seed appears more separated (Fig. 2D). The LEV is most prominent near the base of the seed, shown at 25% span, where there is a strong concentration of vorticity (first row in Fig. 3, A to D). Toward the tip (at 75% span), the LEV merges with the tip vortex, resulting in a long trail of vorticity in the seed's wake. The chordwise flow around the maple seeds reattaches behind the LEV near the trailing edge, whereas the flow around the hornbeam seed is more separated at the wing tip and fails to reattach. This difference in flow structure is also apparent in images of the 3D and 2D streamlines (Fig. 2 and last row in Fig. 3, A to D) and the vorticity plots (first row in Fig. 3, A to D).

To verify that real autorotating seeds do indeed generate a stable LEV during their descent,

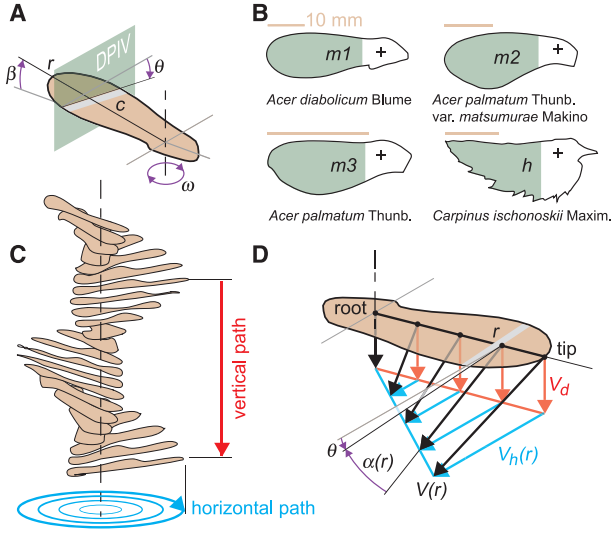

Fig. 1. Kinematics and morphology of all four autorotating seeds studied. (**A**) Free-flight parameters of autorotating seeds [after (*6*)]: local wing radius, *r*; local chord length, *c*; pitch angle, θ; cone angle, β; angular velocity, ω. One of up to 26 planes in which we measured the velocity field along the span using DPIV is indicated in green. (**B**) Planform of the three maple seeds (*m1*, *m2*, *m3*) and hornbeam seed (*h*) studied; the green area indicates the region for which we performed DPIV around the wing. The plus sign indicates the center of gravity, which corresponds closely to the center of rotation (*6*, *8*, *19*). (**C**) Free-flight sequence of an autorotating seed showing both the vertical (red) and horizontal, circular translation (blue) of a wing section during a full period. (**D**) Because of the different horizontal path lengths traveled by subsequent spanwise wing sections (C), the wing's local geometric angle of attack is defined as the arctangent of descent speed, V_d, divided by horizontal speed, V_h. The effective aerodynamic angle of attack, α, is equal to geometric angle of attack minus the absolute value of the pitch angle (*m1*, –1.17°; *m2*, –1.39°; *m3*, –0.90°; *h*, –2.16°), measured at 75% span and approximately constant along span (*6*); α is lowest at the tip and increases toward the base where it approaches 90°. [*V* is velocity and "(*r*)" indicates dependence of a variable on radius.]

[1]Experimental Zoology Group, Wageningen University, 6709 PG Wageningen, Netherlands. [2]Bioengineering and Biology, California Institute of Technology, Pasadena, CA 91125, USA.

*To whom correspondence should be addressed. E-mail: david.lentink@wur.nl

as our model experiments suggest, we built a vertical wind tunnel to study freely flying maple seeds (*Acer pseudo-platanus L.*: *m4*). By matching tunnel speed with the descent rate of the seed, we were able to film 34 seeds spinning at a stationary height in lab frame coordinates (fig. S3) (*18*). The seeds flew at wing-tip angles of attack ranging from 12° to 32° (Reynolds numbers ~ 1000); for 32 of these seeds we successfully visualized the flow around the wing (Fig. 3E; see also movie S1 and fig. S4 for all 32 LEV visualizations) (*18*). These free-flight experiments confirm the findings from our dynamically scaled model that (i) autorotating seeds generate a prominent stable LEV near their base and (ii) the LEV is more compact at lower angles of attack.

How well does the flow structure around the seeds compare to that of insect wings? The gross flow structure shows a prominent LEV (Fig. 2, A and B), as found for insects. For insect wings operating at Reynolds numbers on the order of 100 to 1000, stable attachment of the LEV is thought to depend partly on strong spanwise flow on top of the wing that drains vorticity from the LEV toward the wing-tip vortex (*14*, *21*, *22*). This process, which stretches and tightens the LEV, is a key feature, because it prevents the LEV from growing so large that it becomes unstable and separates. For all four seeds, we found strong spanwise flow on top of the wing (second row in Fig. 3, A to D). The spanwise flow is concentrated in the LEV at 25% span, whereas it is smeared out toward the trailing edge at 50% span and convected into the wake and tip vortex at 75% span—a pattern quite similar to that described for revolving insect wings (*22*).

To find out to which degree the LEV locally amplifies lift over the wing, we computed the seed's spanwise lift distribution by integrating vorticity within each wing section (*18*) (Fig. 4A). Sectional lift displays a clear maximum near 40 to 60% span for maple seeds *m1* and *m2*, whereas it forms a wider plateau for maple seed *m3* and hornbeam seed *h*. The lift distribution for maple seeds *m1* and *m2* resembles that measured on a revolving model fly wing at Reynolds number 1400, which also generates a stable LEV (*22*). The lift distribution is equal to the product of the local chord length, the sectional dynamic pressure, and sectional lift coefficient (*18*) (Fig. 4, B and C). The variation in spanwise lift is less than might be expected, because whereas sectional dynamic pressure rises toward the tip (where local velocities are highest), the sectional lift coefficient rises toward the base (Fig. 4, B and C). This spanwise distribution in lift coefficient is explained largely by the variation in angle of attack, which rises toward the base (Fig. 4D). The sectional lift coefficient reaches very high values ranging from 2 for hornbeam to almost 5 for maple seeds. The flow visualization in Figs. 2 and 3 indicates that the LEV is attached at the 25% span location where the sectional lift coefficient is greatest. The stable attachment of the LEV is noteworthy, given that the local angles of attack are well beyond the stall point for conventional aircraft wings and helicopter blades.

How effectively do these autorotating seeds descend, and how do they perform compared to other autorotating and gliding seeds? For successful dispersion, seeds need to have a long descent time so that the wind can carry them away from their tree of origin. Using a basic aerodynamic performance analysis, Eqs. S1 to S7 (*18*), we show that descent time is inversely proportional to the square root of wing loading (weight per unit surface area) and directly proportional to the square root of the descent factor, a dimensionless number that represents the seed's aerodynamic efficacy for a given descent speed and wing loading. To determine how well autorotating seeds perform, we compared their descent time as a function of wing loading with that of gliding and straying seeds in Fig. 5A. The color-coded hyperbolic lines in Fig. 5 indicate values of constant descent factor and thus constant aerodynamic efficacy. Gliding and straying seeds achieve long descent times, but they do so using low descent factors and thus must operate with very small wing loading, typically much less than 1 N m^{-2}. Because they operate with higher descent factors, autorotating seeds can achieve comparably long descent times at much greater wing loading. For example, the average descent time of autorotating seeds (yellow circle, Fig. 5A) is 36% longer than the value predicted from the low descent factors used by gliding and straying seeds (blue star, Fig. 5A).

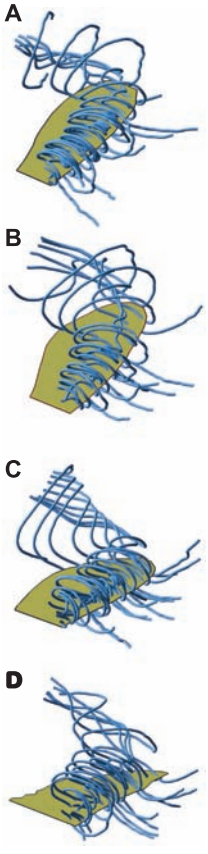

Fig. 2. The large LEV measured for all four model seeds. (**A** to **D**) Flow visualization of absolute (in lab frame) streamlines (shown in blue), calculated from the 3D velocity field measured using DPIV. The models of the three maple seeds [(A) *m1*, (B) *m2*, (C) *m3*] and the hornbeam seed [(D) *h*] generate a LEV with substantial spanwise flow that is connected to the tip vortex. The angle of attack of the seed increases from (A) to (D). Note that the seed spins clockwise (in all figures).

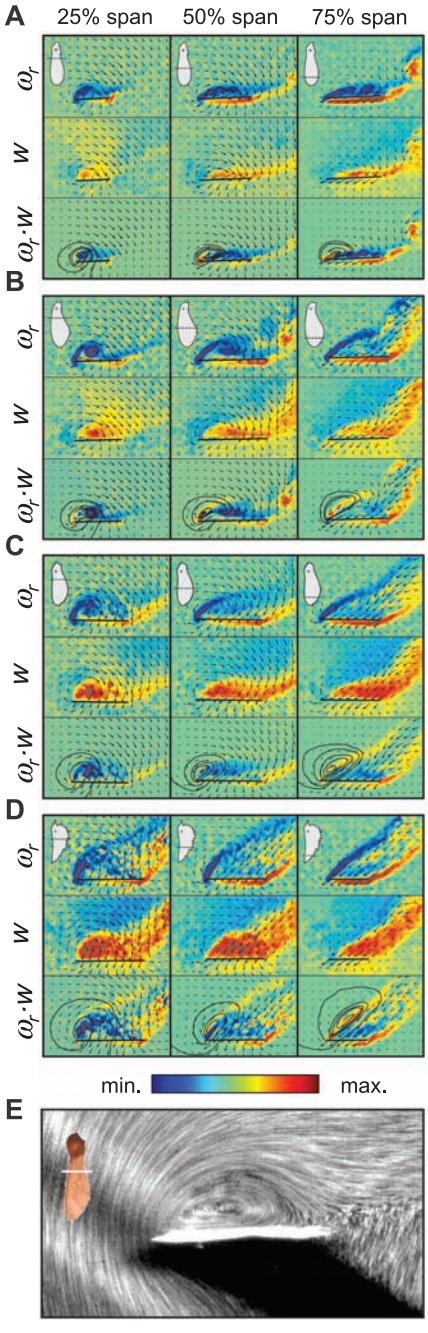

Fig. 3. The vorticity concentration that builds up the LEV at the wing's base is drained by concentrated spanwise flow. (**A** to **D**) Measured flow fields of seeds *m1* (A), *m2* (B), *m3* (C), and *h* (D) subsequently shown in the three columns of every block for three spanwise sections: 25, 50, and 75% span. First row shows spanwise vorticity (ω_r), which builds up into a prominent LEV at 25% span for all four seeds [color bar (A to D): ±70, ±50, ±30, ±30 s^{-1}]. Second row shows spanwise flow speed (w), which peaks at 25% span [color bar (A to D): ±0.5, ±0.4, ±0.2, ±0.2 ms^{-1}]. Third row shows spanwise transport of vorticity ($\omega_r \cdot w$), which peaks at 25% span [color bar (A to D): ±13, ±8, ±3, ±3 ms^{-2}]. (**E**) We found that freely flying *m4* maple seeds in our vertical wind tunnel generated a prominent LEV near the base (n = 32). The angle of attack at the wing tip of this specimen is 20° (between *m1* and *m2*).

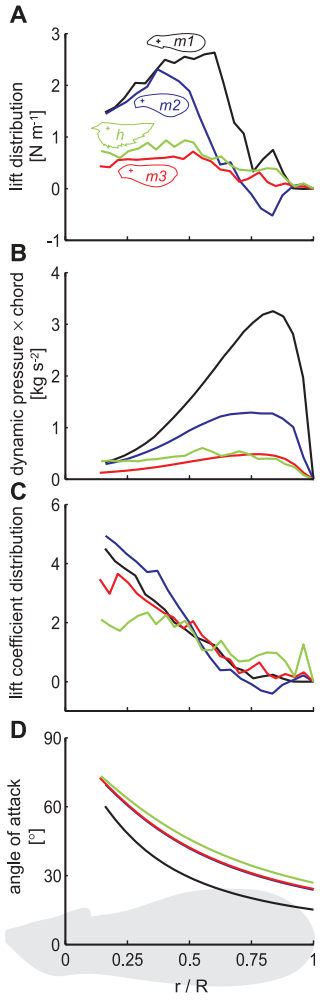

Fig. 4. The LEV induces exceptional high local lift coefficients near the wing's base. (**A**) Spanwise lift distribution. The wing's sectional lift is particularly low near the wing tip due to the presence of the tip vortex (*r*, local radius; *R*, wing-tip radius; seed code, Fig. 1B). (**B**) Product of sectional dynamic pressure and chord length. (**C**) The wing's sectional lift coefficient [(A) divided by (B)] peaks near the wing's base (where a LEV is present) and is minimal at the tip. (**D**) The distribution of angle of attack with span. The high lift coefficients near the base of the wing (C) and the corresponding LEV result from the extremely high local angles of attack, well beyond 30°.

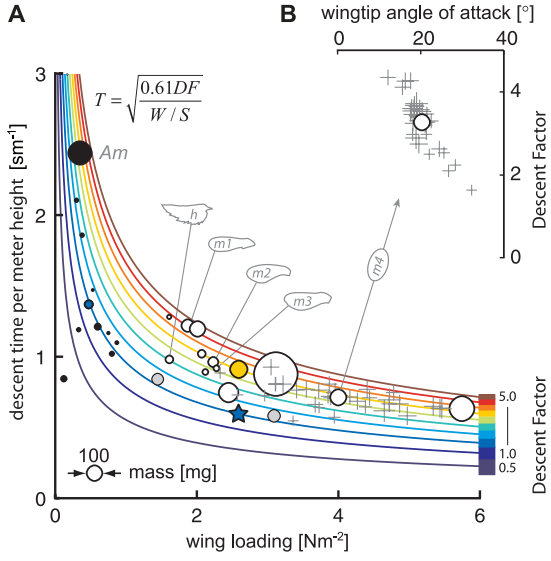

Fig. 5. Autorotating seeds operate at high aerodynamic efficacy, which is greatest at low wing-tip angle of attack. (**A**) Descent time of autorotating seeds (○,+) compared to gliding and straying seeds (●) as a function of wing loading. Symbol width indicates seed mass. Inset equation (see Supporting Online Material) indicates that descent time (*T*) is proportional to the square root of descent factor (*DF*), which is a measure of aerodynamic efficacy, divided by wing loading (*W*/*S*). The average descent time and wing loading of gliding and straying seeds is indicated by the blue circle. The average descent time and wing loading of the autorotating seeds is indicated by the yellow circle. The blue star indicates the predicted performance of gliding and straying seeds if they operated at the wing loading of autorotating seeds. The color-coded hyperbolic curves represent descent time as a function of wing loading at constant descent factor. The flight data have been measured by Azuma and co-workers (*6*, *8*, *29*, *30*), whereas crosses and the corresponding circle of *m4* indicate our vertical wind tunnel measurements of *Acer pseudo-platanus L*. seeds. The spread of the *m4* data illustrates the variance in performance that is typical of seeds (*6*, *8*, *29*, *30*). The specialized gliding seed *Alsomitra macrocarpa* (*Am*) is the only seed in this comparison that does not rely on substantial wind for dispersal (*29*). Ash and tulip tree seeds (gray circles) also autorotate, but spin along two major axes. (**B**) Within a population of *m4* seeds, descent factor increases with decreasing wing-tip angle of attack.

The 100% higher aerodynamic efficacy (on average) of autorotating seeds explains how they can descend only 30% faster than gliding and straying seeds even though their wing loading is 450% higher. Descent factor is highest for maple *m1* and is sequentially lower for *m2*, *m3*, and hornbeam *h*, which operate at higher angle of attacks. The compact and well-attached LEV generated by the maple seeds corresponds to higher aerodynamic efficacy than that of the partially stalled hornbeam seed, neglecting Reynolds number and morphological effects. Our free-flight experiments with 34 *m4* specimens in a vertical wind tunnel confirm this trend: A seed's aerodynamic efficacy increases with decreasing angle of attack (Fig. 5B), because at lower angles the LEV is more compact (fig. S4) (*18*).

The high lift generated by LEVs is exploited not only by autorotating seeds during their descent; hovering insects (*11*, *12*–*16*), bats (*23*), and probably birds (*24*–*27*) use the same mechanism. This suggests that the use of LEVs represents a convergent aerodynamic solution in the evolution of high-performance flight of both animal wings and plant seeds. Our results show that the LEV enhances the descent time of autorotating seeds for a given value of wing loading. This allows a plant to achieve high dispersal performance while investing more resources in each seed's embryo relative to those invested in building the seed's aerodynamic surface. Reliance on a LEV therefore expands the seed dispersal range and most likely the fitness of the tree. The enhanced aerodynamic performance of autorotating seeds could inspire the design of more effective autorotating vehicles (*9*, *28*).

References and Notes

1. L. Van der Pijl, *Principles of Dispersal in Higher Plants* (Springer-Verlag, Berlin, ed. 3, 1982).
2. R. Nathan *et al.*, *Nature* **418**, 409 (2002).
3. R. Nathan, *Science* **313**, 786 (2006).
4. R. A. Norberg, *Biol. Rev. Camb. Philos. Soc.* **48**, 561 (1973).
5. F. M. Burrows, in *Seed Dispersal*, D. R. Murray, Ed. (Academic Press, San Diego, 1986), pp. 1–49.
6. A. Azuma, K. Yasuda, *J. Theor. Biol.* **138**, 23 (1989).
7. K. J. Niklas, *Plant Biomechanics* (Univ. of Chicago Press, Chicago, 1992).
8. A. Azuma, *The Biokinetics of Flying and Swimming* (AIAA Education Series, Reston, VA, ed. 2, 2006).
9. H. J. Lugt, *Annu. Rev. Fluid Mech.* **15**, 123 (1983).
10. D. Seter, A. Rosen, *Trans. ASME* **59**, 1000 (1992).
11. J. R. Usherwood, C. P. Ellington, *J. Exp. Biol.* **205**, 1547 (2002).
12. T. Maxworthy, *J. Fluid Mech.* **93**, 47 (1979).
13. M. H. Dickinson, K. G. Götz, *J. Exp. Biol.* **174**, 45 (1993).
14. C. P. Ellington, C. van den Berg, A. P. Willmott, A. L. R. Thomas, *Nature* **384**, 626 (1996).
15. M. H. Dickinson, F.-O. Lehmann, S. P. Sane, *Science* **284**, 1954 (1999).
16. R. B. Srygley, A. L. R. Thomas, *Nature* **420**, 660 (2002).
17. W. B. Dickson, M. H. Dickinson, *J. Exp. Biol.* **207**, 4269 (2004).
18. Materials and methods are available as supporting material on *Science* Online.
19. K. Yasuda, A. Azuma, *J. Theor. Biol.* **185**, 313 (1997).
20. C. Poelma, W. B. Dickson, M. H. Dickinson, *Exp. Fluids* **41**, 213 (2006).
21. J. M. Birch, M. H. Dickinson, *Nature* **412**, 729 (2001).
22. J. M. Birch, W. B. Dickson, M. H. Dickinson, *J. Exp. Biol.* **207**, 1063 (2004).
23. F. T. Muijres *et al.*, *Science* **319**, 1250 (2008).
24. J. J. Videler, E. J. Stamhuis, G. D. E. Povel, *Science* **306**, 1960 (2004).
25. D. R. Warrick, B. W. Tobalske, D. R. Powers, *Nature* **435**, 1094 (2005).
26. T. Hubel, thesis, TU Darmstadt, Fachbereich Biologie, Germany (2006).
27. D. Lentink *et al.*, *Nature* **446**, 1082 (2007).
28. R. D. Lorenz, *Spinning Flight* (Springer, New York, 2006).
29. A. Azuma, Y. Okuno, *J. Theor. Biol.* **129**, 263 (1987).
30. S. Minami, A. Azuma, *J. Theor. Biol.* **225**, 1 (2003).

31. We thank M. Lino, E. W. Karruppannan, E. Janssen, J. G. M. van den Boogaart, K. M. Leon, and H. Schipper for help with the free-flight experiments. We thank G. E. Elsinga, J. R. Usherwood, and G. J. F. van Heijst for valuable comments. Research was funded by Netherlands Organisation for Scientific Research–Earth and Life Sciences Council (NWO-ALW, grant 817.02.012) (to D.L. and J.L.v.L.) and NSF grant IBN-0217229 (to M.H.D.).

Supporting Online Material

www.sciencemag.org/cgi/content/full/324/5933/1438/DC1
Materials and Methods
Figs. S1 to S7
Equations S1 to S7
References

30 March 2009; accepted 14 May 2009
10.1126/science.1174196

Fluorescent False Neurotransmitters Visualize Dopamine Release from Individual Presynaptic Terminals

Niko G. Gubernator,[1]*† Hui Zhang,[2,3]* Roland G. W. Staal,[2] Eugene V. Mosharov,[2] Daniela B. Pereira,[2] Minerva Yue,[2] Vojtech Balsanek,[1] Paul A. Vadola,[1] Bipasha Mukherjee,[4] Robert H. Edwards,[4] David Sulzer,[2,3,5]‡ Dalibor Sames[1]‡

The nervous system transmits signals between neurons via neurotransmitter release during synaptic vesicle fusion. In order to observe neurotransmitter uptake and release from individual presynaptic terminals directly, we designed fluorescent false neurotransmitters as substrates for the synaptic vesicle monoamine transporter. Using these probes to image dopamine release in the striatum, we made several observations pertinent to synaptic plasticity. We found that the fraction of synaptic vesicles releasing neurotransmitter per stimulus was dependent on the stimulus frequency. A kinetically distinct "reserve" synaptic vesicle population was not observed under these experimental conditions. A frequency-dependent heterogeneity of presynaptic terminals was revealed that was dependent in part on D2 dopamine receptors, indicating a mechanism for frequency-dependent coding of presynaptic selection.

Decision making, memory, and learning require activation and modification of particular synapses. Synaptic transmission in turn requires neurotransmitter accumulation into synaptic vesicles followed by neurotransmitter release during synaptic vesicle fusion with the plasma membrane. Optical methods have been developed to observe synaptic vesicle membrane fusion (*1*–*4*), but there has been no means for observing neurotransmitter release from individual synapses in the brain.

We designed optical tracers of monoamine neurotransmitters, or fluorescent false neurotransmitters (FFNs), inspired by classic reports that tyramine, amphetamine, and other phenylethylamines can be taken up into secretory vesicles and discharged during exocytosis (*5*). We designed FFNs by targeting neuronal vesicular monoamine transporter 2 (VMAT2), which carries monoamine neurotransmitters from the cytoplasm into synaptic vesicles (*6*). VMAT2 is relatively nonspecific and transports cellular monoamines (such as dopamine, serotonin, and norepinephrine) as well as synthetic amines (such as amphetamine, 3,4-methylenedioxymethamphetamine, and 1-methyl-4-phenylpyridinium) (*7*, *8*). We predicted that bulkier fluorescent monoamines might also be substrates (*9*) and developed compound FFN511 [Fig. 1A and fig. S1; design criteria are in the supporting online material (SOM)] (*10*). FFN511 inhibited serotonin binding to VMAT2-containing membranes, providing an apparent half maximal inhibitory concentration IC_{50} of 1 μM, a value close to dopamine itself (*7*).

In adrenal chromaffin cells, catecholamines are stored in large dense core vesicles (LDCVs) that possess the vesicular monoamine transporter 1 (VMAT1). FFN511 accumulated in a pattern consistent with LDCVs in cultured mouse chromaffin cells (Fig. 1B), and the accumulation was abolished by the lipophilic base chloroquine, which collapses the vesicle pH gradient (fig. S2) (*11*). Exposure to 350 nM FFN511 (30 min) had no effect on the quantal size of evoked catecholamine release (fig. S3), and total internal reflection fluorescence microscopy (TIRFM) showed that FFN511 undergoes stimulation-dependent exocytosis from LDCVs (Fig. 1C, fig. S4, and movie S1) (*12*).

We then examined FFN511 accumulation and release in mouse brain using multiphoton microscopy. FFN511 incubation of acutely prepared slices from the striatum resulted in fluorescent puncta that correlated well with the size of axon terminals (~1 μm) (Fig. 2). No label was observed in striatal cell bodies [chiefly medium spiny neurons (MSNs)], indicating that accumulation into lysosomes or other acidic organelles was below detection limits. As expected, no labeling was observed in the corpus callosum (CC), which lacks monoamine terminals, and sparser distribution was observed in the cortex (Fig. 2, A and G) and hippocampus than in the striatum.

Extensive experimental evidence was accumulated in order to confirm that FFN511 labels dopamine presynaptic terminals in striatum, including (i) the overlap of FFN511 signal with that of green fluorescent protein (GFP) by using striatal slices prepared from transgenic mice expressing GFP under the control of the tyrosine hydroxylase (TH) promoter (Fig. 2B) (*13*); (ii) exclusion of FFN511 from γ-aminobutyric acid (GABA)–releasing striatopallidal MSNs by use of bacterial artificial chromosome (BAC)–transgenic mice that express enhanced green fluorescent protein (EGFP) under the control of the promoter of dopamine D2 receptor (D2R) (fig. S5 and movie S2); (iii) loss of FFN511 labeling by lesioning dopamine neurons by in vivo injection of the selective dopaminergic neurotoxin 6-hydroxydopamine (6-OHDA) into the striatum of one hemisphere (Fig. 2C) (*14*); (iv) inhibition of FFN511 labeling by the VMAT2 inhibitors reserpine (Fig. 2D) and Ro 4-1284 (fig. S6); and (v) an extensive overlap of FFN511 with the endocytic synaptic vesicle marker FM1-43 (Fig. 2E and fig. S7). Furthermore, amphetamine (20 μM for 20 min), which redistributes vesicular dopamine to the cytosol and induces dopamine release without synaptic vesicle fusion (*15*), caused a substantial loss of fluorescence in striatum (Fig. 2F) and the medial prefrontal cortex (mPFC) (Fig. 2G).

Levels of FFN511 sufficient to label terminals in the striatum (10 μM for 30 min) did not significantly

[1]Department of Chemistry, Columbia University, New York, NY 10027, USA. [2]Departments of Neurology, Psychiatry, and Pharmacology, Columbia University, New York, NY 10032, USA. [3]Departments of Psychiatry and Pharmacology, Columbia University, New York, NY 10032, USA. [4]Departments of Neurology and Physiology, University of California School of Medicine, San Francisco, San Francisco, CA 94143, USA. [5]Division of Molecular Therapeutics, New York Psychiatric Institute, New York, NY 10032, USA.

*These authors contributed equally to this work.
†Present address: eMolecules, San Diego, CA 92014, USA.
‡To whom correspondence should be addressed. E-mail: ds43@columbia.edu (D. Sulzer); sames@chem.columbia.edu (D. Sames)

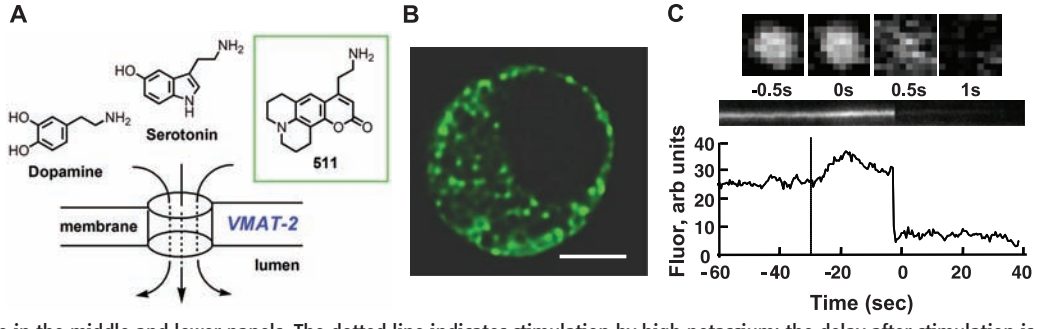

Fig. 1. In mouse chromaffin cells, FFN511 is accumulated in LDCVs and is released by exocytosis. (**A**) Chemical structure of FFN511. (**B**) Multiphoton image of a chromaffin cell reveals a distribution of FFN511 that is consistent with LDCVs. Scale bar, 5 μm. (**C**) FFN511 exocytosis from a LDCV observed with TIRFM images acquired at 500 ms intervals. The upper row shows consecutive images of a single vesicle. Orthogonal section through this vesicle and its integrated intensity are in the middle and lower panels. The dotted line indicates stimulation by high potassium; the delay after stimulation is typically observed in this preparation (movie S1).

alter evoked dopamine release as measured with cyclic voltammetry (a reduction of 7.5 ± 4%, mean ± SEM, $n = 4$ slices, $P > 0.5$). FFN511 cannot be oxidized during electrochemical detection, and higher concentrations of FFN511 (40 μM) decreased the evoked dopamine release by 35.4 ± 1.4% ($n = 3$ slices), presumably by displacing vesicular dopamine. The probe thus acts as an optical tracer of dopamine, and is sufficiently fluorescent so as to provide resolution of individual dopamine terminals at concentrations that do not interfere with normal catecholamine accumulation and transmission.

We examined activity-dependent release of FFN511 from dopamine synaptic terminals using a "pulse-chase" protocol in which an acute striatal brain slice was labeled with FFN511 (10 μM for 30 min) and then stimulated with current applied by a bipolar electrode (Fig. 3A and movie S3) or high potassium (fig. S8). Bipolar stimulation at 1, 4, and 20 Hz each evoked exponential destaining (Fig. 3B) with a mean half-time ($t_{1/2}$) of destaining of 330, 257, and 114 s, respectively, whereas negligible destaining occurred in the absence of stimulation or when stimuli were applied, but calcium channels were blocked by 200 μM cadmium (Fig. 3B). For each stimulus frequency and at all times during the protracted stimuli, the destaining was

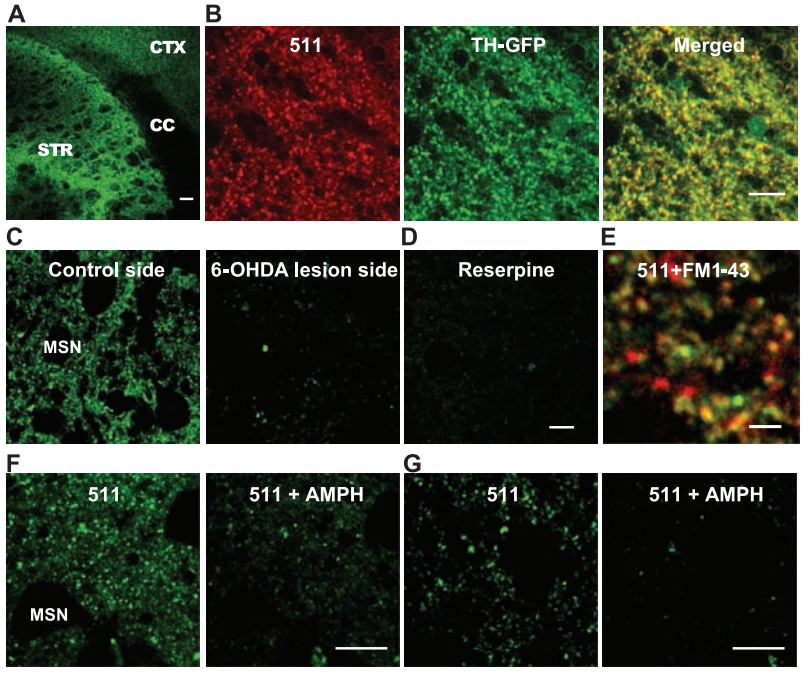

Fig. 2. FFN511 labels dopamine terminals in live cortical-striatal acute slices. (**A**) Labeling by FFN511 in acute live cortical-striatal slice: abundant labeling in the striatum (STR), sparser labeling in cortex (CTX), and no label in corpus callosum (CC). Scale bar, 100 μm. (**B**) Overall pattern of FFN511 (red) and TH-GFP (green) fluorescent markers shows extensive overlap (yellow) as expected for dopamine terminals. The GFP-label (green) is cytosolic and thus fills both terminals and axons, whereas FFN511 labels terminals and is more punctate. Scale bar, 10 μm. (**C**) Nearly complete inhibition of striatal FFN511 labeling 21 days after unilateral 6-OHDA lesion. Striatal slices were examined by means of cyclic voltammetry to ensure the complete loss of dopamine release in the lesion side. (**D**) FFN511 labeling was strongly inhibited by reserpine (20 μM). Scale bar for C and D, 10 μm. (**E**) Colocalization of FM1-43– (red) and FFN511-labeled (green) terminals. Slices were sequentially loaded with 10 μM FM1-43 and 5 μM FFN511. A representative image from four independent experiments depicts extensive colocalization of FFN511- and FM1-43–labeled terminals. Scale bar, 4 μm. (**F** and **G**) Destaining of FFN511 from the striatum (F) and mPFC (G) by amphetamine. (Left) Before amphetamine; (Right) after 20 min of 20 μM amphetamine. Scale bar, 10 μm.

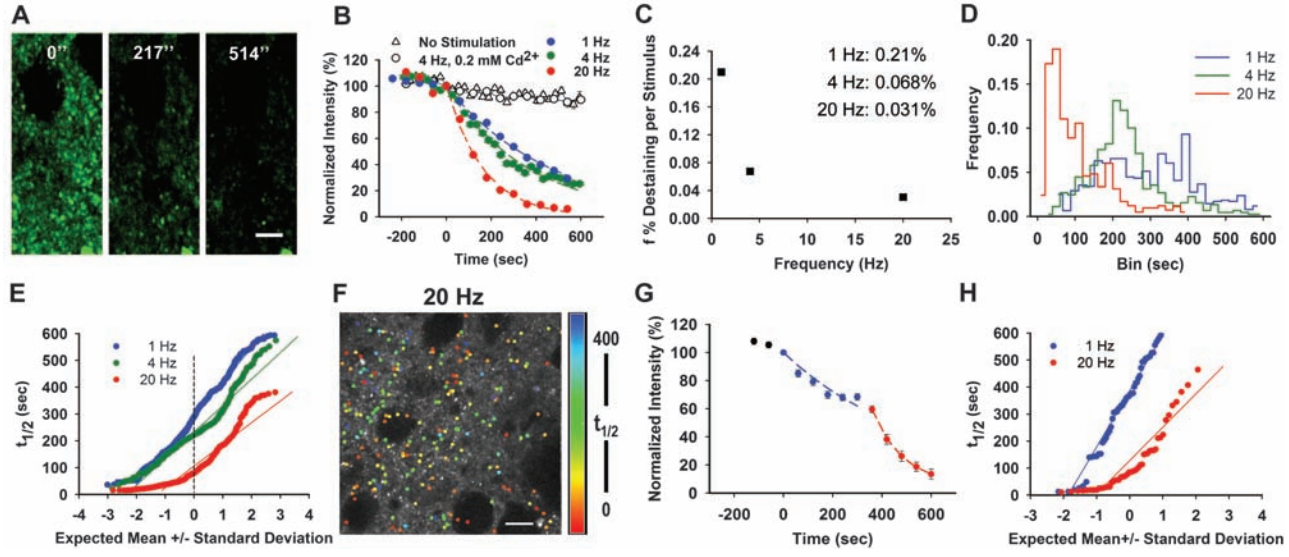

Fig. 3. Frequency-dependent induction of multiple dopamine terminal populations. (**A**) Local stimulation at 4 Hz resulted in destaining from the terminals. Stimulation began at $t = 0$. Scale bar: 5 μm. (**B**) Destaining of FFN511 at 4 Hz is Ca^{2+}- and frequency-dependent. Controls received no stimulation (153 puncta from 3 slices). Destaining with cadmium chloride (200 μM) was identical to unstimulated controls (475 puncta from 5 slices). The destaining curves for each stimulation frequency were fit by a single exponential decay function and half-life ($t_{1/2}$) values calculated as $\tau \times 0.693$ (1 Hz, 765 puncta from 9 slices; 4 Hz, 410 puncta from 7 slices; 20 Hz, 416 puncta from 6 slices). (**C**) The dependence of mean fractional release parameter (f, i.e., destaining per stimulus) on stimulus frequency. (**D**) Histogram of $t_{1/2}$ values of individual dopamine terminals stimulated at 1 Hz, 4 Hz, and 20 Hz. Bin size, 20 s. (**E**) Normal probability plot of half-time values for each terminal at 1, 4, and 20 Hz. The deviation from normality was increased with stimulation frequency. (**F**) Spatial distribution of FFN511 destaining rates of individual puncta stimulated at 20 Hz are shown in false color. Scale bar, 10 μm. (**G**) Averaged destaining kinetics of 60 puncta from one region of a slice stimulated consecutively first at 1 Hz (blue) and then at 20 Hz (red). (**H**) Distribution of $t_{1/2}$ values for the terminals in G; distribution at 1 Hz was well fit by a normal distribution, whereas the distribution deviated from normality at 20 Hz (movie S3).

well described by a single exponential. Thus, under these experimental conditions, neurotransmitter accumulation-competent presynaptic terminals do not display a population of kinetically distinct "reserve" synaptic vesicles.

This approach provides a means to address the long-standing question of the fractional neurotransmitter released from terminals during stimulation-dependent exocytosis. The data suggest that 0.03 to 0.21% of dopamine synaptic vesicles fused per stimulus, depending on the stimulation frequency (Fig. 3C). The apparent low probability of release is consistent with cyclic voltammetry recordings that indicate that stimulation-dependent release of dopamine represents a very small fraction of that released with amphetamine (*16*). There was a depression at more rapid stimulation, with twofold less destaining per pulse at 4 Hz and sixfold less destaining per pulse at 20 Hz than at 1 Hz (Fig. 3C). If dopamine terminals are mostly releasing neurotransmitter by full fusion of the synaptic vesicle (*17*), these measurements indicate the fraction of transmitter accumulation–competent synaptic vesicles fused per stimulus and revealed a stimulation-dependent form of presynaptic plasticity. The level of fractional destaining was enhanced with higher extracellular calcium (table S1), suggesting that frequency-dependent effects may be related to an activity-dependent decrease of calcium entry per stimulus, although other possibilities such as altered fusion mechanisms, depletion of a readily releasable pool, or decreased signal propagation through axons cannot be ruled out.

We next analyzed the heterogeneity within large ensembles of dopamine terminals in the striatum. The distribution of individual terminal activities showed a rightward skew at all stimulus frequencies when individual terminal half-times were displayed as histograms [$P < 0.005$, different from normal distribution by Kolmogorov-Smirnov (KS) test for all three frequencies] (Fig. 3D). In normal probability plots, in which normally distributed data are linear, multimodal distributions can be seen that deviate further from normality with increased stimulus frequency (1 Hz, $D = 0.0628$; 4 Hz, $D = 0.1160$; 20 Hz, $D = 0.1321$; D statistics were obtained with the KS test and indicate the deviation from normality) (Fig. 3E). All distributions were different from normal distribution and from each other ($P < 0.005$, KS test). The highly skewed distribution at 20 Hz indicates multiple populations of presynaptic terminals, including the most active population in which the probability of terminal content release per stimulus ($P_{terminal}$) is ~0.2%, and the slowest population, with $P_{terminal} \sim 0.005\%$. The spatial distribution of presynaptic activity appeared to be complex, with very active and inactive terminals often nearby (Fig. 3F). There was no relationship between initial fluorescent intensity and terminal destaining rates (fig. S9), suggesting that the heterogeneity in terminal activity was unrelated to the number of functional synaptic vesicles. To examine whether terminal heterogeneity may be due to variation in the depolarization of the terminals, we stimulated the same slice preparation at two frequencies and measured FFN511 destaining, first at 1 Hz and then at 20 Hz (Fig. 3, G and H). The distribution of half-time values obtained from the same set of presynaptic terminals is well fit by a normal distribution at 1 Hz ($D = 0.062$, $P > 0.1$, KS test) (Fig. 3, G and H, blue) and is in an apparent multiple population distribution at 20 Hz that is not fit by a normal distribution ($D = 0.194$, $P < 0.0001$, KS test) (Fig. 3, G and H, red). This confirms that presynaptic terminal heterogeneity is stimulation frequency–dependent, although we cannot exclude the possibility that this is due to differences in axonal action potential propagation. Differential activity of individual glutamate presynaptic terminals has been observed by using either postsynaptic electrophysiological measurements (*18*, *19*) or optical imaging, indicating membrane fusion (*4*); FFN511 reveals heterogeneity of dopamine release from individual terminals in the striatum and shows that this is a dynamic phenomenon dependent on stimulation frequency.

Cyclic voltammetry recordings in the striatum indicate that dopamine D2R activation inhibits the evoked release of dopamine in a frequency-dependent manner (*20*), and we thus examined how the frequency-dependent dopamine terminal heterogeneity was affected by the D2R antagonist sulpiride (10 μM for 20 min) (Fig. 4). There was no significant change in the mean values of terminal kinetics at 1 and 4 Hz, although sulpiride accelerated release in the slow population of terminals more than one SD slower than the expected mean (Fig. 4, A and B). At 20 Hz, however, sulpiride increased the mean $t_{1/2}$ by more than 50% (mean $t_{1/2} = 106.2 \pm 4.0$ s for control versus 161.0 ± 4.7 s for sulpiride), slowing the destaining kinetics of >65% of the terminals (Fig. 4C). The distributions of the destaining kinetics were closer to normal in the presence of sulpiride ($D = 0.0445$ at 1 Hz with sulpiride versus $D = 0.0628$ with 1 Hz control; $D = 0.0729$ at 4 Hz with sulpiride versus $D = 0.1160$ with 4 Hz control; $D = 0.1033$ at 20 Hz with sulpiride versus $D = 0.1321$ with 20 Hz control by KS normality test). Except for 1 Hz with sulpiride, all distributions deviated from normality ($P < 0.005$) and from the corresponding controls ($P < 0.001$), confirming that the emergence of multiple populations was dependent in large part on D2R activation. Consistently, cyclic voltammetry recordings confirm that sulpiride enhanced dopamine release by the second stimulus pulse at 20 Hz (2 single pulses with an interval of 0.05 s) (fig. S10A), and enhanced dopamine release by 2 pulses at 20 Hz but did not enhance dopamine release by 30 pulses at 20 Hz (fig. S10B). The phenomenon of frequency and pulse-dependent reversal of receptor inhibition of dopamine overflow has been identified using nicotinic antagonists (*21*, *22*). Thus the activity-dependent terminal heterogeneity is associated with receptor-mediated responses, and indicates the presence of frequency-dependent coding (*23*) that may determine how particular synapses are activated during decision-making, habit formation, and learning.

Spatial heterogeneity of dopamine release has been demonstrated by means of electrochemical

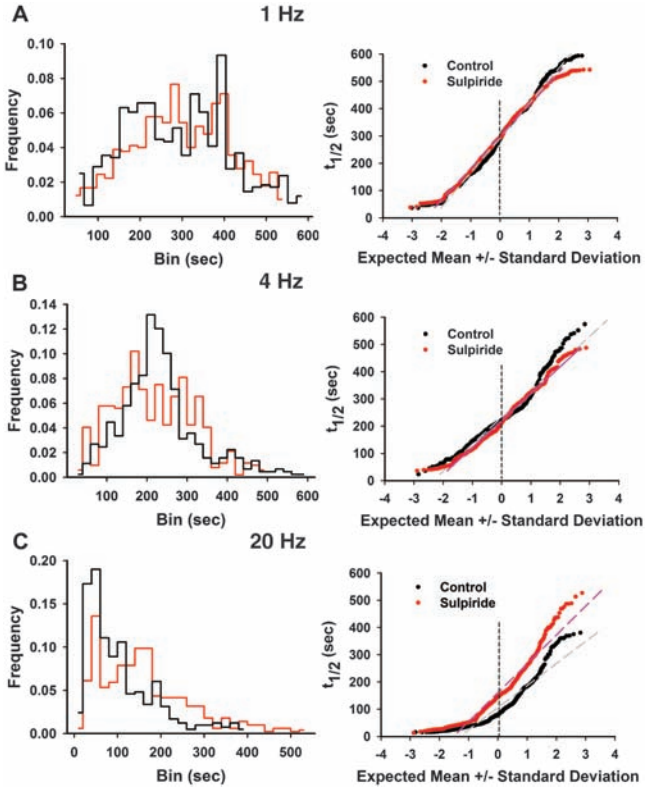

Fig. 4. Effect of dopamine D2R antagonist sulpiride on presynaptic terminal populations is frequency-dependent. (**A**) Effect of sulpiride on dopamine terminals stimulated at 1 Hz (765 puncta from 9 slices for the control and 901 puncta from 8 slices for sulpiride). Normal probability plot reveals that sulpiride accelerated transmitter release from the slowest terminals. (**B**) Effect of sulpiride on dopamine terminals stimulated at 4 Hz (519 puncta from 10 slices for the control, and 520 puncta from 5 slices for sulpiride). The effect of sulpiride was similar to that at 1 Hz stimulation. (**C**) Effect of sulpiride on dopamine terminals stimulated at 20 Hz (416 puncta from 6 slices for the control and 508 puncta from 4 slices for sulpiride). Sulpiride inhibited release from >65% of the terminals, except for the most active population. At each stimulation frequency, sulpiride shifted the entire population of the $t_{1/2}$ values closer to a normal distribution.

recordings with a resolution of ~100 μm (*24*) and has been suggested to play an important role in the modulation of synaptic circuitry involved in motivation, reward, and learning. Here we find that the activity of individual dopaminergic presynaptic terminals is modulated by neuronal activity and receptor activation. FFNs enable optical measurements of key presynaptic processes in the central nervous system, including accumulation of a vesicle transporter substrate and release by evoked activity or drugs such as amphetamine, at unprecedented spatial resolution. FFN511 is compatible with GFP-based tags, the FM1-43 endocytic marker, and other optical probes, which will allow the construction of fine-resolution maps of synaptic microcircuitry and presynaptic activity, particularly in regions such as the hippocampus and cortex where monoamine innervation can be too sparse for electrochemical recording.

References and Notes

1. W. J. Betz, G. S. Bewick, *Science* **255**, 200 (1992).
2. G. Miesenbock, D. A. De Angelis, J. E. Rothman, *Nature* **394**, 192 (1998).
3. Q. Zhang, Y. Li, R. W. Tsien, *Science* **323**, 1448 (2009).
4. V. N. Murthy, T. J. Sejnowski, C. F. Stevens, *Neuron* **18**, 599 (1997).
5. I. J. Kopin, *Annu. Rev. Pharmacol.* **8**, 377 (1968).
6. A. Merickel, P. Rosandich, D. Peter, R. H. Edwards, *J. Biol. Chem.* **270**, 25798 (1995).
7. J. S. Partilla *et al.*, *J. Pharmacol. Exp. Ther.* **319**, 237 (2006).
8. Y. Liu *et al.*, *Cell* **70**, 539 (1992).
9. G. Chen, D. J. Yee, N. G. Gubernator, D. Sames, *J. Am. Chem. Soc.* **127**, 4544 (2005).
10. Materials and methods are available as supporting material on *Science* Online.
11. D. Sulzer, S. Rayport, *Neuron* **5**, 797 (1990).
12. J. A. Steyer, H. Horstmann, W. Almers, *Nature* **388**, 474 (1997).
13. K. Sawamoto *et al.*, *Proc. Natl. Acad. Sci. U.S.A.* **98**, 6423 (2001).
14. T. F. Oo, R. Siman, R. E. Burke, *Exp. Neurol.* **175**, 1 (2002).
15. D. Sulzer, M. S. Sonders, N. W. Poulsen, A. Galli, *Prog. Neurobiol.* **75**, 406 (2005).
16. Y. Schmitz, C. J. Lee, C. Schmauss, F. Gonon, D. Sulzer, *J. Neurosci.* **21**, 5916 (2001).
17. R. G. Staal, E. V. Mosharov, D. Sulzer, *Nat. Neurosci.* **7**, 341 (2004).
18. N. A. Hessler, A. M. Shirke, R. Malinow, *Nature* **366**, 569 (1993).
19. C. Rosenmund, J. D. Clements, G. L. Westbrook, *Science* **262**, 754 (1993).
20. Y. Schmitz, C. Schmauss, D. Sulzer, *J. Neurosci.* **15**, 8002 (2002).
21. M. E. Rice, S. J. Cragg, *Nat. Neurosci.* **7**, 583 (2004).
22. H. Zhang, D. Sulzer, *Nat. Neurosci.* **7**, 581 (2004).
23. N. S. Bamford *et al.*, *Neuron* **42**, 653 (2004).
24. R. M. Wightman *et al.*, *Eur. J. Neurosci.* **26**, 2046 (2007).

25. We thank R. Burke for 6-OHDA injections and advice, M. Sonders for discussion, M. Siu for imaging analysis programming, and J. Schmoranzer for technical support with the TIRFM setup. Columbia University has applied for a patent on fluorescent false neurotransmitters. D. Sames thanks The G. Harold and Leila Y. Mathers Charitable Foundation and Columbia University's Research Initiatives in Science and Engineering. D. Sulzer thanks the National Institute on Drug Abuse (NIDA), the National Institute of Mental Health (NIMH), and the Picower and Parkinson's Disease Foundations. H.Z. thanks the National Alliance for Research on Schizophrenia and Depression. R.H.E. thanks the Michael J. Fox Foundation, the National Parkinson Foundation, NIDA, and NIMH.

Supporting Online Material

www.sciencemag.org/cgi/content/full/1172278/DC1
Materials and Methods
Figs. S1 to S10
Table S1
Movies S1 to S3
References

13 February 2009; accepted 20 April 2009
Published online 7 May 2009;
10.1126/science.1172278
Include this information when citing this paper.

Structure of Rotavirus Outer-Layer Protein VP7 Bound with a Neutralizing Fab

Scott T. Aoki,[1] Ethan C. Settembre,[1]* Shane D. Trask,[1]† Harry B. Greenberg,[2] Stephen C. Harrison,[1,3]‡ Philip R. Dormitzer[1]*‡

Rotavirus outer-layer protein VP7 is a principal target of protective antibodies. Removal of free calcium ions (Ca^{2+}) dissociates VP7 trimers into monomers, releasing VP7 from the virion, and initiates penetration-inducing conformational changes in the other outer-layer protein, VP4. We report the crystal structure at 3.4 angstrom resolution of VP7 bound with the Fab fragment of a neutralizing monoclonal antibody. The Fab binds across the outer surface of the intersubunit contact, which contains two Ca^{2+} sites. Mutations that escape neutralization by other antibodies suggest that the same region bears the epitopes of most neutralizing antibodies. The monovalent Fab is sufficient to neutralize infectivity. We propose that neutralizing antibodies against VP7 act by stabilizing the trimer, thereby inhibiting the uncoating trigger for VP4 rearrangement. A disulfide-linked trimer is a potential subunit immunogen.

Rotaviruses are multilayered, non-enveloped particles with double-stranded RNA (dsRNA) genomes (*1*). Four structural proteins form a complex, three-layered capsid, which packages two viral enzymes and 11 dsRNA genome segments. A double-layered particle (DLP) assembles in the cytoplasm, buds into the endoplasmic reticulum (ER), receives in this process a transient bilayer membrane, and ultimately acquires an outer layer of protein, viral protein 7 (VP7), in place of the transient envelope. VP7 must be present in sufficient quantity and must fold correctly in order to displace the intermediate membrane (*2*–*4*). This unusual maturation pathway results in the coating of a cytoplasmically synthesized and assembled inner particle with an ER-synthesized glycoprotein, but with no intervening membrane in the mature virion.

The surface of the DLP is a $T = 13$ icosahedral lattice of the trimeric protein, VP6, anchored on a $T = 1$ inner layer of VP2 (Fig. 1A). VP7 is likewise a trimer, stabilized by Ca^{2+} ions (*5*). It forms the outermost virion layer, also with $T = 13$ icosahedral packing, by capping the VP6 pillars (*6*–*8*). Assembly of the VP7 shell locks into place a second outer-layer protein, VP4, which is anchored between VP6 pillars and protrudes above the VP7 layer (*9*, *10*). VP4 spikes mediate attachment to cells and undergo a sequence of conformational changes that lead to endosomal membrane penetration (*11*, *12*). Uncoating of VP7, probably by withdrawal of Ca^{2+}, is necessary for these changes to occur (*13*). Thus, VP7 participates both in a membrane-displacing assembly step and in a membrane-disrupting entry step.

Rotavirus infection is the principal cause of severe, dehydrating diarrhea in infants (*14*). Live attenuated vaccines are now being introduced, but the efficacy and practicality of these vaccines in the impoverished settings in which most infant deaths from rotavirus occur have not yet been established (*15*). VP7 and VP4 are the targets of neutralizing and protective antibodies, and the structures and immunogenicities of these proteins underlie ongoing efforts to produce next generation subunit vaccines. Viruses bearing VP7 of at least 15 different serotypes (designated G1 to G15) have been isolated, 11 from humans (*16*, *17*). Epitopes of a number of neutralizing monoclonal antibodies (mAbs) have been determined, but the lack of a three-dimensional structure has precluded systematic study of neutralization mechanisms.

We have determined the crystal structure of the rhesus rotavirus (RRV, serotype G3) VP7 trimer in complex with the Fab fragment of neutralizing mAb 4F8 (*18*). The core of the subunit folds into two compact domains, with disordered N- and

[1]Laboratory of Molecular Medicine, Children's Hospital, Boston, MA 02115, USA. [2]Department of Microbiology and Immunology and Department of Medicine, Stanford University School of Medicine, Stanford, CA 94305, USA, and VA Palo Alto Health Care System, Palo Alto, CA 94304, USA. [3]Howard Hughes Medical Institute, Children's Hospital, Boston, MA 02115, USA.

*Present address: Novartis Vaccines and Diagnostics Inc., 350 Massachusetts Avenue, Cambridge, MA 02139, USA.
†Present address: Laboratory of Infectious Diseases, National Institute of Allergy and Infectious Diseases, Bethesda, MD 20892, USA.
‡To whom correspondence should be addressed. E-mail: harrison@crystal.harvard.edu (S.C.H.); philip.dormitzer@novartis.com (P.R.D.)

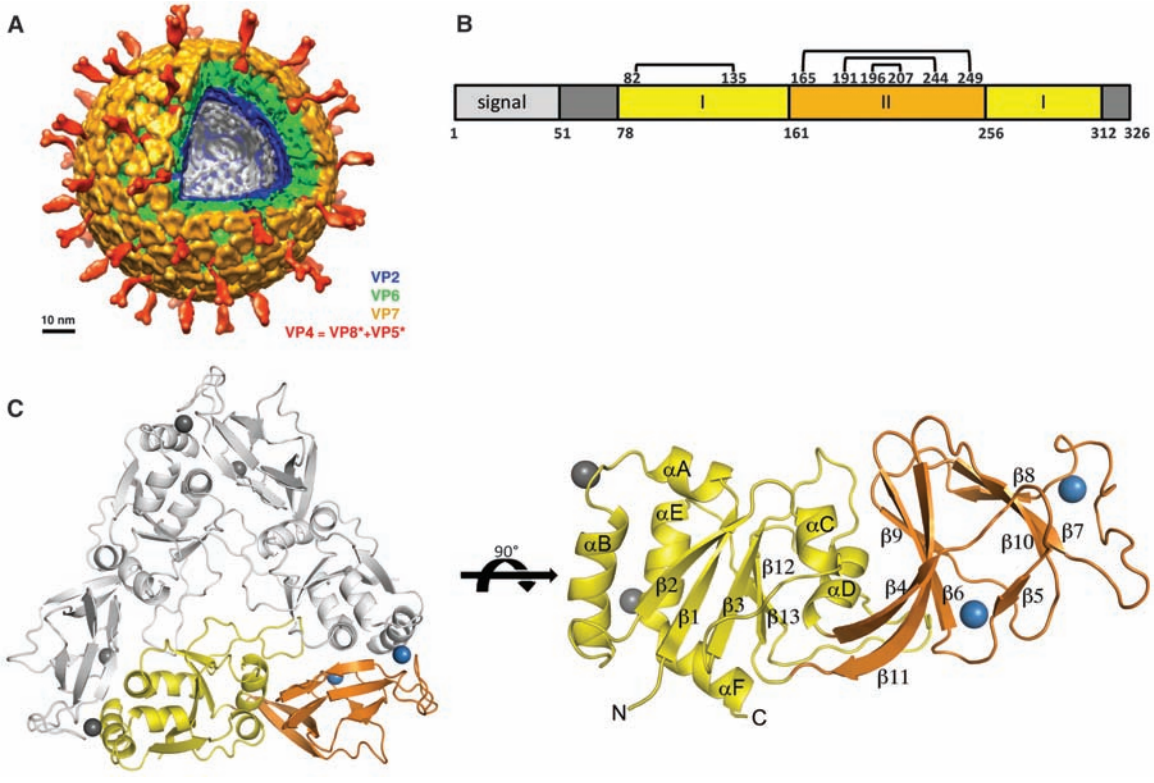

Fig. 1. Structure of RRV VP7. (**A**) Structure of the complete virion as determined by cryo-EM and filtered at 25 Å resolution. The segmentation of the structure is based on reconstructions of the complete virion (*13*) and the VP7-coated DLP (*13*) and on published work of others (*6*–*8*). (**B**) Schematic diagram of the VP7 primary structure, including the signal sequence (residues 1 to 50, light gray). The two domains are in the same colors as in (C); the N- and C-terminal arms, disordered in the crystal structure, are in dark gray. The pattern of intrasubunit disulfide bonds is also shown, with numbers corresponding to the positions of the cysteine residues. (**C**) Ribbon diagram of the trimer (left), viewed along its three-fold axis (i.e., as if looking onto the surface of the virion) with one subunit and one pair of Ca^{2+} ions in color and the other two subunits in gray. The Rossmann-fold domain (domain I) is in yellow, the β-barrel domain (domain II) in orange, and the Ca^{2+} ions in blue. A single subunit, in side view, is shown on the right, with secondary structure elements labeled. See fig. S3 for amino acid sequence of RRV VP7, with secondary structural elements designated.

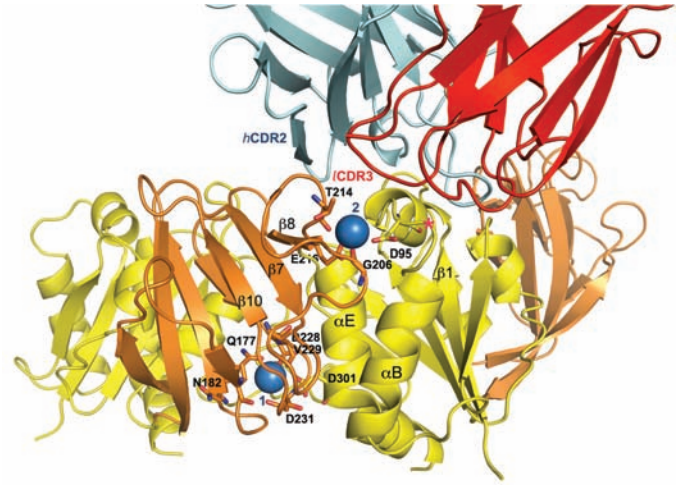

Fig. 2. View of the subunit interface, showing Ca^{2+} ion binding sites (labeled as 1 and 2) and the Fab contact. The view is from a direction that would be 60° around to the right in Fig. 1C, right panel. Residues that contribute to Ca^{2+} ligation (through side-chain groups or main-chain carbonyls) are included in stick representation and labeled. The light chain is in red, the heavy chain in cyan. VP7 colors are as in Fig. 1. The light-chain CDR3, the heavy-chain CDR2, and several secondary-structure elements in VP7 are labeled to provide points of reference and to facilitate comparison with Fig. 1. The heavy-chain CDR3, which like the light-chain CDR3 has extensive contacts with VP7, is the loop in the rear with a projected figure 8–like appearance. The red asterisk on VP7 (at center right) shows the location of the 4F8 escape mutation at position 96. Amino acid abbreviations: D, Asp; E, Glu; G, Gly; N, Asn; Q, Gln; T, Thr; V, Val.

C-terminal arms. There are two Ca^{2+} ions bound at each subunit interface in the trimer. The 4F8 Fab also binds across the trimer interface, apparently stabilizing it even at Ca^{2+} concentrations that would normally lead to dissociation. Known epitopes map either to the same region of the trimer surface or to a region at the interdomain boundary within a subunit. We show that the 4F8 Fab fragment neutralizes infectivity, with a median inhibitory concentration (IC_{50}) only about 30 to 50 times that of the intact, divalent immunoglobulin G (IgG), and we conclude that trimer stabilization, which will block uncoating, is the principal mechanism of neutralization by antibodies that recognize epitopes at the subunit interface. In other work (*13*), we have described a cryoelectron microscopy (cryo-EM) image reconstruction at 4 Å resolution of a DLP recoated with recombinant VP7, showing that the N-terminal arms of a VP7 trimer grip the underlying trimer of VP6. A hinge-bending rearrangement at the VP7 intrasubunit domain interface accompanies DLP binding. The 4F8 epitope at the intersubunit contact remains unaltered.

Recombinant RRV VP7 [expressed in insect cells as described (*5*)] and the Fab fragment of mAb 4F8 form a 1:1 complex that can be isolated by size exclusion chromatography (fig. S1) and crystallized in space group $P4_132$ (a = 244.18 Å, one VP7 subunit plus one Fab fragment per asymmetric unit) from polyethylene glycol (molecular weight 4000) in a pH 5.6 sodium citrate buffer with 0.1 mM $CaCl_2$. Previous efforts to crystallize the VP7 trimer had yielded only very disordered crystals. We recorded diffraction to a minimum Bragg spacing of 3.4 Å resolution, using beamline ID-24C at the Advanced Photon Source, Argonne National Laboratory (table S1). We obtained starting phases by carrying out a molecular replacement search with a library of 244 antibody fragment structures. We performed the rotation function calculations with an integration radius of 35 Å, using the program MOLREP (*19*), with each of the 244 structures as probe. Of these calculations, eight yielded promising solutions, as judged by a distinct difference between the ratio of rotation-function score

to sigma (RF/σ) for the best solution and that for the next best. Inspection showed that the Fab fragments that yielded these solutions all had similar elbow angles and that the positions and orientations of the fragment in the unit cell all had similar values. One of the top solutions was PDB accession number 1DBM, a murine IgG1-κ Fab similar to 4F8. We therefore used this model, modified to display the correct residues of the 4F8 variable domains (sequenced from the hybridoma cell line), for further calculations and model building. Most of the VP7 polypeptide chain was evident in the molecular-replacement electron density, with the exception of N- and C-terminal segments, and we could build a preliminary model without difficulty. The high solvent content (87%) allowed us to calculate a very clear map by solvent flipping (fig. S2), despite the modest resolution (3.4 Å).

The VP7 subunit is a "Rossmann fold" (domain I), with a jelly-roll β sandwich (domain II) inserted between α-helix D and β-strand 12 (Fig. 1, B and C). There are four disulfide bonds, one within domain I and the other three within domain II (Fig. 1B). After initial refinement, a difference map revealed two strong peaks at the subunit interface. Addition of Ca^{2+} ions to the model at each of these positions improved the free *R*-factor. The final model contains residues 78 to 312 (table S1). Asn^{69}, the single glycosylated residue in RRV VP7, is in the disordered, N-terminal arm (fig. S3). Three subunits assemble into a thin triangular plate with a central depression, a variable surface that faces outward on the virion, and a more conserved, somewhat negatively charged, inward-facing surface.

The two Ca^{2+} sites both have side-chain carboxylate and main-chain carbonyl neighbors appropriate for divalent cations, and the contributing side chains are conserved among group A rotaviruses (Fig. 2). There are six protein-derived ligands at site 1 and four at site 2; one or two water molecules, not included because of the limited resolution, presumably complete the coordination sphere at the latter site. Site 2 is close to the Fab interface. The presence of the bound ion might influence the conformation of VP7 loops in contact with the antibody. Mutants in strain RF that confer resistance to low calcium have a Pro^{75} → Leu substitution, sometimes accompanied by a Pro^{279} → Ser mutation (*20*). The former site is in the N-terminal arm, at a location where a leucine might enhance the grip on VP6; the latter, on the inward-facing surface of VP7, is at a point of contact with the outward-facing surface of VP6 (*20*). The resistance to low Ca probably arises from the indirect effect of either mutation in stabilizing the contact with VP6, rather than from a direct effect on the Ca^{2+} sites.

The Fab binds across the intersubunit junction, on the surface of the trimer that will face outward when VP7 coats the virion (*13*) (Fig. 2). The heavy chain carries a majority of the contacts (78% of total buried surface area at the Fab-VP7 interface) to domain I of one subunit and domain II of the other. The one clear light-chain contact is at the site of a neutralization escape mutation (Asn^{96} → Asp) (*21*). Like all well-characterized, VP7-directed neutralizing antibodies, 4F8 binds only trimeric VP7 and not the Ca^{2+}-free monomer (*22*). A number of neutralizing antibodies, including 4F8 and 159, block VP7 uncoating from virions, even in the presence of Ca^{2+} chelators (*22*, *23*). By locking down the subunit interface, these antibodies probably stabilize the trimer, even at very low divalent cation concentrations.

If 4F8 prevents uncoating by stabilizing individual trimers, then the Fab fragment should also neutralize. Figure 3 shows the results of neutralization assays with intact 4F8 mAb and with 4F8 Fab. The IC_{50} for the Fab is about 30 to 50 times that of the intact, bivalent mAb, presumably because of an avidity effect, but the neutralization activity of the Fab is unambiguous. Earlier experiments that came to the opposite conclusion generated the Fab by papain digestion of virion-antibody complexes (*23*, *24*); the concentration of Fab thus produced was probably not sufficient to give a measurable effect.

The sites of mutations in VP7 that permit escape from neutralization by various mAbs map to two regions, 7-1 and 7-2, on the exposed surface of the protein. Each region includes several "epitopes" previously designated by letters (see Fig. 4 and table S2, in which we group the published epitopes into the two structurally defined regions). Region 7-1, which spans the intersubunit boundary, is immunodominant. It contains the positions of escape mutations selected by 58 of 68 tested neutralizing mAbs, including 4F8. Two mAbs select escape mutations in both regions 7-1 and 7-2 (table S2). Modification at position 211 by an oligosaccharide, which would block antibody binding to region 7-1, confers resistance to neutralization by hyperimmune anti-rotavirus serum (*21*). Most or all of the antibodies that bind region 7-1 probably neutralize by a mechanism similar to that proposed above for 4F8. Region 7-2 is at the interdomain boundary within a single VP7 subunit. Antibodies that bind region 7-2 may neutralize by a different mechanism. Analysis of a high-resolution cryo-EM reconstruction of VP7-coated DLPs shows that the subunit undergoes a conformational change when it binds the DLP, with a substantial dislocation at the domain interface but little or no change at the intersubunit contact (*13*). We suggest that antibodies that bind in region 2 stabilize the trimer by fixing the virion-associated conformation, by cross-linking subunits within a trimer, or by cross-linking adjacent trimers on the surface of the virus particle.

The sequences of amino acid residues at positions 87 to 101 and 208 to 211 are conserved among strains within a G serotype but not across different serotypes. These sequences are "signatures" that can be used to predict the serotype of a new isolate (*25*). They correspond to surface ridges on either side of the subunit interface, in regions 7-1a and 7-1b, respectively. Because both homotypically and heterotypically neutralizing mAbs select mutations in region 7-1 (and also in region 7-2), some aspect of antibody binding other than epitope location must determine the breadth of neutralizing capacity (*21*, *26*, *27*).

Regions 7-1 and 7-2 together cover much of the outward-facing surface of VP7. Analysis of

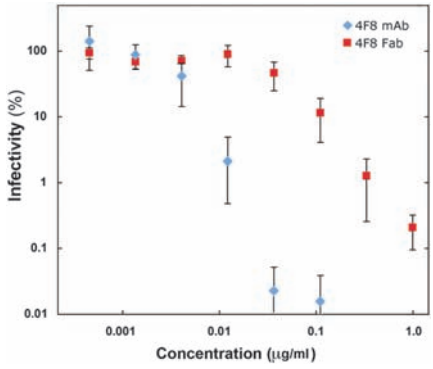

Fig. 3. Neutralization of RRV by the IgG and Fab of mAb 4F8. Percent infectivity is plotted (on a log scale) against antibody or Fab concentration (also on a log scale). Error bars calculated (SDs) are from three independent measurements. See supporting online material for details of the assay.

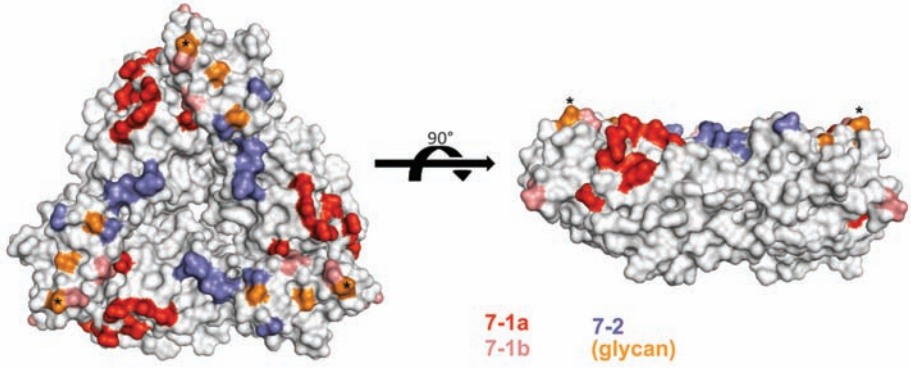

Fig. 4. Positions of neutralization escape mutations selected by various mAbs. The residues cluster roughly into two regions designated 7-1 and 7-2 (see text). Region 7-1 spans the intersubunit boundary; we have divided it into 7-1a (red), on one side of the interface, and 7-1b (pink), on the other. Residues in 7-2 are in blue. The 4F8 Fab (and, by inference, the Fabs of most mAbs that recognize residues in region 7-1) has contacts in both 7-1a and 7-1b (see Fig. 2). Positions at which escape is through a mutation that produces a new glycosylation site are in orange and lie either in 7-1 or 7-2; an asterisk labels residue 211 (see text).

sequences from all 11 human G serotypes shows that most of the variability is in residues on the outward-facing surface of the VP7 trimer (fig. S4). Because there is no extensive conserved patch on this surface, any potential cellular receptor that binds VP7 on the virion must have a very small binding footprint, or its identity and site of interaction must vary among serotypes or isolates. It has been suggested that VP7 may interact with αXβ2 integrins after attachment (*28*). The site proposed as an integrin-binding motif (GPR, resides 253 to 255) is on the inward-facing surface of the trimer and would only be available to interact with integrins after uncoating.

We have designed a disulfide-linked variant of the VP7 trimer by substituting cysteines for Thr^{276} and Gln^{305}, which face each other across the subunit contact. The resulting disulfide is largely buried at the interface. The secreted product of insect cell expression is indeed stably trimeric (fig. S5). The arm-grip mode of association with VP6 thus allows the VP7 trimer to bind and to lock VP4 in place, but cross-linking of the core subunits retards dissociation, probably by several orders of magnitude. These observations support the notion that withdrawal of Ca^{2+} is the uncoating trigger in an endosome.

Rotavirus infection and parenteral immunization with virions both induce a strong VP7-specific neutralizing antibody response (*1*). Recombinant VP7 elicits neutralizing antibodies only inefficiently, probably because the free trimer dissociates; the response can be enhanced by adding a C-terminal membrane anchor, which presumably increases trimer stability by immobilizing the subunit in two dimensions on the cell surface (*5*, *29*). The disulfide cross-linked VP7 trimer, which binds neutralizing antibodies such as mAb 159, is a good first candidate for a more effective, stable, structurally engineered subunit immunogen.

References and Notes

1. M. K. Estes, A. Z. Kapikian, in *Fields Virology*, D. M. Knipe, P. M. Howley, Eds. (Lippincott, Williams & Wilkins, Philadelphia, ed. 5, 2007), pp. 1918–1974.
2. L. Svensson, P. R. Dormitzer, C. H. von Bonsdorff, L. Maunula, H. B. Greenberg, *J. Virol.* **68**, 5204 (1994).
3. T. Lopez *et al*., *J. Virol.* **79**, 184 (2005).
4. F. Michelangeli, F. Liprandi, M. E. Chemello, M. Ciarlet, M. C. Ruiz, *J. Virol.* **69**, 3838 (1995).
5. P. R. Dormitzer, H. B. Greenberg, S. C. Harrison, *Virology* **277**, 420 (2000).
6. B. V. Prasad, G. J. Wang, J. P. Clerx, W. Chiu, *J. Mol. Biol.* **199**, 269 (1988).
7. M. Yeager, K. A. Dryden, N. H. Olson, H. B. Greenberg, T. S. Baker, *J. Cell Biol.* **110**, 2133 (1990).
8. Z. Li, M. L. Baker, W. Jiang, M. K. Estes, B. V. Prasad, *J. Virol.* **83**, 1754 (2009).
9. A. L. Shaw *et al*., *Cell* **74**, 693 (1993).
10. S. D. Trask, P. R. Dormitzer, *J. Virol.* **80**, 11293 (2006).
11. L. Fiore, H. B. Greenberg, E. R. Mackow, *Virology* **181**, 553 (1991).
12. P. R. Dormitzer, E. B. Nason, B. V. Prasad, S. C. Harrison, *Nature* **430**, 1053 (2004).
13. J. Z. Chen *et al*., *Proc. Natl. Acad. Sci. U.S.A.* 10.1073/PNAS.0904024106 (2009).
14. U. D. Parashar, C. J. Gibson, J. S. Bresse, R. I. Glass, *Emerg. Infect. Dis.* **12**, 304 (2006).
15. B. Jiang, J. R. Gentsch, R. I. Glass, *Vaccine* **26**, 6754 (2008).
16. N. Santos, Y. Hoshino, *Rev. Med. Virol.* **15**, 29 (2005).
17. N. Santos *et al*., *J. Clin. Microbiol.* **46**, 462 (2008).
18. R. D. Shaw, P. T. Vo, P. A. Offit, B. S. Coulson, H. B. Greenberg, *Virology* **155**, 434 (1986).
19. A. Vagin, A. Teplyakov, *J. Appl. Crystallogr.* **30**, 1022 (1997).
20. R. Gajardo, P. Vende, D. Poncet, J. Cohen, *J. Virol.* **71**, 2211 (1997).
21. E. R. Mackow *et al*., *Virology* **165**, 511 (1988).
22. P. R. Dormitzer, G. W. Both, H. B. Greenberg, *Virology* **204**, 391 (1994).
23. J. E. Ludert, M. C. Ruiz, C. Hidalgo, F. Liprandi, *J. Virol.* **76**, 6643 (2002).
24. F. M. Ruggeri, H. B. Greenberg, *J. Virol.* **65**, 2211 (1991).
25. K. Y. Green *et al*., *J. Virol.* **62**, 1819 (1988).
26. K. Nishikawa *et al*., *Virology* **171**, 503 (1989).
27. B. S. Coulson, C. Kirkwood, *J. Virol.* **65**, 5968 (1991).
28. K. L. Graham *et al*., *J. Virol.* **77**, 9969 (2003).
29. M. E. Andrew *et al*., *J. Virol.* **64**, 4776 (1990).

30. We thank M. Babyonyshev for help with protein preparations, the staff of the Northeastern Collaborative Access Team (Advanced Photon Source, Argonne National Laboratory) for assistance with x-ray data collection, R. Stanfield for the library of Fab structures, and J. Patton for help with sequence variability analysis. Supported by NIH grant CA-13202 (S.C.H.), by a VA Merit Award and NIH grants AI-21362 and DK-56339 (H.B.G.), and by an Ellison Medical Foundation New Investigators in Infectious Diseases Award (P.R.D.). S.C.H. is an Investigator of the Howard Hughes Medical Institute. Atomic coordinates and structure factor amplitudes for the VP7-4F8 Fab complex have been deposited in the Protein Data Bank (www.rcsb.org) with accession code 3FMG.

Supporting Online Material

www.sciencemag.org/cgi/content/full/324/5933/1444/DC1
Materials and Methods
Figs. S1 to S5
Tables S1 and S2
References

5 January 2009; accepted 28 April 2009
10.1126/science.1170481

Extensive Demethylation of Repetitive Elements During Seed Development Underlies Gene Imprinting

Mary Gehring, Kerry L. Bubb, Steven Henikoff*

DNA methylation is an epigenetic mark associated with transposable element silencing and gene imprinting in flowering plants and mammals. In plants, imprinting occurs in the endosperm, which nourishes the embryo during seed development. We have profiled *Arabidopsis* DNA methylation genome-wide in the embryo and endosperm and found that large-scale methylation changes accompany endosperm development and endosperm-specific gene expression. Transposable element fragments are extensively demethylated in the endosperm. We discovered new imprinted genes by the identification of candidates associated with regions of reduced endosperm methylation and preferential expression in endosperm relative to other parts of the plant. These data suggest that imprinting in plants evolved from targeted methylation of transposable element insertions near genic regulatory elements followed by positive selection when the resulting expression change was advantageous.

Cytosine DNA methylation is a stable epigenetic modification that has roles in transposable element silencing and gene imprinting in plant and animals. In plants, gene imprinting occurs in the endosperm during seed development (*1*). At fertilization, one sperm fertilizes the haploid egg cell, which becomes the diploid embryo, and the other sperm fertilizes the diploid central cell, generating the triploid endosperm. In *Arabidopsis*, the 5-methylcytosine DNA glycosylase DEMETER (DME) demethylates maternal alleles of imprinted genes in the central cell before fertilization, thus establishing methylation asymmetry between embryo and endosperm. Similarly, in maize an imprinted gene is less methylated in the central cell than in the egg cell or sperm (*2*). The asymmetry between embryo and endosperm represents an opportunity to characterize DNA methylation in parallel genomes established simultaneously at fertilization within the same seed.

To compare tissue-specific methylation patterns within developing seeds, we dissected embryo and endosperm from torpedo-stage seeds of two *Arabidopsis thaliana* accessions, Col-*gl* and L*er* (fig. S1A) (*3*). Methylated DNA was immunoprecipitated with an antibody to 5-methylcytosine, sequenced with Illumina Genome Analyzer technology (Illumina, San Diego, CA), and aligned to the reference Col-0 genome. We created methylation profiles using high-quality reads that mapped to only one position in the genome (table S1). Embryo and endosperm methylation profiles were highly correlated (Pearson's $R = 0.91$ for Col-*gl* and 0.89 for L*er*) and share similar features with other whole-

Howard Hughes Medical Institute (HHMI), Fred Hutchinson Cancer Research Center (FHCRC), 1100 Fairview Avenue North, Seattle, WA 98109, USA.

*To whom correspondence should be addressed. E-mail: steveh@fhcrc.org

genome methylation profiles that have been generated for *Arabidopsis* with other platforms (Fig. 1 and fig. S1B) (*4*, *5*). Methylation levels are relatively high in gene-poor heterochromatic regions around centromeres and decrease in gene-rich chromosome arms (Fig. 1A). Transposable element genes (a set of 3900 elements with open reading frames) are more heavily methylated than protein-coding genes, and genes are more methylated within their bodies than at their 5′ and 3′ ends (Fig. 1B). However, transposable element genes and regions flanking genes are on average less methylated in the endosperm than embryo (Fig. 1B). If the calculation of average methylation profiles 5′ and 3′ of protein-coding genes excludes methylation from transposable elements or their fragments, the methylation difference between embryo and endosperm in regions flanking genes almost entirely disappears, which indicates that repetitive elements are hypomethylated in the endosperm (Fig. 1C). These results suggest that there is a genome-wide decrease in methylation in the endosperm as compared with the embryo. Reduction in methylated DNA in the endosperm is also observed when immunoprecipitated methylated DNA is hybridized to genomic tiling arrays (fig. S2). This small genome-wide reduction is consistent with the report that maize endosperm has 13% less 5-methylcytosine than do embryos or leaves (*6*).

To identify regions of the genome subject to the largest changes in DNA methylation [differentially methylated regions (DMRs)], we calculated an embryo-endosperm difference score in overlapping 300–base pair (bp) segments and set the cutoff to include the top 0.5% of differences (top DMRs) (Fig. 2A). This cutoff detects the previously described methylation differences 5′ and 3′ of the imprinted *MEA* gene (*7*), whereas those 5′ of *FWA* (*8*) fall just below it (+1.18 versus a cutoff of 1.20) (Fig. 2B). This cutoff also detects previously hypothesized methylation differences (*9*, *10*) at the *PHE1* and *FIS2* imprinted genes (Fig. 2B). About 90% of the top DMRs have a positive score, which indicates greater methylation in the embryo than endosperm (fig. S3). In plants, DNA methylation is actively targeted by small RNAs, which often arise from and target repetitive elements (*11*). The top DMRs were almost threefold enriched in regions of the genome corresponding to transposable elements (*12*) and small RNAs (*13*) (table S2), which indicates that demethylation occurs at regions that are actively targeted for DNA methylation in other tissues. The distribution of the DMRs along the chromosomes parallels the distribution of transposable elements (fig. S4).

Bisulfite sequencing around 15 different regions that fell above and below the top 0.5% cutoff largely validated the predictions from the deep-sequencing analysis (fig. S5). For DMRs with a positive score, methylation of individual bisulfite clones from the endosperm was more variable than from the embryo. Often, two distinct subpopulations of clones were observed in the endosperm, including clones with no methylation, which were never observed in the embryo. Therefore, unmethylated clones in the endosperm might represent specific demethylation of the maternal genome by DME in the central cell before fertilization. In support of this possibility, clones with no methylation were nearly eliminated in *dme* mutant endosperm.

More than half of the top positive DMRs (endosperm less methylated than embryo) occur within 2 kilobase (kb) upstream or 2 kb downstream of genes (fig. S3) (*7*, *14*). We identified all protein-coding genes in which a top positive DMR fell within the body of the gene or 1 kb 5′ or 3′. This yielded 1276 genes for the Col-*gl* embryo-endosperm comparison (table S3) and 1163 for L*er* embryo-endosperm comparison (table S4). Embryo methylation profiles for these genes display prominent peaks centered at ~700 bp both upstream and downstream that are largely absent in the endosperm (Fig. 3 and fig. S6). This change represents loss of methylation in the endosperm and not gain of methylation in the embryo because these genes are similarly methylated in embryos and adult plants (figs. S1C and S6C). Upstream and downstream methylation peaks are partially restored in *dme* mutant endosperm (Fig. 3), despite the fact that *dme* endosperm is

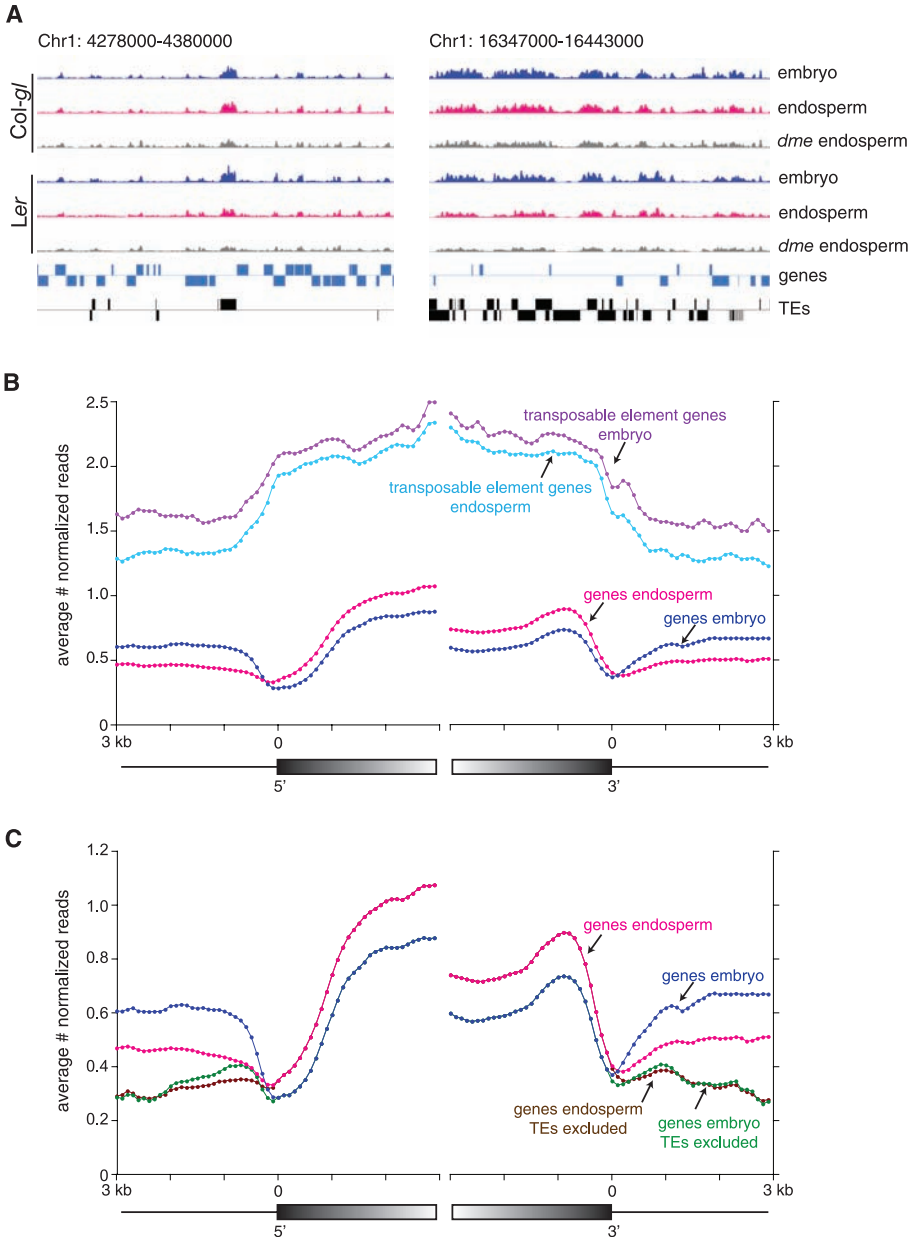

Fig. 1. Endosperm is less methylated than embryo. (**A**) Typical methylation profiles from a gene-rich and gene-poor region of the genome showing highly similar methylation patterns in embryo, endosperm, and *dme* endosperm from the L*er* and Col-*gl* accessions. (**B**) Average methylation in 100-bp windows of protein-coding genes and transposable element genes aligned at either their 5′ or 3′ ends in Col-*gl* embryo and endosperm. (**C**) Methylation profiles of protein-coding genes when a set of 31,076 transposable element fragments (*12*) are and are not excluded from the averaging.

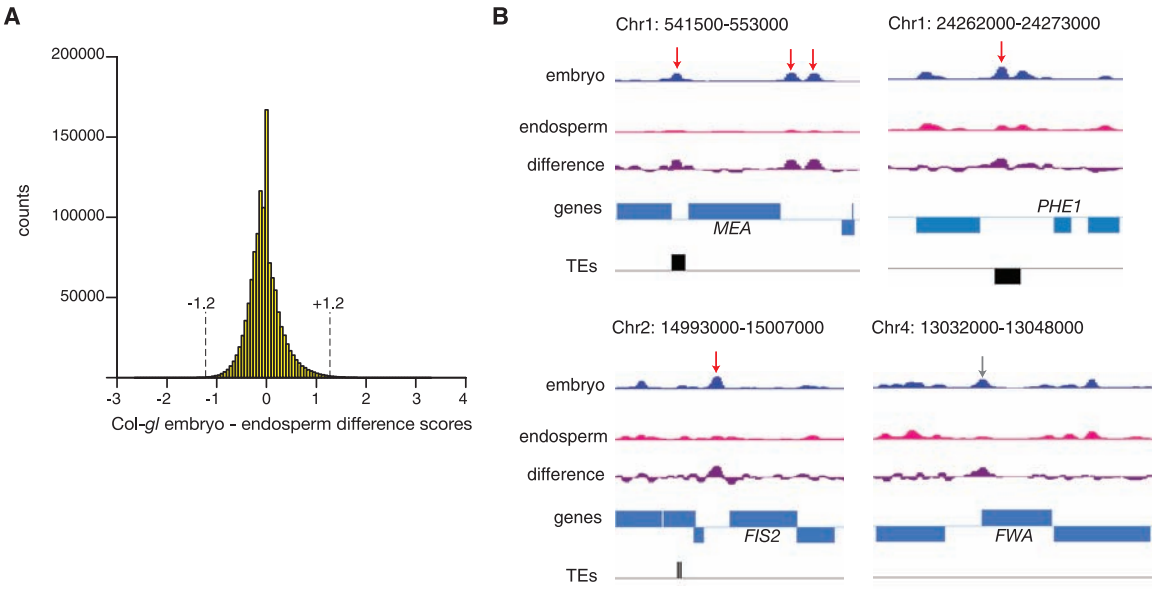

Fig. 2. Known imprinted genes are associated with top DMRs. (**A**) Histogram of Col-*gl* embryo–endosperm difference scores for 1.2 million overlapping 300-bp segments. Dashed lines represent the cutoff for the top 0.5% of methylation differences (~6000 300-bp segments). (**B**) Embryo and endosperm methylation profiles of known imprinted genes. Red arrows indicate regions within the top 0.5% of methylation differences; the gray arrow indicates a region below the cutoff.

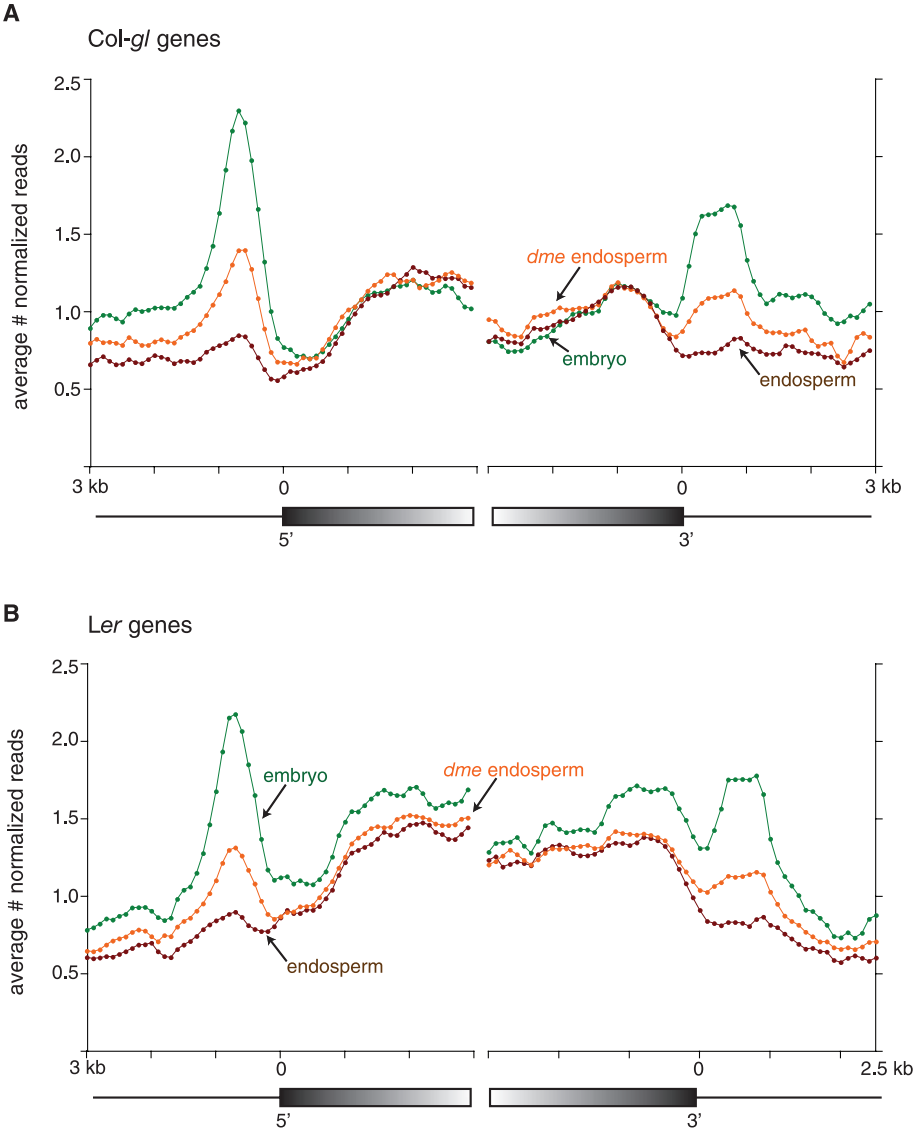

Fig. 3. Methylation is lost 5′ and 3′ of genes in the endosperm. Shown are average methylation profiles in embryo, endosperm, and *dme* endosperm of the (**A**) 1276 Col-*gl* and (**B**) 1163 L*er* genes associated with more methylation in embryo than endosperm. Genes were aligned at their 5′ or 3′ end, and the average methylation was determined every 100 bp.

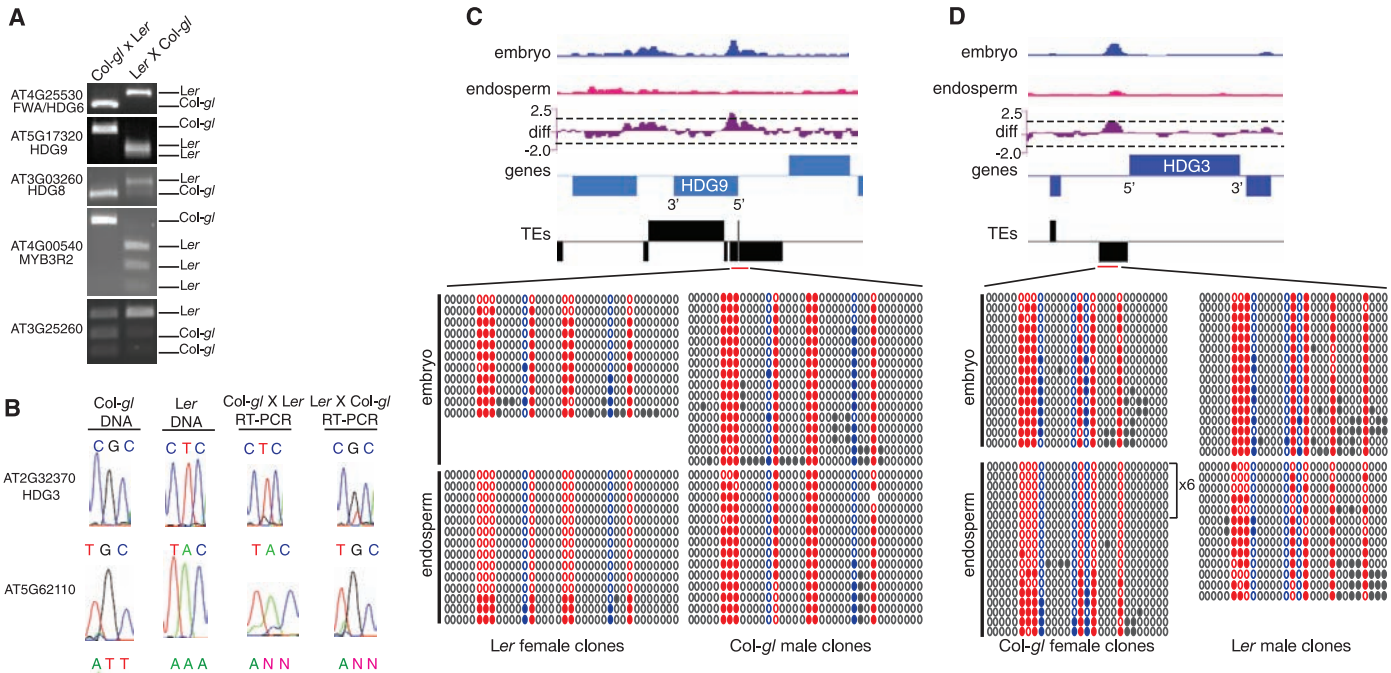

Fig. 4. Expression and methylation analysis of new imprinted genes. (**A**) RT-PCR allele-specific expression analysis from endosperm RNA of Col-*gl* females crossed with L*er* males and L*er* females crossed with Col-*gl* males. *FWA* is a control imprinted gene; AT3G25260 is biallelic. (**B**) RT-PCR sequencing chromatograms for the paternally expressed genes AT2G32370 and AT5G62110. The biallelically expressed gene α*VPE* is shown as a control. (**C** and **D**) Methylation profiling and allele-specific bisulfite sequencing analysis of new imprinted genes. Dashed lines represent the cutoff for the top 0.5% of differences. Each line of circles represent a bisulfite sequencing clone from embryo or endosperm. Filled circles indicate methylated cytosine. Red, CG; blue, CHG; gray, CHH.

overall hypomethylated as compared with wild type [supporting online material (SOM) text]. Thus, much of the methylation 5′ and 3′ of genes that is depleted in the endosperm is probably lost because of active demethylation by DME in the central cell before fertilization, although other mechanisms probably also contribute (*15*).

DNA methylation of promoters inhibits transcriptional initiation. The most prominent losses of gene-associated methylation in endosperm occur well upstream of the transcriptional start site (Fig. 3) and, for most genes, the presence of nearby DNA methylation apparently has little effect on gene expression (fig. S7). However, we found that genes with endosperm-preferred expression (*16*) are less methylated at 5′ sequences in the endosperm than embryo (fig. S8), which suggests that 5′ loss of methylation is associated with increased expression of a subset of genes in the endosperm.

Known imprinted genes are less methylated in the endosperm than embryo (Fig. 2B) and exhibit endosperm-preferred expression (*16*). To identify previously unkown imprinted genes, we chose genes with top DMRs in comparisons between embryo and endosperm and between wild type and *dme* endosperm for Col-*gl* and L*er* data sets. A set of 113 genes have top DMRs in three of the four comparisons, including the known imprinted gene *MEA* (table S5). Two of these genes, *HDG3* and *HDG9*, belong to the 16-member class IV homeodomain leucine zipper transcription (HD-ZIP) factor gene family that also includes the known imprinted gene *FWA*. As with *FWA*, three HD-ZIP genes are expressed primarily or exclusively in siliques: *HDG3*, *HDG8*, and *HDG9* (*17*).

To test parent-of-origin–specific expression of putative imprinted genes, we performed reciprocal crosses between L*er* and Col-*gl* and assayed expression patterns by means of reverse transcriptase polymerase chain reaction (RT-PCR). Only the maternal *HDG9* allele was expressed in the endosperm (Fig. 4A). We confirmed that methylation was lost around the 5′ end of the gene specifically on maternal alleles in the endosperm, a region annotated as overlapping the remnant of a Helitron transposable element (Fig. 4C). *HDG8* is also primarily, but not exclusively, expressed from the maternal allele (Fig. 4A and SOM text). *HDG3* is reciprocally imprinted; expression is predominantly paternal (Fig. 4B and SOM text). Methylation is lost from maternal alleles on a 1.4-kb Helitron remnant that begins 100 bp 5′ of the gene (Fig. 4D). We confirmed allele-specific expression of two other genes in the endosperm: the ATMYB3R2 transcription factor, which is maternally expressed, and AT5G62110, a gene annotated as containing a homeodomain-like domain, which is predominantly paternally expressed (Fig. 4 and SOM text).

We tested several other genes that were less methylated in the endosperm than embryo for imprinting (table S6). CYCA1;1 is a differentially methylated A-type cyclin that exhibits endosperm-preferred expression but is also expressed at many other stages of development (fig. S8C). It is biallelically expressed in the endosperm. All of the differentially methylated genes with endosperm-preferred expression that were not imprinted were expressed in other tissues throughout development, whereas the five genes with top positive DMRs that we confirmed as imprinted were expressed at very low levels or not at all in other tissues (fig. S9). This suggests that genes with low levels of expression in other plant tissues require loss of methylation for gene expression in the endosperm. Thus, the best candidates for imprinted genes are those that are less methylated in the endosperm than embryo, exhibit endosperm-preferred expression (*16*), and are expressed at low levels in other parts of the plant (table S7). On the basis of these considerations, we estimate that there are ~50 imprinted genes in *Arabidopsis*. Gene ontology analysis of molecular function indicates that these genes are enriched in what is termed "DNA or RNA binding," which includes transcription factors and genes with chromatin-related functions (fig. S9).

Our identification and verification of five previously unknown imprinted genes, all of which are flanked by repetitive elements or harbor them in coding sequences, doubles the number of known imprinted genes in *Arabidopsis*. Four of the 10 imprinted genes are class IV homeodomain transcription factors, which offers the opportunity to study the evolution of imprinting (SOM text). Our results support the theory that imprinting arose as a byproduct of silencing invading foreign DNA (*18*). Transposable elements (TEs) have demonstrated toxic effects on genomes, but they are also a source

of genetic and epigenetic material that can be utilized by the host (*19*). Insertion of a TE near a gene will have little functional impact in most instances, and strongly deleterious TE insertions will be selected against. However, a subset of genes, perhaps depending on promoter strength, is susceptible to epigenetic regulation by TEs. Regulation of gene expression by means of DNA methylation could be selected for if imprinting of these genes is adaptive in the context of parental conflict or gene dosage balance in the triploid endosperm.

References and Notes

1. J. H. Huh, M. J. Bauer, T. F. Hsieh, R. L. Fischer, *Cell* **132**, 735 (2008).
2. J. F. Gutierrez-Marcos *et al*., *Nat. Genet.* **38**, 876 (2006).
3. Materials and methods are available as supporting material on *Science* Online.
4. D. Zilberman, M. Gehring, R. K. Tran, T. Ballinger, S. Henikoff, *Nat. Genet.* **39**, 61 (2007).
5. X. Zhang *et al*., *Cell* **126**, 1189 (2006).
6. M. Lauria *et al*., *Plant Cell* **16**, 510 (2004).
7. M. Gehring *et al*., *Cell* **124**, 495 (2006).
8. T. Kinoshita *et al*., *Science* **303**, 521 (2004).
9. G. Makarevich, C. B. Villar, A. Erilova, C. Kohler, *J. Cell Sci.* **121**, 906 (2008).
10. P. E. Jullien, T. Kinoshita, N. Ohad, F. Berger, *Plant Cell* **18**, 1360 (2006).
11. S. W. Chan, I. R. Henderson, S. E. Jacobsen, *Nat. Rev. Genet.* **6**, 351 (2005).
12. N. Buisine, H. Quesneville, V. Colot, *Genomics* **91**, 467 (2008).
13. R. Lister *et al*., *Cell* **133**, 523 (2008).
14. J. Penterman *et al*., *Proc. Natl. Acad. Sci. U.S.A.* **104**, 6752 (2007).
15. P. E. Jullien *et al*., *PLoS Biol.* **6**, e194 (2008).
16. R. C. Day, R. P. Herridge, B. A. Ambrose, R. C. Macknight, *Plant Physiol.* **148**, 1964 (2008).
17. M. Nakamura *et al*., *Plant Physiol.* **141**, 1363 (2006).
18. D. P. Barlow, *Science* **260**, 309 (1993).
19. R. K. Slotkin, R. Martienssen, *Nat. Rev. Genet.* **8**, 272 (2007).

20. We thank the FHCRC Genomics Shared Resources for performing microarray hybridizations and Illumina sequencing, J. Henikoff for assistance with computational analyses, R. Deal and J. Cooper for comments on the manuscript, and D. Zilberman and R. Fischer for sharing unpublished data. M.G. is a HHMI Fellow of the Life Sciences Research Foundation. Illumina and NimbleGen data are deposited in the Genome Expression Omnibus (GEO) (accession number GSE14570).

Supporting Online Material

www.sciencemag.org/cgi/content/full/324/5933/1447/DC1
Materials and Methods
SOM Text
Figs. S1 to S9
Tables S1 to S9
References

29 January 2009; accepted 24 April 2009
10.1126/science.1171609

Genome-Wide Demethylation of *Arabidopsis* Endosperm

Tzung-Fu Hsieh,* Christian A. Ibarra,* Pedro Silva,* Assaf Zemach, Leor Eshed-Williams, Robert L. Fischer,† Daniel Zilberman†

Parent-of-origin-specific (imprinted) gene expression is regulated in *Arabidopsis thaliana* endosperm by cytosine demethylation of the maternal genome mediated by the DNA glycosylase *DEMETER*, but the extent of the methylation changes is not known. Here, we show that virtually the entire endosperm genome is demethylated, coupled with extensive local non-CG hypermethylation of small interfering RNA–targeted sequences. Mutation of *DEMETER* partially restores endosperm CG methylation to levels found in other tissues, indicating that CG demethylation is specific to maternal sequences. Endosperm demethylation is accompanied by CHH hypermethylation of embryo transposable elements. Our findings demonstrate extensive reconfiguration of the endosperm methylation landscape that likely reinforces transposon silencing in the embryo.

Gene imprinting, the differential expression of alleles of the same gene depending on parent-of-origin, independently evolved in mammals and in flowering plants (*1*). Imprinting occurs in the placenta of mammals and the endosperm of plants, structures that nourish the developing embryo. Maternal allele expression in the central cell, the diploid maternal plant cell that is fertilized to give rise to the triploid endosperm, is activated by the DEMETER (DME) DNA glycosylase, which excises 5-methylcytosine, resulting in imprinted expression of several genes in the endosperm (*2*–*8*). Although important for imprinting, DNA methylation in flowering plants primarily silences transposons, retrotransposons, and repeated sequences (*9*). In addition to methylation in the CG sequence context, plant DNA methylation occurs at CHG (H is A, C or T) and CHH sites, with CHH and to a lesser extent CHG methylation mediated through active targeting by RNA interference (RNAi) machinery (*9*). *Arabidopsis* gene bodies are commonly methylated in the CG context, whereas all types of methylation are present in repeats (*10*, *11*). A given CG site is generally methylated over 80% or not at all, whereas methylation of a CHG site is typically 30 to 80%, and methylation of a CHH site tends to be below 30% (*10*, *11*).

To determine the methylation landscape during *Arabidopsis* seed development, we isolated DNA from wild-type embryos, wild-type endosperm, endosperm from seeds with a defective maternal allele of *DME*, and adult aerial tissues, and used the Illumina Genome Analyzer platform to quantify DNA methylation by high-throughput bisulfite sequencing (*10*–*12*) (bisulfite treatment converts unmethylated cytosine to uracil) (fig. S1). We aligned 2.5 billion bases for embryo, 2.2 billion bases for wild-type endosperm, 2.0 billion bases for *dme* endosperm, and 1.5 billion bases for aerial tissues, which corresponds to 21-fold, 18-fold, 16-fold, and 13-fold coverage of the *Arabidopsis* nuclear genome, respectively (*13*) (table S1). Our aerial tissue results closely matched previously published bisulfite sequencing data (table S2 and fig. S2).

Bulk methylation in wild-type endosperm (20.9% CG, 8.9% CHG, 2.8% CHH) was lower in all sequence contexts compared with the embryo (26.9% CG, 10.6% CHG, and 4.4% CHH) (Fig. 1 and fig. S3). CG methylation was reduced in both gene bodies and repeats (Fig. 1, A and B) and was partially restored in *dme* endosperm (23.1%). In the developing seed, *DME* is expressed only in the central cell before fertilization (*2*), indicating that we were primarily detecting demethylation of the maternal endosperm genome. In contrast to CG methylation, CHG methylation was decreased (8.9% to 5.8%) in *dme* endosperm (Fig. 1, C and D), whereas CHH methylation was reduced by a factor of 3.5 (2.8% to 0.8%) (Fig. 1, E and F). CG and CHG methylation in aerial tissues (25.7% and 9.4%, respectively) was somewhat lower than in embryos, and aerial CHH methylation (2.3%) was half of that found in embryos and even lower than that of endosperm (Fig. 1), indicating that small interfering RNA (siRNA)–mediated DNA methylation is enhanced in the seed. Reduced non-CG methylation in *dme* endosperm suggests that DME activity is necessary for up-regulating RNAi-mediated methylation, perhaps through activation of transposable elements by DNA demethylation.

To identify sequences that are differentially methylated in the endosperm compared with the embryo, we calculated fractional methylation in each context within 50 base pair (bp) windows and subtracted endosperm methylation from embryo methylation. We identified 36,749 discreet loci corresponding to 10.33 million bp with an absolute change in CG methylation of at least 10% ($P < 0.0001$, Fisher's exact test), 99.4% of which (36,534) were more methylated in embryo (table S3). Using the same criteria, we found 5694 loci (2.87 million bp) with a change in CHG methylation, 91.3% of which (5200) were more methylated in embryo (table S3). We also identified 9749 loci (17.98 million bp) with an absolute change in CHH methylation of at least 5% ($P < 0.0001$, Fisher's exact test), 89.9% of which (8760) were more methylated in embryo (table S3). Although the above values represent a substantial underestimate, they provide a clear indication of the extent of methylation

Department of Plant and Microbial Biology, University of California, Berkeley, CA 94720, USA.

*These authors contributed equally to this work.
†To whom correspondence should be addressed. E-mail: rfischer@berkeley.edu (R.L.F.), daniel.zilberman@nature.berkeley.edu (D.Z.)

differences between embryo and endosperm. Notably, ~10% of identified loci were hypermethylated at CHG and CHH sites in the endosperm, compared with <1% hypermethylated at CG sites. Moreover, non-CG hypermethylated loci were strongly enriched in siRNAs (*13*) (Fig. 2A), further indicating that RNAi drives a substantial reconfiguration of the seed methylation landscape.

To determine how methylation changes in the endosperm affect gene expression, we identified genes with reduced DNA methylation (at a cutoff of $P < 1 \times 10^{-7}$) within 1 kb of either the 5′ or 3′ end and compared their gene expression between endosperm and embryo based on available microarray data (*13*) (table S4) (genes demethylated near both ends were analyzed in the 5′ category). Genes exhibiting reduced methylation upstream of the start of transcription were preferentially expressed in the endosperm to a modest but significant degree ($P = 0.0005$, Wilcoxon rank-sum test) (Fig. 2B), whereas genes demethylated near the 3′ end did not show a significant change in expression ($P = 0.33$). Reduced methylation of the maternal endosperm genome has been implicated in allele-specific expression of all five known *Arabidopsis* imprinted genes (*3*, *5*–*8*), so genes with reduced methylation and greater expression in endosperm than embryo are potentially imprinted.

To visualize methylation differences between tissues, we plotted the distribution density of windows for wild-type endosperm subtracted from embryo (Fig. 3, A to C, blue trace), *dme* endosperm subtracted from embryo (Fig. 3, A to C, red trace), and aerial tissues subtracted from embryo (fig. S4), showing only those windows that were methylated in at least one of the tissues being compared (*13*). We also aligned all *Arabidopsis* annotated genes, which include some pseudogenes and transposable elements, at their 5′ ends, stacked them from the top of chromosome 1 to the bottom of chromosome 5, and displayed fractional embryo methylation (left panels of Fig. 3, D and E) and the difference between embryo and wild-type endosperm methylation (right panels of Fig. 3, D and E) as heat maps. We performed a similar analysis for annotated transposons and other repeats (fig. S5). Virtually all sequences methylated in embryo in the CG context were less methylated in the endosperm (Fig. 3A). Gene bodies, gene adjacent sequences, and transposable elements were all similarly demethylated (Fig. 1, A and B, Fig. 3D, and figs. S5 and S6), with transposons demethylated to a somewhat greater extent than genes and shorter transposons on average demethylated more than longer ones (fig. S6).

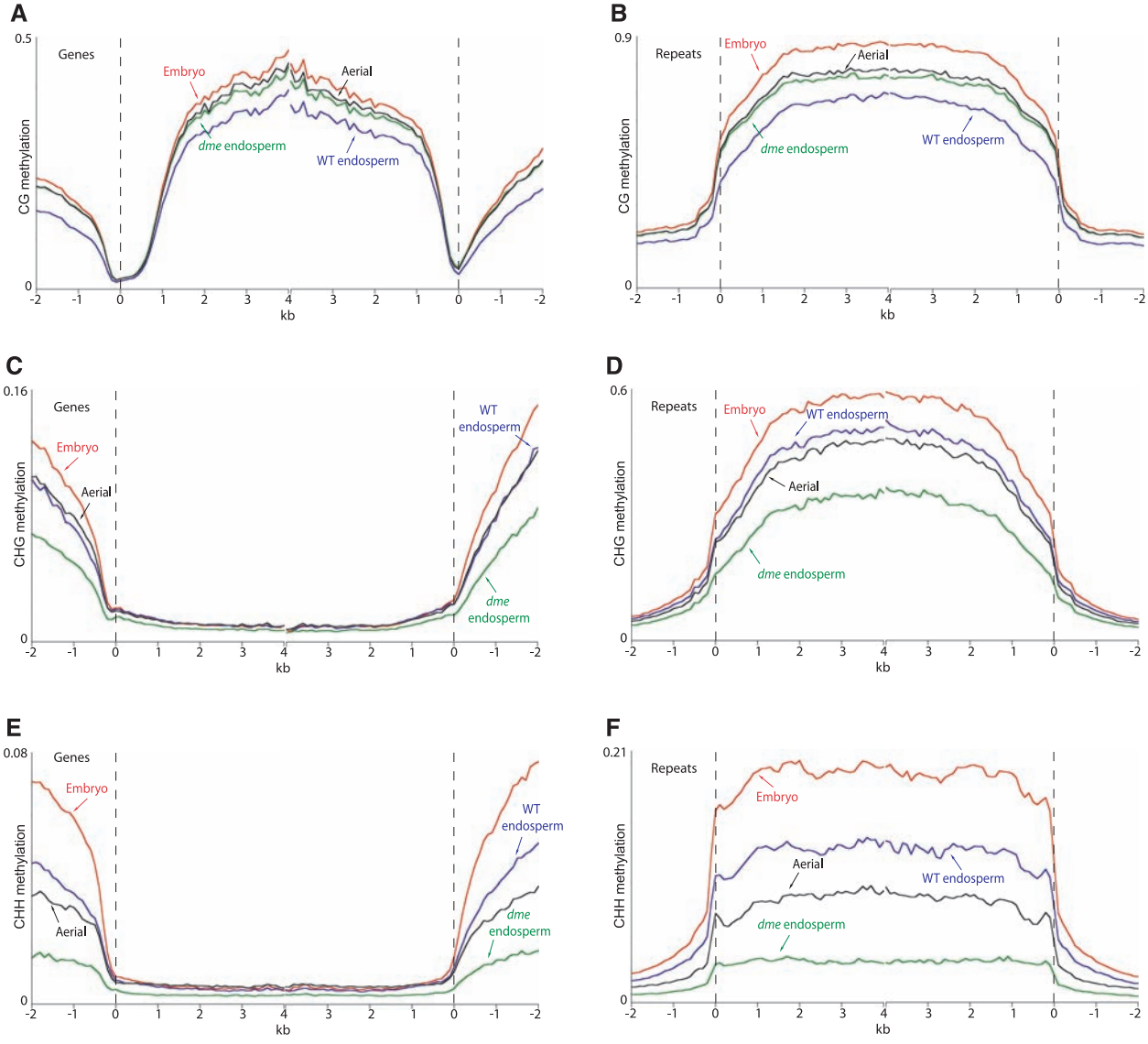

Fig. 1. Profiles of DNA methylation in embryo, wild-type endosperm, and *dme* endosperm. (**A** to **F**) TAIR8-annotated genes [(A), (C), and (E)] or transposons [(B), (D), and (F)] were aligned at the 5′ end (left panel) or the 3′ end (right panel), and average methylation levels for each 100-bp interval are plotted from 2 kb away from the gene (negative numbers) to 4 kb into the gene (positive numbers). Embryo methylation is represented by the red trace, wild-type (WT) endosperm by the blue trace, *dme* endosperm by the green trace, and aerial tissues by the black trace. The dashed line at zero represents the point of alignment. CG methylation is shown in (A) and (B), CHG in (C) and (D), CHH in (E) and (F).

CHG and CHH methylation of most sequences was also higher in embryo (Fig. 1, C to F; Fig. 3, B, C, and E; and fig. S5). The *dme* mutation uniformly restored CG methylation, while uniformly reducing CHG and CHH methylation (Fig. 1 and Fig. 3, A to C). Methylation in all contexts was higher in embryo than in aerial tissues (Fig. 1 and fig. S4), with particularly extensive CHH hypermethylation: We identified 10,858 loci covering 21.88 million bp with an absolute change in CHH methylation of at least 5% ($P < 0.0001$, Fisher's exact test), 96.8% of which (10,510) were more methylated in embryo (table S3). Virtually, genome-wide CG demethylation of the maternal endosperm genome is thus accompanied by similarly extensive CHH hypermethylation in the embryo.

We investigated the source of the substantial non-CG hypermethylation in wild-type endosperm compared with the embryo (table S3) by examining methylation differences between embryo and *dme* endosperm of sequences that were more methylated in wild-type endosperm than in embryo (Fig. 3, B and C, green trace). If endosperm hypermethylation were random, we would expect to see no correlation between hypermethylation in wild-type and *dme* endosperm. Our analysis showed that for both CHG and CHH contexts, loci hypermethylated in

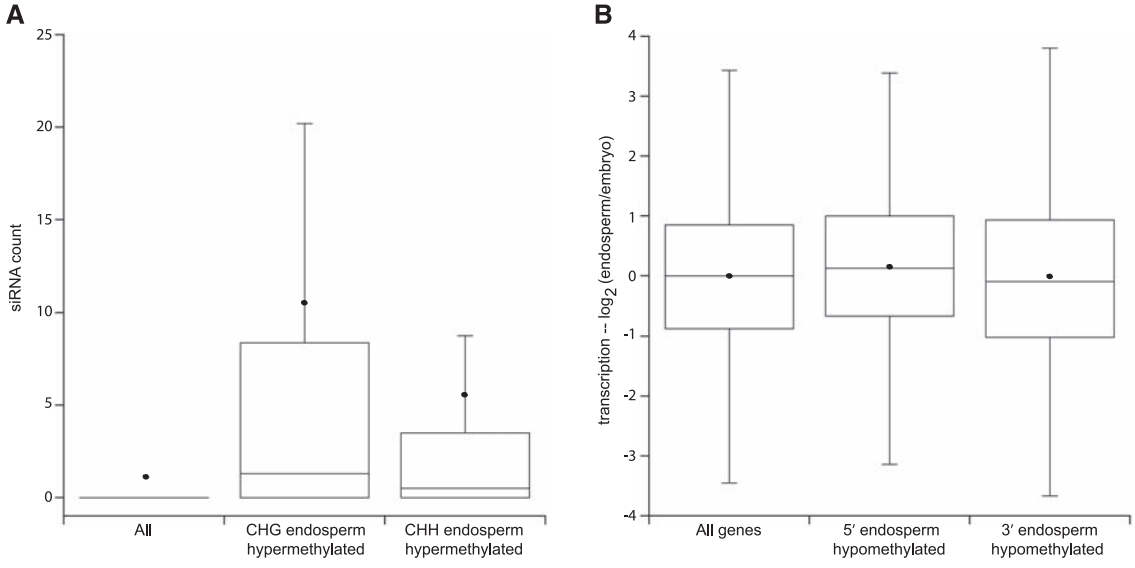

Fig. 2. Associations between endosperm methylation, siRNAs, and expression. (**A**) Box plots showing siRNA abundance within 50-bp windows in the entire *Arabidopsis* genome (All) and in sequences hypermethylated in WT endosperm compared with the embryo in the CHG and CHH contexts. (**B**) Box plots showing differences in gene expression between embryo and endosperm for all genes (n = 21,021), genes with 5′ hypomethylation in endosperm (n = 1097), and genes with 3′ hypomethylation in endosperm (n = 505). Each box encloses the middle 50% of the distribution, with the horizontal line marking the median and the dot marking the mean. The lines extending from each box mark the minimum and maximum values that fall within 1.5 times the height of the box.

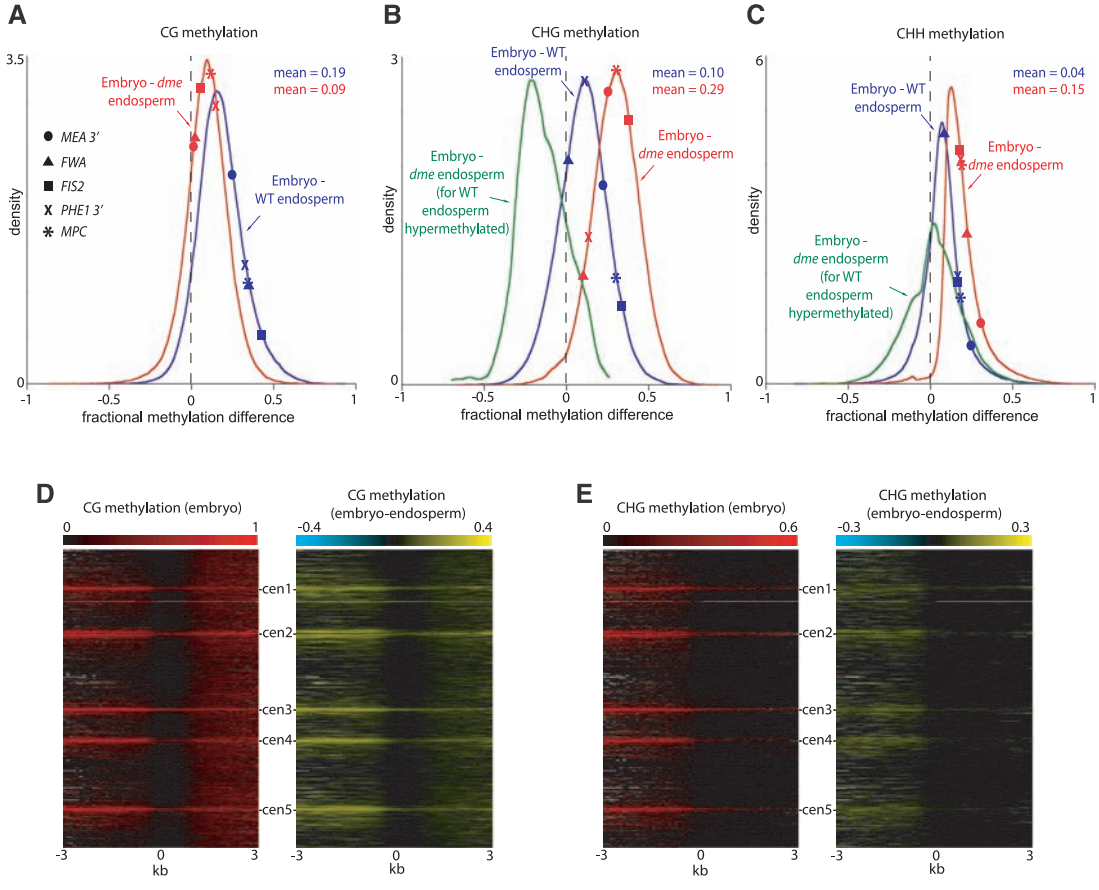

Fig. 3. Genome-wide demethylation of endosperm. (**A** to **C**) Kernel density plots of the differences between embryo and WT endosperm methylation (blue trace) and the differences between embryo and *dme* endosperm methylation (red trace). The green trace in (B) and (C) represents methylation differences between embryo and *dme* endosperm for windows with absolute fractional methylation increase in WT endosperm compared with embryo of at least 0.4 in the CHG context (B) (n = 135) or at least 0.2 in the CHH context (C) (n = 6168). Methylation differences for the 3′ *MEA* repeats, *FWA*, *FIS2*, *PHE1*, and *MPC* are indicated; specifics are listed in table S2. (**D** and **E**) All TAIR8-annotated genes (28,244) were aligned at the 5′ end and stacked from the top of chromosome 1 to the bottom of chromosome 5. Embryo methylation is displayed as a heat map in the left panel, differences between embryo and WT endosperm in the right panel. CG methylation is shown in (D), CHG in (E).

wild-type endosperm had a strong tendency to be hypermethylated in *dme* endosperm as well (Fig. 3, B and C, green trace), despite the overall reduction of non-CG methylation caused by the *dme* mutation. Endosperm hypermethylation is thus a highly specific, RNAi-targeted process.

We calculated methylation levels of sequences either known or strongly inferred to cause imprinted expression of five *Arabidopsis* genes (*3*, *5*–*8*): the *MEA* 3′ repeats, the *FWA* promoter and start of transcription, the *FIS2* promoter, the *PHE1* 3′ repeats, and the *MPC* gene and flanking regions (Fig. 3, A to C, and table S2). *MEA* methylation was reduced from 88% CG, 39% CHG, and 42% CHH in embryo to 63% CG, 16% CHG, and 17% CHH in wild-type endosperm. *MEA* CG methylation was restored to 87% in *dme* endosperm, whereas CHG (13%) and CHH (8%) methylation was further reduced. The other four genes behaved similarly (Fig. 3, A to C, and table S2), in line with the overall trends. Imprinted genes are thus not exceptional sequences specifically targeted for demethylation in the central cell but rather part of a nearly universal process that reshapes DNA methylation of the entire maternal genome in the endosperm (*14*). Imprinted expression of genes regulated by allele-specific DNA methylation could potentially arise whenever a transposable element insertion or a local duplication near a gene's regulatory sequences induces methylation and gene silencing in other tissues, including the paternal endosperm genome.

Genomic imprinting is a fast-evolving process driven by genetic conflict between parents (*1*). In mammals, which exhibit virtually global CG methylation (*15*), imprinting is orchestrated in part by differential methylation of specific sequences in the gametes (*16*). *Arabidopsis*, which targets methylation primarily to transposable elements (*9*), apparently adapted a radical implementation of imprinting by partially suspending its transposon suppression system and globally demethylating central cell DNA, resulting in a hypomethylated maternal endosperm genome. Because the endosperm genome is not transmitted to the next generation, transient transposon activation is likely to carry a fairly low cost, especially in an organism with few functional transposons, like *Arabidopsis*. Transposon activation and siRNA accumulation in the central cell might actually contribute to enhanced methylation and silencing of elements in the egg cell (and later the embryo) through siRNA transport (*17*), which could be the original selective force driving the evolution of central cell demethylation. An analogous mechanism has recently been proposed to operate between the vegetative and reproductive cells of pollen (*18*). It is an open question whether other plants, particularly those with more aggressive transposable elements, have adopted a similar strategy.

References and Notes

1. R. Feil, F. Berger, *Trends Genet.* **23**, 192 (2007).
2. Y. Choi *et al.*, *Cell* **110**, 33 (2002).
3. M. Gehring *et al.*, *Cell* **124**, 495 (2006).
4. J. H. Huh, M. J. Bauer, T.-F. Hsieh, R. L. Fischer, *Cell* **132**, 735 (2008).
5. P. E. Jullien, T. Kinoshita, N. Ohad, F. Berger, *Plant Cell* **18**, 1360 (2006).
6. T. Kinoshita *et al.*, *Science* **303**, 521 (2004).
7. G. Makarevich, C. B. R. Villar, A. Erilova, C. Kohler, *J. Cell Sci.* **121**, 906 (2008).
8. S. Tiwari *et al.*, *Plant Cell* **20**, 2387 (2008).
9. I. R. Henderson, S. E. Jacobsen, *Nature* **447**, 418 (2007).
10. S. J. Cokus *et al.*, *Nature* **452**, 215 (2008).
11. R. Lister *et al.*, *Cell* **133**, 523 (2008).
12. A. Meissner *et al.*, *Nature* **454**, 766 (2008).
13. Materials and methods are available as supporting material on *Science* Online.
14. P. E. Jullien *et al.*, *PLoS Biol.* **6**, e194 (2008).
15. M. G. Goll, T. H. Bestor, *Annu. Rev. Biochem.* **74**, 481 (2005).
16. A. Munshi, S. Duvvuri, *J. Genet. Genomics* **34**, 93 (2007).
17. Y. Z. Han, B. Q. Huang, S. Y. Zee, M. Yuan, *Planta* **211**, 158 (2000).
18. R. K. Slotkin *et al.*, *Cell* **136**, 461 (2009).

19. We thank L. Tonkin for performing Illumina sequencing, J. Shin for gene annotation, and S. Henikoff for sharing unpublished data. This work was partially funded by an NIH grant (GM69415) to R.L.F. A.Z. is a fellow of the Jane Coffin Childs Memorial Fund for Medical Research. Sequencing data are deposited in GEO with accession number GSE15922.

Supporting Online Material

www.sciencemag.org/cgi/content/full/324/5933/1451/DC1
Materials and Methods
Figs. S1 to S6
References

17 February 2009; accepted 1 May 2009
10.1126/science.1172417

Hyper-Recombination, Diversity, and Antibiotic Resistance in Pneumococcus

William Paul Hanage,[1]* Christophe Fraser,[1] Jing Tang,[2] Thomas Richard Connor,[1] Jukka Corander[2]

Streptococcus pneumoniae is a pathogen of global importance that frequently transfers genetic material between strains and on occasion across species boundaries. In an analysis of 1930 pneumococcal genotypes from six housekeeping genes and 94 genotypes from related species, we identified mosaic genotypes representing admixture between populations and found that these were significantly associated with resistance to several classes of antibiotics. We hypothesize that these observations result from a history of hyper-recombination, which means that these strains are more likely to acquire both divergent genetic material and resistance determinants. This could have consequences for the reemergence of drug resistance after pneumococcal vaccination and also for our understanding of diversification and speciation in recombinogenic bacteria.

Many bacteria undergo homologous recombination, in which short tracts of DNA in the recipient are replaced by the corresponding tract from a donor strain, resulting in a mosaic of DNA from different ancestors (*1*). Although this occurs mainly within species and declines markedly with increasing sequence divergence between donor and recipient (*2*), occasional gene transfers between species do occur. Such events have the potential to introduce new phenotypes, such as virulence or antibiotic resistance, into a new genetic background that may or may not be the same as the species of the donor strain (*3*–*7*) and may have considerable impacts on bacterial evolution and human health.

One group in which homologous recombination is frequent is the mitis group streptococci. This includes the major human pathogen *Streptococcus pneumoniae*, the pneumococcus, which is responsible for at least 1 million deaths per year worldwide (*8*). The closely related species *S. oralis*, *S. mitis*, and *S. pseudopneumoniae* (among others) have a history of taxonomic confusion, which may be partly explained by genetic diversity within the mitis group (*9*, *10*). Moreover, rare but important events have led to the acquisition of antibiotic resistance by pneumococcus as a result of the transfer of resistance determinants across species boundaries (*4*, *5*). The high rates of recombination within the species have the potential to shuffle resistance determinants among pneumococcal genotypes. It is not known whether or not recombination, either at resistance loci or housekeeping genes, is equally likely for all members of the species or whether some strains are more likely to be involved in this process.

Although a vaccine is available for 7 of the more than 90 pneumococcal serotypes, this has not eliminated pneumococcal disease because the nonvaccine serotypes derive an ecological advantage from the removal of their competitors and have been increasing in carriage prevalence (*11*) and, concomitantly, in disease (*12*). Alongside

[1]Department of Infectious Disease Epidemiology, Imperial College London, Norfolk Place, London W2 1PG, UK. [2]Department of Mathematics, Åbo Akademi, FI-20500, Turku, Finland.

*To whom correspondence should be addressed. E-mail: w.hanage@imperial.ac.uk

this, we are observing the expansion of existing antibiotic-resistant clones with nonvaccine serotypes and the possible emergence of new ones (*13*, *14*).

Multilocus sequence typing (MLST) (*15*) supplies genetic data to study recombination and population structure in the pneumococcal population. MLST characterizes an isolate by sequencing internal fragments of seven housekeeping genes. Together these define the sequence type (ST) of the isolate, which may readily be compared to others through the MLST database (*16*). This contains sequence data from many thousands of isolates reported by the global community of MLST users. It also contains associated epidemiological data including serotype and antibiotic resistance. We have previously published the sequences of MLST loci from multiple isolates of related species, allowing us to study recombination between them and the pneumococcus (*9*). The *ddl* locus used in MLST for pneumococcus is associated with a high frequency of interspecies gene transfer because of physical linkage with the penicillin binding protein (PBP) 2b locus (*17*), at which alleles containing DNA originating in other species lead to penicillin resistance. Because the linkage could bias any estimates of admixture, we have excluded this locus from the following analysis. Once the *ddl* locus is removed, the data set consists of 1930 distinct genotypes of *S. pneumoniae*, along with 40 identified as *S. mitis*, 39 *S. pseudopneumoniae*, and 15 *S. oralis* (*9*).

To identify populations and rates of admixture between them, we used the program Bayesian Analysis of Population Structure [BAPS (*18*–*20*)]. This program, freely available online (*21*), implements several models to identify clusters characterized by different allele frequencies within a population characterized by multilocus DNA sequences. Furthermore, cases of likely admixture, that is, isolates containing a DNA sequence characteristic of more than one population as a result of recombination, can be identified (*22*).

The results of the analysis of the streptococcal data set are summarized in Table 1 and Fig. 1 [and presented in more detail in (*22*)]. In total, six clusters were identified, three of which corresponded to the nonpneumococcal species (Table 1). The remaining three clusters (1, 2, and 4) represent subpopulations of the pneumococcus as defined within the BAPS analysis. Figure 1A shows the admixture graphic, in which each unique genotype is represented by a column, colored according to the proportion of sequence assigned to each cluster. For clusters 1 and 2, the vast majority of genotypes were characteristic of only one cluster. The reverse was true of cluster 4, which was mostly composed of mosaics. In Fig. 1B, which displays the clustering of these groups by using a phylogenetic tree, this is evident in the scattering of cluster 4 genotypes around the pneumococcal cluster. Two anomalous genotypes were evident and are indicated in Fig. 1B: one assigned to cluster 4 arising from the branch leading to *S. pseudopneumoniae* and *S. mitis* (this is ST 1705 and is a pneumococcal strain containing multiple divergent alleles) and another highly divergent genotype assigned to cluster 3 at the end of a long branch arising from within the *S. pneumoniae* cluster. This strain [IOKOR 484 as described in (*23*)] was previously considered to be an example of *S. pseudopneumoniae* but in this analysis clustered with *S. mitis* strains. These illustrate the difficulty of assigning strains to species in such recombinant taxa.

We estimated the relative amounts of admixture between the clusters (*22*) (Fig. 2). This estimate shows cluster 4 to be a recipient of genetic information from the other clusters and other species. Hence for individual loci, we identified alleles that are divergent from typical pneumococcal alleles and are more similar to those found in related species. Of 93 individual genotypes containing alleles that cluster with nonpneumococcal species (*22*), all but one were found in cluster 4.

The atypical genotypes in cluster 4 reflect a history of recombination; hence, we examined the association between cluster 4 and antibiotic resistance. We used 3732 records deposited in the MLST database, which supplied the input data for the BAPS analysis and contains data on resistance to penicillin, erythromycin, tetracycline, chloramphenicol, and cefotaxime. We categorized an isolate as nonsusceptible if it was recorded as

Table 1. Association between named species and BAPS cluster. Blank fields indicate that no strains in the relevant cluster were identified as that species.

	BAPS cluster					
	1	2	3	4	5	6
S. pneumoniae	753	809		368		
S. pseudopneumoniae			1		39	
S. mitis			39			
S. oralis						15

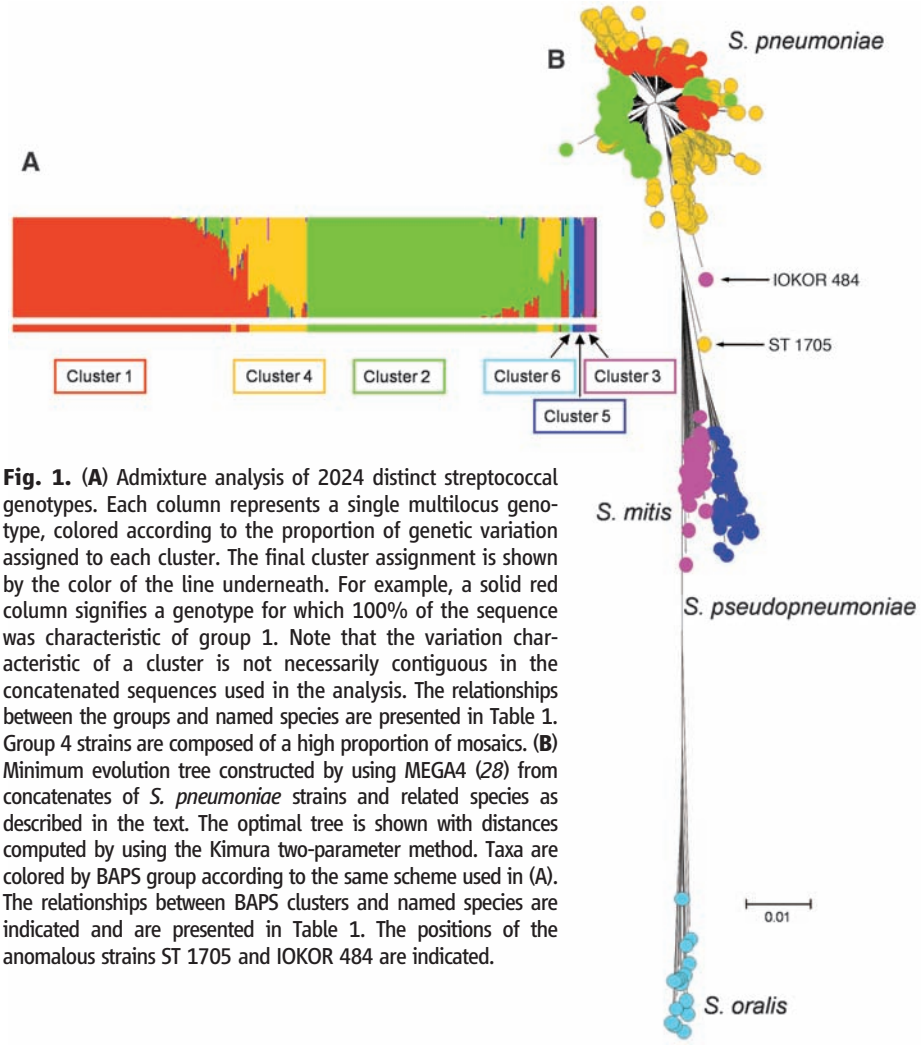

Fig. 1. (**A**) Admixture analysis of 2024 distinct streptococcal genotypes. Each column represents a single multilocus genotype, colored according to the proportion of genetic variation assigned to each cluster. The final cluster assignment is shown by the color of the line underneath. For example, a solid red column signifies a genotype for which 100% of the sequence was characteristic of group 1. Note that the variation characteristic of a cluster is not necessarily contiguous in the concatenated sequences used in the analysis. The relationships between the groups and named species are presented in Table 1. Group 4 strains are composed of a high proportion of mosaics. (**B**) Minimum evolution tree constructed by using MEGA4 (*28*) from concatenates of *S. pneumoniae* strains and related species as described in the text. The optimal tree is shown with distances computed by using the Kimura two-parameter method. Taxa are colored by BAPS group according to the same scheme used in (A). The relationships between BAPS clusters and named species are indicated and are presented in Table 1. The positions of the anomalous strains ST 1705 and IOKOR 484 are indicated.

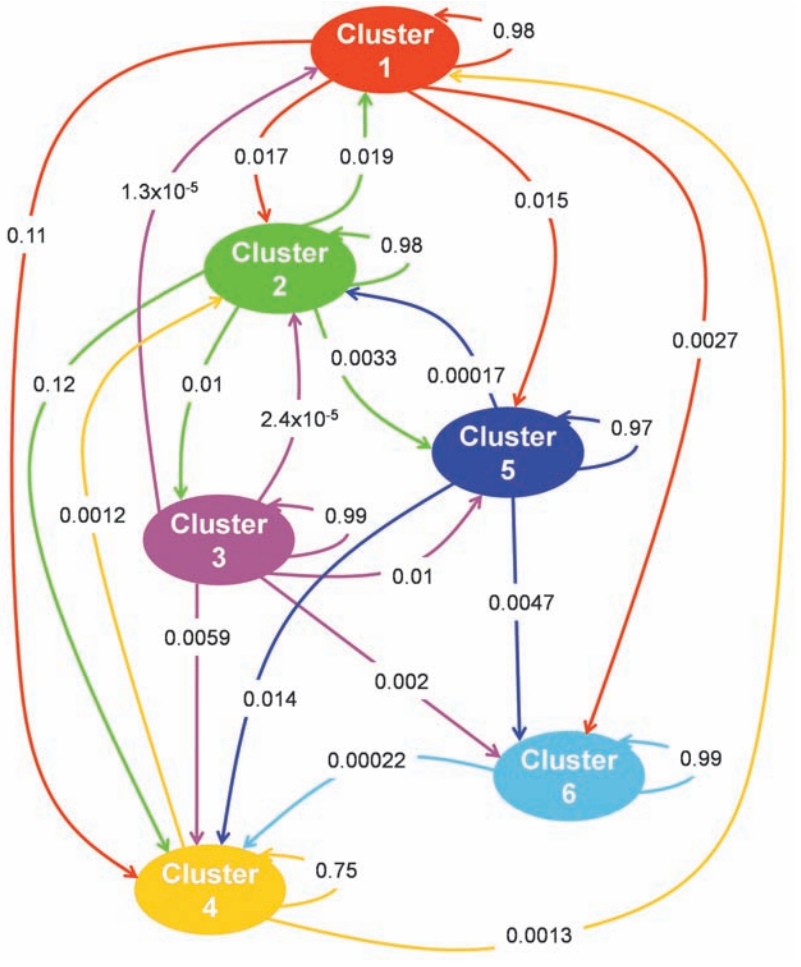

Fig. 2. Admixture between the clusters illustrated in Fig. 1. Arrows indicate the average fraction of sequence variation obtained from the source cluster by the strains assigned to the target cluster. Circular loops indicate the fraction of variation estimated as not arising from outside the cluster.

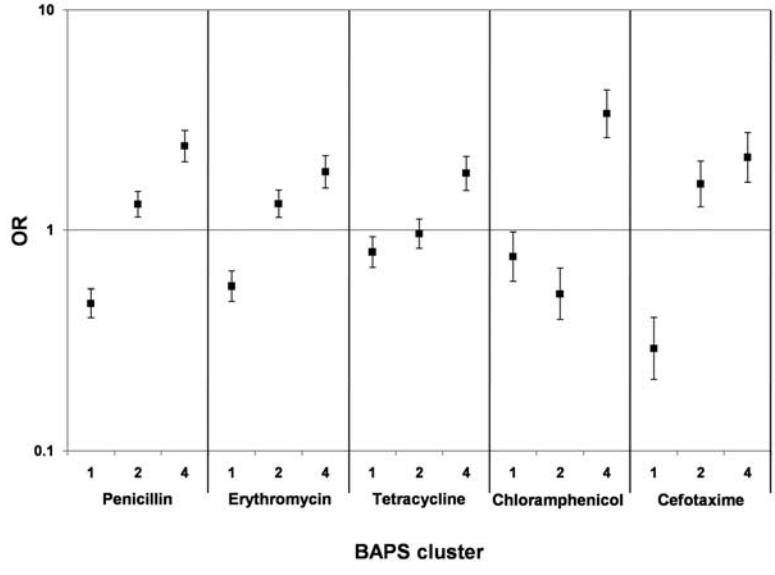

Fig. 3. ORs showing the association between BAPS cluster and nonsusceptibility to five antibiotics. ORs were calculated relative to all other clusters as described in the text. Error bars indicate 95% confidence intervals.

having a minimal inhibitory concentration (MIC) greater than the breakpoint for susceptibility according to British Society for Antimicrobial Chemotherapy or if it was recorded as resistant or of intermediate resistance [i.e., nonsusceptible in accordance with customary usage (*22*)].

Odds ratios (ORs) for the association of resistance with the clusters inferred by BAPS showed (Fig. 3) a significant association with cluster 4 and a negative relationship with cluster 1. Cluster 2 is intermediate in all cases except for chloramphenicol. This may be linked to the fact that cluster 2 contains a high proportion of strains with serotypes included in current conjugate vaccine formulations (Table 2). These serotypes have been previously known to be associated with resistance, and their removal after vaccination has led to a decline in resistance (*14*). In contrast, cluster 4 shows no association with these serotypes. The association between cluster 4 and nonsusceptibility is also robust to different criteria for associating genotypes with resistance (*22*).

The reasons cluster 4 associated with both resistance and mosaicism are unclear. Resistance to the different antibiotics may arise by the acquisition of additional loci (such as efflux pumps in the case of erythromycin resistance) as well as gene conversion–like processes (e.g., homologous recombination at PBP loci for β-lactam nonsusceptibility). Both involve the acquisition of DNA from other lineages. We have considered the possibility that this result could be a consequence of reverse causation: Resistance leads to strains, for some reason, being more likely to be grouped in cluster 4. However, any artifactual association between this cluster and antibiotic resistance seems very unlikely given that the BAPS classification and resistance phenotype are based on unlinked loci.

We hypothesize that cluster 4 is an amalgam of strains with a history of hyper-recombination, which leads to them being grouped together by BAPS because they share anomalous DNA sequences. By having a history of hyper-recombination, such strains are more likely to accept divergent DNA, both at housekeeping and resistance loci, and hence more likely to acquire resistance and housekeeping gene sequences from distantly related pneumococci or other species.

Within many bacterial populations and in particular those under strong antibiotic selective pressure, we can identify strains with an elevated mutation rate (*24*) usually through defects in the mismatch repair (MMR) system. In certain contexts [e.g., the cystic fibrotic lung (*25*)], it is thought that second-order selection on the resistant strains that arise in the mutator lineages leads to strains with a mutator phenotype being more common than predicted (*26*). However, the relationship between elevated recombination and antibiotic resistance is not well understood. Elevated mutation and/or recombination rates should carry a fitness cost, and as a result a high rate of reversion to wild type is predicted, possibly by horizontal acquisition of wild-type MMR genes, as has been proposed for hypermutators in *Escherichia coli* (*27*).

Table 2. Associations between pneumococcal isolates with vaccine serotypes and BAPS clusters. The vaccine serotypes are those present in the seven valent pneumococcal vaccines (4, 6B, 9V, 14, 18C, 19F, and 23F), and all records present in the MLST database at the time of BAPS analysis were used to estimate ORs. Reestimation using records entered into the database since the initial analysis did not substantially alter the results (*22*).

Cluster	Vaccine serotypes	Totals	ORs	95% Confidence intervals
1	604	1357	0.54	0.475 to 0.622
2	1027	1645	1.87	1.639 to 2.133
4	378	730	0.90	0.768 to 1.061

Through analysis of MLST data collected for epidemiological purposes, we have identified pneumococcal strains showing evidence of past recombination, both with other pneumococci and with related species. These strains are significantly more likely to be resistant to all classes of antibiotics for which data are available. Because the resistance mechanisms involved include both homologous and illegitimate recombination, this implies a general tolerance for foreign DNA, suggesting a hyper-recombinant state. It is reasonable to suggest that this state could be important for adaptation to other environmental pressures beyond antibiotics. This demonstrates the importance of recombination in bacterial evolution over the long term and suggests that it may vary markedly within a species. The consequences for speciation and adaptation remain to be determined.

References and Notes

1. E. J. Feil, B. G. Spratt, *Annu. Rev. Microbiol.* **55**, 561 (2001).
2. C. Fraser, W. P. Hanage, B. G. Spratt, *Science* **315**, 476 (2007).
3. R. Hakenbeck, *Electrophoresis* **19**, 597 (1998).
4. C. G. Dowson *et al.*, *Proc. Natl. Acad. Sci. U.S.A.* **87**, 5858 (1990).
5. C. G. Dowson, T. J. Coffey, C. Kell, R. A. Whiley, *Mol. Microbiol.* **9**, 635 (1993).
6. C. G. Dowson *et al.*, *Proc. Natl. Acad. Sci. U.S.A.* **86**, 8842 (1989).
7. B. G. Spratt *et al.*, *Proc. Natl. Acad. Sci. U.S.A.* **86**, 8988 (1989).
8. K. Mulholland, *Lancet* **370**, 285 (2007).
9. W. P. Hanage, C. Fraser, B. G. Spratt, *Philos. Trans. R. Soc. London Ser. B* **361**, 1917 (2006).
10. C. J. Bishop *et al.*, *BMC Biol.* **7**, 3 (2009).
11. S. S. Huang *et al.*, *Pediatrics* **116**, e408 (2005).
12. L. A. Hicks *et al.*, *J. Infect. Dis.* **196**, 1346 (2007).
13. A. B. Brueggemann, R. Pai, D. W. Crook, B. Beall, *PLoS Pathog.* **3**, e168 (2007).
14. M. H. Kyaw *et al.*, *N. Engl. J. Med.* **354**, 1455 (2006).
15. M. C. Enright, B. G. Spratt, *Microbiology* **144**, 3049 (1998).
16. http://spneumoniae.mlst.net/.
17. M. C. Enright, B. G. Spratt, *Mol. Biol. Evol.* **16**, 1687 (1999).
18. J. Corander, P. Waldmann, P. Marttinen, M. J. Sillanpaa, *Bioinformatics* **20**, 2363 (2004).
19. J. Corander, P. Waldmann, M. J. Sillanpaa, *Genetics* **163**, 367 (2003).
20. J. Corander, J. Tang, *Math. Biosci.* **205**, 19 (2007).
21. www.abo.fi/fak/mnf/mate/jc/smack_software_eng.html.
22. Materials and methods are available as supporting material on *Science* Online.
23. W. P. Hanage *et al.*, *J. Bacteriol.* **187**, 6223 (2005).
24. E. Denamur, I. Matic, *Mol. Microbiol.* **60**, 820 (2006).
25. R. del Campo *et al.*, *J. Clin. Microbiol.* **43**, 2207 (2005).
26. M. C. Negri *et al.*, *Antimicrob. Agents Chemother.* **46**, 528 (2002).
27. E. Denamur *et al.*, *Cell* **103**, 711 (2000).
28. K. Tamura, J. Dudley, M. Nei, S. Kumar, *Mol. Biol. Evol.* **24**, 1596 (2007).

29. We acknowledge the support of the Royal Society (W.P.H. and C.F.); the Computational Biology, Bioinformatics, and Biometry graduate school (J.T.); a UK Biotechnology and Biological Sciences Research Council studentship (to T.R.C.); and the Academy of Finland (J.C., grant no. 121301). We thank B. Spratt for helpful discussions.

Supporting Online Material

www.sciencemag.org/cgi/content/full/324/5933/1454/DC1
Materials and Methods
Fig. S1
Tables S1 to S3
References

5 February 2009; accepted 7 May 2009
10.1126/science.1171908

Inhibition of Hedgehog Signaling Enhances Delivery of Chemotherapy in a Mouse Model of Pancreatic Cancer

Kenneth P. Olive,[1] Michael A. Jacobetz,[1]* Christian J. Davidson,[2]* Aarthi Gopinathan,[1,2]* Dominick McIntyre,[1] Davina Honess,[1] Basetti Madhu,[1] Mae A. Goldgraben,[1] Meredith E. Caldwell,[1] David Allard,[1] Kristopher K. Frese,[1] Gina DeNicola,[1,2] Christine Feig,[1] Chelsea Combs,[2] Stephen P. Winter,[1] Heather Ireland-Zecchini,[1] Stefanie Reichelt,[1] William J. Howat,[1] Alex Chang,[3] Mousumi Dhara,[3] Lifu Wang,[2,4] Felix Rückert,[5] Robert Grützmann,[5] Christian Pilarsky,[5] Kamel Izeradjene,[6] Sunil R. Hingorani,[6] Pearl Huang,[7] Susan E. Davies,[8] William Plunkett,[9] Merrill Egorin,[10] Ralph H. Hruban,[3] Nigel Whitebread,[11] Karen McGovern,[11] Julian Adams,[11] Christine Iacobuzio-Donahue,[3] John Griffiths,[1] David A. Tuveson[1]†

Pancreatic ductal adenocarcinoma (PDA) is among the most lethal human cancers in part because it is insensitive to many chemotherapeutic drugs. Studying a mouse model of PDA that is refractory to the clinically used drug gemcitabine, we found that the tumors in this model were poorly perfused and poorly vascularized, properties that are shared with human PDA. We tested whether the delivery and efficacy of gemcitabine in the mice could be improved by coadministration of IPI-926, a drug that depletes tumor-associated stromal tissue by inhibition of the Hedgehog cellular signaling pathway. The combination therapy produced a transient increase in intratumoral vascular density and intratumoral concentration of gemcitabine, leading to transient stabilization of disease. Thus, inefficient drug delivery may be an important contributor to chemoresistance in pancreatic cancer.

Pancreatic ductal adenocarcinoma (PDA) is among the most intractable of human malignancies. Decades of effort have witnessed the failure of many chemotherapeutic regimens, and the current standard-of-care therapy, gemcitabine, extends patient survival by only a few weeks (*1*–*3*). Oncology drug development relies heavily on mouse models bearing transplanted tumors for efficacy testing of agents. However, such models of PDA respond to numerous chemotherapeutic agents, including gemcitabine (*4*–*9*), which suggests that their predictive utility may be limited. Genetically engineered mouse models of PDA offer an alternative to transplantation models for preclinical therapeutic evaluation. We have previously described KPC mice, which conditionally express endogenous mutant Kras and p53 alleles in pancreatic cells (*10*) and develop pancreatic tumors whose pathophysiological and molecular features resemble those of human PDA (*11*). Here, we have used the KPC mice to investigate why PDA is insensitive to chemotherapy.

We first compared the effect of gemcitabine on the growth of pancreatic tumors in four mouse models: the KPC mice and three distinct tumor transplantation models (*12*, *13*). Gemcitabine inhibited the growth of all transplanted tumors, irrespective of their human or mouse origin (Fig. 1A), but did not induce apoptosis (Fig. 1B). Rather, proliferation was substantially reduced in all transplanted tumors (fig. S1A). In contrast, most tumors (15 of 17 tumors) in gemcitabine-treated KPC mice showed the same growth rate as in saline-treated controls (Fig. 1C). This is consistent with clinical results in which only 5 to 10% of patients treated with gemcitabine demonstrate an objective radiographic response at the primary tumor site (*3*). Two KPC tumors demonstrated a transient

response as detected by high-resolution ultrasound (*13*), which correlated with high levels of apoptosis (Fig. 1D and fig S1). Additionally, proliferation was diminished in gemcitabine-treated KPC tumors shortly after treatment but to a lesser extent than in transplantation models (fig. S1).

Transplantation of low-passage cells derived from KPC tumors yielded subcutaneous tumors that were sensitive to gemcitabine treatment (Fig. 1A, syngeneics), suggesting that innate cellular differences are unlikely to explain the chemoresistance of KPC tumors. We therefore assessed the metabolism of gemcitabine [2′,2′-difluorodeoxycytidine (dFdC)] to its active, intracellular metabolite, gemcitabine triphosphate [2′,2′-difluorodeoxycytidine triphosphate, (dFdCTP)], by means of high pressure liquid chromatography (HPLC). Consistent with the results of clinical studies (*14*), circulating gemcitabine in wild-type mice was rapidly deaminated to its inactive metabolite, 2′2′-difluorodeoxyuridine (dFdU), resulting in a short half-life for gemcitabine (fig. S2, A and B). dFdCTP was present in transplanted tumor tissues and control tissues, but was undetectable in KPC tumors (table S1). Thus, dFdCTP accumulation in pancreatic tumor tissue distinguished transplantation and KPC models of PDA and correlated with the responsiveness to gemcitabine. Changes in the expression of genes involved in gemcitabine transport are unlikely to explain the difference in gemcitabine accumulation in transplanted and KPC pancreatic tumors (fig. S2, C and D).

Impaired drug delivery is another possible mechanism of chemoresistance (*15*, *16*). We investigated drug delivery by characterizing tumor perfusion in each model. First, we delineated functional vasculature through the intravenous infusion of a plant lectin (*Lycopersicon esculentum*) in anesthetized mice; we followed this with the coimmunofluorescent detection of blood vessels in harvested tissues using an antibody to CD31 (fig. S3). We found that transplanted tumors demonstrated a patent vasculature, whereas KPC tumors had a dysfunctional vasculature. Indeed, only 32% of $CD31^+$ blood vessels in KPC tumors were labeled with lectin as compared with 78 and 100% of vessels in transplanted tumors and normal pancreas, respectively. Second, to evaluate whether intravascular delivery and penetration of small-molecule drugs is impeded in KPC tumors, we intravenously coadministered lectin with the autofluorescent drug doxorubicin (Fig. 2, A and B, and fig. S4) (*17*). Confocal microscopy revealed a marked decrease in doxorubicin delivery to KPC pancreatic tumors as compared with adjacent control tissues and transplanted tumors, confirming an inefficient drug delivery over a short time course. Third, using high-resolution contrast ultrasound we found that the delivery of gas-filled liposomes (microbubbles with a mean diameter of 2.6 μm) was more efficient in transplanted tumors than in KPC tumors (Fig. 2, C and D, and fig. S5). Finally, we performed dynamic contrast enhanced magnetic resonance imaging (DCE-MRI) on transplanted and KPC tumors (Fig. 2, E and F, and fig. S6). After administration of the contrast agent gadolinium-diethyltriaminepentaacetic acid (Gd-DTPA), we observed substantial signal enhancement in the periphery of transplanted tumors, whereas the tumor cores exhibited a variable heterogeneous pattern of enhancement, which is consistent with the central necrosis observed in histological sections (fig. S6C). In contrast, we observed efficient delivery of Gd-DTPA to the tissues surrounding KPC tumors with little or no signal enhancement within the tumor body, despite little necrosis in these tumors (fig S6D). Collectively, these results suggest that drug delivery is impaired in KPC pancreatic tumors.

We next investigated the vascular content and tissue architecture in transplanted and KPC tumors. The viable (peripheral) portions of transplanted tumors were densely vascularized (fig. S7A), and neoplastic cells made direct contact with blood vessels (Fig. 3A). In contrast, blood vessel density was markedly decreased within the parenchyma of KPC and human pancreatic tumors, and vessels were embedded within the prominent stromal matrix that is characteristic of these tumors and of primary human ductal pancreatic cancer (Fig. 3, B to D, and figs. S7 and S8). Neoplastic cells in both KPC and human pancreatic tumors were widely spaced from blood vessels as compared with those in transplanted tumors, reflecting these differences in stromal content (Fig. 3E). Using computer-aided image analysis, we confirmed the paucity of vasculature in an independent cohort of 18 human PDA specimens as compared with normal pancreatic tissues and chronic pancreatitis (CP) samples (Fig. 3F and fig S9). Our findings demonstrate that increased vascular content is not a prerequisite for ductal pancreatic cancer progression and suggest that the hypovascularity and vascular architecture of PDA tumors may impose an additional limitation to therapeutic delivery.

We hypothesized that disrupting the stroma of pancreatic tumors might alter the vascular network and thereby facilitate the delivery of chemotherapeutic agents. We studied an inhibitor of the hedgehog (Hh) pathway because paracrine Hh signaling from neoplastic cells to stromal cells promotes stromal desmoplasia (*18*, *19*). Binding of Hh ligands to the Patched1 receptor relieves repression of the 12-transmembrane protein Smoothened (Smo), resulting in activation of the Gli family of transcription factors. Although Sonic Hedgehog (Shh) is overexpressed in the neoplastic cells of both human (*20*) and KPC (*10*) pancreatic tumors, Gli activity is restricted to the stromal compartment (*21*).

IPI-926 is a semisynthetic derivative of cyclopamine (the chemical structure is shown in fig. S10) that potently inhibits Smo (EC_{50} = 7nM) with a long half-life (10.5 hours in CD1 mice) and a high volume of distribution (11 L/kg in CD1 mice). The detailed characterization of IPI-926 in cell-based and in vitro assays will be published separately. Daily oral administration of 40mg/kg of IPI-926 to KPC mice resulted in a measurable accumulation of drug in PDA tissues (fig. S11A) and a significant decrease in the expression of Gli1, a transcriptional target of the Hh pathway (fig. S11B). The effects of Smo inhibition on tumor histopathology and perfusion were investigated in KPC mice after 8 to 12 days of treatment with IPI-926 or gemcitabine, alone or in combination (IPI-926/gem). In contrast to mice treated with vehicle or gemcitabine, which exhibited profuse desmoplastic tumor stroma, mice treated with IPI-926 or IPI-926/gem were depleted of desmoplastic stroma, resulting in densely packed ductal tumor cells (fig. S12, A to D). The effect of Smo inhibition on the stroma was also evidenced by a decrease in Collagen I content (fig. S12, E to H). These differences were not apparent in mice treated for only four days (fig. S13, I to L). However, coimmunofluorescence performed on tumors treated for four days with vehicle or IPI-926 found a reduced proliferation in α-smooth muscle actin (αSMA)–positive stromal myofibroblasts (figs. S11C and S13, A and B). This decrease in proliferation was balanced by an increase in proliferation of αSMA-negative cells (fig. S11D).

Smo inhibition also had a profound effect on the tumor vasculature, with a significantly higher mean vessel density (MVD) noted in the tumors from IPI-926–treated mice (Fig. 4A and fig. S14, A to D). This effect was most notable in IPI-926/gem treated mice, in which the MVD approximated that of normal pancreatic tissue. An increased CD31 content was also present after 4 days of treatment (fig. S14, E to H). At this early time point, numerous isolated CD31-positive cells were noted, which is consistent with the active formation of new endothelial precursors after Smo inhibition. Indeed, coimmunofluorescence for proliferation and endothelial markers confirmed a significant increase in proliferating endothelial cells after IPI-926 treatment (figs. S11E and S13, C and D). The increased MVD observed in IPI-926–treated mice also correlated with a more effective delivery of doxorubicin to tumor tissues (Fig. 4B and fig. S14, I to L).

[1]Cancer Research UK, Cambridge Research Institute, The Li Ka Shing Centre, Robinson Way, Cambridge CB2 ORE, UK. [2]Abramson Family Cancer Research Institute, University of Pennsylvania, Philadelphia, PA 19104, USA. [3]Departments of Oncology and Pathology, The Sol Goldman Pancreatic Cancer Research Center, Sidney Cancer Center and Johns Hopkins University, Baltimore, MD 21287, USA. [4]Department of Gastroenterology, Ruijin Hospital, Shanghai Jiaotong University School of Medicine, Shanghai 200025, China. [5]Department of Surgery, University Hospital Dresden, Fetscherstrasse 74, 01307 Dresden, Germany. [6]Clinical Research and Public Health Sciences Division, Fred Hutchinson Cancer Research Center (FHCRC), and University of Washington, Seattle, WA 98109, USA. [7]Oncology Franchise, Merck and Company, North Wales, PA 19454, USA. [8]Department of Histopathology, Addenbrooke's Hospital, Cambridge University Hospitals National Health Service (NHS) Foundation Trust, Cambridge CB2 2QQ, UK. [9]M. D. Anderson Cancer Center, University of Texas, Houston, TX 77030, USA. [10]Division of Hematology and Oncology, University of Pittsburgh Medical Center, Pittsburgh, PA 15213, USA. [11]Infinity Pharmaceuticals, Cambridge, MA 01239, USA.

*These authors contributed equally to this work.
†To whom correspondence should be addressed. E-mail: david.tuveson@cancer.org.uk

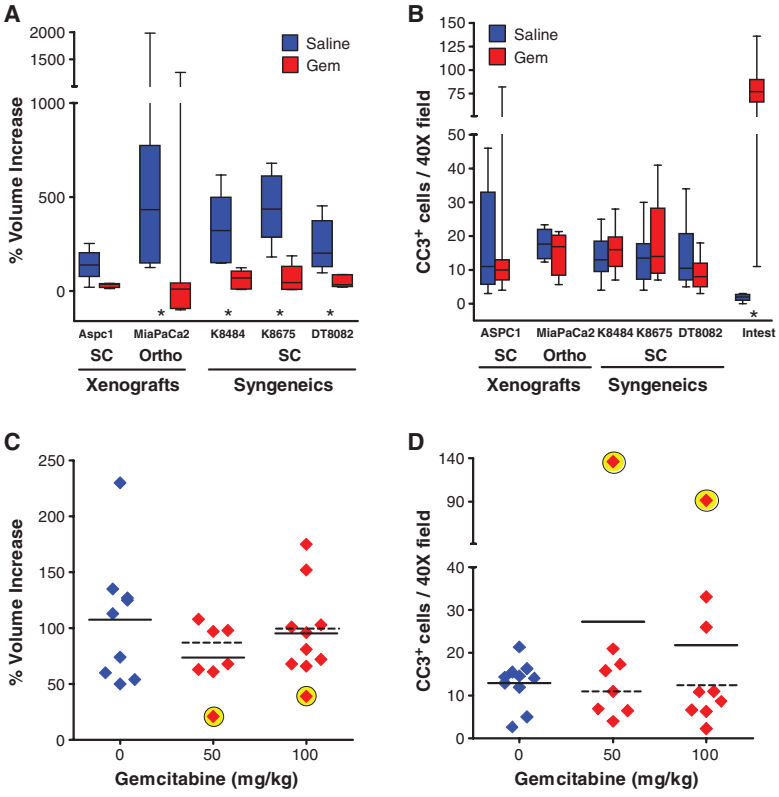

Fig. 1. Pancreatic tumors in KPC mice are largely resistant to gemcitabine. Mice bearing pancreatic tumors were treated systemically with gemcitabine (*$P < 0.05$, Mann-Whitney U rank sum test). Solid lines indicate the mean and dashed lines indicate the mean without responders. (**A**) Percent change in tumor volume in transplantation models (*13*) treated with saline (blue) or 100 mg/kg gemcitabine, Q3Dx4 (red). (**B**) Gemcitabine treatment did not induce tumor cell apoptosis in the transplantation models as measured by immunohistochemistry (IHC) for CC3. (**C**) Percent change in volume of tumors in KPC mice treated with saline (blue), 50 mg/kg, or 100 mg/kg of gemcitabine, Q3Dx4 (red). Two of 17 KPC tumors responded transiently to gemcitabine, as assessed by ultrasonography (yellow). (**D**) Increased apoptosis was evident only in the KPC tumors that transiently responded to the drug (yellow).

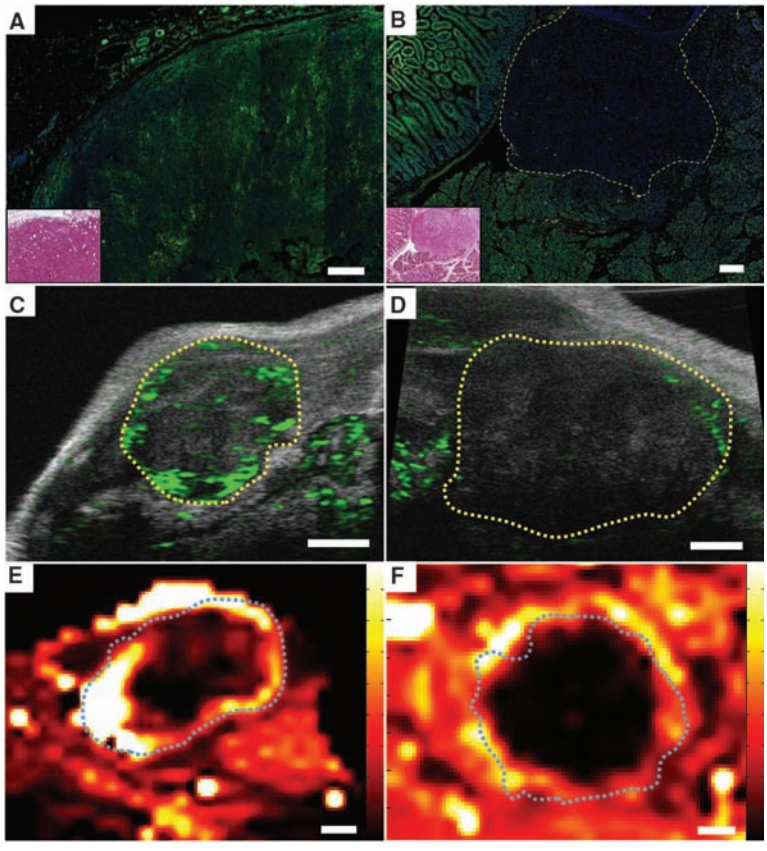

Fig. 2. Pancreatic tumors in KPC mice are poorly perfused. Direct immunofluorescent detection of plant lectin (red) and doxorubicin (green) infused into transplanted (**A**) and KPC (**B**) tumors, along with hematoxylin and eosin–stained adjacent sections (inset). Scale bar, 200 μm. Doxorubicin was effectively delivered to transplanted tumors ($n = 5$ tumors) but poorly delivered to KPC tumors ($n = 4$ tumors) relative to surrounding tissue. Perfusion of microbubbles (green) into transplanted (**C**) and KPC (**D**) tumors visualized with contrast ultrasonography. Transplanted tumors were well perfused ($n = 6$ tumors) as compared with KPC tumors ($n = 8$ tumors). Tumors are outlined in yellow. Scale bars, 1 mm. DCE-MRI demonstrated increased perfusion and extravasation of Gd-DTPA (high delivery is indicated by white or yellow) in (**E**) transplanted tumors ($n = 6$ tumors) as compared with (**F**) KPC tumors ($n = 6$ tumors). Tumors are outlined in blue. Scale bars, 2 mm.

We found that the concentration of gemcitabine metabolites in KPC tumors was elevated by 60% after 10 days of pretreatment with IPI-926/gem (Fig. 4C) ($P = 0.04$, Mann-Whitney U rank sum test). These data suggest that depletion of pancreatic tumor stroma stimulates angiogenesis and consequently augments drug delivery. Whole-tissue mRNA microarray analysis revealed no significant differences in proangiogenic vascular endothelial growth factor (VEGF) expression between vehicle and IPI-926–treated tumors (table S2).

We then investigated the effects of Smo inhibition on cell proliferation and apoptosis. Although IPI-926 alone specifically decreased the proliferation of stromal myofibroblasts, it had little effect on overall cellular proliferation, which is consistent with the finding that conditional Smo deletion in pancreatic cells does not alter the progression of mutant Kras-induced pancreatic tumors (*22*). IPI-926/gem–treated tumors harbored many dead and dying cells as evidenced by a significant increase in staining for the apoptotic marker cleaved caspase 3 (CC3) (Fig. 4D).

Lastly, we performed an intervention survival study on KPC mice, monitoring tumor volume biweekly by means of three-dimensional ultrasonography. KPC mice treated with gemcitabine alone or IPI-926 alone showed no survival benefit in comparison with vehicle-treated controls. In contrast, combination treatment with IPI-926/gem extended the median survival of KPC mice from 11 days to 25 days ($P = 0.001$, log rank test), yielding a hazard ratio of 0.157 ± 0.458 95% confidence interval (CI) (Fig. 4E). Most IPI-926/gem–treated tumors (14 of 17 tumors) exhibited a transient decrease in size within 1 to 2 weeks of treatment (fig. S15). In contrast, only a minority of tumors treated with gemcitabine (2 of 10 tumors) or IPI-926 (2 of 10 tumors) demonstrated objective ultrasonographic responses to treatment. In addition, IPI-926/gem treatment resulted in a significant decrease in metastases to the liver ($P = 0.015$, Fisher's exact test) (Fig. 4F). Investigating the biology of tumors at endpoint, we found no differences in the expression of genes associated with gemcitabine resistance in IPI-926/gem–treated tumors (fig. S11G). However, the hypovascularity of IPI-926/gem–treated tumors was restored at endpoint because the MVD in IPI-926 was similar to controls (fig. S11H).

The general resistance of pancreatic cancer to systemic therapies is unusual among common carcinomas and was not predicted by preclinical models (*23*). Chemotherapeutic agents share two properties: a short half-life and a small therapeutic index (the range of concentration between efficacy and toxicity). Poor tissue perfusion will necessarily produce a substantial decrease in total exposure to drugs with a short half-life. We hypothesize that pancreatic tumors are poorly perfused relative to normal tissues and other tumors and that this is due to aspects of tumor architecture that are specific to the KPC model and to human PDA. Indeed, two groups using contrast-enhanced endoscopic ultrasound have recently reported that human pancreatic ductal adenocarcinomas are poorly perfused and that this feature distinguishes PDA from endocrine tumors and inflammatory diseases of the pancreas (*24*, *25*). A deficient nonangiogenic vasculature that limits drug delivery may also help explain why patients with pancreatic cancer show a poor response to anti-VEGF therapy (*26*).

To counteract this barrier to drug delivery, we propose that agents with a long half-life and a high therapeutic index should be the focus of preclinical investigations in pancreatic cancer. We have provided a proof-of-principle that a drug that disrupts a proposed determinant of poor perfusion in PDA, the desmoplastic stroma, can facilitate the delivery and enhance the efficacy of gemcitabine. Unexpectedly, this drug, which inhibits the Hh signaling pathway through effects on Smo, also increased tumor vascular density, contrasting with earlier work that demonstrated a pro-angiogenic role for Hh signaling during development and in adults (*27*, *28*). Ultimately, the vascular content of KPC tumors returned to lower levels, suggesting that the tumors can adapt to chronic Smo inhibition. Although most of the tumors in KPC mice likewise resumed growth after a transient response, our results nonetheless may open new avenues for improving the delivery

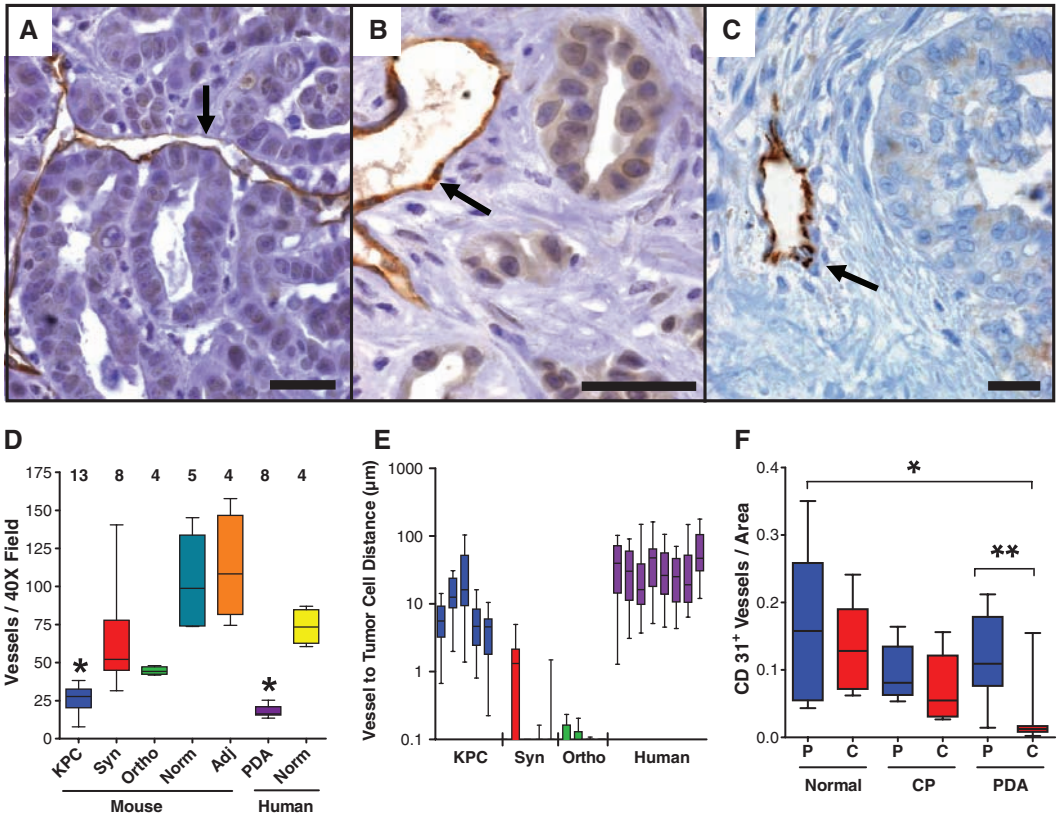

Fig. 3. Pancreatic tumors in KPC mice and humans have diminished vascularity. CD31 IHC from transplanted (**A**), KPC (**B**), and human (**C**) pancreatic tumors (scale bar, 20 μm). Arrows denote blood vessels. Neoplastic cells from transplanted tumors made direct contact with blood vessels, whereas those in KPC and human tumors were more distantly spaced because of prominent stroma. (**D**) MVD was measured in KPC tumors (KPC), syngeneic autografts (Syn), orthotopic xenografts (Ortho), adjacent surrounding tissues in KPC tumors (Adj), human pancreatic tumors (PDA), and normal pancreas from mice and humans (Norm). KPC and human pancreatic tumors were poorly vascularized as compared with transplanted tumors and normal tissues (*$P < 0.004$, Mann-Whitney U rank sum test). (**E**) The distance separating blood vessels and neoplastic cells was significantly higher in KPC tumors and human PDA than in transplanted tumors ($P < .02$, Mann-Whitney U rank sum test). (**F**) Computer-aided image analysis of MVD found human pancreatic tumors ($n = 18$ tumors) to be poorly vascularized as compared with normal pancreas ($n = 5$ samples) and chronic pancreatitis ($n = 5$ samples) samples (*$P < 0.0015$, **$P < 0.0001$, Mann-Whitney U rank sum test). Peripheral (P) and central (C) regions of tissues were distinguished.

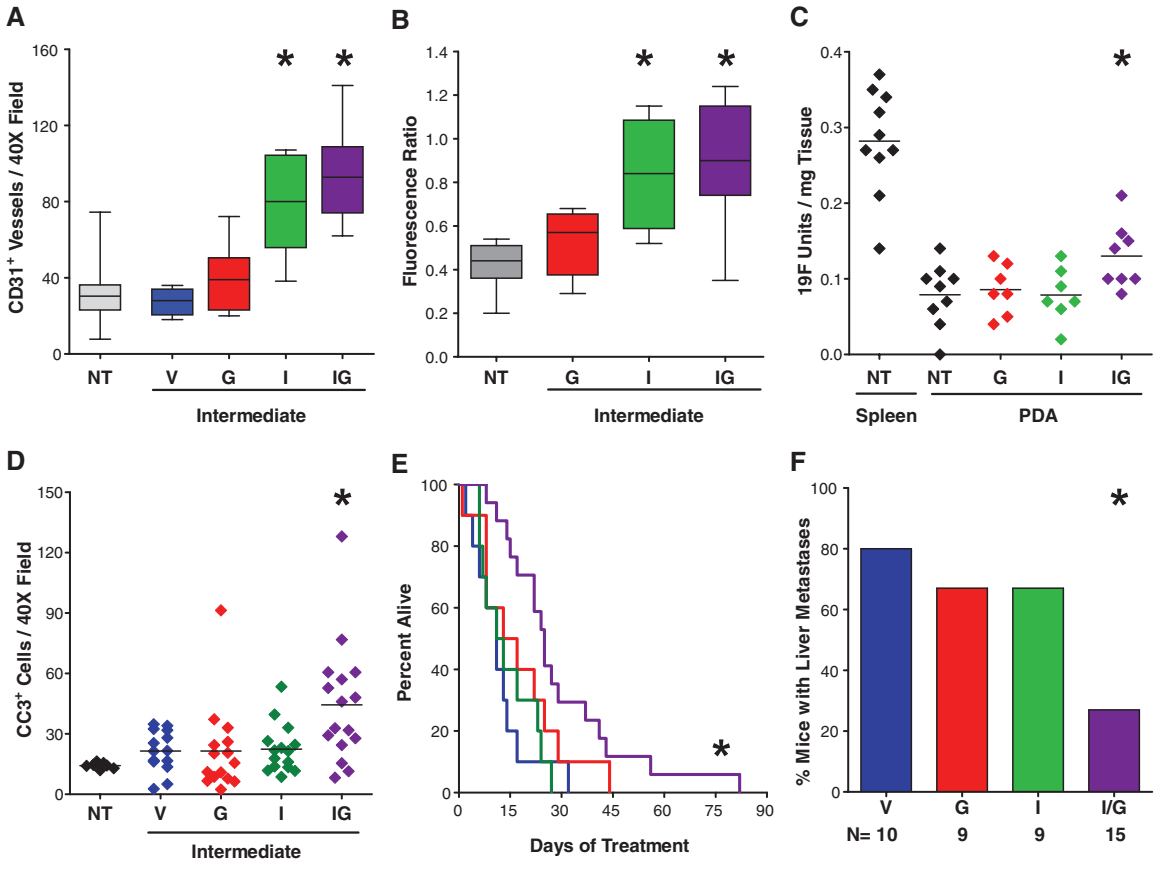

Fig. 4. Smoothened inhibition facilitates gemcitabine delivery and extends survival. KPC mice were treated for 8 to 12 days with no treatment (NT), vehicle (V), gemcitabine (G), IPI-926 (I), or IPI-926/gem (IG). (**A**) MVD was elevated after IPI-926 or IPI-926/gem treatment ($P < 0.05$, Mann-Whitney U rank sum test). (**B**) Doxorubicin fluorescence was elevated after IPI-926 alone or IPI-926/gem treatment (*$P < 0.02$, Mann-Whitney U rank sum test). (**C**) After treatment with the indicated 10-day regimens, all mice were administered a single dose of gemcitabine, and the concentration of fluorine-bearing metabolites was determined in extracted samples by means of ^{19}F nuclear magnetic resonance. Gemcitabine metabolite concentration was elevated in IPI-926/gem–treated tumors ($P = 0.04$, Mann-Whitney U rank sum test). (**D**) IHC for CC3 revealed increased apoptosis in IPI-926/gem–treated tumors ($P = 0.008$, Mann-Whitney U rank sum test). (**E**) IPI-926/gem treatment significantly extended survival in KPC mice ($P = 0.001$, log-rank test; hazard ratio = 0.157 ± 0.458, 95% CI 6.36). (**F**) Fewer liver metastases were observed in IPI-926/gem KPC mice (*$P = 0.015$, Fisher's exact test).

and efficacy of therapeutics in patients with pancreatic cancer.

References and Notes

1. D. Li, K. Xie, R. Wolff, J. L. Abbruzzese, *Lancet* **363**, 1049 (2004).
2. H. A. Burris III *et al.*, *J. Clin. Oncol.* **15**, 2403 (1997).
3. M. Tempero *et al.*, *J. Clin. Oncol.* **21**, 3402 (2003).
4. C. J. Bruns *et al.*, *Int. J. Cancer* **102**, 101 (2002).
5. T. Shimamura *et al.*, *Cancer Res.* **67**, 9903 (2007).
6. A. Verma *et al.*, *Clin. Cancer Res.* **14**, 2476 (2008).
7. J. X. Duan *et al.*, *J. Med. Chem.* **51**, 2412 (2008).
8. D. Melisi *et al.*, *Mol. Cancer Ther.* **7**, 829 (2008).
9. R. M. Schultz *et al.*, *Oncol. Res.* **5**, 223 (1993).
10. S. R. Hingorani *et al.*, *Cancer Cell* **7**, 469 (2005).
11. R. H. Hruban *et al.*, *Cancer Res.* **66**, 95 (2006).
12. N. Cook, K. P. Olive, K. Frese, D. A. Tuveson, *Methods Enzymol.* **439**, 73 (2008).
13. Materials and methods are available as supporting material on *Science* Online.
14. J. L. Abbruzzese *et al.*, *J. Clin. Oncol.* **9**, 491 (1991).
15. O. Tredan, C. M. Galmarini, K. Patel, I. F. Tannock, *J. Natl. Cancer Inst.* **99**, 1441 (2007).
16. A. I. Minchinton, I. F. Tannock, *Nat. Rev. Cancer* **6**, 583 (2006).
17. M. J. Egorin, R. C. Hildebrand, E. F. Cimino, N. R. Bachur, *Cancer Res.* **34**, 2243 (1974).
18. R. L. Yauch *et al.*, *Nature* **455**, 406 (2008).
19. J. M. Bailey *et al.*, *Clin. Cancer Res.* **14**, 5995 (2008).
20. S. P. Thayer *et al.*, *Nature* **425**, 851 (2003).
21. H. Tian *et al.*, *Proc. Natl. Acad. Sci. U.S.A.* **106**, 4254 (2009).
22. O. Nolan-Stevaux *et al.*, *Genes Dev.* **23**, 24 (2009).
23. J. I. Johnson *et al.*, *Br. J. Cancer* **84**, 1424 (2001).
24. A. Sofuni *et al.*, *J. Gastroenterol.* **40**, 518 (2005).
25. H. Sakamoto *et al.*, *Ultrasound Med. Biol.* **34**, 525 (2008).
26. E. Van Cutsem *et al.*, *J. Clin. Oncol.* **27**, 2231 (2009).
27. R. Pola *et al.*, *Nat. Med.* **7**, 706 (2001).
28. S. J. Langer, A. P. Ghafoori, M. Byrd, L. Leinwand, *Nucleic Acids Res.* **30**, 3067 (2002).

29. We thank the animal care staffs of the Cambridge Research Institute (CRI), University of Pennsylvania Translational Research Labs, FHCRC, and University Hospital Dresden as well as the histology and genomics cores at CRI, and P. Calses for technical assistance. We also thank B. Bean of Transnetyx Inc. for developing high-throughput genotyping assays for the KPC mice. This research was supported by the Lustgarten Foundation, the University of Cambridge and Cancer Research UK, The Li Ka Shing Foundation and Hutchison Whampoa Limited, the National Institute for Health Research Cambridge Biomedical Research Centre, and NIH (grants CA101973, CA111292, CA084291, and CA105490 to D.A.T.; K08 CA106610 to C.I.-D.; and CA15704 and CA114028 to S.R.H.). S.R.H. was supported by a grant from the Mead Foundation. Preliminary studies were supported by a grant from the University of Pennsylvania/GlaxoSmithKline Alternative Drug Discovery Initiative. K.P.O. and K.K.F. were supported by NIH under Ruth L. Kirschstein National Research Service Awards F32CA123939-02 (K.P.O.) and F32CA123887-01 (K.K.F.). In addition to being an officer of Infinity Pharmaceuticals, J.A. is a member of the Senior Advisory Boards of Constellation Pharma and Auspex Pharma. Cancer Research Technology, which is associated with Cancer Research UK, has filed a U.S. provisional patent application related to this work.

Supporting Online Material

www.sciencemag.org/cgi/content/full/1171362/DC1
Materials and Methods
SOM Text
Figs. S1 to S15
Tables S1 and S2
References

26 January 2009; accepted 23 April 2009
Published online 21 May 2009;
10.1126/science.1171362
Include this information when citing this paper.

New Products

Continuous Flow Reactor

The Uniqsis FlowSyn continuous flow reactor allows the user to conduct multiple flow chemistry experiments in a single run, making it suitable for reaction optimization, profiling, or scale-up. The optional Multiple Experiment Package integrates the FlowSyn reactor with a Gilson FC203B or FC204 fraction collector to produce a compact system capable of running up to 10 sequential experiments with different reaction times, temperatures, and reagent ratios. Setting up 10 experiments takes only a few minutes: The user needs only to set up one reaction completely, and the process is replicated to conduct a series of experiments, with individual parameters easily modified using a simple spreadsheet interface. Two protocols are available. In fractionation mode, reaction products are collected in programmed fractions. In optimization mode, product is collected in a single vial during a programmable window.

Uniqsis
For information +44-(0)-845-864-7747
www.uniqsis.com

Stackable Shakers

The MaxQ 8000 series of stackable shakers offer high levels of performance and reliability for laboratories that need to shake large quantities of flasks in a minimal space. The shakers offer several unique features, such as run points and set points for temperature, speed, and time that are displayed simultaneously for convenient run cycle monitoring. A built-in high efficiency particulate air filter minimizes the chance of cross-contamination and ensures that the air inside the chamber remains clean. A fold-down door with an ergonomically designed handle allows the shaker platform to slide out for easy sample loading. A flip-down latch on the quick-release base prevents the shaker from running if the platform is not secure. All stacking hardware is included. The chamber of the shaker is crevice-free stainless steel with curved corners and a built-in drain.

ThermoFisher Scientific
For information 508-742-5254
www.thermofisher.com

Laser Scanning Microscope

The LSM 7 MP laser scanning microscope is tailored to the needs of multiphoton microscopy. Offering flexibility, a compact design, and ease of use, it generates high-resolution microscopic images for a wide diversity of experiments in biomedical and basic research. Because it includes two scanners in one compact system, two lasers with different wavelengths can be used sequentially or simultaneously for specimen imaging and manipulation. A wide range of detectors and filter equipment, and an extensive line of accessories, enable system customization. The LSM 7 MP is designed for recording high-resolution images of fluorescent structures. The applications extend from high-resolution three-dimensional imaging in long-term observations of development processes and functional imaging in conjunction with simultaneous photomanipulation to imaging in combination with electrophysiological measuring.

Carl Zeiss
For information +49-(0)-3641-642770
www.zeiss.de/micro

Microplate Washer and Dispenser

The EL406 1536-well Microplate Washer Dispenser offers fast and efficient microplate washing and reagent dispensing in 1,536-well, 384-well, and 96-well microplates. The instrument combines washing with up to three reagent dispensers, eliminating the need for separate instruments for each assay wash and reagent dispense step. The patented Dual-Action manifold performs applications from gentle washing of loosely adherent cell monolayers to complex washing routines. The EL406 incorporates the integrated patent-pending Ultrasonic Advantage to reduce clogged manifold tubes. A valve switching module automates reagent switching of up to four different buffers. Reagent dispensing is available in both peristaltic and microprocessor-controlled syringe drive reagent dispensing technologies. The EL406 is compatible with the BioStack Microplate Stacker to automate processes involving up to 50 standard-height microplates.

BioTek Instruments
For information 888-451-5171
www.biotek.com

Extreme Ultraviolet Spectrometer

The 251MX X-ray and extreme ultraviolet spectrometer is for wavelength dispersive spectral measurements from 0.6 nm to 20 nm. The 251MX provides corrected, flat-field spectra with its selection of specially designed diffraction gratings. Data are acquired quickly and easily with direct-detection charge-coupled detectors. The clean stainless steel chamber and vacuum-prepared internal components allow efficient pumping for high vacuum or ultrahigh vacuum applications. The 251MX's small footprint simplifies integration into other systems. The two available gratings (for 0.6 to 6 nm or 5 to 20 nm) have square groove profiles. The laminar design helps to reduce effects of high diffracted orders. The corrected grating designs deliver high-resolution spectra. This standalone spectrograph enables simultaneous spectral detection over a wide range.

McPherson
For information 978-256-4512
www.McPhersonInc.com

Electronically submit your new product description or product literature information! Go to **www.sciencemag.org/products/newproducts.dtl** for more information.

Newly offered instrumentation, apparatus, and laboratory materials of interest to researchers in all disciplines in academic, industrial, and governmental organizations are featured in this space. Emphasis is given to purpose, chief characteristics, and availabilty of products and materials. Endorsement by *Science* or AAAS of any products or materials mentioned is not implied. Additional information may be obtained from the manufacturer or supplier.

POSITIONS OPEN

SOUTHERN RESEARCH

DIRECTOR OF VIROLOGY
Antiviral Drug Discovery

Southern Research Institute is seeking outstanding applicants for a Director of Virology in our Drug Discovery Division. The successful candidate will report to the vice president of drug discovery. The Division uses an interdisciplinary approach to translate basic research into FDA-approved drugs. We are particularly interested in attracting a scientist with an outstanding research program in virology with translational potential toward the identification or characterization of therapeutic targets. Candidates with an interest in collaboration with medicinal chemists, biochemists, the high throughput screening center, and our contract research groups are particularly encouraged to apply. To be considered, applicants must possess a Ph.D. in virology or related discipline and an established track record of research support. The successful candidate will be expected to maintain grant-based funding for his/her research and to manage and mentor existing independent investigators. This is a significant role within the Institute. The successful candidate will also be expected to set the future strategy and continue to grow our efforts in antiviral drug discovery. Applications should include curriculum vitae, a one- to two-page description of prior research experience, and a description of future research goals.

Southern Research Institute, a not-for-profit research organization affiliated with the University of Alabama at Birmingham (UAB), has annual revenues in excess of $70 million and employs approximately 600 professional, technical, and support personnel. The Institute focuses on three therapeutic areas: infectious diseases, oncology, and central nervous system disease. Five anticancer drugs and a sixth that protects patients against the side effects of chemo- or radiotherapy were discovered by Institute personnel and are now used in the clinic. Several other new anticancer agents are currently in development or undergoing clinical trials. The Institute also has research programs to identify new agents for the treatment of a variety of bacterial, viral, and fungal diseases and these efforts are expected to lead to additional clinical development candidates. In conjunction with this, a state-of-the-art BSL-3/animal and in vitro BSL-3 facility is available for research with risk group 3 pathogens and is approved for select agent use. As part of a large, biomedical research community in Birmingham, we are committed to providing a stimulating and rewarding work environment. Close proximity to the UAB campus facilitates interactions with academic and clinical personnel that are affiliated with UAB basic science departments, Comprehensive Cancer Center, Cell Matrix and Adhesion Center, Center for AIDS Research, Center for Biophysical Sciences and Engineering, and the Alabama Drug Discovery Alliance.

Birmingham, Alabama, has a high standard of living afforded by a moderate climate, beautiful wooded terrain, outstanding residential communities and schools, world-class health care, below average cost of living, and a vibrant arts and entertainment scene. Southern Research Institute offers an excellent compensation and benefits package.

You must apply for this position online at our **website: http://www.southernresearch.org** for **Position sr-02188.** *Equal Opportunity Employer/Affirmative Action.*

POSTDOCTORAL POSITION available in molecular immunology to study B cell antigen receptor signaling and differentiation, B1 cell origin and function, and/or B cell:T cell interaction. Background in immunology, molecular biology, or biochemistry preferred. Send curriculum vitae and three reference names to: **Thomas L. Rothstein, M.D., Ph.D. c/o Jodi Schad, The Feinstein Institute for Medical Research, 350 Community Drive, Manhasset, NY 11030. E-mail: jschad@nshs.edu; fax: 516-562-2533.**

POSITIONS OPEN

FACULTY POSITION IN VIROLOGY/VIRAL IMMUNOLOGY
Department of Microbiology and Immunology
University of Oklahoma Health Sciences Center
Oklahoma City, Oklahoma

The Department of Microbiology and Immunology at the University of Oklahoma Health Sciences Center invites applications for a 12-month, tenure-track position at the **ASSISTANT PROFESSOR** level. This position is expected to fill a programmatic role within the Department, and emphasis will be afforded to those individuals whose research expertise is in virology and/or viral immunology. Applicants are expected to have a Ph.D. or equivalent degree with at least two years of postdoctoral training. The successful candidate will be expected to establish and maintain an extramurally funded research program in his/her field of study and to participate in the team-taught medical and dental curricula within the Department and to play a role in supporting our strong graduate training program. The Department currently has 14 full-time, tenured or tenure-track faculty with more than 40 extramural grants and contracts and a multi-million dollar yearly budget. According to the latest NIH data, the Department ranks in the top third in medical school microbiology department funding. For an overview of the Department, visit our **website: http://www.oumedicine.com/academictemplate_landing.cfm?id=4252.**

Submit curriculum vitae, description of research interests and teaching experience, and the names and contact information, including e-mail addresses, of three references to: **Chair of the Search Committee, Department of Microbiology and Immunology, BMSB-1053, 940 S. L. Young Boulevard, Oklahoma City, OK 73104.** Applications will be reviewed as they are received. *The University of Oklahoma is an Equal Opportunity/Affirmative Action Employer. Applications from women and ethnic minorities are strongly encouraged.*

POSTDOCTORAL RESEARCH POSITION
Molecular Biology/Microbiology

A Postdoctoral position is available immediately in **Dr. Ji Yu**'s group at the University of Connecticut Health Center (**website: http://www.uchc.edu**). Candidates are sought to join a collaborative effort in studying the germination of mechanism of bacterial spores. The focus of the research will be (1) to develop superresolution optical microscopy methods to elucidate protein localizations in bacterial spores and (2) to understand receptor protein dynamics during the germination process. Early-career scientists with a background in molecular and cell biology, who are seeking an interdisciplinary adventure, are encouraged to apply. Interested candidates should electronically send their curriculum vitae to **Dr. Ji Yu, e-mail: jiyu@uchc.edu.** *An Equal Opportunity Employer, Minorities/Females/Veterans/Persons with Disabilities.*

POSTDOCTORAL ASSOCIATE POSITION
Stem Cell Biology and Immunology

We seek motivated researchers. Will conduct research on molecular processes that regulate hematopoietic stem cell function, immune regulation, or natural killer cell biology. Will plan and perform experiments, analyze data, publish results, and assist in training graduate students. Ph.D. in bioscience or related field required. Apply to **position #027084** online **at website: http://www.upstate.edu** and/or **contact William G. Kerr, Ph.D., State University of New York Upstate Medical University, e-mail: kerrw@upstate.edu.** *An Affirmative Action/Equal Employment Opportunity/ADA Employer committed to excellence through diversity.*

POSTDOCTORAL POSITION to study the role of microtubules in intracellular trafficking and signal transduction pathways in cancer. Strong background in molecular and cell biology required. Confocal microscopy and animal experience desirable. Contact: **e-mail: kab2018@med.cornell.edu; visit website: http://www.cornellpharmacolgy.org/faculty/labs/giannakakou.**

MUSC Health
MEDICAL UNIVERSITY of SOUTH CAROLINA

Vice President for Medical Affairs and Dean of Medicine

The Medical University of South Carolina is the state's largest medical complex and is comprised of six academic colleges: Dental Medicine, Graduate Studies, Health Professions, Medicine, Nursing and Pharmacy and the University Medical Center. The campus occupies over 50 acres and 120 buildings and has a total annual operating budget of nearly $2 billion including over $200 million in extramural research and sponsored programs. The University employs over 11,000 staff, including almost 1,600 faculty members and 600 housestaff, and serves over 2,500 students.

The Vice President for Medical Affairs and Dean of Medicine provides leadership for clinical and academic services. As chief academic and administrative official for the College of Medicine, the Dean will guide the development and articulation of the vision for the College, encouraging programs consistent with its mission and promoting high standards of accomplishment. The VP/Dean reports to the President of the University, and has overall responsibility for the College of Medicine including leading the College strategic and long range plans; recruiting chairs and directors, maintaining a faculty of excellence in the educational, research and clinical programs. Educational oversight includes the full spectrum of undergraduate, graduate and continuing medical programs. In the research arena, the VP/Dean enhances the already extensive research initiatives, facilitates linkages between the clinical and basic sciences, and fosters translational science. Clinical responsibilities include continuing to integrate the physician practice plan, working with neighboring hospitals in outreach and working closely with the MUSC academic hospital partners: Medical University Hospital Authority, Children's Hospital, the Institute of Psychiatry and the Ralph Johnson Veterans Administration hospital and clinics. Other duties involve interacting with the state legislature and the public at large, participating in private fundraising, and promoting the quality of life on the Medical University campus for both faculty and students.

Qualified applicants should demonstrate: (1) a distinguished record of scholarly and professional achievement that merits an appointment with tenure at the rank of full professor; (2) senior administrative experience that indicates ability to lead a complex academic enterprise; (3) recognition for excellence in academic clinical practice and leadership; (4) commitment to excellence in research and experience with linking biomedical research activities to clinical practice; (5) commitment to excellence in education at all levels of the medical experience; (6) ability to raise resources for the activities of an academic medical center; (7) ability to plan strategically and work collaboratively with others, both within MUSC and outside; (8) effectiveness in representing the programs and needs of an academic medical center to governmental and other groups.

Applications will be accepted until August 31, 2009 or until the position is filled. Please send letters of inquiry, nominations and applications to: **David Cole, M.D., McKoy Rose Professor of Surgery, Chair, Dept. of Surgery, Chair, Search Committee for VP/Dean College of Medicine c/o Office of the President, Medical University of South Carolina, Colcock Hall, 179 Ashley Avenue, Charleston, SC 29425, Email: carsonb@musc.edu**

The Medical University of South Carolina is an equal opportunity/affirmative action employer.

Unil
UNIL | Université de Lausanne
| live knowledge |

THE FACULTY OF BIOLOGY AND MEDICINE OF THE UNIVERSITY OF LAUSANNE, SWITZERLAND INVITES APPLICATIONS FOR A POSITION OF

Assistant Professor in Neurobiology in the Department of Cell Biology and Morphology

This non tenure-track position will start in fall 2009 or later.

The successful applicant is expected to :

- Establish an independent research program supported by external funds to complement the activities of the DBCM (http://www.unil.ch/dbcm), focused on the study of the biological bases of normal and pathological nervous system function. Candidates interested in the mechanisms controlling neuronal cell death and proliferation are encouraged to apply,
- Participate in the teaching of morphology, cell biology and neurosciences at both undergraduate and postgraduate levels to medical and biology students,
- Share administration responsibilities in the management of the Department.

At the undergraduate level teaching in French is required, but a period of adjustment can be granted.

Applicants must have a record of outstanding research and teaching experience and have shown themselves capable of obtaining external funds.

The job description is available on the Web at the address www.unil.ch/fbm/page64812.html. For further information, please contact Prof. Mehdi Tafti (mehdi.tafti@unil.ch), chair of the search committee.

Applicants should send their full curriculum vitae, a list of publications in which the five most significant ones are identified, a brief summary of the past, present and future research program, and at least three names of reference before August 14th, 2009 to Prof. Patrick Francioli, Dean of the Faculty of Biology and Medicine, Rue du Bugnon 21, CH-1011 Lausanne, Switzerland.

The University of Lausanne wishes to promote the access of women to academic careers and encourages applications from women.

Fonds Fund
InBev-Baillet Latour

NOMINATIONS ARE INVITED

for the prestigious

INBEV-BAILLET LATOUR HEALTH PRIZE

of a value of 200,000 euro

Theme for 2010: "Metabolic Disorders"

The INBEV-BAILLET LATOUR FUND has set itself the goals of encouraging work of great value to humanity and to reward such work through prizes or study grants. The Fund is largely active in medical research, Belgian heritage, university education and the Olympic movement. The InBev-Baillet Latour Fund has been awarding the InBev-Baillet Latour Health Prize within the medical research field, since 1979. This Prize offers the highest monetary reward of all science prizes awarded in Belgium.

The InBev-Baillet Latour Health Prize is intended to encourage fundamental research and its useful applications. Its goal is to reward the scientific achievement of the laureate and to promote the continuation of his/her research.
The first InBev-Baillet Latour Health Prize winner was Sir James W. Black. Since its inception, the Prize has honoured and encouraged 24 researchers. Prize-winners: www.inBev-baillet-latour.com, see chapter Medical Research, Health Prize, Winners.

Nominations InBev-Baillet Latour Health Prize 2010

If you wish to propose a candidate for the InBev-Baillet Latour Health Prize 2010 whose theme is Metabolic Disorders, please download the nomination form from the websites: **www.frs-fnrs.be** or **www.inbev-baillet-latour.com**
The deadline for nominations is 30th September 2009.

For more information and submission or for an application, please contact Chantal Mairesse, Adviser F.R.S.- FNRS
T +32 (0)2 504 92 40 / F +32 (0)2 504 92 92 / mairesse@fnrs.be
Fonds National de la Recherche Scientifique
Rue d'Egmont 5 / 1000 Bruxelles / Belgium

InBev-Baillet Latour Fund
Alain De Waele, secretary-general
T +32 (0)16 27 61 59
GSM + 32 (0)473 80 84 73
E-mail: alain.dewaele@iblf.be

Professor Kari Alitalo, H.R.H. Princess Mathilde, Professor Seppo Ylä-Herttuala

AWARDEES INBEV-BAILLET LATOUR 2009

PROFESSOR KARI ALITALO
Professor at the Finnish Academy of Science; Scientific Head in the Biomedicum Helsinki centre of Excellence, specialising in Molecular, Vascular and Cancer Biology.

PROFESSOR SEPPO YLÄ-HERTTUALA
Head of the Cardiologic Disorders and Diabetes Type 2 department of the A.I. Virtanen Research Institute for Molecular Sciences at the University of Kuopio; Vice-President of the European Community for Genetic and Cell Therapy.

Professors Alitalo and Ylä-Herttuala were awarded the 2009 Health Prize for their pioneering research on cardiovascular disorders and more precisely for their contribution to a better understanding of angiogenesis and lymphangiogenesis and their regulation by growth factors and receptors. Thanks to the achievements of these scientists, the impact of the formation of arteries and the lymphatic system on heart and vascular disorders and cancer, is widely recognized.

The
NATIONAL RESEARCH COUNCIL
OF THE NATIONAL ACADEMIES

is accepting applications for a

Postdoctoral Research Award

tenable at the

Walter Reed Army Institute of Research *in* Silver Spring, MD

The goal of this research is to identify new compounds for the treatment of Post-Traumatic Stress Disorder (PTSD). Evaluation of treatment strategies will use a rodent model of PTSD to identify candidate compounds for advanced development. Proposals involving evaluation of novel pharmacological strategies are encouraged. The successful proposal will build upon the ongoing construction and implementation of the model and extension to specific applications consistent with the program mission.

Qualified applicants should have a recent Ph.D. in Experimental Psychology, Neuroscience, Pharmacology or a related field with a strong background in behavioral assessment.

For further information contact:

Raymond F. Genovese, Ph.D.
US Army Medical Research and Materiel Command (WRAIR)
503 Robert Grant Avenue
Silver Spring, MD 20910-7500
Telephone: 301/319-9721; Fax: 301/319-9905
E-mail: Raymond.Genovese@US.Army.Mil

Eligibility:	**US and non-US citizens**
Duration:	**one year with possible renewal for a total of three years maximum**
Stipend:	**$50,600 per annum for recent Ph.D. recipients; higher for additional experience**
Other:	**relocation, professional travel, health insurance**
Deadline:	**August 1, 2009**

Applicant must initiate dialogue with prospective Adviser at the lab before application deadline. Applications must be submitted online directly to the NRC at:

www.national-academies.org/rap

Questions may be directed to the NRC at
202-334-2760 (telephone)
or rap@nas.edu.

THE NATIONAL ACADEMIES
Advisers to the Nation on Science, Engineering, and Medicine

DEPARTMENT HEAD AND DEAN POSITIONS, ZHEJIANG UNIVERSITY, CHINA

Founded in 1897, Zhejiang University is committed to the highest standards of excellence in education and research, and has been at the forefront of academic scholarship in China.
We invite applications and nominations for visionary leaders in the following Departments and Colleges:

Positions:
- Head, Department of Mathematics (Website: **http://www.math.zju.edu.cn**)
- Head, Department of Physics (Website: **http://physics.zju.edu.cn/**)
- Head, Department of Chemistry (Website: **http://www.chem.zju.edu.cn/**)
- Dean, College of Electrical Engineering (Website: **http://ee.zju.edu.cn/**)
- Dean, College of Civil Engineering and Architecture (Website: **http://www.ccea.zju.edu.cn/**)

Duties:
- Managing properties, financial and human resources of the department or the college as authorized by the University
- Improving the quality of teaching and learning, and research skills
- Recruiting outstanding faculty, training current teachers, and building highly qualified faculty team
- Promoting international cooperation and exchange

Term and Recruitment Package:
- Four years term, eligible for reappointment for another term, and full-time work (or no less than 9 months each year)
- State-of-the-art research facilities and strong supporting staffs
- Internationally competitive start-up support, salary and benefits according to qualifications and experience

Requirements:
- Recognized academic qualification, distinguished leadership and effective relationship with both national and international professionals
- Relevant management experience of high education
- Regardless citizenship, fluency in English or Chinese

Documentation Details:
- A comprehensive curriculum vitae
- Copies of advanced degrees and certification of present employment
- List of publications in the past five years
- Addresses, telephone numbers, and e-mail addresses of three to five scholars as references
- A letter of interest addressing vision objectives and goal

Closing Date: **July 30, 2009**
Contact Person: **Zhu Xiaoyun**
E-mail: **lxbzp@zju.edu.cn** (for department head position applicants) or **fezju@zju.edu.cn** (for dean position applicants);
Tel: +86-571-88981390 88981345; Fax: **+86-571-88981976**

THE HUMAN FRONTIER SCIENCE PROGRAM

2010 POSTDOCTORAL FELLOWSHIPS

Registration deadline: **27 August 2009**

Submission deadline: **10 September 2009**

The Human Frontier Science Program offers fellowships for basic research training in the life sciences across national and scientific boundaries. Applications are invited for two international programs that support postdoctoral investigators who explore new research areas. Frontiers of science are often found at the interface of biological and physical sciences and participation of scientists from outside the life sciences is welcomed. Fellows are expected to be exposed to new literature and methods during the tenure of their award while their previous expertise should be reflected in the research project. Applications from female candidates are particularly encouraged.

- **Long-Term Fellowships** are reserved for applicants with a PhD in biology to embark on a new project in a different field of the life sciences. Preference is given to applicants who propose an original study in biology that marks a departure from their previous Ph.D. or postdoctoral work.

- **Cross-Disciplinary Fellowships** are open to applicants with a PhD from outside the life sciences e.g. in physics, chemistry, mathematics, engineering or computer sciences and who have had limited research experience in biology during their previous training.

Fellowships are for three years and offer flexible use of funding in the final year. The start of the third year can be deferred for up to two years while being supported through other funds thus allowing extension of the training in the host laboratory. Third year funding can also be used to return to the home country allowing the fellows to apply for the

- **HFSP Career Development Award** which provides a 3-year start-up grant of $100.000/year to help establish their first independent laboratory. HFSP fellows can apply after completion of at least two full years of postdoctoral training abroad.

Nationals from any country can apply for training only in a supporting country, while nationals of the HFSP supporting countries can apply to work in any other country. Current supporting members are: *Australia, Canada, the European Union, France, Germany, India, Italy, Japan, the Republic of Korea, New Zealand, Norway, Switzerland, the United Kingdom, and the United States of America*.

The detailed application guidelines are available at http://www.hfsp.org/how/appl_form.php.

20 YEARS IN PURSUIT OF EXCELLENCE 1989 2009

广州医学院招聘长江学者特聘教授

Guangzhou Medical University (GMU) is a highly qualified academic institution located in Guangzhou, China. As one of its unique subordinate divisions, GMU boasts Guangzhou Institute of Respiratory Diseases (GIRD), a worldwide famous institute led by professor Nanshan Zhong (钟南山). GIRD focuses on a wide range of research interests including but not limited to emerging respiratory diseases (SARS, avian flu, etc), asthma, COPD, chronic cough and lung cancer. In 2007, GIRD was selected by the Ministry of National Science and Technology as the "State Key Laboratory of Respiratory Diseases". Currently, GMU aims at greater improvement and advances in scientific teamwork. We welcome motivated biomedical scientist to join us as a:

Cheung Kong (Chang Jiang) Scholarship Guest Professor

Eligible applicant should be:

- Aged below 45 years old.
- A PhD-bearing assistant (or higher-ranked) professor in an academics-oriented institution, competent for teaching with core curriculum.
- With demonstrated competence in leadership and protocol implementation
- With good command of English communication.
- Experienced in collaboration with multicultural and multidisciplinary teams.
- Able to work in Guangzhou Medical University for at least 9 months per year.

Applicants should submit a CV with contact information of three referees; a summary of accomplished research (both in English and Chinese); a future research plan.

Once accepted, you will be endowed with :

1) Regular salary payment at full professor level according to GMU regulation, plus ¥100,000 per year special professorship allowance by The Education Ministry of China for 5-years.
2) At least ¥2,000,000 research funding, favorable working space and living condition.

Contacts:
Jessica Ma , Chen Guanquan
Address: 195 Dongfeng Xi Road, Guangzhou, China 510182
Telephone: 86-20-81340481
Fax: 86-20-81340454
Email: gybgs@vip.163.com; guanquanchen@yahoo.com.cn
Web: www.gzhmc.edu.cn

MOUNT SINAI SCHOOL OF MEDICINE

A faculty position for a **Senior Postdoctoral Fellow** or **Research Assistant Professor** with experience in embryonic stem cell biology is available in the Center of Excellence for Novel Approaches to Neurotherapeutics at Mount Sinai School of Medicine (New York, NY). Preference will be given to candidates interested in establishing translational research in experimental models of neuropsychiatric disorders using either pluripotent human/mouse embryonic stem cells (mhESCs) or induced pluripotent stem cells (iPSCs).

Qualified applicants should send their CV to: **Ms. Hayley Fivecoat, Program Manager, Department of Psychiatry, Mount Sinai School of Medicine, NYC, e-mail: hayley.fivecoat@mssm.edu**.

SCHOOL OF MEDICINE
INDIANA UNIVERSITY

Faculty Positions
Department of Pharmacology and Toxicology

The Department of Pharmacology and Toxicology at the Indiana University School of Medicine in Indianapolis invites applications from outstanding individuals for faculty positions at the **Assistant or Associate Professor** level. More senior individuals with exceptional credentials may be considered. A Ph.D. and/or M.D. degree with at least three (3) years of postdoctoral research experience and strong evidence of productivity are required, and grant support is desirable. Preference will be given to individuals with outstanding scholarship in the fields of molecular and cellular pharmacology or toxicology, but other exceptional candidates will be considered. Competitive start-up packages include ample laboratory space and access to exceptional core research facilities. Successful candidates will be expected to develop strong extramurally supported research programs, to contribute to an already strong, collaborative research environment, and to excel in mentoring graduate and postgraduate trainees. Within the Department of Pharmacology and Toxicology, a number of research areas exemplify the integrative nature of our discipline. Research in the department focuses on various aspects of neuropharmacology and sensory systems. We also attempt to understand mechanisms of drug action on gene expression and on signal transduction cascades. Understanding how oxidative stress and various chemicals modify normal cell cycles and thus cause tumor growth is the major emphasis of faculty members in Toxicology and in the Indiana University Cancer Center. More information about the department can be found on our website (**http://pharmtox.iusm.iu.edu**).

Interested individuals should send a curriculum vitae, a research prospectus, and the names and addresses of three (3) references. Application materials will only be accepted in electronic format by submission to the attention of the **Search Committee, Department of Pharmacology and Toxicology, IU School of Medicine** at **phtxjobs@iupui.edu**.

IU is an EEO/AA Employer, M/F/D.

university of groningen

Faculty of Mathematics and Natural Sciences
Full Professor Position in Applied Physics
Chair: Physics of Organic Semiconductors

The Faculty of Mathematics and Natural Sciences of the University of Groningen is seeking applications and nominations for a full professor position in applied physics, chair: Physics of organic semiconductors. The Faculty offers Bachelor, Master and Ph.D. programmes over the entire range of natural sciences. The research in the Faculty is organized in research institutes. The vacancy exists within the Zernike Institute for Advanced Materials, which unites 21 research groups in physics, chemistry, and biology. The Zernike Institute is one of six recognized National Centres of Excellence in The Netherlands. Its mission is design and functionality of novel materials, with a focus on understanding and control at the microscopic level. The Institute thrives on a strong interdisciplinary nature of its research programme and frequent collaborations between its various groups.

The complete text of the advertisement, listing requirements, conditions and instructions for application, can be found on the website of the Zernike Institute for Advanced Materials at: **http://www.rug.nl/zernike/vacancies/atmsc/pos**

Review of applications will begin **August 1st, 2009**, and will continue until the position is filled. Applications in hard copy should be addressed to: **Head of Personnel Department, University of Groningen, P.O. Box 72, 9700 AB Groningen, The Netherlands; Prof. J. Knoester, Zernike Institute for Advanced Materials, University of Groningen, Nijenborgh 4, 9747 AG Groningen, The Netherlands**; By E-mail (Word or PDF) to: **m.h.derix@rug.nl**. When applying please mention the vacancy number: **AT209220**.

Griffith UNIVERSITY

Rewarding excellence

Griffith University is committed to excellence in teaching and research. The University has five campuses and over 37,000 students in the high growth Brisbane-Gold Coast corridor in Australia. The University has an excellent working environment and a positive culture which supports staff development and encourages innovation, diversity and creativity.

Area of Strategic Investment – Drug Discovery with a focus on infectious diseases

As part of the University's agenda to build reputation and recognition, eight areas of strategic investment (ASI) have been identified. One of these eight is the area of Drug Discovery with a focus on infectious diseases. The University is seeking to appoint a Professor of Medicinal Chemistry and a Professor of Molecular Virology to work in the area of drug discovery. Successful applicants will be offered a five year appointment. A further continuing appointment may be offered at the completion of the five-year term, subject to funding and satisfactory performance. Applications are invited for the following vacancies:

Professor of Medicinal Chemistry

This position will be located within The Eskitis Institute for Cell and Molecular Therapies which commands an international reputation and has four experienced chemistry groups specialising in drug discovery projects. This position will be based on the Nathan campus.

The Professor of Medicinal Chemistry will play a key role in developing medicinal chemistry activities at Eskitis and in building a critical mass of medicinal chemistry expertise as well as strongly pursuing their own research agenda.

Post Doctoral and PhD scholarships

Opportunities may become available with the expansion of the Medicinal Chemistry Group. Expressions of interest are invited from suitable candidates for either post doctoral or PhD scholarship opportunities.

Enquiries: Professor Ron Quinn, Director, email: r.quinn@griffith.edu.au

Reference: ESK0229/09

Closes: 17 July 2009

Professor of Molecular Virology

This position will be located within the Institute for Glycomics which has an international reputation in carbohydrate science and a strong focus in drug discovery. This position will be based on the Gold Coast campus.

The Professor of Molecular Virology will provide leadership for a Molecular Virology group in the area of infectious diseases and will also be expected to achieve excellence in their own research.

Post Doctoral and PhD scholarships

Opportunities may become available with the expansion of the Molecular Virology Group. Expressions of interest are invited from suitable candidates for either post doctoral or PhD scholarship opportunities.

Enquiries: Professor Mark von Itzstein, Director, email: m.vonitzstein@griffith.edu.au

Reference: GLY0228/09

Closes: 17 July 2009

EOWA

To Apply:

1 | Go to **www.griffith.edu.au/hrm/employment/** for further information on the position and selection criteria or phone +61 7 3735 4010 if you do not have internet access.

2 | Follow the specific application process for that position.

3 | Applications must be lodged electronically. All applications will be acknowledged.

GOLD COAST LOGAN MT GRAVATT NATHAN SOUTH BANK | **www.griffith.edu.au**

TMP Q060167

West Virginia University
Robert C. Byrd Health Sciences Center

Hubert A. and Hazel L. Shaffer Chair of Molecular Genetics

The **Center for Neuroscience** (**www.hsc.wvu.edu/wvucn/**) and the **Department of Behavioral Medicine and Psychiatry** (**www.hsc.wvu.edu/som/bmed/**) at West Virginia University are seeking an established M.D. or Ph.D. scientist for the **Hubert A. and Hazel L. Shaffer Chair of Molecular Genetics**. Candidates should have research expertise in molecular genetics or pharmacogenetics of neuropsychiatric illnesses. The selected candidate will be appointed Associate or Full Professor, lead his or her own research group, assume a lead role in the ongoing development of translational research in neuroscience, and have the opportunity to participate in professional education and graduate training. Candidates should have a strong record of externally funded research, with transferable NIH funding, and a commitment to mentoring junior faculty. The position offers a competitive salary and resources needed to develop a strong research program.

West Virginia University is a land grant Carnegie-designated Doctoral/Research-Extensive institution with approximately 20,000 undergraduate and 5,500 graduate/professional students. The Health Sciences Center includes the Schools of Medicine, Pharmacy, Dentistry, and Nursing, each with health professional and graduate programs. Two new research buildings accommodate our aggressive research growth agenda. Patient care facilities include WVU's 460-bed Ruby Memorial Hospital and 70-bed Chestnut Ridge Psychiatric Hospital. Morgantown is rated one of the best small cities in the U.S. with affordable housing, excellent schools, a picturesque countryside, and many outdoor activities (**www.morgantown.com**).

Review of applications will continue until the position is filled. Applicants should send their curriculum vitae, research plans, and contact information for three references by email to: **cnpositions@hsc.wvu.edu**. Inquiries regarding the position can be directed to: **James M. O'Donnell, Ph.D., Professor and Vice Chair for Research, Behavioral Medicine and Psychiatry, and Assistant Vice President for Research, West Virginia University Health Sciences Center (304-293-2433; jodonnell@hsc.wvu.edu)**.

West Virginia University is an Affirmative Action/Equal Opportunity Employer.

SANFORD SCHOOL OF MEDICINE

Faculty Position

The Division of Basic Biomedical Sciences at the Sanford School of Medicine of The University of South Dakota invites applications for a tenure-track faculty position at the Assistant Professor level. Exceptional applicants at higher levels may also be considered. Applicants must have a Ph.D. and/or M.D., or equivalent degree, and post-doctoral experience. Successful candidates will be expected to develop an independent, externally funded research program. Research in the areas of targeted proteolysis, protein turnover, signal transduction, molecular chaperones, protein quality control or conformational diseases is particularly desired though additional areas will be considered. These topics should relate to the genesis and/or treatment of diseases including, but not limited to, cancer and cardiovascular disease. Preference will be given to applicants whose research complements the existing strengths in protein folding, molecular chaperones, targeted proteolysis, and signal transduction. The successful candidate will also be expected to participate in teaching undergraduate, graduate, and medical students. Excellent start-up funds, state-funded salary commensurate with experience and modern research facilities in the new Lee Medical Building, Vermillion, SD will be provided. Application should include curriculum vitae, a summary of past research and teaching experience, a statement of research interests and future plans, as well as three letters of reference. Apply online at **https://yourfuture.sdbor.edu** posting number 0002203. Review of applications will begin on July 13, 2009 and continue until position is filled.

Women and minorities are encouraged to apply. AA/EOE.

TEXAS A&M UNIVERSITY

Faculty Positions In Circadian Biology

The Department of Biology at Texas A&M University invites applications for faculty positions at the **ASSOCIATE** or **FULL PROFESSOR** level in circadian biology.

We are interested in outstanding circadian biologists with well-funded, internationally recognized research programs. We especially invite applications from researchers who will complement a group of seven faculty in the Center for Biological Clocks Research (CBCR) who use molecular, cellular, physiological and behavioral techniques to study circadian clocks in *Neurospora*, chickens, *Drosophila* and mice. The primary criteria for selection will be excellence and creativity in research and scholarship in circadian biology, including sleep. We strongly encourage applications from candidates who will increase the exposure of our students to a diverse culture.

The successful candidates will be expected to maintain a vigorous, externally funded research program and to contribute to the teaching of undergraduate and graduate students. We offer a highly interactive and collegial research environment, a strong modern infrastructure, and competitive startup packages. More information about our department can be found at www.bio.tamu.edu. For full consideration, applicants should send a letter of intent, *curriculum vitae*, statement of research and teaching interests, and three letters of recommendation by **September 1, 2009** to:

Dr. Paul Hardin
Chair, Circadian Biology Faculty Search Committee
Department of Biology
Texas A&M University
3258 TAMU
College Station, TX 77843-3258

Questions about this search should be directed to **Dr. Hardin** at **clocksearch@mail.bio.tamu.edu**.

Texas A&M University is an Equal Opportunity Employer and has a policy of being responsive to the needs of dual-career couples.

UCL

MRC Laboratory for Molecular Cell Biology
Group Leaders

We are seeking new Group Leaders with research interests in Molecular Cell Biology. The posts will be ideal for scientists wishing to establish independent research careers, but established Group Leaders will also be considered.

The MRC Laboratory for Molecular Cell Biology (LMCB) is located in modern research facilities on the main University College London (UCL) campus in central London. It currently houses the MRC Cell Biology Unit, as well as UCL groups funded by Cancer Research UK, The Royal Society and the Wellcome Trust. Work in these groups is focused on understanding fundamental problems of cell biology and their relation to human disease in a variety of experimental models. The new Group Leaders will be selected to enhance or complement the current research areas. The LMCB has an interactive research environment, excellent facilities with particular expertise in imaging, an innovative four-year Graduate Programme and close links to the UCL scientific community. Further information on the Institute can be found at **http://www.ucl.ac.uk/LMCB/**. Informal enquiries can be directed to **Professor Mark Marsh** (**m.marsh@ucl.ac.uk**).

Successful applicants will be expected to win competitive personal fellowships from funding agencies such as the Wellcome Trust, Cancer Research UK or the MRC. Applicants should send a full Curriculum Vitae, an outline of research interests, and the names and addresses of four referees to:

Professor Mark Marsh, MRC LMCB
UCL, Gower Street, London WC1E 6BT
United Kingdom

Closing date: **31st July 2009**

UCL Taking Action for Equality.

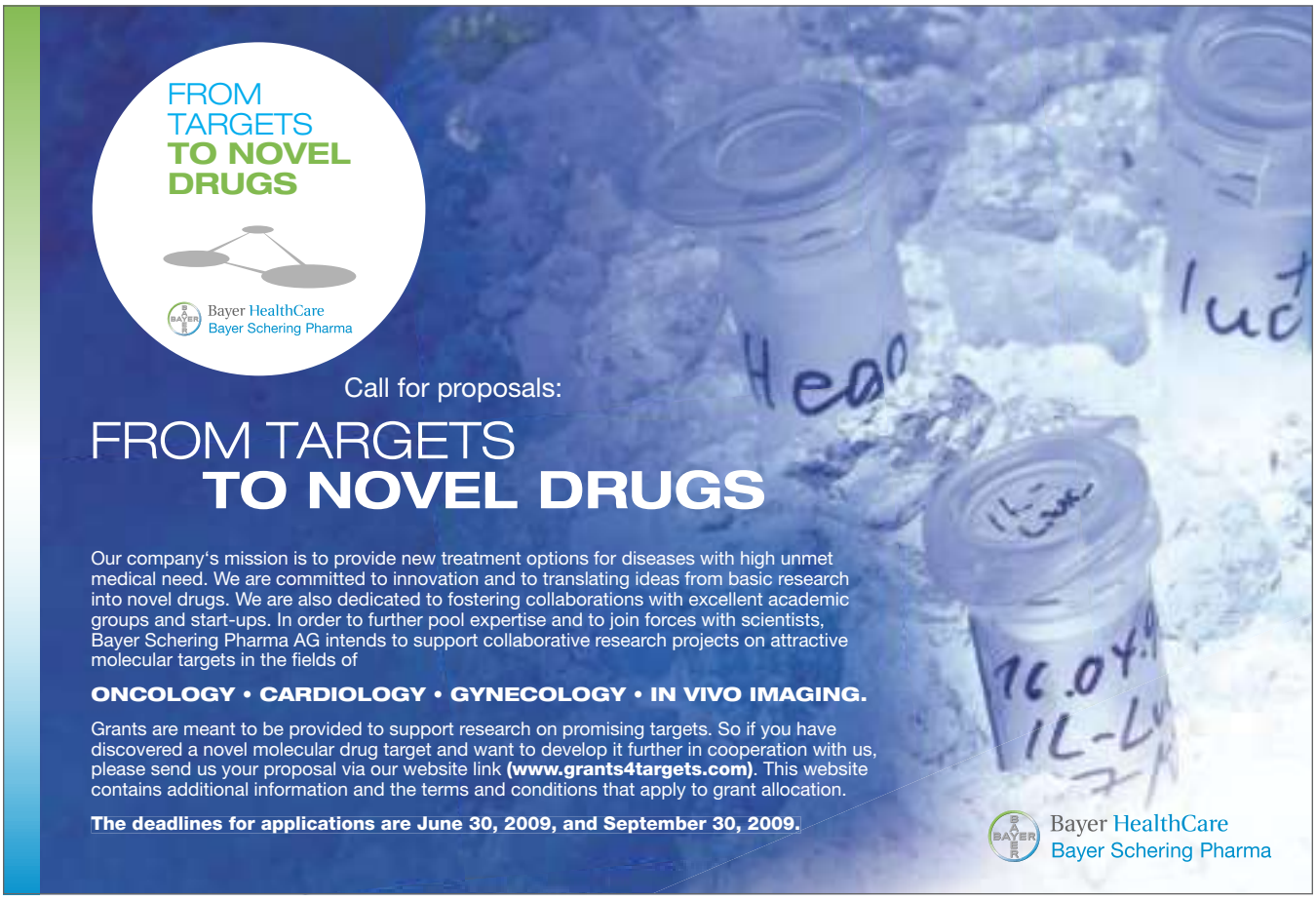

JAXA International Top Young Fellowship

The Institute of Space and Astronautical Science (ISAS), part of the Japan Aerospace Exploration Agency (JAXA) is one of the leading space science centres. In collaboration with universities, it conducts a full range of space science activities, including topics such as the structure and origin of the universe; formation of the earth and solar system; utilization of the space environment for microgravity experiments; and space engineering to enable these activities by developing future technologies.

As part of its on-going commitment to remain at the forefront of space science, ISAS/JAXA has established a prestigious new fellowship program, the JAXA International Top Young Fellowship. This is designed to attract outstanding, highly motivated, young researchers in any of the space science fields covered by ISAS/JAXA to work in Japan for 3 (extendable to 5) years. The excellent remuneration package (see below) includes generous travel support so that the fellows can extend their international profile, as well as developing collaborations within Japan.

This Fellowship program will offer the special salary to the fellows of 780,000 Japanese Yen/month (equivalent to 93,600 USD/year at a typical exchange rate of 100 JPY/dollar.) The program will provide them with the financial support for expenses for travel and equipment up to a maximum of 2,500,000 Japanese Yen/year

The closing date: **July 15, 2009**

For further information about JAXA International Top Young Fellowship, visit: **http://www.jaxa.jp/employ/index_e.html**

Contact information
Personnel, Research Promotion Office
Institute of Space and Astronautical Science
Japan Aerospace Exploration Agency
E-mail: young_fellowship@jaxa.jp

Weill Cornell Medical College

Weill Cornell Medical College is recruiting an outstanding investigator for the Department of Dermatology

The Weill Cornell Department of Dermatology is recruiting an investigator in cutaneous biology at the Assistant or Associate Professor level. We are seeking outstanding candidates working at the intersection of immunology and cancer biology with relevance to the skin. A successful candidate will be highly motivated and will have a strong independent research program or demonstrate the potential to develop and maintain a strong and independent research program. Applicants must hold an appropriate doctoral degree (M.D., Ph.D. or M.D./ Ph.D.).

The Department of Dermatology has strong ongoing research programs in immunology, neuroimmunology, cancer biology and tissue repair. Weill Cornell Medical College is located adjacent to Rockefeller University and Memorial Sloan-Kettering Cancer Institute. These three institutions have world renowned programs in immunology, molecular biology, cancer biology, pharmacology as well as many other areas of research offering extremely rich opportunities for collaboration.

Interested applicants should submit a copy of their curriculum vitae, funding history, and a letter describing their academic interests to:

Richard D. Granstein, M.D.
Department of Dermatology
Weill Cornell Medical College
1305 York Avenue, 9th Floor
New York, NY 10021
Email: rdgranst@med.cornell.edu

Weill Cornell Medical College is an Equal Opportunity/Americans with Disabilities Act Employer.

ANNOUNCEMENTS

USC UNIVERSITY OF SOUTHERN CALIFORNIA

ADVANCED BIOLOGY TRAINING COURSE IN ANTARCTICA January 2010

"Integrative Biology and Adaptation of Antarctic Marine Organisms"

This National Science Foundation sponsored course will be held in Antarctica at the United States' McMurdo Station for one month, starting January 2010. This is an international course, open to all nationalities. Applications are invited from graduate students currently enrolled in a Ph.D. program, postdoctoral fellows, and early-career faculty who are interested in the study of extreme environments and the biology of Antarctic marine organisms. Full scholarships are available for each participant accepted into the course to cover the cost of travel from home institution to Antarctica, and room and board while in Antarctica. The emphasis of the Antarctic Biology Course is on integrative biology, with laboratory- and field-based projects focused on biological adaptations in extreme environments, with an emphasis on rapid climate change in polar regions. A diverse teaching faculty will offer students the opportunity to study a wide range of Antarctic organisms (bacteria/archaea, algae, invertebrates, and fish), as well as studying several different levels of biological analysis (molecular biology, biomechanics, physiological ecology, species diversity, and evolution).

Deadline for receipt of completed applications is **August 1, 2009**.

For more information and on-line applications, please see:
http://antarctica.usc.edu

The Department of Chemistry and the Center for NanoIntegration Duisburg-Essen (CeNIDE) invite applications for

Two Full Professorships (W3) in Chemistry:
(a) Chair in Physical Chemistry
(b) Chair in Technical Chemistry/Chemical Engineering

We are seeking two internationally renowned scientists with outstanding track records of scientific achievements, who will establish a highly visible research program preferentially in one or more of the following areas:

- Colloidal chemistry
- Functional polymeric materials with an emphasis on reaction engineering
- Functional nanoparticles
- Biomimetic Membranes
- Nanoscale organic inorganic hybrid materials
- Rheological and structural properties of suspensions, dispersions, gels

As the positions will be joint appointments by the Department of Chemistry and CeNIDE and have been identified as part of the University's strategic appointments, competitive start-up packages will be made available. This includes laboratory space in the new Chemistry Building and the NanoEnergy Technology Center. The successful candidates are explicitly invited to play a leading role in the further development of the broad nano-initiative of the University of Duisburg-Essen, represented by CeNIDE.

CeNIDE, established in 2005, is the University's framework for its strategic efforts in nanosciences. 40 research groups from Chemistry, Electrical Engineering, Physics and Mechanical Engineering with a total of about 200 scientists presently participate. CeNIDE research groups are well funded by state, federal and European funding agencies. The German Research Foundation has recognized the strength of nanosciences at the University of Duisburg-Essen by granting three Collaborative Research Centers and a Research Training Network with a combined annual budget of 5.5 Mio. € (one of the highest numbers of cooperative networks funded in the nanosciences in Germany).

The Department of Chemistry with a faculty of 24 tenured professors attracts about 250 new students every academic year. It runs an international graduate program with presently 160 PhD students and has a research income of 3 Mio. € per year. Fundamental research on functional materials linked to the CeNIDE nanosciences activities and/or towards the life sciences is one research focus and of particular importance with regard to the positions to be filled. Supramolecular chemistry, biofilms, water sciences, and chemical education are further foci of the research program. It is expected that the candidates will participate in teaching all relevant courses in Physical or Technical Chemistry, respectively, in the various B.Sc. and M.Sc. study programs at the department.

The preconditions according to the university law § 36 Hochschulgesetz NRW (HG) are a university degree, pedagogical abilities, a doctoral degree and further scientific qualifications. These qualifications may - among others - consist of a junior professorship or a post-doctoral degree (Habilitation).

The Universität Duisburg-Essen is an equal-opportunity employer committed to excellence through diversity and therefore explicitly encourages applications from women. Disabled persons with equivalent qualifications will be considered preferentially.

Candidates are invited to submit their application, including curriculum vitae, publication list, statement of research interests and future research plans at UDE, teaching and fund raising records, as well as documentation of their academic degrees, to the **Dean of the Department of Chemistry, Prof. M. Epple, University of Duisburg-Essen, Universitätsstr. 2, 45141 Essen, Germany; e-mail matthias.epple@uni-due.de.**

It must be clearly stated in the application to which position (i.e. Physical Chemistry or Technical Chemistry) it refers. In the case of a suitable qualification, a candidate may also apply to both positions. Again, this must be clearly stated in the application letter.

You may also contact Prof. M. Epple (Department of Chemistry), Tel. (+49) (201) 183 2413 and Prof. A. Lorke (CeNIDE), Tel. (+49) (203) 379 3265, for further information.

You will find additional information at www.uni-due.de (on the University of Duisburg-Essen), at www.uni-due.de/chemie (on the Department of Chemistry), and at www.cenide.de (on CeNIDE).

POSITIONS OPEN

The **University of Nebraska–Lincoln Institute of Agriculture and Natural Resources** is in the process of enhancing the molecular biosciences in its maize program. There is an expectation that the successful candidates will translate research discoveries into technologies usable in plant species of economic or ecological interest. The Department of Agronomy and Horticulture invites applications for the following positions.

The Plant Quantitative Geneticist/Statistical Genomicist position (**requisition #090232**) is a nine-month, tenure-track, **ASSISTANT/ASSOCIATE/FULL PROFESSOR** position with an 80 percent research and 20 percent teaching appointment. Requires Ph.D. in plant breeding, genetics, agronomy, or other relevant discipline; postdoctoral or private sector competency in genetics, plant breeding, genomics, and bioinformatics relating specifically to improving selection efficiency in maize or other crop species; demonstrable expertise/experience in quantitative genetics, statistical genomics, and bioinformatic approaches to the study of genes that control quantitative traits influencing crop productivity; publication of previous original research in peer-reviewed journals. Successful candidate will have an internationally recognized, competitively funded research program in plant quantitative genetics/statistical genomics relating specifically to improving selection efficiency in maize and other crop species.

The Plant Molecular Physiologist position (**requisition #090229**) is a nine-month, tenure-track, **ASSISTANT PROFESSOR** position with an 80 percent research and 20 percent teaching appointment. Requires Ph.D. in molecular biology/physiology, agronomy/horticulture, or other relevant discipline; postdoctoral or private sector competency in molecular plant physiology relating to plant response and adaptation to abiotic stress; demonstrable expertise/experience in using molecular, biochemical, physiological, genetic, and genomic tools and protocols common to such studies; publication of previous original research in peer-reviewed journals; evidence of written or co-written successful grant applications; and expertise/effectiveness in classroom instruction.

To apply: Go to **website: http://employment.unl.edu** and search for **requisition #090229** for the Plant Molecular Physiologist position or **requisition #090232** for the Plant Quantitative Geneticist/Statistical Genomicist position. Complete the Faculty Academic Administrative Information Form. Attach a letter of application, curriculum vitae, and two personal statements, one describing your research focus/interest and one describing your teaching expertise/experience. Review of applications will begin on August 14, 2009, and continue until the position is filled or the search is closed. Arrange for three letters of reference to be sent electronically by August 14, 2009, to **e-mail: cwendt1@unl.edu.** *The University of Nebraska has an active National Science Foundation ADVANCE gender equity program, and is committed to a pluralistic campus community through affirmative action, equal opportunity, work-life balance, and dual careers.*

Memorial Sloan-Kettering Cancer Center – RESEARCH ASSOCIATE POSITION in Cancer Population Genetics and Genomics. Starting July 1, 2009. Focus on inherited susceptibility to cancers of the breast, ovary, colon, prostate, and lymphoma. Methodologies include whole genome association studies, population genetics, and candidate gene associate studies (see, for example, PubMed ID 18326623; 18251999; 17999359). Applicant must have strong background in population genetics, molecular biology, and high throughput genotyping. Send application and three letters of reference to: **Kenneth Offit, M.D., M.P.H., Clinic Genetics Service, Box 192, Memorial Sloan-Kettering Cancer Center, 1275 York Avenue, New York, NY 10065. Fax: 646-888-4081; e-mail: offitk@mskcc.org.** *Memorial Sloan-Kettering Cancer Center is an Equal Opportunity Employer with a strong commitment to enhancing the diversity of its faculty and staff. Women and applicants from diverse racial, ethnic, and cultural backgrounds are encouraged to apply.*

POSITIONS OPEN

ASSISTANT OR ASSOCIATE PROFESSOR
Center of Excellence for Infectious Diseases

The newly created Center of Excellence for Infectious Diseases at the Paul L. Foster School of Medicine, Texas Tech University Health Sciences Center, El Paso, Texas, is seeking candidates for tenure-track faculty positions at Assistant or Associate Professor level. This is part of a state-funded initiative to enhance research in infectious diseases. The Center is primarily interested in investigators with research interests in molecular immunology, host-pathogen interactions, vaccine development, and animal models for translational studies.

Successful candidates are expected to develop and maintain independently funded research programs in infectious diseases or a related field. The position reports to the co-directors of the Center of Excellence for Infectious Diseases.

Minimum qualifications: M.D. or Ph.D. degree in a related field and at least three years of postdoctoral experience with a strong publication record.

Preferred qualifications: Candidates with funded grant support and experience in emerging infectious diseases and cutting edge technologies are particularly encouraged to apply.

The Center offers competitive salary and startup packages, newly constructed laboratory space, BSL-2 and BSL-3 laboratories, and a supportive interactive environment. Interested candidates must apply online at **website: http://jobs.texastech.edu, requisition #77147** by submitting curriculum vitae, a short write-up of research interests, and three letters of recommendation. For further information, please e-mail or contact:

Manjunath Swamy, M.D.
E-mail: manjunath.swamy@ttuhsc.edu or
Premlata Shankar, M.D.
E-mail: premlata.shankar@ttuhsc.edu
Co-Directors of the Center of Excellence for Infectious Diseases

The positions are open until filled. Application review will begin immediately.

Texas Tech University Health Sciences Center is an Equal Opportunity/Affirmative Action Employer.

FACULTY POSITION

The University of California, San Diego (UCSD) Departments of Psychiatry and Cellular and Molecular Medicine are seeking candidates for a full-time academic faculty position (tenure track/tenured) at the **ASSISTANT** or **ASSOCIATE PROFESSOR** level. Candidates must have a Ph.D. (or M.D.-Ph.D.) degree in molecular genetics or a related field. Individuals should have a documented track record of research in conducting genomewide analyses of CNVs (copy number variations) with respect to identifying risk factors for a wide variety of neuropsychiatric diseases. Collaborations are available to work with research scholars in examining the genetic bases for schizophrenia, bipolar disorders, alcoholism, anxiety disorders as well as post traumatic stress disorder and other serious mental disorders. A proven track record in a research- or academic-related setting and a demonstrated track record in publishing peer-reviewed research articles and obtaining research grants are necessary. Candidates are invited to view the websites of the two departments at: **http://psychiatry.ucsd.edu and http://cmm.ucsd.edu.** The candidate's rank and step will be determined by individual academic qualifications and achievements. Salary is based upon University of California salary scales. Review of applications will begin on June 30, 2009, and continue until the position is filled. Candidates should send curriculum vitae, letter of interest, and any other supporting documents to: **Search Committee P/CMM, UCSD Department of Psychiatry, 9500 Gilman Drive, La Jolla, CA 92093-0603.**

UCSD is an Equal Opportunity/Affirmative Action Employer with a strong institutional commitment to excellence through diversity.

POSITIONS OPEN

ASSISTANT/ASSOCIATE PROFESSOR OF PHYSIOLOGY
Southern Illinois University Carbondale

The Department of Physiology at Southern Illinois University Carbondale's School of Medicine, Carbondale, invites applications for a tenure-track faculty position at the rank of Assistant or Associate Professor effective January 1, 2010. The specific area of research of the candidate should be competitive for extramural funding and preferably complement existing departmental strengths in cancer biology, neuroscience, reproduction, endocrinology, aging, and metabolism/obesity. The successful candidate will be expected to contribute to the medical school, graduate, and/or undergraduate teaching responsibilities of the Department. The position includes a 100 percent time, 12-month, state-funded competitive salary, spacious research facilities, and substantial startup funds. The University has over 22,000 students, making it the second largest public university in Illinois. Applicants must have a Ph.D. (or equivalent degree) and evidence of high-quality research potential. Postdoctoral experience is required. For appointment at the associate level, the candidate should have faculty status at a university (or equivalent), an extramurally funded research program, and a strong record of research productivity as evidenced by a history of extramural funding and extensive publications in scientific journals. Additional departmental information is available at **website: http://www.siumed.edu/physiology/.**

Review of applications will begin July 1, 2009, and will continue until the position is filled. Applicants should submit curriculum vitae and description of research and teaching interests and should arrange to have at least three letters of reference sent to:

Faculty Search Committee
c/o Dr. Peter R. Patrylo
Department of Physiology
School of Medicine
Mail Code 6512
Southern Illinois University Carbondale
1125 Lincoln Drive
Carbondale, IL 62901

SIUC is an Affirmative Action/Equal Opportunity Employer that strives to enhance its ability to develop a diverse faculty and staff to increase its potential to serve a diverse student population. All applications are welcomed and encouraged, and will receive consideration. This is a security sensitive position. Before any offer of employment is made, the University will conduct a preemployment background investigation, which includes a criminal background check.

POSTDOCTORAL POSITIONS available for recent graduates with Ph.D. and/or M.D. degrees with a commitment to research careers in diabetes and related diseases. Studies are being conducted in the areas of islet biology and transplantation, beta cell proliferation, endodermally derived endocrine tissue, immune tolerance and histocompatibility molecules in type 1 diabetes, electrophysiology of ATP-sensitive potassium channels, insulin resistance in aging, diabetic neuropathy, insulin signaling, glucose transporters, lipid synthesis, metabolism, vascular diseases, pregnancy loss and malformations in diabetes. Send curriculum vitae to: **Dr. Michael L. McDaniel, Department of Pathology and Immunology, Campus Box 8118, Washington University School of Medicine, St. Louis, MO 63110. E-mail: mmcdaniel@wustl.edu.** *Affirmative Action/Equal Opportunity Employer.*

MARKETPLACE

Call for Papers

Science Signaling

Science Signaling features top-notch, peer-reviewed, original research. Each week, the journal publishes leading-edge findings in addition to the current features, including Perspectives, Reviews, Protocols, Meeting Reports, Book Reviews, Teaching Resources and the Database of Cell Signaling.

Science Signaling showcases high-impact research in cellular regulation in fields such as molecular biology, development, immunology, neuroscience, microbiology, physiology and medicine, pharmacology, biochemistry, cell biology, bioinformatics and systems biology.

Subscribing to ***Science Signaling*** ensures that you and your lab have the latest cell signaling resources. From basic science to design of therapeutics, from molecules to networks and systems design, read the best source, ***Science Signaling.*** Subscribe at http://pubs.aaas.org/pub7/pub7_setup.asp.

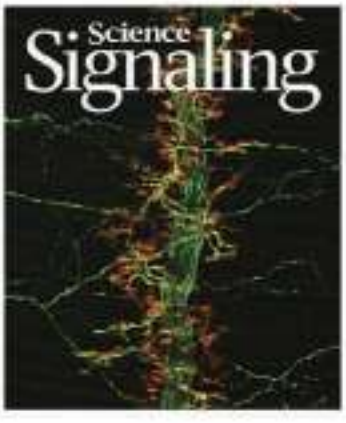

ISSN: 1937-9145

Submit your research that provides new concepts and new understanding of biological signal transduction for consideration at www.sciencesignaling.org/about/help/research.dtl.

Chief Scientific Editor
Michael B. Yaffe, M.D., Ph.D
Associate Professor, Department of Biology
Massachusetts Institute of Technology

Editor
Nancy R. Gough, Ph.D
American Association for the Advancement of Science

Science Signaling
AAAS

www.sciencesignaling.org

R&D Systems Bioactive Proteins

High quality proteins aren't a luxury, they are a necessity.

WHAT'S THE RISK? ✓ Missed opportunities ✓ Non-specific results ✓ Experiments that can't be repeated ✓ Weeks or months of wasted time

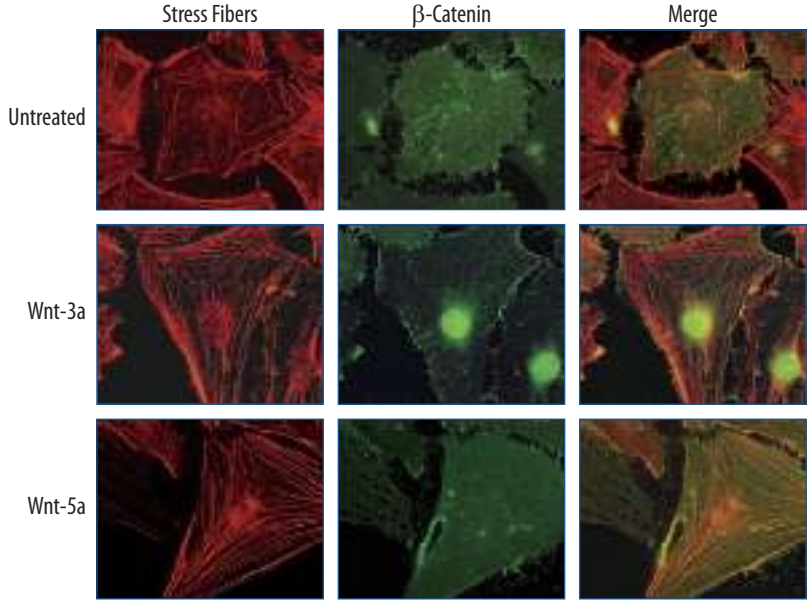

R&D Systems recombinant mouse Wnt-3a (Catalog # 1324-WN) and Wnt-5a (Catalog # 645-WN) promote stress fiber formation in NIH-3T3 cells, while only Wnt-3a promotes nuclear β-Catenin accumulation. Please visit our website for information about our new high purity human Wnt-3a (Catalog # 5036-WNP). *Images Courtesy of Dr. Raymond Habas, Robert Wood Johnson School of Medicine.*

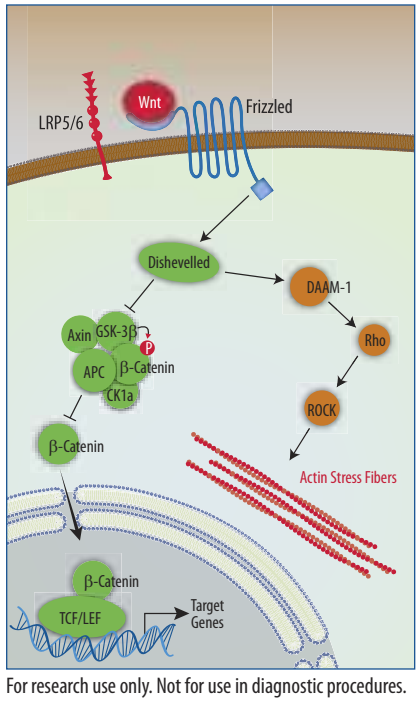

For research use only. Not for use in diagnostic procedures.

R&D Systems has spent almost 25 years building its reputation as a source for high quality proteins.

Every stage of protein development takes place in R&D Systems' laboratories, from cloning of the gene, to protein purification and testing for bioactivity. Because we control all aspects of protein manufacturing, R&D Systems can better control the quality of our products and the technical assistance we offer. Please visit our website at **www.RnDSystems.com/go/Proteins** for more information.

Cancer Development Endocrinology Glycobiology Immunology Neuroscience Proteases Signal Transduction Stem Cells

R&D Systems Tools for Cell Biology Research™

USA & Canada **R&D Systems, Inc.** Tel: (800) 343-7475 info@RnDSystems.com
Europe **R&D Systems Europe, Ltd.** Tel: +44 (0)1235 529449 info@RnDSystems.co.uk
China **R&D Systems China Co., Ltd.** Tel: (800) 988-1270 info@RnDSystemsChina.com.cn

Selection expanding weekly—visit **www.RnDSystems.com/go/request** to sign up for weekly new product updates.

R&D SYSTEMS®